



**HAL**  
open science

# Laser assisted Atom Probe Tomography as a spectroscopic tool to analyze the materials for energy

Deodatta Shinde

► **To cite this version:**

Deodatta Shinde. Laser assisted Atom Probe Tomography as a spectroscopic tool to analyze the materials for energy. Materials Science [cond-mat.mtrl-sci]. Université de Rouen, 2016. English. NNT: . tel-01380304

**HAL Id: tel-01380304**

**<https://hal.science/tel-01380304>**

Submitted on 12 Oct 2016

**HAL** is a multi-disciplinary open access archive for the deposit and dissemination of scientific research documents, whether they are published or not. The documents may come from teaching and research institutions in France or abroad, or from public or private research centers.

L'archive ouverte pluridisciplinaire **HAL**, est destinée au dépôt et à la diffusion de documents scientifiques de niveau recherche, publiés ou non, émanant des établissements d'enseignement et de recherche français ou étrangers, des laboratoires publics ou privés.

# THESE

**Pour obtenir le grade de Docteur**

**Opéré par l'Université de Rouen**

**Spécialité – Sciences des Matériaux**

**Utilisation de la sonde atomique tomographique laser pour les études spectroscopiques des matériaux pour l'énergie**

**Présentée et soutenue publiquement par**

**M. Deodatta SHINDE**

**Thèse soutenue publiquement le 25 Janvier 2016  
devant le jury composé de**

M. Fabrice GOURBILLEAU	Directeur de recherche / CiMAP Caen	Rapporteur
M. Jérôme PLAIN	Professeur des Universités / Université de Technologie Troyes	Rapporteur
M. Satish OGALE	Professeur des Universités / IISER, Pune, INDIA	Président
M. Aurélien CRUT	Maitre de Conférences / Université Claude Bernard Lyon1	Examineur
Mme. Angela VELLA	Maitre de Conférences / Université de Rouen	Directrice de thèse
M. Bernard DECONIHOUT	Professeur des Universités / Université de Rouen	Co-directeur de thèse
M. Lorenzo RIGUTTI	Maitre de Conférences / Université de Rouen	Co-encadrant

**Thèse dirigée par Angela VELLA (Directrice) et Bernard DECONIHOUT (Co-directeur),**

**Groupe de Physique des Matériaux, UMR CNRS 6634**

**Université et INSA de Rouen**



## **Dedication**

**Dedicated**

***To my Family.....***

*for their constant support, encouragement and love to pursue my dreams.....*



## Acknowledgements

First and foremost I would like to express my sincere thanks to my director of the thesis Dr. Angela Vella for providing me an excellent opportunity to undertake the Ph.D. in Université de Rouen. This thesis would not be possible without her constant motivation and encouragement throughout the course of this work. Fruitful discussion with her at numerous occasions made it possible to understand the subject very well. Special thanks to Prof. Bernard Deconihout (co-director) and Dr. Lorenzo Rigutti (co-supervisor) for their guidance at various instances. Bernie's experience and Lorenzo's innovative ways of presenting the findings were the key advantages of working with them.

I also take this opportunity to thank the Jury panel of the thesis, Dr. Fabrice Gourbilleau from Centre de Recherché sur les Ions, les Matériaux et la Photonique (CiMAP), Caen, France, Prof. Jérôme Plain from Laboratoire de Nanotechnologie et Instrumentation optique (LNIO), Université de Technologie Troyes, France and Dr. Aurélien Crut from Institut Lumière Matière (ILM), Lyon for reviewing the thesis and giving their insightful comments and suggestions to improve the same.

I owe a special thanks to the Prof. Satish Ogale from Indian Institute of Science Education and Research (IISER), Pune for recommending me to work on this Ph.D. position and who was also the President of Jury committee of the thesis. During the course of this thesis I have worked with him and it was always an enriching experience. His infinite energy and enthusiasm gives an inspiration to work harder and efficiently.

I am grateful to the Director of the laboratory Groupe de Physique des Matériaux (GPM), Prof. Philippe Pareige, for providing me an ideal working environment. The administrative staff of the laboratory was always friendly and helping, thanks to Christine, Germain, Caroline, Romain and Agnes.

Working on the subject which needs rigorous experimentation is not possible without extended helping hand from other members of the laboratory. I would like to thank Fabien Cuvilly and Emmanuel Cadel for training and time to time help for sample preparation using SEM/FIB method, Williams Lefebvre and David Hernández-Maldonado for STEM imaging of the specimens, Jonathan Houard for training me to use the atom probe effectively and Gerald da Costa for his assistance to rectify the problems related to the analysis software and answering the questions related to it very patiently.

I am quite fortunate to be part of the ERIS (l'Equipe de Recherché en Instrumentation Scientifique) team, one of the pioneering research groups in the field of atom probe

tomography around the globe. Your job becomes easy and more importantly joyful when you are surrounded by one of the best expertise in the field and are willing to help you. Sharing the new findings and difficulties encountered through regular group meetings were helpful to increase the understanding of the subject as well as gave new ideas and inputs to this work. Big thanks to all members of the ERIS team for their support. Special thanks to Prof. Francois Vurpillot and Dr. Ivan Blum for their insightful suggestions and comments. I am also thankful to the past and present Ph.D. and post-doctoral fellows of the group namely Dr. Laurent Arnoldi, Dr. Nicolas Sevelin-Radiguet, Dr. Elena Silaeva, Dr. Matthieu Gilbert, Lorenzo Mancini and Aurore Gaillard for their friendly and assisting environment.

I cannot thank enough to Prof. Beatrice Hannoyer for her generous help and support at number of occasions since the beginning of the thesis.

I am always grateful to the friends from the lab for giving me so many moments to be cherished and good social life outside the lab, as well as their helping hand whenever needed. Thanks to Nooshin, Isabelle, Mohit, Monika, Megha, Manon, Mykola, Yana, Claire for keeping friendly atmosphere in the lab. Also living away from home for so long would not be so easy without friends like Harsh, Vineet, Irfan, Pranav, Abhishek, Anirudha, Shreya, Saicharan, Sangan and so many others.

And finally, I would like to express my gratitude towards my lovely family. None of my achievements would be possible without constant support and encouragement from my family and so does this thesis as well. My sisters, Santoshi, Sharada, Sapana and Vidya are four pillars of my success and my brother Somdatta is the backbone. Thanks to Mr. Digambar and Mr. Sameer as well for their kind support. I cannot express my affection enough towards my nephew Aaditya and nieces Sakshi, Gauri and Arya for their unconditional love which always motivated me to work harder. Of course the blessings of my parents from heaven were always source of my energy to achieve the goals in life.

Mr. Deodatta Ramchandra SHINDE  
Rouen, France

# Table of Contents

## Acknowledgements

List of Figures..... *i*

INTRODUCTION..... 1

CHAPTER 1 : Overview.....5

1.1 Introduction..... 5

1.2 Optical Properties of Materials..... 6

1.2.1 Optical Absorption and Thermal Properties at Nanoscale..... 7

1.2.2 Optical Emission at nanoscale..... 13

1.3 Choice of Material..... 20

1.3.1 Types of Absorbers..... 21

1.3.2 Specimens analyzed to study the absorption and thermal behavior of nanostructured materials (CERMETS) by LaAPT..... 23

1.3.3 Specimen analyzed to study the correlation between optical emission and structural properties..... 33

1.4 Conclusions..... 35

CHAPTER 2 : Experimental Methods..... 39

2.1 Introduction..... 39

2.2 Atom Probe Tomography : State of the art..... 41

2.2.1 History..... 41

2.2.2 Basic Principle of APT..... 42

2.2.3 Theory of field evaporation..... 45

2.3 LaAPT to analyze the optical absorption and thermal properties of nanoscale material..... 46

2.3.1 Metals..... 47

2.3.2 Semiconductors and Insulators..... 51

2.4 Scanning Transmission Electron Microscopy (STEM)..... 56

2.4.1 High Angle Annular Dark Field (HAADF) imaging..... 58

2.5 Micro-photoluminescence ( $\mu$ -PL) Spectroscopy..... 58

2.6 Spatial Modulation Spectroscopy (SMS)..... 60

2.7 Conclusion..... 62

<b>CHAPTER 3 : Au-nanoparticles in MgO matrix : Understanding optical absorption using LaAPT.....</b>	<b>65</b>
3.1 Introduction.....	65
3.2 Materials and Characterization.....	67
3.2.1 Bulk optical absorption.....	67
3.2.2 Sample preparation for APT.....	68
3.3 Influence of the Laser Wavelength.....	69
3.4 Influence of the length of the tip and tip support.....	72
3.4.1 Experimental Results and discussion.....	73
3.4.2 Numerical calculations of temperature evolution.....	75
3.4.3 Long and delayed evaporation at 343nm and 1030nm.....	80
3.5 Influence of the analysis depth.....	82
3.5.1 Region before Au-NPs.....	82
3.5.2 Inside the Au-NPs region.....	85
3.6 From optical properties to thermal properties.....	92
3.7 Analyzing single Au-Nanoparticle.....	95
3.8 Conclusions.....	100
<b>CHAPTER 4 : Au-nanoclusters in Fe<sub>2</sub>O<sub>3</sub> matrix: Optical and thermal Investigations using LaAPT.....</b>	<b>105</b>
4.1 Introduction.....	105
4.2 Materials and characterization.....	106
4.2.1 Synthesis of Au-Fe <sub>2</sub> O <sub>3</sub> films.....	106
4.2.2 Structural Characterization of Bulk samples.....	107
4.2.3 Optical Characterization of bulk sample.....	108
4.3 Sample Preparation for LaAPT.....	109
4.4 Structural Characterization of Single Nanoparticles.....	113
4.5 Optical characterization of nano-objects.....	118
4.5.1 Optical absorption of Au-NCs.....	119
4.5.2 Optical absorption of nanotips using FDTD method.....	121
4.6 Analyzing Time of Flight (ToF) Spectra .....	124
4.6.1 Experimental Methods used in LaAPT.....	124
4.6.2 Time of flight (ToF) Spectra at $\lambda=343\text{nm}$ .....	126
4.6.3 Time of flight (ToF) Spectra at $\lambda=515\text{nm}$ .....	131
4.7 Conclusions.....	133

<b>CHAPTER 5: InGaN/GaN quantum wells : Correlation between structural and optical emission properties.....</b>	<b>137</b>
5.1 Introduction.....	137
5.2 Materials and methods.....	139
5.2.1 Synthesis of microwires.....	139
5.2.2 Microphotoluminescence ( $\mu$ PL) and Scanning Transmission Electron Microscopy (STEM).....	140
5.2.3 Sample Preparation for $\mu$ PL and Atom Probe tomography.....	140
5.2.4 Atom probe tomography of InGaN/GaN QW's.....	145
5.3 Correlation of $\mu$ PL Spectroscopy, STEM and APT on single nano-object.....	157
5.3.1 Micro-Photoluminescence ( $\mu$ PL).....	157
5.3.2 Scanning Transmission Electron Microscopy (STEM).....	159
5.3.3 Atom Probe tomography (APT).....	161
5.3.4 Correlating the data obtained.....	164
5.4 Conclusion and Perspectives.....	167
 <b>CONCLUSION AND PERSPECTIVES.....</b>	 <b>171</b>



## List of Figures

### Chapter 1

**Figure 1.1 :** (a) Au-nanoparticles of different sizes show change in its color appearance, (b) the absorption maxima shifts to higher wavelength as the diameter of the Au-nanoparticles is increased.

**Figure 1.2 :** Absolute extinction cross-section,  $\sigma_{\text{ext}}$ , spectra of different (a) Gold nanorods with aspect ratios of 2.5, 3, and 4 (with increasing SPR wavelength) for light polarized along their main axis (the dotted line shows the absorption spectrum of the NRs solution) and (b) A single gold nanorod for light polarized along its long and short axis (long axis of 20.5 nm and aspect ratio of 2). Inset:  $\sigma_{\text{ext}}$  polarization dependence measured at 630 nm. [5]

**Figure 1.3 :** (a)–(c) A typical micrograph of a single plain silica NW, single Au-NPs silica NW and single Au-filled silica NW, respectively. Scale bar = 1 $\mu$ m. (d)–(f) The corresponding photoresponses under the wavelength of 532 and 808nm excitations, respectively [6]

**Figure 1.4 :** (a) Measured thermal conductivity of different diameter Si nanowires. The number beside each curve denotes the corresponding wire diameter. (b) Low temperature experimental data on a logarithmic scale. Also shown are  $T^3$ ,  $T^2$ , and  $T^1$  curves for comparison.[7]

**Figure 1.5 :** (a) SEM images of ultrafast-laser-induced micro/nano structured silicon surface, inset shows optical photograph of laser-treated silicon surface that looks black, (b) Specular light reflection from polished bare silicon and laser micro/nano structured silicon surface shown in (a).

**Figure 1.6 :** Schematic diagram of the interband luminescence process in (a) direct band gap semiconductor and in (b) indirect band gap semiconductor : the transition must involve emission or absorption of phonon to conserve the momentum. The shading indicates that the states are occupied by electrons. The filled states at the bottom of conduction band and empty states at the top of valence band are created by injecting electrons and holes into the semiconductor. ( $E_g$  : band gap,  $\hbar\omega$  : energy of the emitted photon).

**Figure 1.7 :** Schematic diagram of the processes occurring during photo-luminescence in direct gap semiconductor after excitation at frequency  $\nu_L$ . The electrons and holes rapidly relax to the bottom of their bands by phonon emission before recombining by emitting photon

**Figure 1.8 :** Electronic DOS for a bulk 3D crystalline material, a 2D QW, a 1D NW or NT, and a 0D QD. The insets report a cartoon showing the corresponding spatial confinement: confinement directions are defined by arrows[15].

**Figure 1.9 :** Size-tunable fluorescence spectra of CdSe quantum dots (A), and illustration of the relative particle sizes (B). From left to right, the particle diameters are 2.1 nm, 2.5 nm, 2.9 nm, 4.7 nm, and 7.5 nm.

**Figure 1.10 :** (a) Schematic of semiconducting QW with band gap  $E_g^{QW}$  sandwiched in between two thicker semiconducting layers of band gap  $E_g^{barr.} > E_g^{QW}$ . (b) HR-STEM image of InGaN as QW and GaN as barrier. (c)-(i) Potential profile and confined electron and hole energy wavefunctions within a rectangular quantum well of a given composition and thickness. Change in the composition (c)-(ii) and thickness (c)-(iii) of the QW results change in the energy of states and the main radiative recombination respectively.

**Figure 1.11 :** Spectral performance of an ideal selective solar absorber

**Figure 1.12 :** Schematic designs of six types of coatings and surface treatments for selective absorption of energy.

**Figure 1.13 :** XRD and SEM characterization of Au-Al<sub>2</sub>O<sub>3</sub> films on stainless steel (SS) substrate. The unindexed peaks correspond to the substrate. The XRD and adjacent SEM image correspond to same sample.

**Figure 1.14 :** Cross-sectional SEM image of the 850°C annealed Au-Al<sub>2</sub>O<sub>3</sub> specimen

**Figure 1.15 :** (a) TEM image of Au-TiO<sub>2</sub> nanorod, Au nano-clusters seen in dark contrast, (b) Au-TiO<sub>2</sub> nanorod before annular milling and (c) after milling, the final atom probe tip.

**Figure 1.16 :** (a) SEM image of Au-Fe<sub>2</sub>O<sub>3</sub> film, tiny bright spots correspond to Au-NPs, (b) XRD pattern showing existence of Au-NPs, all unindexed peaks correspond to  $\alpha$ -Fe<sub>2</sub>O<sub>3</sub> phase, (c) cross-sectional SEM image of the film deposited on Si-Substrate, tiny bright spots inside the film are due to the Au-NPs

**Figure 1.17 :** (a) Cross-sectional SEM image of Au-Ag bimetallic NPs sandwiched in SiO<sub>2</sub> layers, (b) an atom probe tip prepared from (a) along the thin film direction.

**Figure 1.18 :** (a) HR-TEM image from ref.[21], (b) STEM image of the Au-SiO<sub>2</sub> tip, absence of Au NPs in the tip

**Figure 1.19 :** (a) Cross-sectional STEM image of Au-MgO specimen showing formation of highly dense Au-NPs inside the MgO matrix, (b) magnified view of the top low dense Au-NP region of shown in (a)

**Figure 1.20 :** ITO/Au/ITO sample preparation during (a) initial stage of annular milling and (b) just before final stage of annular milling.

**Figure 1.21 :** HAADF-STEM image of (a) Au-MgO tip and (b) Au Fe<sub>2</sub>O<sub>3</sub> tip

**Figure 1.22 :** STEM (a) and HR-STEM (b) images from an atom probe tip sample prepared from InGaN/GaN multi quantum wells. The bright contrasted stripes are InGaN QW's and the thicker barrier between them is GaN.

## Chapter 2

**Figure 2.1 :** Schematic view of a field ion microscope. (a) Only the atoms from the very last shell (in green) of the tip surface can be imaged, as seen in the example of a pure W field ion

micrograph (on phosphor screen) after [11], (b) field ion micrograph of Au-tip and that of (c) Silicon tip (showing (111) pole) (Image Courtesy F. Vurpillot)

**Figure 2.2 :** Schematic showing the principle of atom probe tomography. (Blue and red circles represented as atoms)

**Figure 2.3 :** (a) The field evaporation process. The ad-atom is depicted in grey and the ion in black. (b) Atomic and ionic potential energy diagram with and without electric field.  $V$  is the potential,  $L$  is the sublimation energy,  $n$  is the degree of ionization,  $I_i$  is the  $i^{\text{th}}$  ionisation energy and  $\phi_e$  is the work function of the surface emitting the ion,  $Q_0$  and  $Q(F)$  are the energy barrier without and with electric field respectively. From [11].

**Figure 2.4 :** Variation of the temperature after the laser pulse for a laser polarized along the tip axis, (Intensity of laser =15 mJ/cm<sup>2</sup>). The temperature decay is fitted by the formula,  $T(\mathbf{0}, t) = T_0 + T_{\text{rise}}/\sqrt{[1 + 2(Dt/\sigma^2)]}$  with,  $T_0 = 40$  K,  $T_{\text{max}} = 160$  K, and  $\sigma = 1.5 \mu\text{m}$

**Figure 2.5 :** Evaporation rate as a function of time obtained (a) from an aluminum tip & (b) from a stainless-steel tip, for different wavelengths in axial polarization

**Figure 2.6 :** Normalized absorption density profile along the tip axis computed for  $\lambda = 360$  nm blue,  $\lambda = 515$  nm green,  $\lambda = 800$  nm red, and  $\lambda = 1200$  nm brown. Inset: zoom of absorption profiles at the end of the tip for  $\lambda = 360$  nm blue and for  $\lambda = 515$  nm green.

**Figure 2.7 :** Experimental (thin line) and theoretical (thick line) evaporation rate of a metallic glass tip analyzed at  $\lambda = 360$  nm [red (black)],  $\lambda = 500$  nm [green (half-gray)], and  $\lambda = 1200$  nm [violet (gray)]

**Figure 2.8 :** SEM image of a Si specimen irradiated with 20mW average-power (a) IR pulses, holes indicative of locally enhanced absorption are observed only along the shank of the specimen, i.e. far from the apex and (b) green pulses, trenches indicative of locally enhanced absorption are observed in proximity to the apex region

**Figure 2.9 :** Normalized evaporation rate as function of time obtained from an Si tip (a) for IR laser, using the laser intensities bottom to top  $I = 0.2$  GW/cm<sup>2</sup>,  $I = 1.2$  GW/cm<sup>2</sup>,  $I = 2.2$  GW/cm<sup>2</sup>, and  $I = 5.7$  GW/cm<sup>2</sup>, respectively; (b) Green laser light 9.1 J/m<sup>2</sup>

**Figure 2.10 :** (a) 3D reconstructed volume of Fe/MgO/Fe tunnel barrier, (b) ToF spectra of Fe ions from the first and last layers (blue and black line, respectively) and Mg ions (pink line)

**Figure 2.11 :** Schematic diagram illustrates the various signals generated inside a scanning transmission electron microscope that can be used to form high-resolution images, nano-diffraction patterns or spectra of the region-of-interest. X-ray energy dispersive spectroscopy (XEDS); Auger electron spectroscopy (AES) and scanning Auger microscopy (SAM); secondary electron spectroscopy (SES) and secondary electron microscopy (SEM); annular dark-field (ADF) and high-angle annular dark-field (HAADF); coherent electron nano-diffraction (CEND); parallel electron energy-loss spectroscopy (PEELS); bright-field (BF) and dark-field (DF), After [41].

**Figure 2.12** : HAADF-STEM of the Au-nanoparticle. The Au-NP is protruding from the surface of the atom probe tip specimen of Au-NPs embedded in MgO matrix. (Image courtesy: W. Lefebvre)

**Figure 2.13** : Experimental set-up for micro-photoluminescence Spectroscopy (PL signal observed with the camera is shown in the right bottom corner of the figure)

**Figure 2.14** : The  $\mu$ PL signal recorded by camera from three different regions of same InGaN/GaN microwire. (From left to right) PL signal emitted when the base, middle and, top region of the microwire is illuminated by the laser light.

**Figure 2.15** : (a) Schematics of SMS, laser beam is illuminated through 100X objective on the nano-object, while the spatial position is modulated along Y-direction. The light transmitted is collected using another 100X objective and the signal is recorded using lock-in amplifier, (b) Position of particle during modulation, (c) normalized change in transmission induced by single nanoparticle at modulation frequency of ' $f$ ' and (d) at modulation frequency of ' $2f$ '

### Chapter 3

**Figure 3.1** : Cross-sectional STEM image of the Au-NPs embedded in MgO matrix, (a) Band of Au-NPs formed nearly 200nm from the surface of the MgO, (b) high resolution image from the less dense region of Au in (a) showing the variation in size distribution of Au-NPs

**Figure 3.2** : Bulk Optical absorption spectra for pure MgO and Au-NP's embedded in MgO

**Figure 3.3** : Sample preparation for atom probe experiments, tip shaped samples prepared from bulk sample using FIB based protocol.

**Figure 3.4** : (a) HAADF-STEM image of the tip, the bright contrasted spots are Au-NPs covering the apex region, (b) Expected temperature profile when the tip shown in (a) is illuminated by laser light of wavelength 515 nm,  $T_{max}$  : maximum temperature rise due to absorption of Au-NP's,  $T_0$  : Base temperature (c) ToF spectrum obtained after analyzing the tip shown in (a), displays the delayed evaporation as a hump in ToF spectrum. The red solid line corresponds to the temperature evolution at the apex of the tip corresponding to the temperature profile shown in (b).

**Figure 3.5** : Absorption map in the incident plane ( $y, z$ ) at  $\lambda=515$  nm calculated by Lumerical or Au-NP's embedded in MgO matrix. The Au-NP's are present only in near apex region (The dotted white line is drawn to guide the eye).

**Figure 3.6** : ToF spectra obtained from Au-MgO tip at laser wavelength of (a) 570nm and (b) 650nm and 750nm

**Figure 3.7** : Absorption map in the incident plane ( $y, z$ ) at  $\lambda=515$  nm calculated by Lumerical for Au-NP's embedded in MgO matrix with W-pretip support. The Au-NP's are present only in near apex region.

**Figure 3.8** : Comparison of the length of the tip, SEM image of Au-MgO tip (a) 4.2 $\mu$ m long and (b) 1.5 $\mu$ m long tip. The length is defined as the distance between the tip apex and the interface of tip/W-pretip support, the slanted black line represents the tip/W-pretip interface

**Figure 3.9 :** Comparison of time of flight (ToF) spectra obtained for short tip (black curve) and long tip (red curve) at  $\lambda=515\text{nm}$ .

**Figure 3.10 :** Temperature evolution at the tip apex (a) and associated number of evaporated ions per pulse  $N_{\text{ions}}$  (b) for an absorption located at the apex (blue line) and far from the apex (red line).

**Figure 3.11 :** SEM image of the sample, (b) Absorption map in the incident plane ( $y, z$ ). The color bar corresponds to the power absorption density for an incoming intensity of  $1 \text{ W/m}^2$ . (c) Absorption density profile along the tip computed from absorption map shown in (c) and (d) Schematic representation of the two Gaussian heated zones along the tip axis ( $z$ ).

**Figure 3.12 :** Log of the normalized number of detected ions  $N_{\text{ions}}$  as a function of ToF at  $515\text{nm}$  wavelength for the  $1.5\mu\text{m}$  length sample. The origin of ToF corresponds to the ToF of  $\text{Mg}^{2+}$  ions. Black, green, blue and yellow lines correspond to the evolution of  $\text{Log}(N_{\text{ions}})$  from Eq.(3.1) and Eq.(3.3) with:  $\omega_1 = \omega_2 = 100 \text{ nm}$ ,  $A_1=1$ ,  $A_2=1.5$ ,  $D=7\times 10^{-2} \text{ cm}^2/\text{s}$ ,  $Q=0.1\text{eV}$ ,  $T = 450\text{K}$  and  $z_0 = 1 \mu\text{m}$ . Red line is obtained by the sum of blue and yellow line.

**Figure 3.13 :** Log of the normalized number of detected ions  $N_{\text{ions}}$  as a function of ToF at  $515\text{nm}$  wavelength for the  $4.2\mu\text{m}$  length sample. The origin of ToF corresponds to the ToF of  $\text{Mg}^{2+}$  ions. Black, green, blue and yellow lines correspond to the evolution of  $\text{Log}(N_{\text{ions}})$  from Eq.(3.1) and Eq.(3.3) with:  $\omega_1 = \omega_2 = 100 \text{ nm}$ ,  $A_1=1$ ,  $A_2=1.5$ ,  $D=7\times 10^{-2} \text{ cm}^2/\text{s}$ ,  $Q=0.1\text{eV}$ ,  $T = 450\text{K}$  and  $z_0 = 4 \mu\text{m}$ .

**Figure 3.14 :** Comparison of ToF spectra of  $1.5\mu\text{m}$  long tip and  $4.2\mu\text{m}$  long tip obtained after atom probe analysis carried out at (a) UV ( $343\text{nm}$ ) and (b) IR ( $1030\text{nm}$ ) wavelength. All analyses were carried out in high density Au-NPs region and the experimental conditions were similar. The laser power used for UV analyses was around  $1.4\text{mW}$  and that of for IR analyses was  $30\text{mW}$ .

**Figure 3.15 :** (a) 3D reconstructed volume obtained from the data acquired after atom probe experiment; only 5% of  $\text{Mg}^{2+}$  ions are shown for clarity, (b) corresponding 1D concentration profile; purple dotted rectangle shows the concentration profile for 3D reconstructed volume shown in (a) as well as the volume analyzed by atom probe highlighted by yellow dots in (c), (c) HAADF-STEM image of the Au-MgO tip. The laser efficiency (L.E.) of Green laser ( $515\text{nm}$ ) as a function depth is shown by Red data points in (b).

**Figure 3.16 :** (a) HAADF-STEM image of the tip, (b) Schematic representation of the temperature along the tip after illuminated by Green light and (c) corresponding tip apex temperature evolution; Blue dotted curve : temperature due to near apex absorption, Red dotted curve : temperature due to Au-NP's absorption, Green solid curve : Resultant variation of temperature with respect to time,  $t$ .

**Figure 3.17 :** ToF spectra obtained after analyzing the pure MgO region before Au-NP's. Black dotted curve is for the analysis carried out at  $1\text{mW}$  laser power and the blue solid curve is at  $0.2\text{mW}$  laser power. The red and green lines correspond to the evolution of  $\text{Log}(N_{\text{ions}})$  from Eq. 3.1 and Eq. 3.3 with:  $\omega_1 = \omega_2 = 100\text{nm}$ ,  $A_1 = 1$ ,  $D=7\times 10^{-2} \text{ cm}^2/\text{s}$ ,  $Q = 0.1\text{eV}$ ,  $T = 170\text{K}$ ,  $z_0=330 \text{ nm}$  and  $A_2 = 1.5$  (for red line) and  $A_2 = 1$  (for green line).

**Figure 3.18** : Comparison of ToF spectra obtained at different spatial regions for  $\lambda=343\text{nm}$  along the depth of the tip as represented by different colored circles in HAADF-STEM image of the tip. The 2D detection hit maps shown above represents the Au-atoms (black dots) distribution in these respective regions with indication of Au concentration in at.%

**Figure 3.19** : Comparison of ToF spectra obtained at different spatial regions for  $\lambda=515\text{nm}$  along the depth of the tip as represented by different colored circles in HAADF-STEM image of the tip. The 2D detection hit maps shown above represents the Au-atoms (black dots) distribution in these respective regions with indication of Au concentration in at.%

**Figure 3.20** : Comparison of ToF spectra obtained at two different spatial regions for  $\lambda=1030\text{nm}$  along the depth of the tip as represented by different colored circles in HAADF-STEM image of the tip.

**Figure 3.21** : Au concentration obtained from atom probe analysis, in atomic % and in volume fraction

**Figure 3.22** : (a) Real,  $n$  and (b) imaginary,  $k$  part of complex refractive index calculated for Au-NPs embedded in MgO matrix with Au volume fractions of 0.1%, 0.25% and 0.5%.

**Figure 3.23** : Absorption maps (left) calculated for tip of radius  $R=50\text{nm}$  and cone angle of  $5.5\text{deg}$  at wavelength of  $343\text{nm}$ ,  $515\text{nm}$  and  $1030\text{nm}$ . The Au volume fraction used to calculate these maps is 0.5% and the direction of laser incidence is into the paper. The absorption density profile (right) plotted from the absorption maps obtained for Au-fraction of 0.5% (top curves in the graph) and 0.1% (bottom curves in the graph, except the red curve which corresponds to 0.5% of Au fraction)

**Figure 3.24**: Relative change in the transmitted light as a function of the laser spot position along the tip axis.  $X=10\ \mu\text{m}$  corresponds to the tip apex. The SEM image of the analyzed tip is also shown.

**Figure 3.25**: Comparison of ToF spectra obtained for pure MgO (red curve) and Au-MgO (black curve) at wavelength of (a)  $515\ \text{nm}$  and (b)  $343\ \text{nm}$ . The field conditions are comparable in these analyses.

**Figure 3.26** : Absorption maps calculated for Pure MgO tip with  $R=50\ \text{nm}$  and cone angle of  $5.5\text{deg}$ . at wavelength of (a)  $343\ \text{nm}$  and (b)  $515\ \text{nm}$

**Figure 3.27** : (a) 2D representation of Au-atoms (black dots) distribution for UV and Green wavelength analyses with different laser powers for Green analyses, (b) Cumulated Erosion composition profile measured for the single Au-NP highlighted by square in (a), and (c) Schematic showing the composition measurement using erosion protocol.

**Figure 3.28** : 3D reconstructed data obtained after analysis carried out Green wavelength and  $5.0\text{mW}$  of laser power. (Top) Distribution of Au and  $\text{Mg}^+$  ions in (X,Y) plane and in (Y,Z) plane shown in middle. Distribution of  $\text{Mg}_3\text{O}_2^{2+}$  and  $\text{Mg}_2\text{O}_2^+$  ions in (Y,Z) plane (bottom)

**Figure 3.29** : (a) 2D Spatial distribution of Au and  $\text{Mg}^+$  ions obtained from UV wavelength analysis at  $5\text{mW}$  and  $10\text{mW}$  of laser power, (b) 3D atomic distribution of  $\text{Mg}^+$ ,  $\text{Mg}_3\text{O}_2^{2+}$  and  $\text{Mg}_2\text{O}_2^+$  ions in the vicinity of Au-NP highlighted by yellow square in (a). The Au-NP here is

represented by the 5 at.% iso-surface. (c) 2D atomic distribution maps of Au obtained at different laser powers.

## Chapter 4

**Figure 4.1 :** Characterization of Au-Fe<sub>2</sub>O<sub>3</sub> film (a) Top-down SEM image showing the surface of the film deposited on Si-substrate, the bright tiny spots corresponds to the Au-NCs, (b) XRD pattern recorded for the same film deposited on Quartz substrate, Au-peaks are indexed and all other unindexed peaks corresponds to the  $\alpha$ -Fe<sub>2</sub>O<sub>3</sub> phase, (c) Cross-sectional SEM image showing the presence of Au-NCs inside the Fe<sub>2</sub>O<sub>3</sub> matrix.

**Figure 4.2 :** Absorption spectra obtained from thin film of Au-Fe<sub>2</sub>O<sub>3</sub> deposited on Quartz

**Figure 4.3 :** (a) Cross-sectional SEM image of Au-Fe<sub>2</sub>O<sub>3</sub> showing film and Si-substrate, yellow highlighted tip shaped area shows the region from which tip is prepared, (b) Final atom probe tip prepared from (a), high magnification image is shown in (c), the interface between and film and substrate is denoted by white arrow, also the bright contrast Au-NCs are clearly visible, and (d) 3D tomographic reconstruction obtained by analyzing the tip shown in (b)-(c).

**Figure 4.4 :** (a) Cross-sectional SEM image of the Au-Fe<sub>2</sub>O<sub>3</sub> film, yellow highlighted tip shaped area shows the region from which tip is prepared, (b) SEM image during the initial stage of annular milling (c) final atom probe tip

**Figure 4.5 :** HAADF-STEM image of Au-Fe<sub>2</sub>O<sub>3</sub> tip prepared along the thin film : Low magnification image showing Au-NCs are distributed all over the tip, the length of the tip is nearly 4 $\mu$ m (left) and magnified view from the near apex region (right).

**Figure 4.6 :** Typical mass spectra obtained from the Au-Fe<sub>2</sub>O<sub>3</sub> tip prepared along the thin film (top) and direct correlation of the 3D tomographic reconstruction of atom probe data to HAADF-STEM image (bottom)

**Figure 4.7 :** 3D tomographic reconstruction and 10% Au concentration isosurfaces

**Figure 4.8 :** Structural and chemical characterization of single Au-NC in 3D : 10% Au isosurface (right) and corresponding erosion profile (left)

**Figure 4.9 :** Voltage curve (b) measured for the 3D reconstruction shown in (a) and corresponding number density of atoms inside and outside Au-NC (c)

**Figure 4.10 :** Calculated optical absorption spectra for Au-NCs of different aspect ratios (see text) embedded in Fe<sub>2</sub>O<sub>3</sub> matrix compared with the experimentally measured absorption spectra obtained from bulk thin-film sample.

**Figure 4.11 :** (a) Absorption maps calculated for  $\lambda=343$ nm illumination using FDTD method for Pure Fe<sub>2</sub>O<sub>3</sub> and Au-Fe<sub>2</sub>O<sub>3</sub> nanotips and (b) corresponding absorption profiles obtained from (a)

**Figure 4.12 :** *a) Absorption maps calculated for  $\lambda=515\text{nm}$  illumination using FDTD method for Pure  $\text{Fe}_2\text{O}_3$  and  $\text{Au-Fe}_2\text{O}_3$  nanotips and (b) corresponding absorption profiles obtained from (a)*

**Figure 4.13 :** *Comparison of  $\text{Au-Fe}_2\text{O}_3$  and Pure  $\text{Fe}_2\text{O}_3$  nanotips : Low magnification SEM image (Left) and high magnified view of the near apex region (right)*

**Figure 4.14 :** *Time of flight (ToF) spectra comparison of Pure  $\text{Fe}_2\text{O}_3$  and  $\text{Au-Fe}_2\text{O}_3$  nanotips obtained at  $\lambda=343\text{nm}$  and laser power of  $2\text{mW}$  in log time scale (a) and magnified view of the  $\text{Fe}^{2+}$  peak (b)*

**Figure 4.15 :** *Experimental and simulated evaporation rate as a function of time for a Pure  $\text{Fe}_2\text{O}_3$  and  $\text{Au-Fe}_2\text{O}_3$  specimen in APT. Fit parameters:  $D=2.5\times 10^{-2}\text{cm}^2/\text{s}$  and  $T_{\text{rise}}= 50\text{K}$  (orange line),  $D=6\times 10^{-2}\text{cm}^2/\text{s}$  and  $T_{\text{rise}}= 50\text{K}$  (green line) and  $D=2.5\times 10^{-2}\text{cm}^2/\text{s}$  and  $T_{\text{rise}}= 100\text{K}$  (black solid line).*

**Figure 4.16 :** *Comparison of Mass-spectra from two different volumes one with  $\text{Au-NC}$  in it and one without  $\text{Au-NCs}$*

**Figure 4.17 :** *Time of flight (ToF) spectra comparison of Pure  $\text{Fe}_2\text{O}_3$  and  $\text{Au-Fe}_2\text{O}_3$  nanotips obtained at  $\lambda=515\text{nm}$  and laser power of  $3\text{mW}$  at long time scale in (a) and at short time scale in (b)*

## Chapter 5

**Figure 5.1 :** *(a) Scanning electron micrograph of a GaN wire containing an InGaN/GaN multi-QW system. (b) Schematic illustration of the heterostructure geometry, with the quantum well system depicted in Green and GaN barriers and core in Blue. (c) Pictorial representation of the nanowire from lateral and top view*

**Figure 5.2 :** *Schematic depicting the Si-layer deposition on InGaN/GaN micro-wires extracted on substrate (Si-deposition is represented by red color)*

**Figure 5.3 :** *Schematic and corresponding SEM image of  $\mu$ -manipulation of microwires, (a) Welding  $\mu$ -manipulator to the microwire using Pt-C deposition, (b) Lift-off process*

**Figure 5.4 :** *Welding the microwire on W-post; (1) Aligning the microwire on top of the W-post, (2) Making groove for Pt-deposition by cutting the base of microwire using Ga ions, (3) FIB assisted Pt-deposition to weld the microwire on W-post, (4) Making a cut through microwire using Ga ions, (5) & (6) Repeating the steps (3 & 4) to prepare another couple of samples from the same microwire.*

**Figure 5.5 :** *SEM images (top view) of the steps (1), (4) and (6) shown in fig. 5.4. (The  $\mu$ -manipulator attached to the microwire is not shown here)*

**Figure 5.6 :** *Process of annular milling, (a) First step of high current milling, (b) cut-out cylinder ready for  $\mu\text{PL}$  measurements, (c) tip sample ready for STEM and APT analysis (Si :*

Silicon protective layer, QW's : region of set of InGaN/GaN QW's, Pt : Platinum deposition used for welding)

**Figure 5.7 :** Total fraction of Ga and N as a function of Laser energy at constant flux.

**Figure 5.8 :** Total Ga and N fractions as a function of (a) applied voltage ( $V_{dc}$ ) at constant laser energy (0.7nJ and 2.0nJ) and (b) laser energy at constant applied voltage ( $V_{dc}=5.4kV$ ). From [15].

**Figure 5.9 :** Total Fraction of atoms as a function of Ga charge state ratio ( $Ga^{2+}/Ga^+$ ). The data acquired at constant flux (fig. 5.7) and constant laser energies (fig. 5.8) were used. The effective field is calculated after Kingham [16]

**Figure 5.10 :** Concentration maps recorded from the detector at constant flux and laser energy of 0.7nJ for (a)  $Ga^+$ , (c)  $Ga^{2+}$  and for laser energy of 2.0nJ for (b)  $Ga^+$  (The direction of laser incidence is shown at the bottom right of the figure)

**Figure 5.11 :** Effect of high field conditions on the data acquired, 3D reconstructed volume showing only Ga atom distribution in (a), Ga and In atom distribution in (b) and (c) corresponding Ga charge state ratio measured along the depth of the 3D volume shown in (a,b)

**Figure 5.12 :** Effect of high field conditions on the data acquired, (a) 3D reconstructed volume showing only In atom distribution, (b) Sub-volume extracted from (a) showing only  $Ga^+$  ions and (c) linear concentration profile of sub-volume shown in (b) in the direction shown by Yellow arrow

**Figure 5.13 :** Mass Spectrum acquired from InGaN/GaN QW's sample

**Figure 5.14 :** 3D reconstructed volume and the corresponding composition profile obtained. A sub-volume along the dotted black line drawn on 3D reconstruction used to calculate the composition. The Ga charge state ratio along the analysis depth is also shown (top)

**Figure 5.15 :** (a) SEM image of one of the analyzed microwires; (b) SEM image of analyzed cut-out cylinder; (c) Optical microscopic image of the PL (highlighted by the arrow) emitted by cut-out cylinder mounted on a tungsten tip under excitation with a 244 nm cw laser at 4K. (d)  $\mu$ PL spectra of two whole microwires A and B mounted on a tungsten tip (Red and blue curve, upper part of the graph) and of cut-out cylinder which have been subsequently analyzed by STEM and APT.

**Figure 5.16 :** (a) STEM-HAADF micrograph of a portion of the atom probe tip prepared from cut-out cylinder. (b) HAADF contrast profile extracted from the red dashed line in a). (c) High-resolution image from QW#3, showing the details of the quantum well interface and the atomic columns observed along the  $[11\bar{2}0]$  zone axis of the GaN wurtzite crystal. (d) Schematic representation of the crystal structure as observed in c).

**Figure 5.17 :** 3D reconstruction of the data obtained, (b) reconstructed volume oriented as observed in STEM image shown in (a), (c) and (d) reconstructed volume shown from different orientations. (showing only distribution of In atoms for clarity)

**Figure 5.18 :** (a) One-dimensional profiles of the InN fraction obtained through the analysis of boxes with their z-axis perpendicular to the QW interfaces. (b) Profile through the whole QW system; (c-d-e) Selected profiles across QWs #4, #12 and #17, respectively. (f) HR-STEM image of QW#3 and corresponding APT reconstructed image showing the interface geometry of QW.

**Figure 5.19 :** (a) Measurement of quantum well thickness taking into account the FWHM of the STEM HAADF contrast profile (red empty squares) and from the APT 1D InN fraction profiles, and as the FWHM of the InN-rich region (black empty triangles). (b) Maximum InN fraction obtained from the 1D APT composition profiles.

**Figure 5.20 :** (a) 3D In distribution within the QW#4, #12 and #17 (The red and blue arrow shows the propagation of stripe-like feature from well-to-well) (b) InN fraction maps calculated within the 1 nm thick slices of QW #12 shown in the upper part of the figure

**Figure 5.21 :** Dependence on InN fraction of the InGaN bandgap (blue line) and of the InGaN/GaN PL transition energies calculated for rectangular quantum wells of different thickness  $t_{\text{QW}}=2\text{nm}$  (filled squares), and  $t_{\text{QW}}=4\text{nm}$  (open triangles). The red shaded region corresponds to the interval in which the PL narrow lines have been observed in the analyzed cut-out cylinder; the  $\mu\text{PL}$  spectrum is also reported on the left-hand side axis (black line).

# INTRODUCTION

The modern human life is surrounded by number of devices, there is no doubt these devices are making life easier and one could not imagine the life without these appliances. The main challenge in front of the researchers today is to make new devices or improve the existing ones in order to have better performance in all aspects. Requirement of efficient, cost-effectiveness and longevity at the same time makes this goal even more challenging. On the other hand, the problem of new energy sources is increasing every day. The fossil fuels will not be able to serve the increasing demand of energy in near future. The renewable energy sources can fulfill these requirements, but the difficulties to achieve desired efficiency and storage of energy are the decisive factors affecting the use of these sources of energy. Fortunately, in recent times, researchers are giving more attention to utilize the renewable energy sources as a potential source of energy, which reflects in the scientific literature as well. One way to overcome these problems is to understand the materials properties at atomic scale. The ultimate performance of any electronic device or the materials used for energy is dependent on the fundamental electro-optical properties at atomic scale dimensions.

Atom Probe Tomography has already proven its abilities to study the structural and chemical properties of material at near atomic resolution and in three dimensions. With the use ultra-fast laser pulses, since last decade, it is possible to analyze the technologically important materials based on semiconductor and insulators. Certainly, the technique is primarily used to study the structural properties only, but considering the nanoscale specimen and the use of ultra-fast laser pulses in the technique, it is possible to understand the complex behavior of light interaction at nanoscale. This will not only leads to improve our understanding of the material, but also the optical properties of the material can be understood and hence its electrical properties.

In this regard, the prime objective of this thesis is to study the feasibility of Laser assisted Atom Probe Tomography (LaAPT) as a tool to investigate the spectroscopic properties of the nanoscale material with particular emphasis on materials for energy like METallic CERamics (CERMET). Although with the use of ultra-fast laser pulses, the use of LaAPT is questionable to particular class of materials due to the complex laser-nanotip interaction. The fate of the data obtained is strongly dependent on how the laser energy is absorbed by the material under study taking into account the nanometric shape of the sample in LaAPT. Having said that, the La-APT can be utilized as an opportunity to understand their absorption properties. In this regard, attempts have been made in this thesis to understand the optical absorption properties of nanotips of Au-nanoparticles embedded in MgO and Fe<sub>2</sub>O<sub>3</sub> matrix. Moreover, the temperature induced by the laser absorption will also be discussed. Apart from understanding the optical absorption properties of nanotips, study of understanding the optical emission properties of quantum confined system of InGaN/GaN quantum wells is also performed. A novel correlative approach to study the direct correlation between structural and optical emission properties is introduced using LaAPT, Scanning Transmission Electron Microscopy (STEM) and micro-photoluminescence ( $\mu$ -PL) spectroscopy.

At the outset, in chapter 1, a brief review of optical absorption at nanoscale is introduced with few examples from the available literature along with the fundamentals of optical emission properties of the solids. In addition, the change in thermal properties upon nano-structuring is also incorporated. At the end of the chapter, the samples analysed during the course of this thesis are listed with discussion on their failure either during sample preparation or LaAPT analysis with possible reasons.

In chapter 2, the experimental methods used during this work are introduced. Use of LaAPT as spectroscopic tool to study the absorption and thermal properties is in itself a subject of new aspect, so that it is inevitable to introduce the approach with which most of the analysis is carried out in this thesis. The atom probe tomography technique, its basic operating principle and the theory of field evaporation are briefly summarized. More attention is given to explain how the analysis of time of flight (ToF) spectra leads to the absorption behavior of the sample under study. The discussion begins with the case of metallic emitters and the framework to understand the temperature evolution at the tip surface using 1D thermal model is introduced. The description of evaporation behavior with respect to different wavelengths used to trigger the field evaporation is explained using the reports available in literature. The importance of numerical calculations to aid

the experimental observations is also highlighted. Subsequently, relatively complex case of semiconductors and insulators is incorporated to complete the discussion. In addition, other techniques used to understand the structural and optical properties of the tip shaped materials like STEM,  $\mu$ -PL and Spatial Modulation Microscopy (SMS) are presented briefly, at the end of the chapter.

The chapter 3 is chiefly related to the effect of optical absorption of Au-nanoparticles (Au-NPs) embedded in MgO matrix on the results obtained with LaAPT. The system of Au-NPs in MgO is interesting due to its resonant absorption when illuminated with Green wavelength. After introducing the structural and bulk optical properties, the influence of laser wavelength on the results obtained with LaAPT by analyzing the ToF spectra are shown. Considering the changes in Au concentration along the depth of the sample, to understand the effect of the Au concentration on the ToF spectra various experiments were carried out in different regions of Au-NPs with UV, Green and IR wavelength. Moreover to have an idea on the thermal properties, the ToF spectra obtained at UV and Green wavelength, with and without Au inclusions are compared. In the last section of the chapter, structural analysis of single Au-nanoparticles using 3D reconstruction of the data obtained from LaAPT analysis is presented.

The chapter 4 deals with the optical and thermal investigation of Au-nanoclusters embedded in  $\text{Fe}_2\text{O}_3$  matrix using LaAPT. This material has a potential to be used as a light harvesting material and with the inclusion of Au-NCs the absorption efficiency is expected to increase as reported in the literature. The synthesis and structural characterization of the material is followed by the optical absorption properties of the bulk sample. A good correlation between the STEM analysis of Au-NPs and the 3D reconstructed data from LaAPT is shown. In addition, the structural and chemical composition characterization of individual Au-NCs is performed to understand the size as well as chemistry of the particles, both being the decisive parameters for the optical absorption. The optical absorption spectra are calculated using the size parameters obtained from the LaAPT analysis and are compared with the experimental bulk absorption spectra. In the last section of the chapter, the ToF spectra obtained from Au- $\text{Fe}_2\text{O}_3$  and that of Pure  $\text{Fe}_2\text{O}_3$  is compared and analyzed using the methodology described in chapter 2. The experiments and the analysis performed thereafter at UV (343 nm) and Green (515 nm) wavelength supports the hypothesis that, the inclusion of Au-NCs increases the temperature owing to the larger absorption of laser energy.

In chapter 5, the optical emission properties of InGaN/GaN quantum well system is studied and correlation between the structural properties and optical emission for the single nano-object is performed. For structural characterization of the quantum wells, LaAPT and STEM analysis were performed while for optical emission study  $\mu$ -PL spectroscopy is used. The sample preparation protocol for LaAPT experiments is discussed in detail and more attention is given to the optimization of experimental parameters for LaAPT analysis, which will result in the accurate measurement of elemental composition. At the end of the chapter, correlative analysis performed on the same nano-object is presented and a good correlation between local variations in composition of In inside quantum wells is found with the emission lines observed in  $\mu$ -PL spectra.

Finally conclusion and perspectives for this work are presented.

# Chapter 1

## Overview

### 1.1 Introduction

Light interacts with matter in many different ways. Metals are shiny but water is transparent. Stained glass and gemstones transmit some colors, but absorb others. Other materials such as milk appear white because they scatter the incoming light in all directions. This interaction of light with matter is governed by different optical phenomena and can be categorized roughly as reflection, diffraction and transmission of light through the optical medium. These processes are correlated to each other and their interplay will decide the appearance of the matter to be colored or transparent to the incident radiation [1]. The phenomenon of propagation of light through the medium is further classified in optical processes like reflection, refraction, absorption, luminescence and scattering. Understanding these optical processes has been a subject of interest since long time. The optical properties are governed by the electronic structure of the material and hence studying these processes will not only give the information on the optical behavior of the material but also one can figure out the electronic properties as well.

Optical properties of solids have always been a fascinating to researchers since long time due to their numerous applications in various technologies ranging from space based applications to medical sciences. With the advent of nanotechnology in last few decades and with number of methods to prepare the materials smaller and smaller down to nano-metric scale, it is now possible to manufacture the devices with reduced size and more efficient in every sense. Due to these remarkable advances, in the last few decades the society has watched in astonishment how the science has become a fundamental part of the daily life due to the everyday more efficient, fast, safe and cheap technological devices. This advance has been mainly thanks to the modern tools and the available experimental techniques which have reached the ability to control the size, composition

and functionality of matter and also to perform a complete and more accurate characterization of its physical and chemical properties.

Although these technological improvements made the life easier, understanding the optical properties of materials at nanoscale is not as straightforward as their bulk counterparts. The electronic structure of materials substantially changes with its size and shape and hence its optical properties also, especially when we are dealing with micro-nano regime, so it is crucial to study the optical properties of materials at nanoscale. Thus with the increasing importance of nanostructured and nanoscale functional materials in the domain of photonics and optoelectronics, more and more attention is dedicated to the problem of determining the relationship between structural and optical properties of these materials.

In this context, if one is able to understand the optical behavior of the nanostructures in correlation to their structural properties then it will be of great importance to scientific community studying nanostructures and their applications. We believe that the Laser assisted Atom probe tomography (LaAPT) is capable to carry out this kind of analysis on different types of materials, analyzing their structural and chemical properties at near atomic resolution along with the optical and thermal behavior simultaneously.

This chapter is dedicated to the absorption and luminescence properties of the material in relation to their structural properties. In addition, absorption of laser light in solids is well known to result in heating of the absorbing material; this heating has strong consequences on the LaAPT analysis and the rate of diffusion of this heat is dependent on the size, shape and the intrinsic thermal properties of the material. This gives us a unique opportunity to study the thermal behavior of the nanoscale material as well. So in this chapter more attention is given to the absorption, luminescence as well as the thermal properties of the nanoscale material which can be analyzed by LaAPT.

Moreover, the numbers of specimens studied during the course of this thesis are introduced at the end of this chapter. The possible reasons for the failure of specimens analyzing with LaAPT are also mentioned which can also be helpful for future studies on similar kind of materials.

## **1.2 Optical Properties of Materials**

Optical properties of materials as a whole can be a topic of discussion for another new thesis itself. Considering the vast number of optical processes and their physical

mechanisms, it is not possible and also inappropriate to incorporate all of them in this thesis. But as the requirement of the thesis it is essential to introduce the optical properties which are going to be integral part of this work.

In this regard, a brief introduction to the optical absorption properties of nanoscaled materials is given along with the discussion on thermal properties induced by the absorption of light. Instead of reproducing the fundamental mechanisms involved in these processes, the effect of nanostructuring on the absorption and thermal properties of the materials are explained on the basis of examples available in the literature.

In addition, optical emission from solids is also introduced along with the factors affecting on the emission properties. A general remark on the Quantum Well (QW) structures is presented and more attention is given to the photo-luminescence (PL) spectroscopy and dependence of the PL signal on the structural and chemical properties of QW's.

### **1.2.1 Optical Absorption and Thermal Properties at Nanoscale**

Light or Electromagnetic waves absorption by the material and the thermal processes involved thereafter is very well known phenomenon, extensively studied and is thoroughly presented in almost every graduate level texts on Solid State Physics [2,3]. The absorption of the laser energy takes place through photon interaction with bound and free electrons in the material structure, which raises them to the higher energy levels. Energy conversion takes place through various collision processes involving electrons, lattice phonons, ionized impurities and defect structures.

It is fundamental to remember that only the amount of energy absorbed by the material can contribute to processes like heating and/or melting. In semiconductors, the absorption of photons leads to the creation of electron-hole pairs with a certain amount of kinetic energy. These "hot" carriers thermalize amongst each other forming plasma. Once a common carrier temperature is reached, they transfer their kinetic energy to the lattice via recombination and phonon generation, leading to lattice heating. The characteristic time scale for these processes is on the order of few 100's of femto-second (fs) to 100's of pico-second (ps) and hence studying these processes are always been challenging.

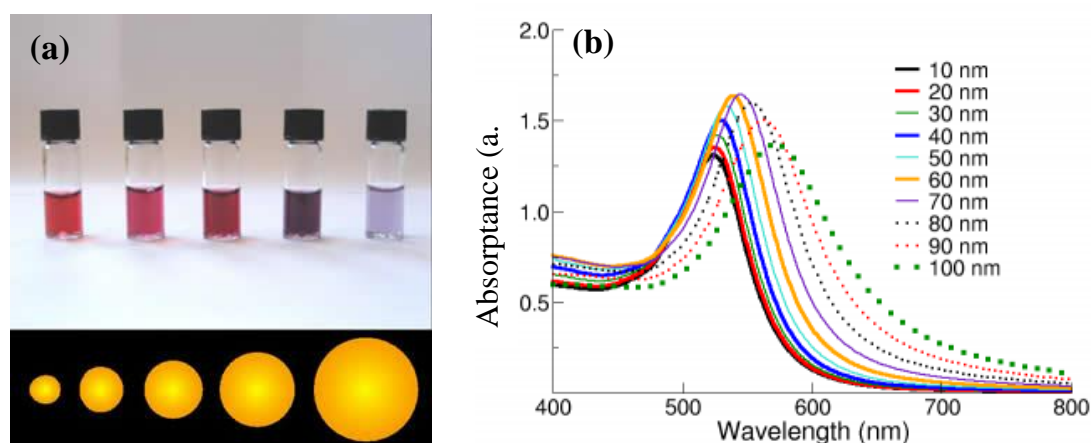


**Figure 1.1 :** (a) Au-nanoparticles of different sizes show change in its color appearance, (b) the absorption maxima shifts to higher wavelength as the diameter of the Au-nanoparticles is increased.

But when the material is in nanof orm, i.e. when at least one of its physical dimensions is reduced to nanometric scale then its electronic as well as optical properties are changing substantially. This is due to the number of atoms on the surface are comparable to its volume and this surface to volume ratio increases to few orders of magnitude compare to its bulk counterpart. This effect plays the decisive role in the fascinating properties of nanomaterials. For example, the bulk gold appears shiny bright yellow whereas the suspension of Au-nanoparticles (NP's) can show almost every color in the visible range of electromagnetic spectrum. As shown in fig. 1.1(a) changing the size (diameter) of the Au-NPs its color appearance is changing, this is related to its optical absorption, and how this absorption is dependent on the size is shown in fig.1.1 (b)

This resonant absorption is related to the phenomena known as Surface Plasmon Resonance (SPR) and is strongly dependent on the size, shape, and dielectric environment of the NPs [4]. Varying these physical properties one can tune the optical absorption of the NPs system.

In case of Au-Nanorods (NRs) this resonant absorption is dependent on the aspect ratio (Length/diameter) as well as on the polarization of the incident electromagnetic radiation. In addition the optical response of these nanostructures is also dependent on the number of neighbors they have, i.e. measurement of optical absorption of ensemble of NPs or NRs will not be the same as that of single isolated NP or NR. But measuring the optical absorption at single nano-object level is highly challenging due to the complexities involved in the measurement of weak electrical signal.

Recently, Crut et.al [5] has reviewed the different techniques to measure the optical absorption and scattering of single nano-objects. The technique known as spatial modulation spectroscopy (SMS) is able to measure the absolute extinction (absorption + scattering) cross-section of single NP as small as 5nm. The technique is based on the modulating the position of the single nano-object inside the light beam and detecting the induced modulation of the transmitted power using lock-in amplifier. The absolute extinction cross-section spectra of individual Au NRs of different aspect ratios measured by SMS is shown in figure 1.2 (a) and is compared with the spectra of randomly oriented solution of NRs, the difference is clearly visible. Also the effect of polarization on the extinction spectra of single nanorod is shown in figure 1.2 (b).

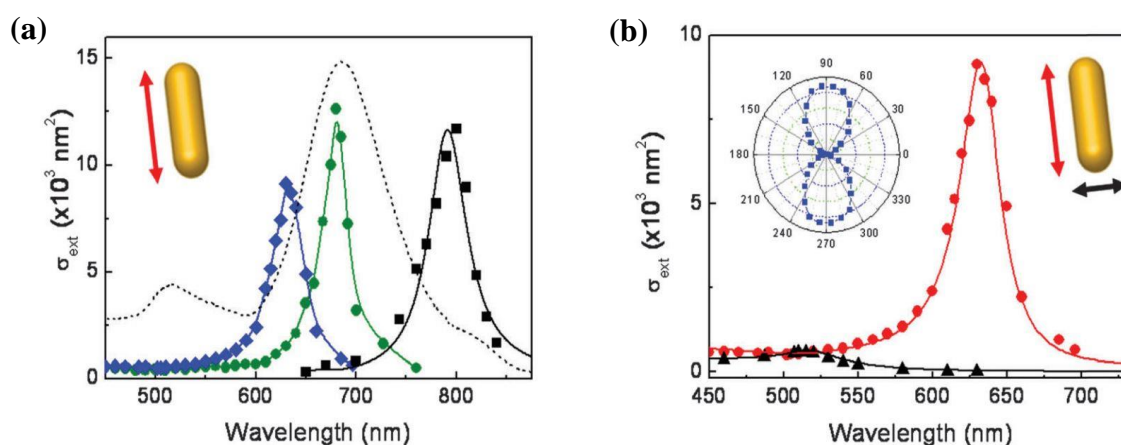


**Figure 1.2 :** Absolute extinction cross-section,  $\sigma_{ext}$  spectra of different (a) Gold nanorods with aspect ratios of 2.5, 3, and 4 (with increasing SPR wavelength) for light polarized along their main axis (the dotted line shows the absorption spectrum of the NRs solution) and (b) A single gold nanorod for light polarized along its long and short axis (long axis of 20.5 nm and aspect ratio of 2). Inset:  $\sigma_{ext}$  polarization dependence measured at 630 nm. [5]

But combination of optical and structural characterization of the same nano-object constitutes a major advance for fundamental investigations and is being explored nowadays with different techniques [5].

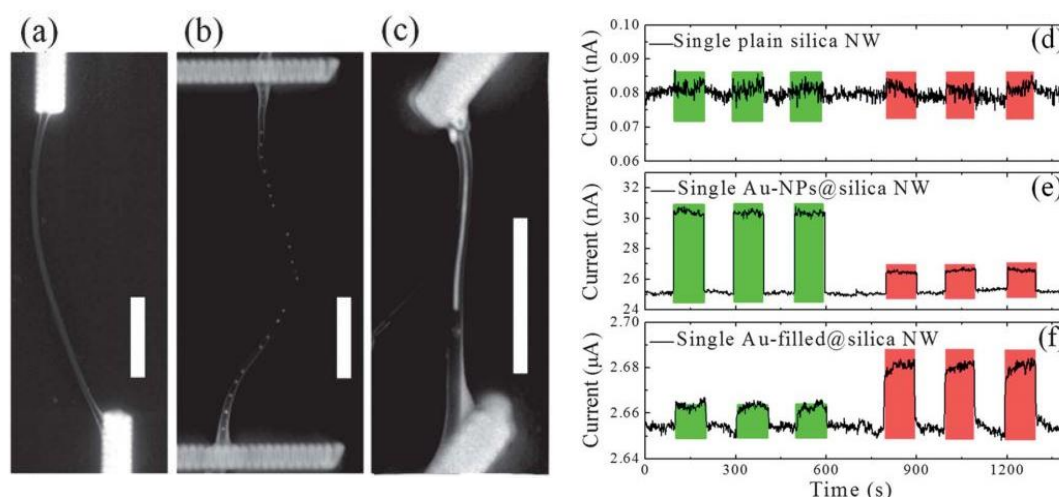


**Figure 1.3 :** (a)–(c) A typical micrograph of a single plain silica NW, single Au-NPs silica NW and single Au-filled silica NW, respectively. Scale bar =  $1\mu\text{m}$ . (d)–(f) The corresponding photoresponses under the wavelength of 532 and 808nm excitations, respectively [6]

Similarly, inorganic nanowires have already shown tremendous potential to be integrated in modern electronic devices due to their exciting electrical and optical properties. Nanowires are being used as gas sensors, photo diodes, light emitting diodes (LEDs), and in numerous other applications. With the advent of various techniques like molecular beam epitaxy, MOCVD it is possible to synthesize the nanowires very efficiently, but studying their properties as a single nano-object is always challenging. The flexibility to alter the electronic and optical properties by functionalization, hetero-structuring, and/or doping is the key advantage when working with inorganic nanowires. An example of how these properties can be enhanced is shown in fig. 1.3. As shown in this figure inclusion of Au inside the Silica NW changes its optical response. Measurement of photocurrent shows that, optical response can be selectively tune by changing the form of Au nanostructure inside the Silica NW [6].

Due to their long dimensions along the axis of nanowires and various device fabrication techniques available using electron microscopes and standard lithography, it is now routine job to measure the electrical and optical properties of single nanowires as shown in figure 1.3. But correlation of these properties with their structural and chemical properties and that too at nanoscale resolution is yet to be explored thoroughly.

Along with optical properties, thermal properties will also get altered with the nanostructuring. It is found that the thermal conductivity of individual Si nanowire is reduced to two orders of magnitude than the bulk Si [7] and is found to be dependent on the diameter of the nanowire. These measurements were carried out at cryogenic

temperatures and the variation of thermal conductivity with temperature is shown in figure 1.4(a) and (b).

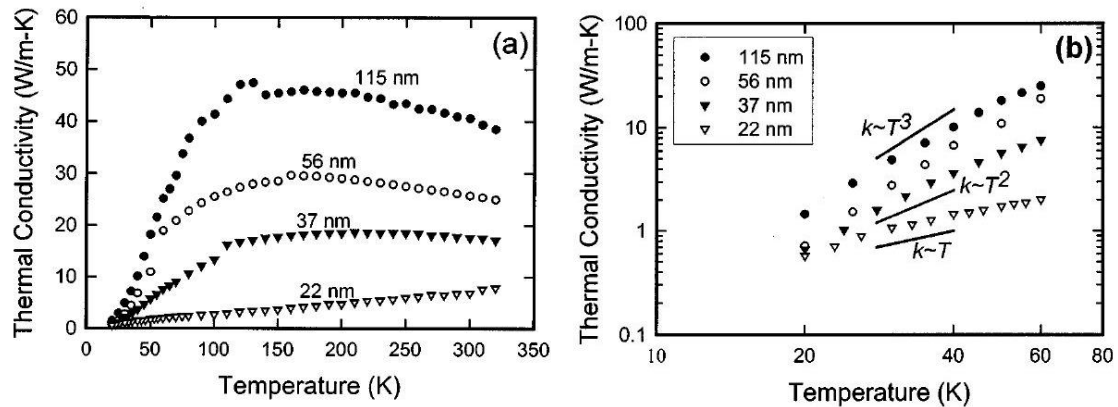


**Figure 1.4 :** (a) Measured thermal conductivity of different diameter Si nanowires. The number beside each curve denotes the corresponding wire diameter. (b) Low temperature experimental data on a logarithmic scale. Also shown are  $T^3$ ,  $T^2$ , and  $T^1$  curves for comparison.[7]

Due to this reduced thermal conductivity upon nanostructuring, nanowires were efficiently used to improve the thermoelectric performance [8,9] enhancing the figure of merit closed to 2. The ability of a given material to efficiently produce thermoelectric power is related to its dimensionless figure of merit and is given ( $ZT = \sigma S^2 T / K$ ), where ‘ $\sigma$ ’ is electrical conductivity, ‘ $S$ ’ is Seebeck coefficient and ‘ $K$ ’ is thermal conductivity. By varying the nanowire size and impurity doping levels, figure of merit values representing an approximately 100-fold improvement over bulk Si are achieved over a broad temperature range.

In addition to single nanowire analysis, a vast number of reports are available in the literature utilizing the properties of bunch or ensemble of nanowires grown on the substrate for various applications. Surface structuring is being used since long time to increase the light absorption efficiency compare to their planar thin film counterparts. In case of planar thin films, their optical absorption is limited by the short optical path length and minority carrier diffusion length and to improve the absorption efficiency one needs a material with high absorption coefficient or excellent light trapping. Light trapping can be achieved by creating the nano-structured surfaces or by growing the array of nanowires on the substrate. With the numerous techniques available to synthesize the nanowires array or structured surfaces researchers were able to increase the optical absorption efficiency in such kind of structures and the methods were successfully employed to improve the device performance. One such example of preparing the nano-structured surface from crystalline-Si (c-Si) using ultra-fast laser machining is shown in figure

1.5(a) [10]. c-Si is the building block for the solar photovoltaics industry and the photon conversion efficiency over the wide range of wavelengths and incidence angles can be enhanced by increasing the absorption efficiency by nanostructuring. Inset in figure 1.5(a) shows the optical image of c-Si, where ultrafast-laser-treated area looks completely black. This is confirmed by the results, shown in Figure 1.5(b), which shows that the specular reflection is virtually negligible in the visible range from an ultrafast-laser-treated Si surface [10].

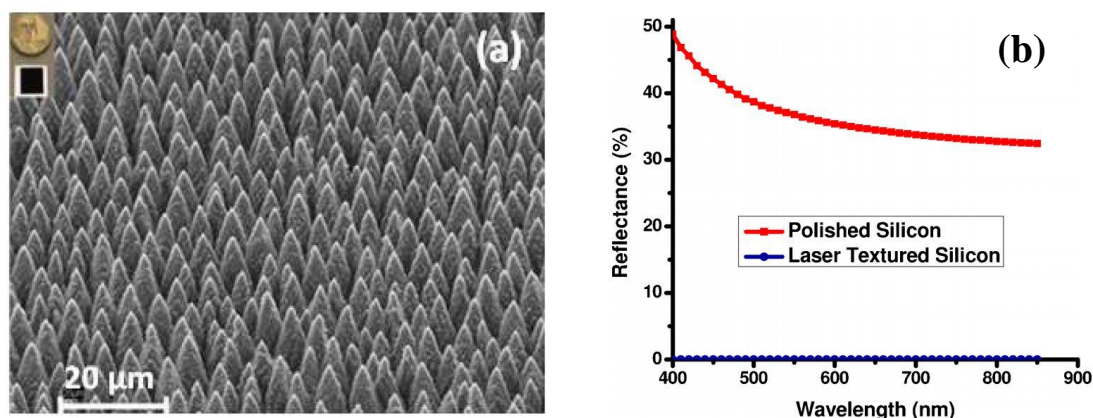


**Figure 1.5 :** (a) SEM images of ultrafast-laser-induced micro/nano structured silicon surface, inset shows optical photograph of laser-treated silicon surface that looks black, (b) Specular light reflection from polished bare silicon and laser micro/nano structured silicon surface shown in (a).

Similar kind of study has also been performed on the Silicon nanowire arrays prepared by deep reactive ion etching, the absorption efficiency owing to the light trapping can be varied by changing the length of the nanowires [11]. Because of this behavior most of the commercial solar cells use surface texturing to achieve reduction in front surface reflection to enhance the light trapping.

Along with this light trapping behavior, the large surface area provided by the array of nanowires/nanorods is being utilized by various applications like photocatalytic activity [12], photo-detectors [13] and many more. Although, these structures are easy to fabricate in large scale, cost effective and, efficient as well; their performance is limited by the response of individual nanostructure upon light illumination. And studying the optical properties of individual nanowire/nanorod will be beneficial to improve the characteristic properties of this array of nanostructures. We believe that the laser assisted atom probe tomography can fulfill this requirement by analyzing the individual nanowire/nanorod structurally and chemically in 3D with near atomic resolution and by correlating their structural properties with optical and thermal properties.

In laser assisted atom probe tomography (LaAPT) the specimen is in the form of nano-needle with diameter less than 100nm. The quality of data obtained in LaAPT experiment is significantly dependent on the optical absorption of the needle shaped specimen upon laser illumination and the thermal diffusivity (conductivity) of the specimen. So the data obtained in LaAPT experiment can be utilized to understand the absorption and thermal properties of material at nanoscale and moreover it can be correlated to its 3D structure as well. Since LaAPT is based on evaporation of the atoms located at the very apex of the specimen, the ability of the specimen to absorb electromagnetic energy close to this region upon nanostructuring, which depends on the type of the material and wavelength of the incident radiation can be utilized to understand the optical and thermal behavior down to surface level which is defined by few atomic layers.

### **1.2.2 Optical Emission at nanoscale**

Another important and relatively complex phenomena than absorption in solids is the optical emission. The physical mechanism responsible for light emission varies considerably from material to material. Atoms emit light by spontaneous emission when electrons in excited state drop down to lower level by radiative transition. In solids, the radiative emission process is called “Luminescence”. Luminescence can occur by number of mechanisms, e.g. electroluminescence: the emission of light by passing the electric current through the material, cathodoluminescence: the emission of light when struck by electrons and many other types as well [1]. However, in this chapter and thesis more attention is given to the process of light emission after absorbing a photon of higher energy; called Photoluminescence (PL).

The emission of photons upon absorbing a high energy photon has great importance in the field of devices based on this principle. A number of semiconducting materials shows the PL characteristics, but the probability of the radiative transitions depends on various factors such as the type of semiconductor (direct or indirect), amount of doping and defects etc. In direct band gap semiconductors, the optical transition from valence to conduction band after absorption of photon can occur without absorbing and/or emitting phonon (lattice vibrations) while on the other hand in indirect band semiconductors, phonon must be absorbed or emitted to absorb the photon. Similarly, the emission of photon in these semiconductors is also governed by the process which is opposite to the absorption of photon, i.e. emission of photon without absorbing or

emitting phonon in direct band gap semiconductors and a phonon must be either emitted or absorbed when the photon is emitted in indirect band gap semiconductors. These processes are called as interband transitions where the lowest occupied level in conduction band and highest un-occupied level in valence band are involved in the transitions. This behavior of luminescence is schematically depicted in figure 1.6.

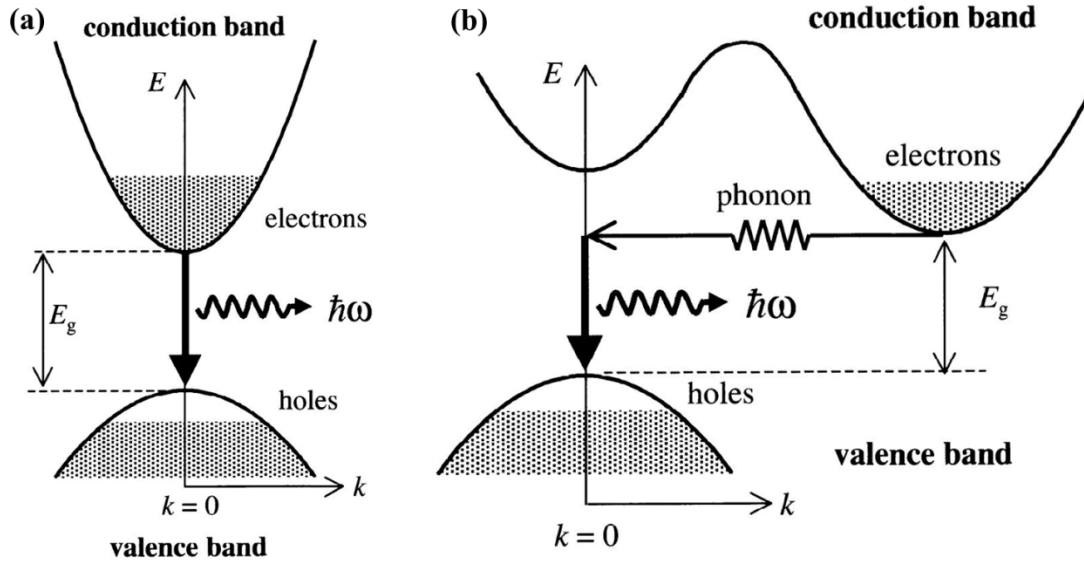


**Figure 1.6 :** Schematic diagram of the interband luminescence process in (a) direct band gap semiconductor and in (b) indirect band gap semiconductor : the transition must involve emission or absorption of phonon to conserve the momentum. The shading indicates that the states are occupied by electrons. The filled states at the bottom of conduction band and empty states at the top of valence band are created by injecting electrons and holes into the semiconductor. ( $E_g$  : band gap,  $\hbar\omega$  : energy of the emitted photon).

A band diagram for bulk direct and indirect band gap and SC is shown in fig. 1.6(a) and (b) respectively. The figure shows only luminescence behavior, i.e. the excitation of electrons from valence to conduction band by any means (e.g. photon, electron etc.) is not shown, but already considered to be in excited state. The bands are represented by approximately parabolas and the shading indicates that states are occupied by electrons. In case of indirect band gap semiconductors, the requirement of emitting both phonon and photon during the transition makes it a three-body process and hence less likely and weaker when compared to the two-body process in direct band gap semiconductor. For this reason indirect gap materials are generally bad light emitters e.g. Si, Ge, SiC. As can be seen from the fig. 1.6 that the luminescence is characteristic of band gap of the semiconductor, i.e. the energy of the emitted photon depends on the band gap of the material and the band gap depends on the composition and crystal symmetry of the material. So that, it is possible to change the energy of the emitted photon (and hence

its wavelength) as per the requirement by just changing the band gap of material. This gave rise to the concept of band gap engineering or band gap tuning where tuning the band gap of material by changing the composition and/or crystal symmetry is achieved. It also means that the bandgap can be continuously tuned by controlling the chemical composition of binary, ternary or quaternary alloys (e.g.  $\text{Si}_x\text{Ge}_{1-x}$ ,  $\text{In}_x\text{Ga}_{1-x}\text{As}$ ,  $\text{In}_x\text{Ga}_{1-x-y}\text{Al}_y\text{As}$ ) during the synthesis of the material.

The processes involved during photo-luminescence (PL) are explained with the help of band diagram shown in fig. 1.7. This is a more detailed version of diagram already given in fig. 1.6 (a). Photons are absorbed from excitation source such as laser or lamp, and this injects electrons into the conduction band and holes into valence band. This will be possible if the frequency  $\nu_L$  of the source is chosen so that  $h\nu_L$  is greater than  $E_g$ , the band gap of the material. It is apparent from fig. 1.7 that the electrons are initially created in states high up in the conduction band. The electrons do not remain in these initial states for very long time, because they can lose their energy very rapidly by emitting phonon. This process is indicated by cascade of transitions within the conduction band shown in fig. 1.7. Each step corresponds to the emission of phonon with the correct energy and momentum to satisfy the conservation laws. The electron-phonon coupling in most solids is very strong and these scattering events take place on time scales as short as  $\sim 100\text{fs}$  [3]. The same conditions apply to the relaxation of holes in the valence band. After the electrons and holes are relaxed, they can recombine radiatively to emit the photon with energy  $h\nu < E_g$ .

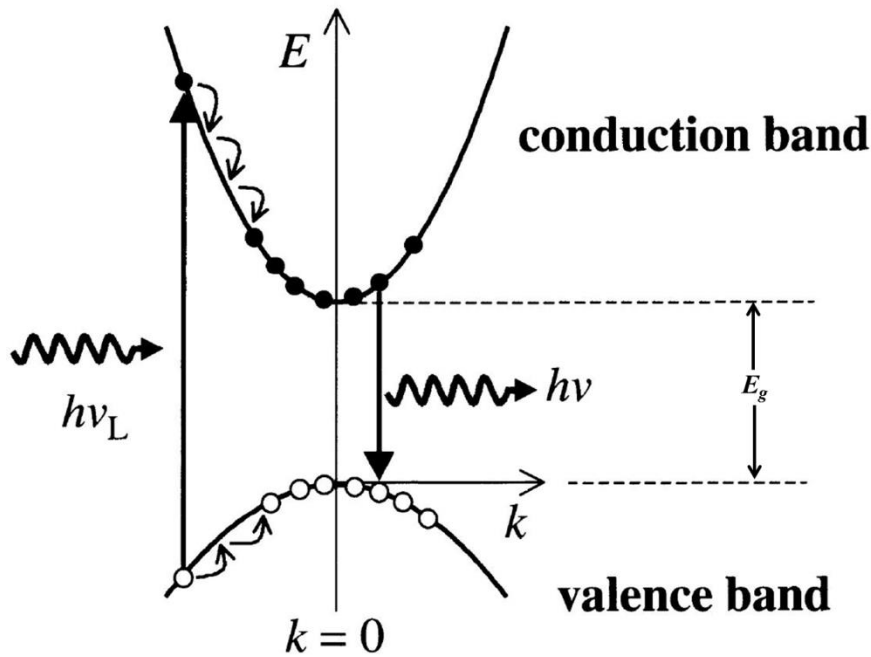


**Figure 1.7 :** Schematic diagram of the processes occurring during photo-luminescence in direct gap semiconductor after excitation at frequency  $\nu_L$ . The electrons and holes rapidly relax to the bottom of their bands by phonon emission before recombining by emitting photon

Along with the interband emission, other emission mechanisms may arise due the defect induced electronic states within the band gap. Some of these levels may yield radiative recombination. These defect levels can be intrinsic or created intentionally to tune the luminescence properties of the material. The PL measurements can yield a good amount of information to understand the emission properties of material which will be helpful to develop the electroluminescent devices such as light emitting diode and lasers.

As mentioned earlier, tuning the band gap of the material one can tune the optical emission from the material. This idea of band gap engineering is further elevated by preparing heterostructures. In semiconductor heterostructures, semiconductors with different bandgap are arranged in order to occupy different spatial regions. The primary goal of this approach is the possibility of designing semiconductor systems with specific electronic properties, which constitute the functional building block of electronic and optoelectronic devices such as high electron mobility transistors, light-emitting diodes, laser diodes, single photon emitters or photodetectors. In many cases these specific properties can be achieved by confining the charge carriers (electrons and/or holes) by reducing at least one of the dimensions of the material to nanometric scale. This mechanism of confining the charge carriers, also known as “quantum confinement” can be observed when one of the dimensions of the material is of the order of de Broglie

wavelength of the electron wave function [14]. In a bulk material, electrons behaves as if it was free when the confining dimension is large compared to the de Broglie wavelength. During this state, the bandgap remains at its original energy due to a continuous energy state. However, as the confining dimension decreases and reaches a certain limit, typically in nanoscale, the energy spectrum becomes discrete. As a result, the bandgap becomes size-dependent. The 2-dimensional (2D) solids (1D confinement) are called as quantum wells, similarly 1D solids (2D confinement) as quantum wire (e.g. nanowire, nanorods, nanotubes etc.) and zero-dimensional solids (3D confinement) as quantum dots. The density of states (DOS); i.e. the allowed number of allowed electron or hole states per volume at given energy can be derived using basic quantum mechanics [2,3] for 3D (bulk) solids and also for 2D, 1D and 0D solids by applying the spatial boundary conditions. A comparison of DOS is shown in figure 1.8.

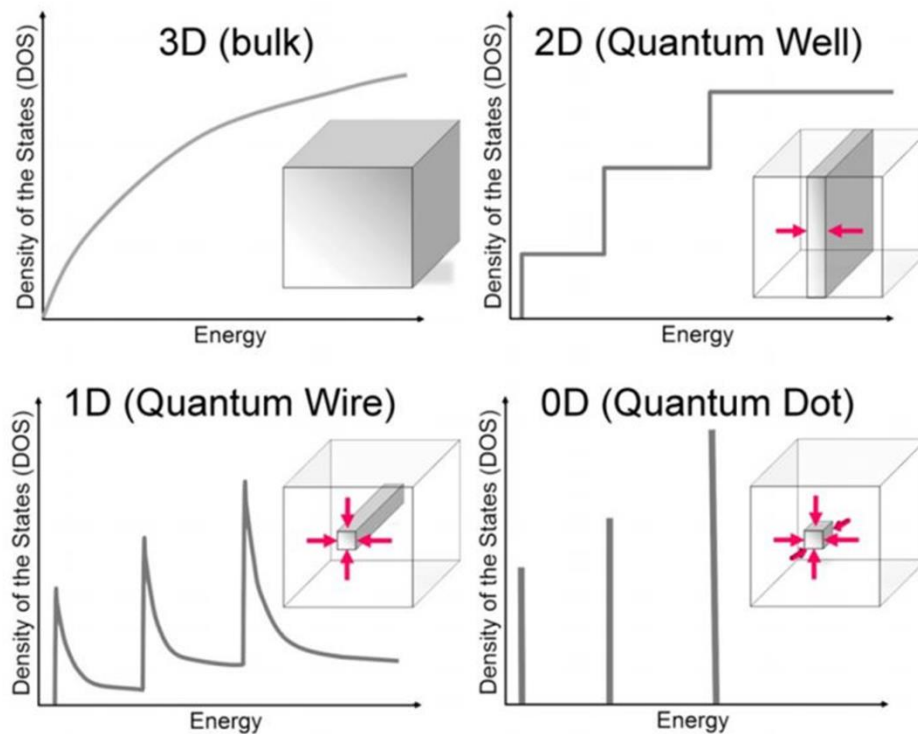


**Figure 1.8** : Electronic DOS for a bulk 3D crystalline material, a 2D QW, a 1D NW or NT, and a 0D QD. The insets report a cartoon showing the corresponding spatial confinement: confinement directions are defined by arrows[15].

As shown in fig. 1.8, a bulk material exhibits a square root energy ( $E^{1/2}$ ) dependence of the DOS, while the DOS of a 2D system is described by a step function ( $E^0$  dependence for the single quantized state), the 1D systems show a  $E^{-1/2}$  dependence for each quantized state and the QD DOS is a  $\delta$ -function since the electron is confined in all three spatial dimensions and all available states exist only at discrete energies [15].

This change in electronic properties upon confining the carriers will have substantial effect on the optical emission properties of the semiconductors at nanoscale. An example of size dependent emission from CdSe QD's is presented in fig. 1.9 [16].

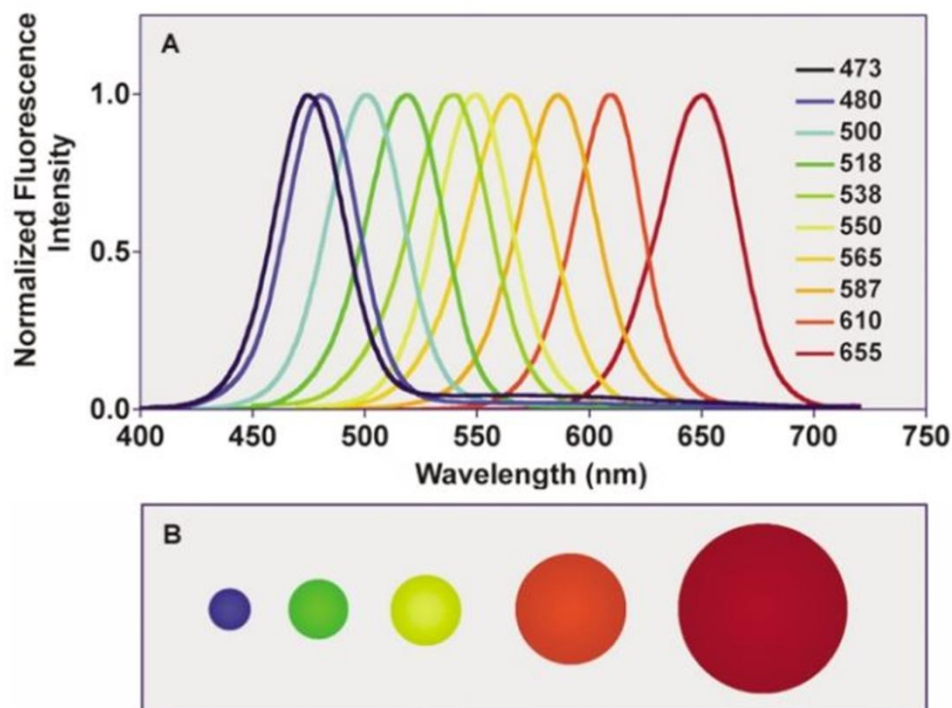


**Figure 1.9 :** Size-tunable fluorescence spectra of CdSe quantum dots (A), and illustration of the relative particle sizes (B). From left to right, the particle diameters are 2.1 nm, 2.5 nm, 2.9 nm, 4.7 nm, and 7.5 nm.

Due to its exciting features quantum confined solids have been considered as potential candidate for various application ranging from bio imaging to optoelectronics. Although it is possible to synthesize these materials using different techniques including chemical as well as physical (e.g. MOVPE, MOCVD etc.), it is not straightforward to understand the physical mechanisms behind the optical processes involved in these solids particularly at single emitter level.

In this regard, in this thesis an attempt have been made to understand the correlation between optical emission and structural properties of InGaN/GaN multi quantum well's system. As mentioned before quantum well (QW) is a 2D solid, i.e. the carriers are confined in one dimension. The simplest way to explain QW is schematically shown in fig. 1.10 (a) where a thin layer of semiconductor with band gap  $E_g^{QW}$  and thickness  $t_{QW}$  is synthesized between two thicker semiconductors with band gap  $E_g^{barr.} > E_g^{QW}$ . An example of InGaN/GaN quantum well observed by high-resolution scanning electron transmission microscopy (HR-STEM) is also reported in fig. 1.10 (b)

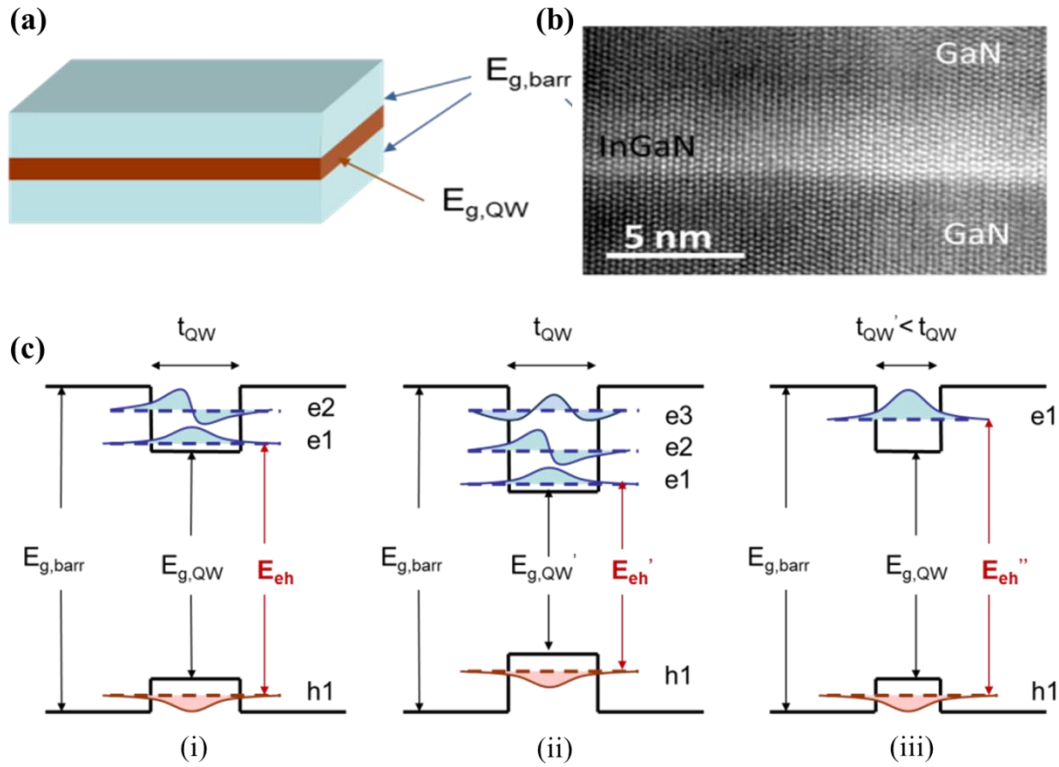


**Figure 1.10 :** (a) Schematic of semiconducting QW with band gap  $E_g^{QW}$  sandwiched in between two thicker semiconducting layers of band gap  $E_g^{barr.} > E_g^{QW}$ . (b) HR-STEM image of InGaN as QW and GaN as barrier. (c)-(i) Potential profile and confined electron and hole energy wavefunctions within a rectangular quantum well of a given composition and thickness. Change in the composition (c)-(ii) and thickness (c)-(iii) of the QW results change in the energy of states and the main radiative recombination respectively.

The resultant potential profile after aligning the bands of different phases of semiconductor is shown in fig. 1.10(c)-(i). The effect of quantum confinement is that both electron and hole ground states are not at the bottom of conduction or valence bands of the QW phase material but are lifted by certain amount and is called as “confinement energy”. This energy can be approximated by considering the infinite potential barrier and solving the Schrodinger’s equation [17] and this energy for electron/hole state can be expressed

$$E_{n(e,h)} = \frac{\hbar^2 \pi^2 n^2}{m_{e,h}^* t_{QW}^2} \quad n=1,2,3\dots$$

where,  $m_{e,h}^*$  is the electron/hole effective mass.

Change in the QW composition and/or QW thickness has strong impact on the energy of the electron/hole states as well as on the main radiative recombination as shown in figure 1.10(c)-(ii) and (iii). These two parameters govern the optical emission performance of the QW based devices and understanding the relation between these

structural properties and its effect on the optical emission is being the key topic for many researchers around the globe. But direct or one-to-one correlation between structural and optical properties is yet not explored thoroughly due to the limitations of analyzing nanoscale material using both structural and optical characterization tools available.

Laser assisted Atom Probe Tomography (LaAPT) is known to be a powerful technique to analyze the sharp needle shaped nanoscale samples structurally and chemically in 3-dimension. LaAPT will be useful to study the elemental composition of QW's as well as will give the information on the structural and compositional anomalies within the QW samples, if any. Along with LaAPT, Scanning transmission electron microscopy (STEM) can also be effectively used to complement and support the results obtained with LaAPT. Both these technique will give unprecedented information on the structural properties of the QW samples. To study the optical emission properties of QW's  $\mu$ -photoluminescence ( $\mu$ -PL) spectroscopy can be utilized, which will give the information on the radiative recombination processes. To draw the direct correlation between optical and structural properties of a nanoscaled material, there is need to perform the experiments on same nano-object instead of analyzing it separately by different techniques and correlating the results (or comparative approach). In this regards, in this thesis we have performed the  $\mu$ -PL spectroscopy, LaAPT and STEM on the same nano-object to have insights on the relation between optical and structural properties down to sub-nanometric scale.

### **1.3 Choice of Material**

To demonstrate the ability of LaAPT to investigate the optical absorption and thermal properties of nano materials, we chose CERMET as material. CERMET; an acronym for METallic CERamics are group of materials widely used as solar selective coating in solar thermal power plants owing to their high solar absorptance and low thermal emittance properties. Various types of CERMETS are being studied since long time [18,19] and there optical absorption as well as thermal properties are widely studied owing to their applications in concentrating solar power (CSP) systems. CSP systems use solar absorbers to convert sunlight to thermal electric power. To have more efficient CSP systems, more efficient selective coatings are needed that have both high solar absorptance and low thermal emittance at higher operational temperature. A high

absorptance at wavelengths ( $\lambda$ )  $\leq 3\mu\text{m}$  and a low absorptance at  $\lambda \geq 3\mu\text{m}$  characterize spectrally selective surfaces, as shown in Fig 1.11

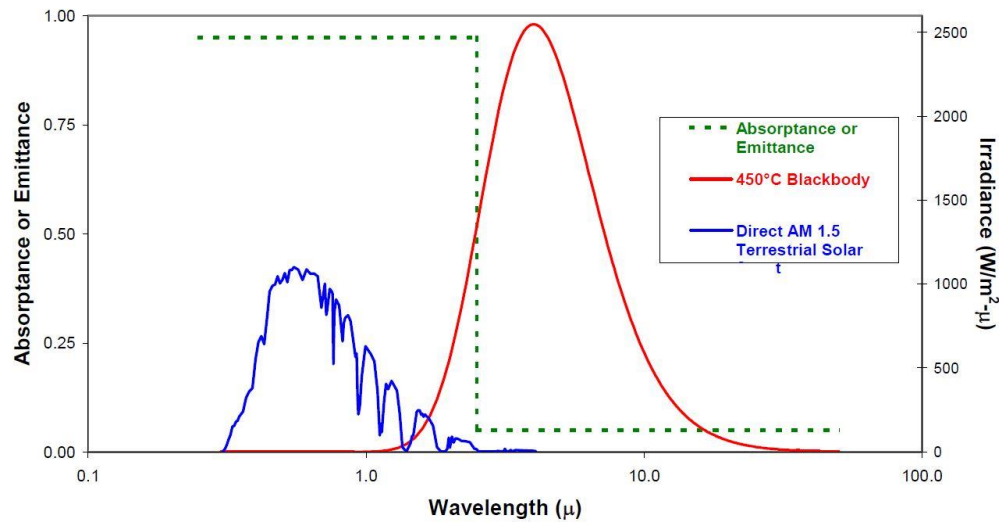


**Figure 1.11** : Spectral performance of an ideal selective solar absorber

The CERMETS are good candidate to prove the capacity of LaAPT to investigate the optical absorption and thermal behavior of materials at nanoscale. Please note that, even though the optical and thermal properties of CERMETS are widely studied, these properties are subjected to change with the nanostructuring as explained in the previous section of this chapter. And hence studying the optical and thermal behavior of CERMETS at nanoscale has its own importance. With LaAPT analysis one might be able to have new information which can be used further to improve the performance of solar selective coatings and this method in general can be utilized to characterized nanostructured materials especially 1D nanomaterials like nanowires, nanorods etc.

For studying the optical emission properties and its correlation to their structural properties using LaAPT, the ideal material will be quantum confined solids like quantum wells (QW), self-assembled quantum dots (QD) or embedded in nanowires. As explained in the previous section the optical emission properties of these solids are strongly dependent on the variation in elemental composition as well as the on the structural deformations within the QW or QD systems. Due to these reasons we decided to work on the InGaN/GaN QW system.

### 1.3.1 Types of Absorbers

Selective absorber surface coatings can be categorized into six distinct types: a) intrinsic, b) semiconductor-metal tandems, c) multilayer absorbers, d) multi-dielectric

composite coatings, e) textured surfaces, and f) selectively solar-transmitting coating on a blackbody-like absorber. Intrinsic absorbers use a material having intrinsic properties that result in the desired spectral selectivity. Semiconductor-metal tandems absorb short wavelength radiation because of the semiconductor bandgap and have low thermal emittance as a result of the metal layer. Multilayer absorbers use multiple reflections between layers to absorb light and can be tailored to be efficient selective absorbers. Metal-dielectric composites - CERMETS - consist of fine metal particles in a dielectric or ceramic host material. Textured surfaces can produce high solar absorptance by multiple reflections among needle-like, dendritic, or porous microstructure. Additionally, selectively solar-transmitting coatings on a blackbody-like absorber are also used but are typically used in low-temperature applications. These constructions are shown schematically in Figures 1.12(a)-(f), respectively [20]

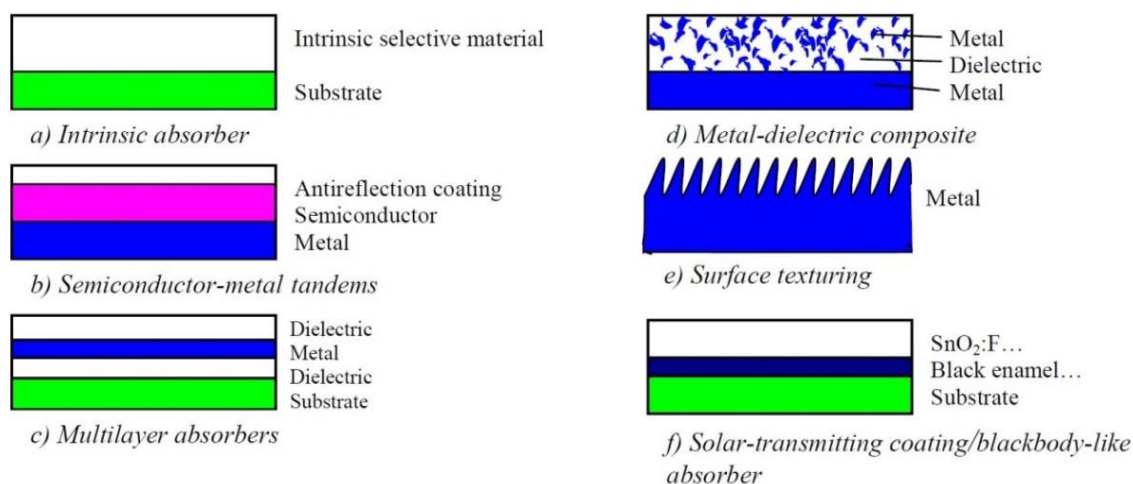


**Figure 1.12** : Schematic designs of six types of coatings and surface treatments for selective absorption of energy.

All these types are discussed in great detail by Kennedy et. al. in his review of mid- to high-temperature solar selective absorber materials [20]. Since we are more interested in CERMETS i.e. metal-dielectric composites selective absorbers, henceforth will discuss the same in more details.

The highly absorbing metal-dielectric composite, or cermet, consists of fine metal particles in a dielectric or ceramic matrix, or a porous oxide impregnated with metal. These films are transparent in the thermal IR region, while they are strongly absorbing in the solar region because of interband transitions in the metal and the small particle resonance. The absorbing cermet layer can have either a uniform or graded metal content. The metal-dielectric concept offers a high degree of flexibility, and the absorption selectivity can be optimized by proper choice of constituents, particle concentration, size,

shape, and orientation. A variety of techniques, such as electroplating, anodization, Chemical Vapor Deposition (CVD), and co-deposition of metal and insulator materials by physical vapor deposition (PVD) like sputtering and pulsed laser deposition, can produce the CERMET coatings.

In cermets, solar absorptance is mainly determined by the response of the absorbing particles. There is a shift of the absorption and scattering cutoffs to higher wavelengths when the particle radius,  $r$ , increases. This effect is accompanied by a reduction in the maximum of the scattering and absorption efficiencies roughly proportional to  $1/r$  [21]. Alumina is well known as a ceramic, stable at high temperature, but  $\text{SiO}_2$  and  $\text{AlN}$  have also been used [22]. In addition,  $\text{ZrO}_2$  films could find applications as the dielectric medium in cermets, as multilayer solar-selective absorbers, or as anti-reflection (AR) coatings because of its high refractive index, high dielectric constant, low thermal conductivity, and corrosion-resistant properties [23].

In this thesis we have used Gold nanoparticles (Au-NPs) as a metallic inclusion in different dielectric matrices. Along with the properties mentioned earlier the system of Au-NPs embedded in dielectric matrix have generated considerable interest in the field of opto-electronics and non-linear optics [24] due to their strong coupling to incident electromagnetic radiation and therefore will be a good candidate for this study. It was decided to begin with the simple system with inclusion of low dense Au-NPs ranging in diameters from 10-15 nm uniformly distributed in the matrix so as to avoid the complications involved in the sample preparation for LaAPT experiments. Considering the volume analyzed in the LaAPT experiment, i.e. roughly  $50 \times 50 \times 100 \text{ nm}^3$ , the specimen should be prepared in such a way that the presence of Au-NPs should be evident in this volume. The details regarding the specimens analyzed in this study and the problems encountered therein are summarized in the following section.

### **1.3.2 Specimens analyzed to study the absorption and thermal behavior of nanostructured materials (CERMETS) by LaAPT**

In the course of this work various samples of Au-NPs embedded in dielectric/ceramic matrices were studied. As explained in previous section sample should be compatible with the techniques used to prepare the LaAPT samples as well as it should be successfully analyzed in LaAPT without any damaged to the specimen during analysis. Although metallic nano-objects embedded in dielectric matrix are one of the building

blocks of optoelectronics and plasmonics, there are very few reports in the literature concerning the LaAPT analysis, owing to the complexities involved therein. So studying these materials thoroughly will be helpful to resolve the problems arise during the LaAPT analysis.

We were collaborating with different laboratories in and out of France for synthesizing Au NPs embedded in different matrices. A comprehensive list of materials analyzed during the course of this thesis along with the difficulties encountered is given below. Though the list includes unsuccessful attempts more than the effective one, the experience gain was efficiently utilized further.

**(a) Au-Al<sub>2</sub>O<sub>3</sub> :**

The Au-NPs embedded in alumina matrix were the first specimen analyzed in this list. The specimens were synthesized at National Chemical Laboratory (NCL), Pune, INDIA. Thin films of Au-Al<sub>2</sub>O<sub>3</sub> were deposited using co-sputtering technique with targets of Aluminum (Al) and Gold (Au). Various deposition parameters like deposition temperature, time, Ar and O<sub>2</sub> flux, and RF & DC power were varied to get the required uniform size distribution of Au-NPs in the matrix. Annealing the samples at 500°C and 850°C after deposition was also performed. To confirm the phase and structure all the samples were characterize by X-ray diffraction (XRD) and Scanning Electron microscopy (SEM) and are shown in fig. 1.13.

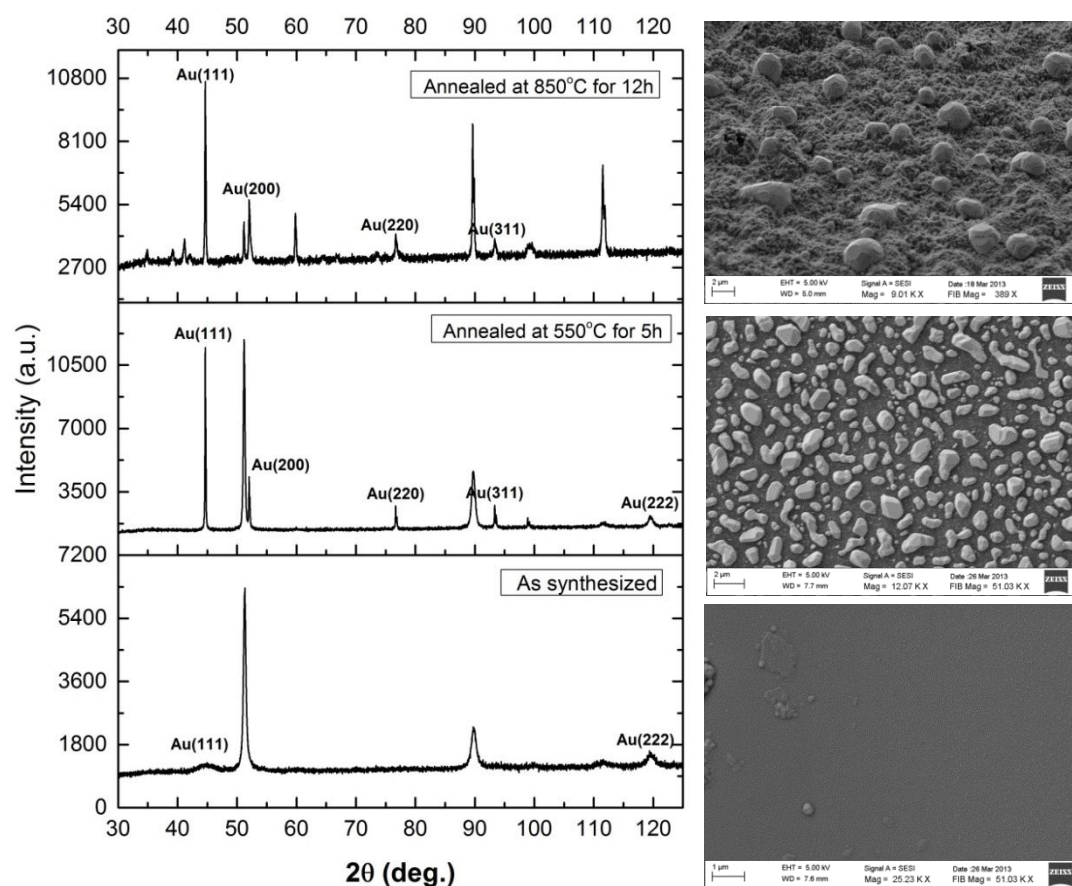


**Figure 1.13** : XRD and SEM characterization of Au- $\text{Al}_2\text{O}_3$  films on stainless steel (SS) substrate. The unindexed peaks correspond to the substrate. The XRD and adjacent SEM image correspond to same sample.

In figure 1.13, the XRD pattern obtained from as synthesized, annealed at 550°C and 850°C are shown and the SEM images adjacent to these XRD patterns correspond to the same sample. All Au peaks are indexed while all unindexed peaks correspond to the substrate SS. As shown in this figure, the XRD pattern of as synthesized specimen shows a broad Au-peak, but very less in intensity, corresponding SEM image for as synthesized specimen shows a uniform surface morphology with no sign of Au NPs on the surface. But once the specimen is annealed to the elevated temperatures, the XRD pattern shows strong and sharp Au-peaks. The SEM image of these samples shows odd sized particulates on the surface of the film. Looking at the bright contrast of these particles they are probably the Au-particles. But their size is in the range of 250-500nm which is not suitable for LaAPT analysis. In addition, there is no evidence of alumina observed in any of the XRD pattern; it is probably due to the amorphous nature of the  $\text{Al}_2\text{O}_3$ . The cross-sectional SEM image of the 850°C annealed film is shown fig. 1.14.

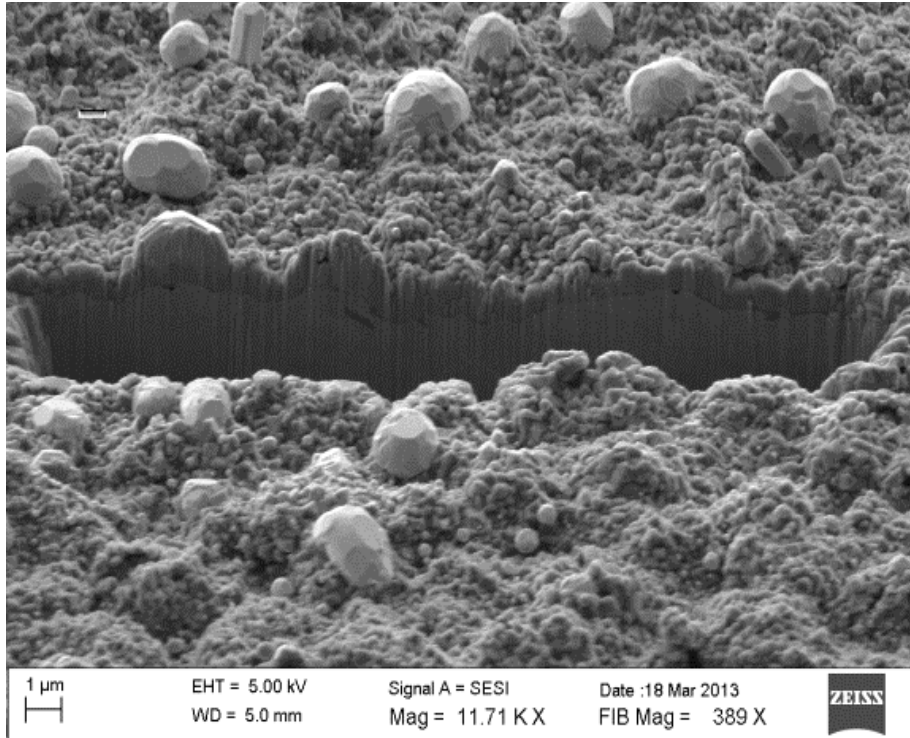


**Figure 1.14 :** Cross-sectional SEM image of the 850°C annealed Au-Al<sub>2</sub>O<sub>3</sub> specimen

The film surface is quite rough, and the interface between substrate and the film is visible. Several attempts were made to prepare the LaAPT sample from this specimen but all of them were ended up with the failure.

### **(b) Au-TiO<sub>2</sub>:**

This is second specimen we received from NCL, Pune INDIA. Au-nanoclusters embedded in TiO<sub>2</sub> nanorods were synthesized by chemical route. The transmission electron microscope (TEM) image of the single isolated nanorods is shown figure 1.15(a). The sample was in powder form, so method using optical microscope manipulation was used to prepare the atom probe tip. Attempts were made to pick up the single nanorods under the optical microscope and once succeeded, and then with the use of focused ion beam (FIB) annular milling final atom probe tip was prepared. The SEM image before and after annular milling is shown in figure 1.15(b) and (c) respectively.

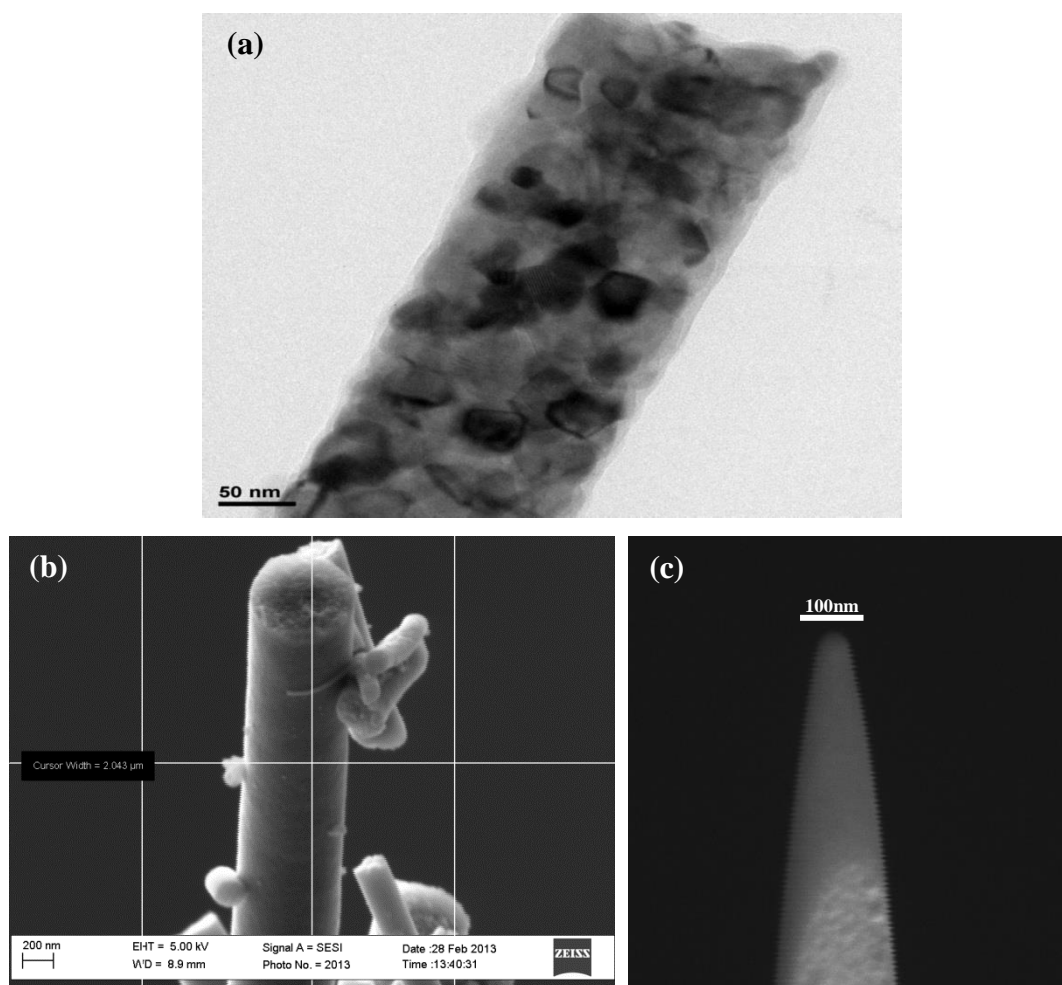


**Figure 1.15 :** (a) TEM image of Au-TiO<sub>2</sub> nanorod, Au nano-clusters seen in dark contrast, (b) Au-TiO<sub>2</sub> nanorod before annular milling and (c) after milling, the final atom probe tip.

Although we succeeded to prepare atom probe tips from this specimen, analyzing the same in atom probe was a real challenge. The analysis used to begin normally but all of the tips were damaged or flashed without giving sufficient data for analysis. This can be due to the differences in field of evaporation of the Au and TiO<sub>2</sub>, also the specimen is prepared via chemical route, so the adhesion or the contact between Au-nanoclusters and TiO<sub>2</sub> matrix will not be strong enough to withstand the stress generated by the high electrostatic field applied in the LaAPT experiment.

### (c) Au-Fe<sub>2</sub>O<sub>3</sub>:

This is the third specimen we have received from NCL, Pune, INDIA. The specimen was prepared by using pulsed laser deposition (PLD) technique. The targets were prepared by mixing the commercially available Au powder in the α-Fe<sub>2</sub>O<sub>3</sub> powder in different proportions (e.g. 5 and 10 at.% Au). Deposition parameters were varied to get

the uniformed film with formation of Au-NPs inside the matrix. From different samples prepared at different conditions, the sample prepared at 500°C deposition temperature with 10 at.% Au shown commendable results. The SEM image and XRD pattern from this specimen is shown in figure 1.16(a) and (b) respectively. The cross-sectional SEM image showing the formation of Au-NPs inside the  $\alpha$ -Fe<sub>2</sub>O<sub>3</sub> matrix is shown in figure 1.16(c).

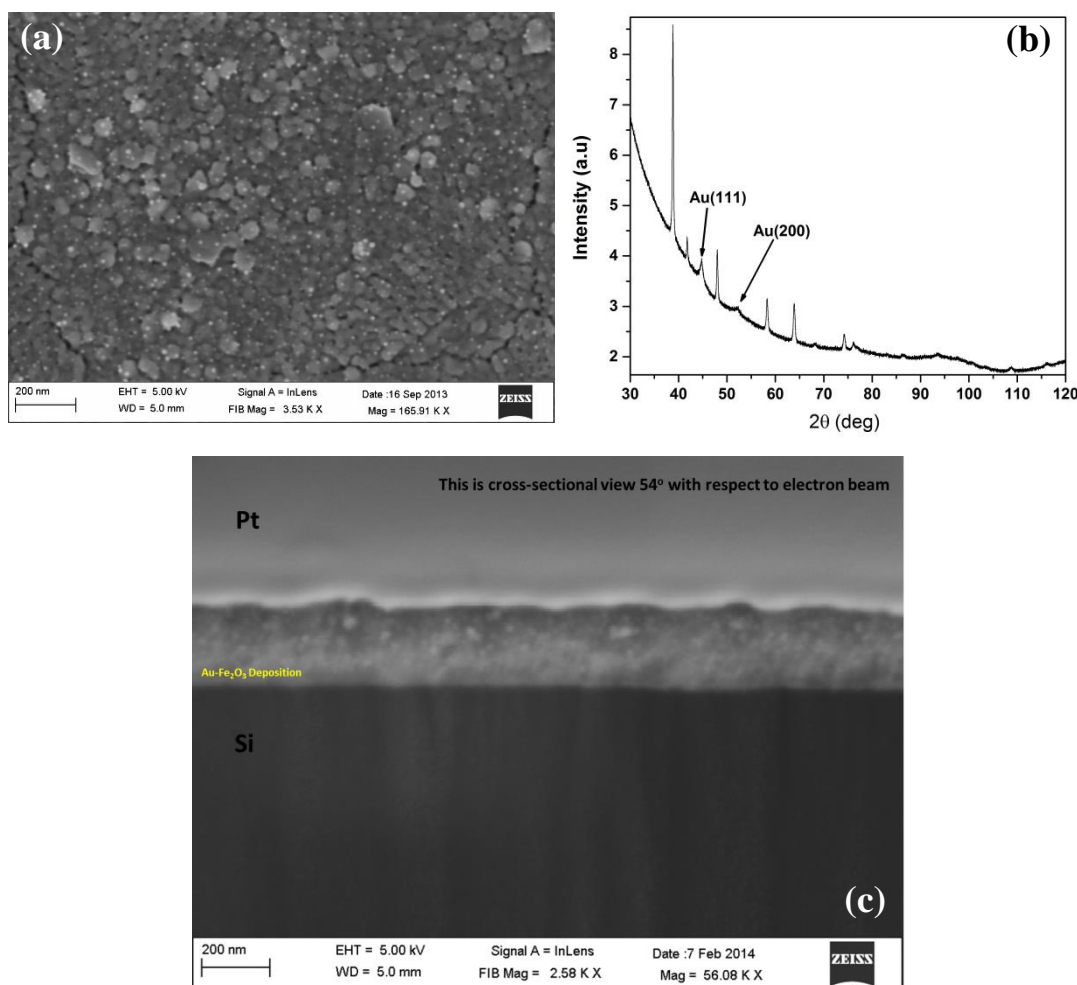


**Figure 1.16 :** (a) SEM image of Au-Fe<sub>2</sub>O<sub>3</sub> film, tiny bright spots correspond to Au-NPs, (b) XRD pattern showing existence of Au-NPs, all unindexed peaks correspond to  $\alpha$ -Fe<sub>2</sub>O<sub>3</sub> phase, (c) cross-sectional SEM image of the film deposited on Si-Substrate, tiny bright spots inside the film are due to the Au-NPs

This specimen is one of the successfully analyzed specimens in this thesis; there was not any difficulty to prepare the atom probe tip from this specimen. The tips were prepared across the thin film as well as along the thin film which gives advantage to analyze more Au-NPs.

**(d) Au@Ag-SiO<sub>2</sub>:**

This bimetallic alloy NPs embedded in SiO<sub>2</sub> matrix was provided by Dr. Etienne Talbot and synthesized by his collaborators. A layer of SiO<sub>2</sub> is deposited on Si substrate, then the chemically prepared Au@Ag NPs were dispersed on this SiO<sub>2</sub> layer using spin coating and finally another layer of SiO<sub>2</sub> is deposited on top of it to sandwich the bimetallic alloy NPs in SiO<sub>2</sub> matrix. The cross-sectional SEM image in figure 1.17(a) clearly shows the evidence of these bimetallic NPs sandwiched in SiO<sub>2</sub> matrix. An atom probe tip prepared from this specimen along the thin film direction is shown in figure 1.17(b).

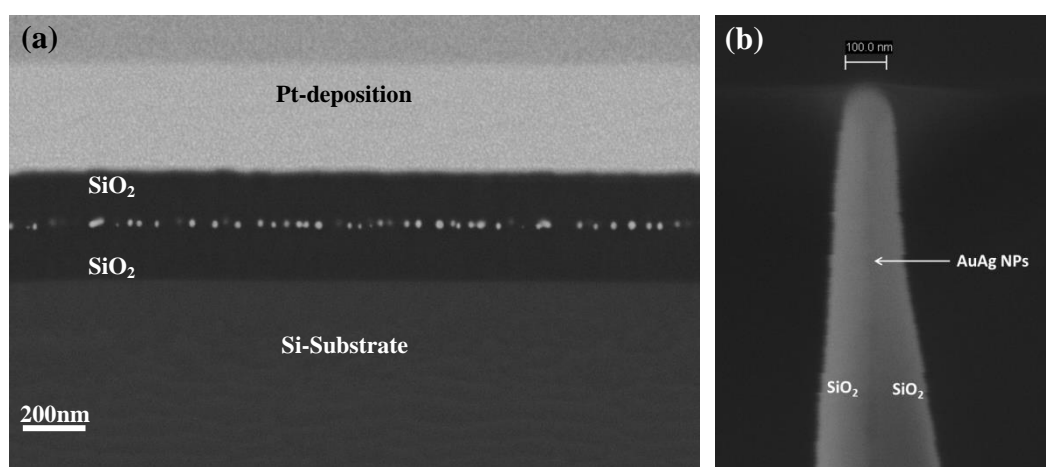


**Figure 1.17 :** (a) Cross-sectional SEM image of Au-Ag bimetallic NPs sandwiched in SiO<sub>2</sub> layers, (b) an atom probe tip prepared from (a) along the thin film direction.

So that, many attempts were made to prepare the atom probe tip in this case, but unfortunately none of the successfully prepared tip were able to produce commendable LaAPT analysis. The reason can be a poor contact between the SiO<sub>2</sub> film and NPs.

**(e) Au-SiO<sub>2</sub> :**

This Silica Photonic crystal fiber doped with Au-NPs was received from COMplexe de Recherche Interprofessionnel en Aérothermochimie (CORIA), a laboratory situated in Rouen, France. This sample was synthesized by sol-gel route with capillaries drawn from commercially available silica tubes [25]. The high resolution (HR) TEM image from Ref.[25] is shown along with the Scanning transmission electron microscope (STEM) image of the tip prepared from this sample in figure 1.18 (a) and (b) respectively. Even though the Au-NP is visible in HR-TEM image shown in fig. 1.18(a), the observation of Au-NP's inside the atom probe tip was not evident owing to the less density of NPs in bulk sample.

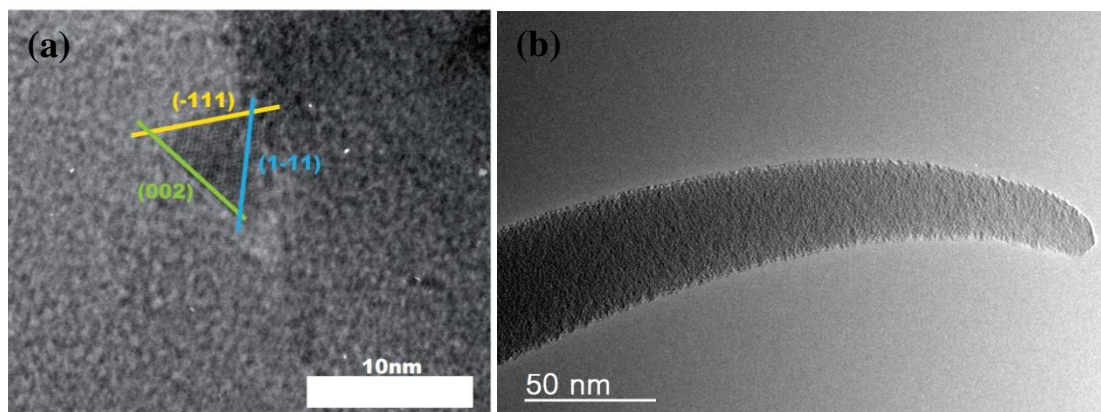


**Figure 1.18 :** (a) HR-TEM image from ref.[21], (b) STEM image of the Au-SiO<sub>2</sub> tip, absence of Au NPs in the tip

In addition, it was quite difficult to analyze the tip in electron microscope; strange behavior of bending upon imaging with electron beam was observed and is shown in fig. 1.18(b). Although the samples were successfully analyzed in atom probe but never observed the existence of Au-NPs, only ionic species related to matrix were observed.

#### (f) Au-MgO :

This sample was received from Pacific Northwest National Laboratory (PNNL), Washington, USA. Specimen with Au nanoparticles embedded in MgO matrix were synthesized by ion beam implantation of 2MeV Au<sup>2+</sup> ions on single crystalline MgO substrate followed by annealing at 1275°K for 10 hours. A band of cubic Au-nanoparticles with sizes ranging from 3-8nm with Gaussian density distribution in depth is formed nearly 200nm from the MgO surface [26]. After Au-Fe<sub>2</sub>O<sub>3</sub> this is the second sample which was analyzed successfully, though preparing atom probe samples was challenging due to the highly insulating MgO matrix. The structural characterization using LaAPT has already been carried-out on this sample by the researchers from PNNL and is published in [27,28]. The cross-sectional STEM image of the specimen is shown in figure 1.19 (a) showing the highly dense Au NPs inside the matrix. Magnified view from the low dense Au NPs region is shown in figure 1.19 (b).

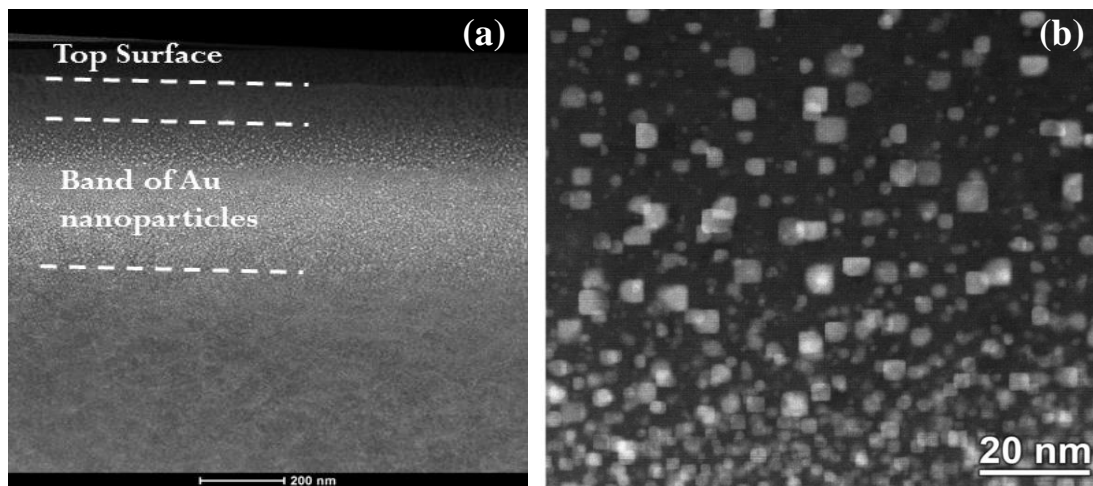


**Figure 1.19 :** (a) Cross-sectional STEM image of Au-MgO specimen showing formation of highly dense Au-NPs inside the MgO matrix, (b) magnified view of the top low dense Au-NP region of shown in (a)

### (g) ITO/Au/ITO

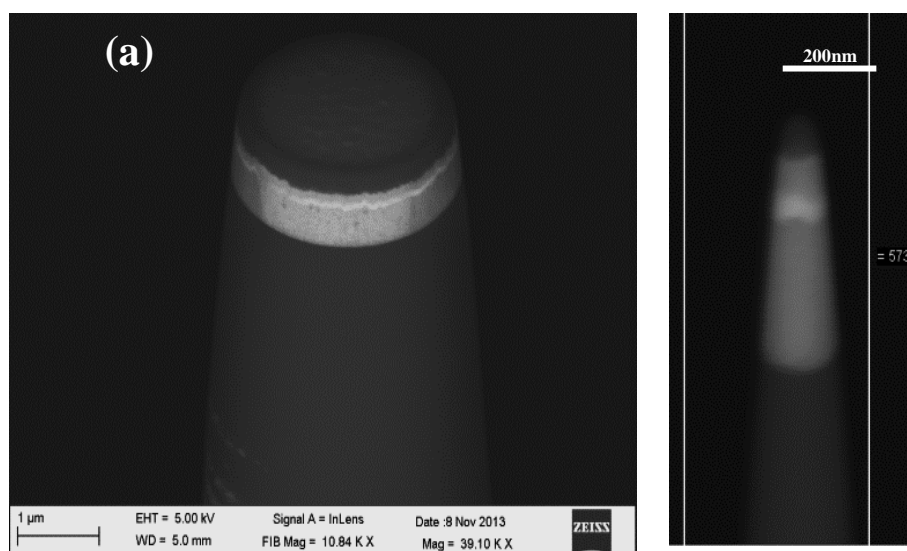


**Figure 1.20 :** ITO/Au/ITO sample preparation during (a) initial stage of annular milling and (b) just before final stage of annular milling.

Apart from all other samples where Au-NPs are embedded in dielectric matrices, we also tried to study the layered sample. In this sample a thin layer of Au (20-50nm) is sandwiched in between Indium tin oxide (ITO) layers. The layers were deposited on the Si-microposts, these microposts then glued to the W-pretip under the optical microscope and then annular milling using FIB was performed to prepare the final atom probe sample. Although tip preparation is easy in this case compare to other samples, the successful analysis from atom probe is challenging. Most of the tips were flashed during the analysis. This might be related to the adhesion between the layers which is not good

enough to sustain the high dc electrostatic field applied in LaAPT experiment. The SEM image during initial stage of annular milling of the Si-micropost and during the final stage is shown in figure 1.20 (a) and (b) respectively, the bright contrast layer corresponds to Au-layer.

All these samples were studied during the tenure of this Ph.D. work, however only two samples, viz. Au-Fe<sub>2</sub>O<sub>3</sub> and Au-MgO have shown possibility to be analyzed in LaAPT with good repeatability and reproducibility of results. So we decided to concentrate on these two specimens. Considering the different optical properties of these materials, we believe that these samples will give complimentary experimental data sufficient enough to draw some solid conclusions on the possibility to study the optical and thermal properties of these materials by LaAPT.

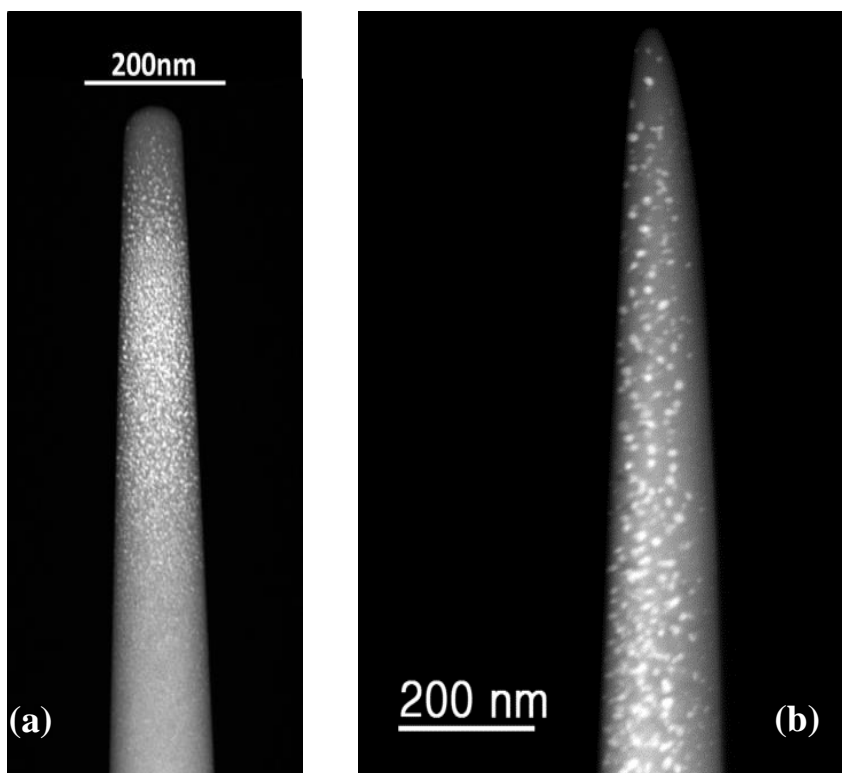


**Figure 1.21** : HAADF-STEM image of (a) Au-MgO tip and (b) Au Fe<sub>2</sub>O<sub>3</sub> tip

The differences in the properties of both matrices can be effectively use to compare the findings therein. The MgO matrix is transparent to the laser wavelengths used in the standard LaAPT experiment, viz UV (343nm), Green (515nm) and IR (1030nm), while on the other hand Fe<sub>2</sub>O<sub>3</sub> matrix is opaque to UV and Green wavelength. So it will be interesting to see how the optical properties will change with the inclusion of Au-NPs in these matrices. In addition, the thermal diffusivity of bulk MgO is superior (10

times) to that of  $\text{Fe}_2\text{O}_3$ , this gives us an opportunity to compare their thermal behavior as well. Along with this, the size and density of Au-NPs is different in both the samples, this aspect can also be used to understand the optical and thermal properties in both the cases. The High angle Annular Dark Field (HAADF)-STEM image of Au-MgO and Au- $\text{Fe}_2\text{O}_3$  tip is shown in figure 1.21 (a) and (b) respectively for comparison.

The results obtained with these two specimens are presented in Chapter 3 (Au-MgO) and Chapter 4 (Au- $\text{Fe}_2\text{O}_3$ ) of this thesis. To study the effect of Au-NPs inclusion, samples without Au NPs were also prepared for both the samples (i.e. Pure  $\text{Fe}_2\text{O}_3$  and Pure MgO tips).

### 1.3.3 Specimen analyzed to study the correlation between optical emission and structural properties

As explained in the previous section of this chapter, the optical emission properties of quantum well system depends essentially on the elemental composition and the thickness of the quantum well. To draw one to one correlation between optical emission and structural properties of quantum well system it is decided to characterize the same nano-object containing a system of quantum wells by  $\mu$ -photoluminescence spectroscopy, STEM, and LaAPT.

In this regard, system of InGaN/GaN multi-quantum wells (MQW's) has been analyzed during the course of this thesis. The InGaN/GaN MQW's were radially deposited on self-assembled GaN microwires grown by Metalorganic Vapor Phase Epitaxy (MOVPE) method at CEA/CNRS/Universite Joseph Fourier, Grenoble, France.

The STEM image of the atom probe sample prepared from this specimen is shown in figure 1.22 (a) along with the HR-STEM image in fig. 1.22(b). The bright contrasted stripes in these images are InGaN quantum wells separated by relatively dark and thicker GaN barrier. The thick Si- capping layer on top shown in fig.1.22 (a) was deposited to protect the sample from Ga-ion beam damage during sample preparation.

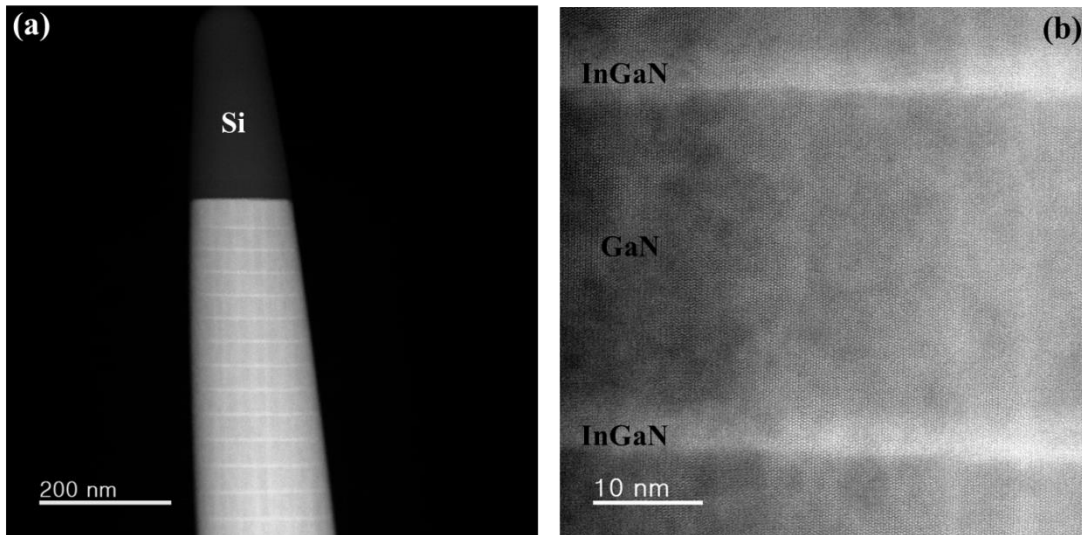


**Figure 1.22** : STEM (a) and HR-STEM (b) images from an atom probe tip sample prepared from InGaN/GaN multi quantum wells. The bright contrasted stripes are InGaN QW's and the thicker barrier between them is GaN.

A number of samples were analyzed individually by each technique (i.e.  $\mu$ -PL, STEM and APT) before analyzing the same nano-object by these techniques for correlation analysis. A rich set of data were obtained after performing the analysis on single nano-object and the correlation between optical emission and structural properties have been drawn from the results obtained. The detailed results and analysis carried out on this sample are presented in chapter 5 of this thesis.

As compared to the specimens analyzed to understand the relation between absorption and thermal properties of nanoscale material by LaAPT, we have analyzed only one specimen to understand the correlation between optical emission and structural properties. This is due to the limitation to finish the work in stipulated time of three years of the thesis. In the beginning of the thesis it was decided to work on both type of specimens which will give insights on optical absorption and emission by LaAPT analysis. But at the middle of the thesis we realized that, it is not possible to finish all the tasks involved in given time constraint. As a result, we decided to concentrate more on the absorption and thermal properties instead of optical emission and its correlation to the structural properties. Because of this reason, the samples analyzed to understand optical absorption and thermal properties by LaAPT are more in number in this thesis.

## 1.4 Conclusions

In this chapter more attention is given to the optical processes triggered upon illuminated by Light. Special emphasize was given to the optical absorption and emission properties of the materials.

In the first section of the chapter, after introducing the optical properties in general; how the absorption and thermal properties are subjected to change upon nanostructuring are described with some examples available in the literature. The importance of measuring these properties at single nano-object level is mentioned along with the challenges and limitations to do so.

Along with the optical absorption properties, optical emission properties of the materials are also introduced in the sub-sequent section. The dependence of optical emission on the elemental composition and on the electronic properties of the materials was explained. The emission properties of the quantum confined solids like quantum wells is then explained and how these properties can be modified with the thickness and composition of quantum well are introduced.

In the last section, the materials analyzed during the thesis are introduced and a decision to study the CERMET materials for absorption and thermal properties is made. With the introduction of different types of CERMET materials, the materials analyzed during the course of this thesis work were shortly introduced with the challenges and limitations encounter therein. At the end, decided to work on two successfully analyzed samples viz, Au-Fe<sub>2</sub>O<sub>3</sub> and Au-MgO, which we believe are sufficient enough to draw the solid conclusions about feasibility of LaAPT to use as a tool to investigate the absorption and thermal properties of the material at nanoscale. The results obtained and conclusions therein are presented in the further chapters of this thesis. In addition, to study the correlation between optical emission and structural properties; InGaN/GaN multi quantum well sample was analyzed and it was introduced at the end of the chapter. The results and discussion related to this sample are thoroughly described in chapter 5 of the thesis.

## References

1. Fox M. *Optical Properties of Solids*. Second Edition. Oxford Master Series in Physics 3 (2010).
2. Wiley: Introduction to Solid State Physics, 8th Edition - Charles Kittel. Available at: <http://eu.wiley.com/WileyCDA/WileyTitle/productCd-EHEP000803.html> [Accessed May 4, 2015]
3. Ashcroft NW, Mermin ND. *Solid State Physics*. 1 edition. New York: Cengage Learning (1976).
4. Noguez C. Surface Plasmons on Metal Nanoparticles: The Influence of Shape and Physical Environment. *J Phys Chem C* (2007) **111**:3806–3819. doi:10.1021/jp066539m
5. Crut A, Maioli P, Fatti ND, Vallée F. Optical absorption and scattering spectroscopies of single nano-objects. *Chem Soc Rev* (2014) **43**:3921–3956. doi:10.1039/C3CS60367A
6. Wang S-B, Chen R-S, Chang SJ, Han H-C, Hu M-S, Chen K-H, Chen L-C. Surface plasmon resonance-induced color-selective Au-peapodded silica nanowire photodetectors with high photoconductive gain. *Nanoscale* (2014) **6**:1264–1270. doi:10.1039/C3NR04533A
7. Li D, Wu Y, Kim P, Shi L, Yang P, Majumdar A. Thermal conductivity of individual silicon nanowires. *Appl Phys Lett* (2003) **83**:2934–2936. doi:10.1063/1.1616981
8. Hochbaum AI, Chen R, Delgado RD, Liang W, Garnett EC, Najarian M, Majumdar A, Yang P. Enhanced thermoelectric performance of rough silicon nanowires. *Nature* (2008) **451**:163–167. doi:10.1038/nature06381
9. Majumdar A. Thermoelectricity in Semiconductor Nanostructures. *Science* (2004) **303**:777–778. doi:10.1126/science.1093164
10. Nayak BK, Iyengar VV, Gupta MC. Efficient light trapping in silicon solar cells by ultrafast-laser-induced self-assembled micro/nano structures. *Prog Photovolt Res Appl* (2011) **19**:631–639. doi:10.1002/pip.1067
11. Garnett E, Yang P. Light Trapping in Silicon Nanowire Solar Cells. *Nano Lett* (2010) **10**:1082–1087. doi:10.1021/nl100161z
12. He JH, Lao CS, Chen LJ, Davidovic D, Wang ZL. Large-Scale Ni-Doped ZnO Nanowire Arrays and Electrical and Optical Properties. *J Am Chem Soc* (2005) **127**:16376–16377. doi:10.1021/ja0559193
13. Gao H, Liu C, Jeong HE, Yang P. Plasmon-Enhanced Photocatalytic Activity of Iron Oxide on Gold Nanopillars. *ACS Nano* (2012) **6**:234–240. doi:10.1021/nn203457a
14. Agrawal DC. *Introduction to Nanoscience and Nanomaterials*. WORLD SCIENTIFIC (2013). Available at: <http://www.worldscientific.com/worldscibooks/10.1142/8433> [Accessed December 5, 2015]
15. Mino L, Agostini G, Borfecchia E, Gianolio D, Piovano A, Gallo E, Carlo Lamberti. Low-dimensional systems investigated by x-ray absorption spectroscopy: a selection of 2D, 1D and 0D cases. *J Phys Appl Phys* (2013) **46**:423001. doi:10.1088/0022-3727/46/42/423001
16. Smith AM, Nie S. Chemical analysis and cellular imaging with quantum dots. *The Analyst* (2004) **129**:672. doi:10.1039/b404498n
17. Pearson - Introduction to Quantum Mechanics, 2/E - David J. Griffiths. Available at: <http://www.pearsonhighered.com/educator/academic/product/0,3110,0131118927,00.html> [Accessed October 13, 2015]
18. Granqvist CG. OPTICAL PROPERTIES OF CERMET MATERIALS. *J Phys Colloq* (1981) **42**:C1–247–C1–284. doi:10.1051/jphyscol:1981118
19. Berthier S, Lafait J. Compared optical properties of noble and transition metal-dielectric granular films. *J Phys* (1986) **47**:249–257. doi:10.1051/jphys:01986004702024900

20. Kennedy CE. Review of Mid- to High-Temperature Solar Selective Absorber Materials. National renewable Energy Laboratory (2002).
21. Arancibia-Bulnes CA, Estrada CA, Ruiz-Suárez JC. Solar absorptance and thermal emittance of cermets with large particles. *J Phys Appl Phys* (2000) **33**:2489. doi:10.1088/0022-3727/33/19/320
22. Tesfamichael T. Characterization of selective solar absorbers; experimental and theoretical modeling. (2001)
23. Gao P, Meng LJ, dos Santos MP, Teixeira V, Andritschky M. Study of ZrO<sub>2</sub>-Y<sub>2</sub>O<sub>3</sub> films prepared by rf magnetron reactive sputtering. *Thin Solid Films* (2000) **377-378**:32-36. doi:10.1016/S0040-6090(00)01395-X
24. Guillet Y, Rashidi-Huyeh M, Prota D, Palpanta B. Gold nanoparticle assemblies: interplay between thermal effects and optical response. *Gold Bull* (2008) **41**:341-348. doi:10.1007/BF03214892
25. Bigot L, El Hamzaoui H, Le Rouge A, Bouwmans G, Chassagneux F, Capoen B, Bouazaoui M. Linear and nonlinear optical properties of gold nanoparticle-doped photonic crystal fiber. *Opt Express* (2011) **19**:19061. doi:10.1364/OE.19.019061
26. Wang CM, Thevuthasan S, Shutthanandan V, Cavanagh A, Jiang W, Thomas LE, Weber WJ. Microstructure of precipitated Au nanoclusters in MgO. *J Appl Phys* (2003) **93**:6327-6333. doi:10.1063/1.1569032
27. Kuchibhatla SVNT, Shutthanandan V, Prosa TJ, Adusumilli P, Arey B, Buxbaum A, Wang YC, Tessner T, Ulfig R, Wang CM, et al. Three-dimensional chemical imaging of embedded nanoparticles using atom probe tomography. *Nanotechnology* (2012) **23**:215704. doi:10.1088/0957-4484/23/21/215704
28. Devaraj A, Colby R, Vurpillot F, Thevuthasan S. Understanding Atom Probe Tomography of Oxide-Supported Metal Nanoparticles by Correlation with Atomic-Resolution Electron Microscopy and Field Evaporation Simulation. *J Phys Chem Lett* (2014) **5**:1361-1367. doi:10.1021/jz500259c



# Chapter 2

## Experimental Methods

### 2.1. Introduction

The study of applicability of LaAPT as a spectroscopic tool involves lot of experiments, and comparison of these experimental results with numerical data. The experiments performed during the tenure of this thesis are integral and essential part of the thesis. Various experimental methods were used during this study to understand and correlate the structural and optical properties of nanometric tip shaped samples. The methods which are extensively used are introduced in this chapter.

The most frequently used experimental tool in this work is LaAPT. The LaAPT technique in general is introduced in the beginning of the chapter followed by the basic principle behind the technique. The LaAPT technique is usually used as a powerful tool to characterize the materials structural properties at near atomic resolution with parts per million (ppm) chemical sensitivity. But the subject of utilizing LaAPT as a spectroscopic tool is in itself a novel approach towards understanding the correlation between optical, thermal and, structural properties of material at nanoscale dimensions. Though this approach is new, there is number of reports available in the literature showing the effect of intrinsic optical properties of the material on the results obtained with LaAPT. With the help of these results an attempt have been made in this chapter to explain how the optical and thermal properties can also be deduced from the results obtained with LaAPT. The examples from existing literature for metals, semiconductors and insulators are included to cover the wide range of materials which can be analyzed by this method.

Another powerful tool which has been consistently used during this work is Scanning Transmission Electron Microscopy (STEM). As explained in the previous

chapter that the optical properties of solids at nanoscale are strongly dependent on their structural properties. In case of metallic nanoparticles (NP's) embedded in dielectric matrices, the size, shape, density and, dielectric environment of the NP's can substantially alter the optical absorption properties. On the other hand, the thickness and interface geometry of quantum wells is decisive parameter to characterize the optical emission from quantum wells. Owing to these facts, it is essential to perform the ultimate structural characterization before correlating the same to its optical properties. STEM analysis will provide the complementary information to the LaAPT analysis. In addition, the STEM imaging of the tip shaped samples will serve as an input parameter for the reliable and better 3D reconstruction of the data obtained with LaAPT. It is even possible to perform direct one-to one correlation between optical and structural properties with the results obtained with LaAPT and STEM together. Due to these reasons, using STEM for imaging is necessity of this work and is used almost for every successful sample analyzed in this thesis. Thus, a brief introduction to STEM and High angle annular dark field (HAADF) imaging is also incorporated in this chapter.

Along with the structural characterization tools like STEM and LaAPT, to understand the optical properties of the solids at nanoscale two different techniques were used. For studying the optical emission properties, micro-photoluminescence ( $\mu$ PL) spectroscopy were used, in which a small part of the sample (few microns) is excited by the laser light and the luminescence signal is recorded using the spectrometer. While for studying the optical absorption of nanoscale tip shaped samples, we have used the technique called as Spatial Modulation spectroscopy (SMS). The technique have been successfully employed to analyzed the absolute absorption spectra of single isolated metallic nanoparticle (as small as 5nm in diameter) [1] and semiconducting single wall carbon nanotube [2]. We have used this technique for the first time to investigate the absorption properties of the tip shaped samples used in LaAPT . Although we have not came to definitive conclusions on the results obtained with this technique up till now, the primary analysis obtained on different samples are discussed in the thesis along with the difficulties to understand the same. Both the techniques, i.e.  $\mu$ PL and SMS are concisely introduced in this chapter along with the reports available in the existing literature for more detailed discussions.

## 2.2. Atom Probe Tomography : State of the art

Atom Probe Tomography (APT) is a unique technique to analyze the material structurally and chemically in 3-dimensions (3D) at near atomic scale. Right from its invention APT has witnessed considerable improvements in its instrumental design, reconstruction protocols, detection system etc. to push the technique to its limit. One of the very important advances APT has ever seen is the application of ultrafast laser pulses to trigger the field evaporation process (or removal of atoms from the surface of the material). So the APT became the Laser-assisted APT (LaAPT) and open up the new era to study the materials (e.g. semiconductors and insulators) at near atomic resolution. The technique became very popular amongst semiconductor and nano-electronics researchers due to its unique and unmatched qualities to probe the material to near atomic resolution in real space and that too in 3D. In this section a short introduction to the APT technique is given with the fundamental mechanisms of field evaporation and applications of this technique in various fields.

### 2.2.1 History

The atom probe tomography is an outcome of the vast research carried out in high-field Physics from late 1920's to 1950's. The predecessors of APT are the field emission microscope and the field ion microscope. Field emission microscopy (FEM) is based on the extraction of electrons from metal tip by applying a very high negative potential which generates an intense electric field (few V/ $\mu\text{m}$ ) at the surface of the tip. In short, when a sufficiently strong electric field is present around a metal tip, electrons will quantum mechanically tunnel through the metal/vacuum barrier. The theoretical framework for this phenomenon were extensively discussed by J. R. Oppenheimer [3] and Fowler and Nordheim [4] in 1928. In 1936, Erwin Muller has experimentally shown the evidence of electron emission from solids under high electric field [5]. The electron emission sources based on the field emission are now used very frequently in electron microscopes. On the other hand, in field ion microscopy (FIM), by applying the high positive potential on the field emitter used in FEM, Muller was able to achieve the emission of positive ions from the surface of the metal tip in 1941 [6]. As the signal from the positive ions evaporated from the surface was very weak, trace hydrogen was introduced into the vacuum chamber. The ionization of gas atoms on the surface increased the number of ions emitted from the surface significantly. After cooling the

field emitter to liquid nitrogen temperature and using Helium gas for imaging, Bahadur and Muller in 1955 [7] were able to produce the first ever atomically resolved image of the tungsten surface using FIM. With the technological improvements in next decade it was possible to amplify the signal using microchannel plate which further enhanced the signal on the Phosphor screen of FIM. Later in 1968 [8], Muller and his co-workers developed a One-dimensional atom probe (1D-AP) or an Atom Probe Field Ion Microscope (AP-FIM), in which they combine the FIM with Time of flight (ToF) mass spectrometry. This was the first step towards simultaneously imaging and identifying the individual atom from the material. With the developments in detection system, fast electronic digitizers [9] and, reconstruction protocol [10], it is now possible to determine the position of atoms in 3D with sub-nanometer resolution. The technique was limited to only metallic and highly doped semiconducting samples for long time. This is due to the inability to transmit the electrical pulses to the apex of the samples in non-conducting materials. But this difficulty is also resolved by using ultra-fast laser pulses to trigger the process of field evaporation [2] since last decade. With the application of ultra-fast laser pulses, it is possible to analyze any material including insulating materials as well. This fact makes the laser assisted atom probe tomography (LaAPT) as a unique tool to analyze any kind of material structurally and chemically in 3D with near atomic resolution. The basic principle of the technique and underlying mechanism are explained in the subsequent sections of this chapter.

### **2.2.2 Basic Principle of APT**

As explained in the previous section the atom probe is combination of FIM with ToF mass spectrometry. So before going to discuss the details regarding atom probe, it is inevitable to have discussion on FIM. In FIM, the sharp needle shaped specimen with end radius in the range of 50 nm to 100 nm is placed at cryogenic temperature (10K-80K) and in ultra-high vacuum conditions. The electric field at the apex of the specimen is applied and is of the order of  $10^{10}$  V/m. A rare gas (He, Ne, Ar), called the imaging-gas, is introduced in the vicinity of this positively charged sharp needle. Gas atoms are ionized very close to the tip surface and subsequently accelerated away by the intense electric field. The image that is formed by the impact of these gas ions onto a phosphor screen maps the distribution of the electric field at the surface, which is intrinsically related to the local topography of the tip. The cryogenic temperature is to optimize the spatial resolution, which is high enough to provide direct imaging of individual surface atoms.

The schematic of the FIM is presented in fig. 2.1(a) along with the experimentally observed field ion micrographs on gold tip and Si-tip.

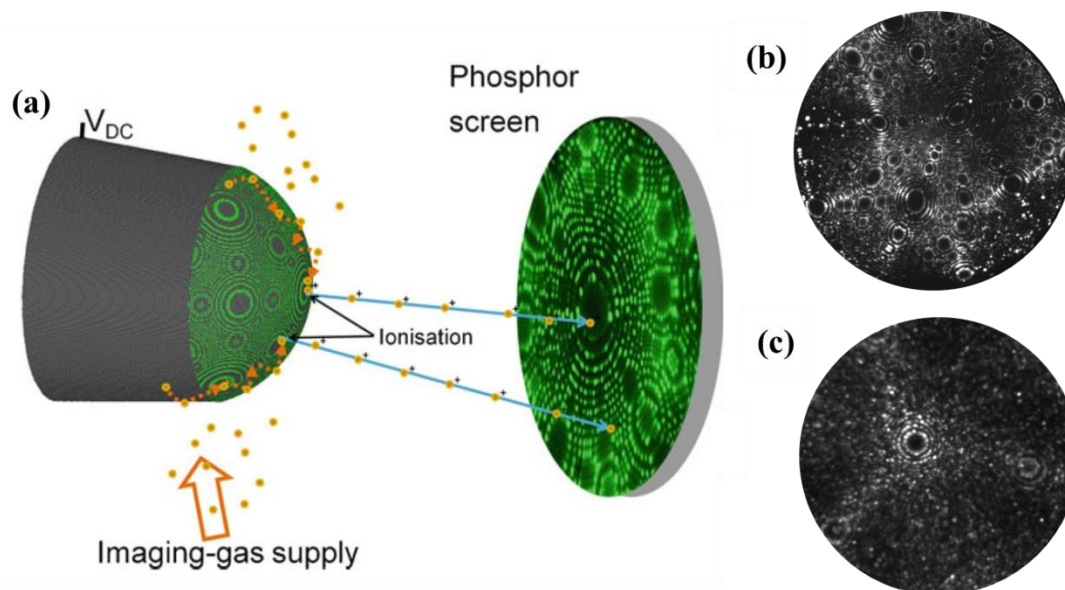


**Figure 2.1** : Schematic view of a field ion microscope. (a) Only the atoms from the very last shell (in green) of the tip surface can be imaged, as seen in the example of a pure W field ion micrograph (on phosphor screen) after [11], (b) field ion micrograph of Au-tip and that of (c) Silicon tip (showing (111) pole) (Image Courtesy F. Vurpillot)

The very high spatial resolution and high contrast for features on the atomic scale arises from the fact that the electric field is enhanced in the vicinity of the surface atoms because of the higher local curvature (shown in green color). Resolution of the order of  $1\text{\AA}$  (atomic resolution) can be achieved by FIM. It is the first step in visualizing the single atoms on the surface of the material before APT analysis. It can be used basically to study dynamics of surfaces and behavior of ad-atoms on the surface of sample [12].

In APT, in order to find the chemical identity of the atoms (ions) evaporated from the tip surface, ToF mass spectrometry is introduced. Unlike the FIM, instead of phosphor screen a detector with single ion sensitivity is placed in front of the tip specimen which will record the spatial (X,Y) positions of the detected atom [9]. The schematic of atom probe is shown in fig. 2.2.

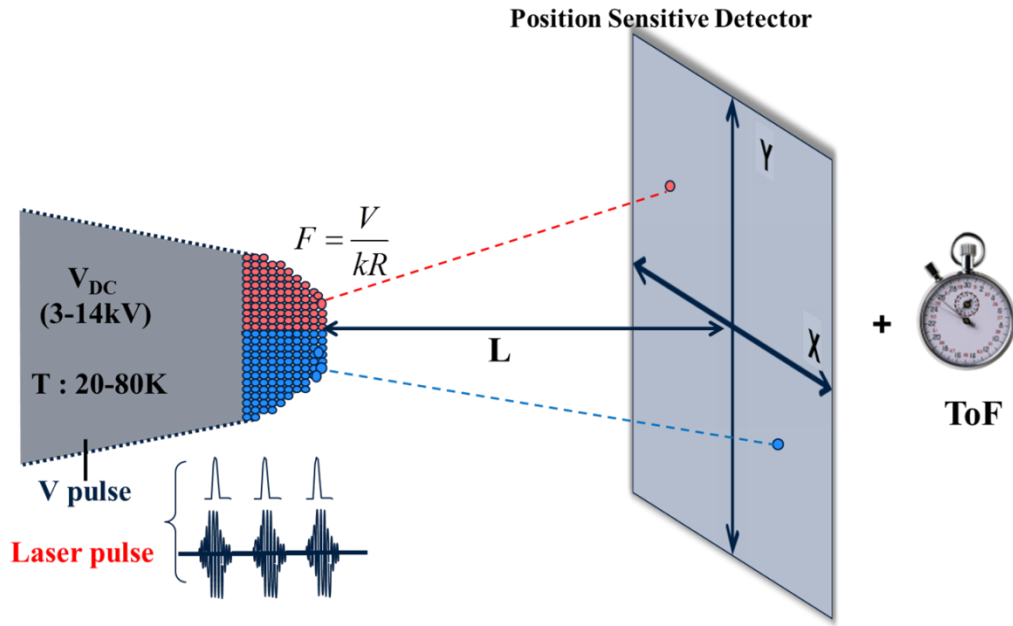


**Figure 2.2 :** Schematic showing the principle of atom probe tomography. (Blue and red circles represented as atoms)

The basic principle of atom probe tomography is as follow: the surface atoms of the needle shaped specimen are field evaporated by applying additional voltage (electric mode APT) in form of series of high voltage pulses with nano second rise-time or by applying ultra-fast laser pulses with sub-femtosecond duration to trigger the field evaporation process (LaAPT). Ions created at surface follow trajectories of electric field lines established between detector and specimen where they are chemically identified by time-of-flight mass spectrometry (TOF-MS). The information from the detected atom is obtained from its mass-to-charge ratio ( $m/n$ ).  $m/n$  is calculated from the equivalence between the potential energy of the atom on the specimen surface at the voltage  $V$  to the kinetic energy that ion acquires to a grounded counter electrode positioned immediately in front of the specimen. This relation is given by,

$$neV = \frac{1}{2} m \frac{L^2}{t^2} \quad (2.1)$$

$$\frac{m}{n} = 2eV \frac{t^2}{L^2} \quad (2.2)$$

where,  $L$  is the distance covered by ions from specimen surface to detector,  $e$  is elementary charge and  $t$  is the flight time of the ion over that distance.

Once the chemical identity and the (X, Y) spatial positions of the atom are recorded, with the help of reconstruction protocol based on the back projection law [10]

and the sequence of atom hits on the detector can be used to deduce the Z-position (depth) of atoms. Thus the three dimensional reconstruction of the data obtained is a combination of two-dimensional hit positions and sequence of field evaporation.

### 2.2.3 Theory of field evaporation

Field evaporation is the term used for field-induced removal of an atom from the surface of the material. It involves a combination of ionisation and desorption of an atom from a surface that is subjected to a very intense electric field. The electric field causes polarization of the surface atoms. When the electric field is sufficiently intense, the atom can be removed from the surface while one of its electrons is drained into the surface, inducing ionization of the atom. The created positive ion is accelerated by the surrounding field away from the surface. The field evaporation process is schematically shown in fig. 2.3 along with the atomic and ionic potential energy diagrams with and without the application of electric field.

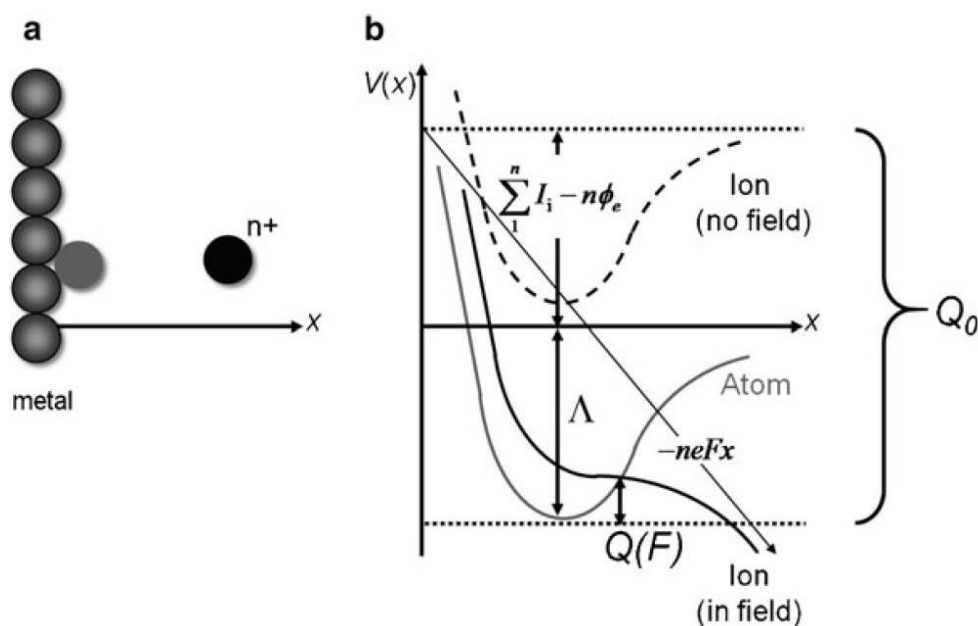


**Figure 2.3 :** (a) The field evaporation process. The ad-atom is depicted in grey and the ion in black. (b) Atomic and ionic potential energy diagram with and without electric field.  $V$  is the potential,  $L$  is the sublimation energy,  $n$  is the degree of ionization,  $I_i$  is the  $i^{\text{th}}$  ionisation energy and  $\phi_e$  is the work function of the surface emitting the ion,  $Q_0$  and  $Q(F)$  are the energy barrier without and with electric field respectively. From [11].

The field evaporation process is thermally activated process, where ion will leave the surface of the material by crossing the lowered potential barrier (due to electric field) with thermal activation. This transition from an atomic to an ionic state is schematically

depicted in fig. 2.3(b), which shows the atomic and ionic potential energies as a function of the distance from the surface,  $x$ .

The number atoms evaporated per second, i.e. evaporation rate follows the Arrhenius law as given by,

$$K_{evap} = \nu_{atom} \exp\left(\frac{-Q(F)}{kT}\right) \quad (2.3)$$

where,  $\nu_{atom}$  is the surface atom vibration frequency,  $Q(F)$  is the height of the barrier as a function of the applied electric field  $F$ ,  $T$  is the absolute temperature and  $k$  is the Boltzmann constant. For electric field values close to the evaporation field ( $F_{evap}$ ), the height of the energy barrier can be considered as varying linearly with the field:

$$Q(F) = Q_0 \left(1 - \sqrt{\frac{F}{F_{evap}}}\right) \approx Q_0 \left(1 - \frac{F}{F_{evap}}\right) \quad (2.4)$$

where,  $Q_0$  is the barrier without application of electric field as shown in fig. 2.3. This behavior was observed experimentally as well.

### **2.3 LaAPT to analyze the optical absorption and thermal properties of nanoscale material**

Laser assisted atom probe tomography has been widely used to characterize the structural and chemical nature of the materials with near atomic resolution. Various material ranging from metals, semiconductors and even insulators are being studied successfully [11,12,13]. But the quality of data obtained is strongly influenced by the operating conditions of laser, like laser intensity and wavelength. To get the best results one has to tune these parameters according to the material being analyzed, in addition the geometrical parameters like shape, size and length of the tip play crucial role in this analysis. This dependency is possibly due to the change in optical and thermal properties of the tip shaped samples analyzed in LaAPT. And this dependency gives us an opportunity to study the optical and thermal properties of the material by using LaAPT. The behavior in the case of metallic samples is explained in the beginning to form a framework for this discussion. Later relatively complex case of semiconductor and insulators is incorporated for the sake of covering the wide range of materials which can be analyzed by this technique.

### 2.3.1 METALS

The specific laser's contribution to the field evaporation can directly be introduced in the Arrhenius equation that is used to model the evaporation process. The rate of evaporation is given by Arrhenius law as quoted in eq. (2.3). Reformulation of equation (2.3) gives,

$$N_{evap} = \int_{t_{start}}^{t_{end}} \left( N_0 \vartheta_{atom} \exp\left(\frac{-Q(F)}{kT(t)}\right) \right) dt \quad (2.5)$$

where,  $N_{evap}$  is the number of field evaporated ions during the time interval  $[t_{start}, t_{end}]$ ,  $\vartheta_{atom}$  is the surface atom vibration frequency,  $Q(F)$  is the height of the barrier as a function of the applied electric field  $F$ ,  $T(t)$  is the temperature of the sample as a function of time and  $k$  is the Boltzmann constant and  $N_0$  number of kink site atoms. From this equation, field evaporation can be triggered by an increase of the electric field as well as by an increase of the temperature. The laser wave as an electromagnetic wave has an intrinsic electric field and the absorption of laser light in solids is well known to result in heating the absorbing material. Hence, the laser pulse may cause field evaporation via the temperature rise and experimental evidence of this behavior is reported in [14–16].

After the temperature rise induced by laser absorption, the cooling process has also significant consequences on the LaAPT analysis. Here the intrinsic thermal properties like thermal diffusivity and the specific heat capacity comes in the picture. It is possible to deduce the thermal diffusivity of the tip shaped specimen using thermal pulse model (TPM). Detailed study on thermal pulse model (TPM) was carried out by F. Vurpillot et. al. [15,17]. The rise in temperature due to laser illumination is proportional to the laser pulse energy ( $E_p$ ),  $T=T_0+\alpha E_p$ , where  $T_0$  is base (cryogenic) temperature,  $\alpha$  is absorption coefficient [17]. Considering this proportionality, the evaporation rate can be rewritten (from equation 2.3) as,

$$K_{evap} = \vartheta_{atom} \exp\left(\frac{-Q(F)}{k(T_0+\alpha E_p)}\right) \quad (2.6)$$

Once the energy of the laser is deposited on the needle shaped specimen, the kinetic of temperature simply follows the diffusion equation of the heat conduction,

$$\frac{\partial T}{\partial t} - D\nabla^2 T = 0 \quad (2.7)$$

where,  $D$  is the thermal diffusivity of the material,  $T$  is the temperature and  $t$  is the time. The thermal diffusivity can be expressed as thermal conductivity ( $k$ ) divided by the volumetric heat capacity  $c_p$ , and the density of the material  $\rho$ .

$$D = \frac{k}{\rho c_p} \quad (2.8)$$

These parameters are considered to be independent of temperature, although this is not strictly correct. Since the actual absorption is not known as a function of the position inside the sample, the temperature distribution is assumed to follow a Gaussian law centered on the tip apex along the  $z$  (along the tip) axis just after the laser illumination. Then, the solution to equation (2.7) with the tip approximated as cylinder or wire is given by [15]

$$T(t) = T(0, t) = T_0 + \frac{T_{rise}}{\sqrt{1 + \frac{2Dt}{\sigma^2}}} \quad (2.9)$$

with  $T_0$  the base temperature,  $T_{rise}$  the maximum temperature rise and  $\sigma$  the size of the heated zone. The cooling time constant is given by  $\sigma^2/D$ . This expression relates the temperature evolution at the apex with physical constants of the material and the size of the heated area. The temperature evolution after laser illumination on the Tungsten tip was studied by Vurpillot et al. [15] and the fig. 2.4 gives temperature profile vs. time during the cooling process.

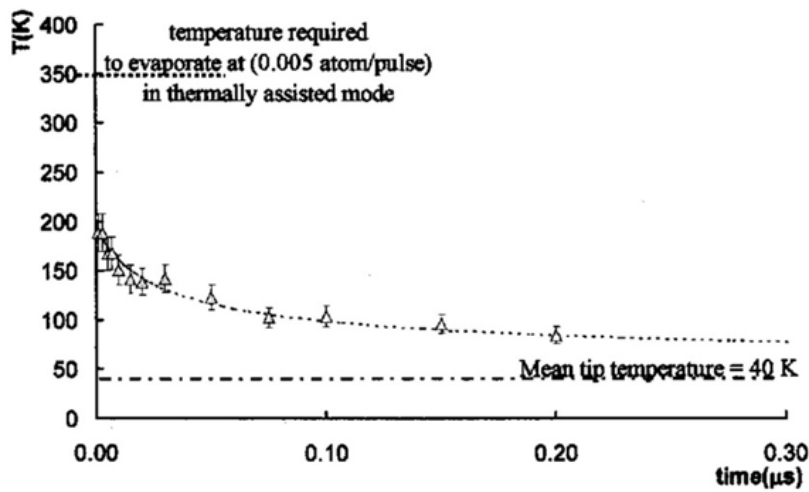


**Figure 2.4 :** Variation of the temperature after the laser pulse for a laser polarized along the tip axis, (Intensity of laser =  $15 \text{ mJ/cm}^2$ ). The temperature decay is fitted by the formula,  $T(0, t) = T_0 + T_{rise} / \sqrt{1 + 2(Dt/\sigma^2)}$  with,  $T_0 = 40 \text{ K}$ ,  $T_{max} = 160 \text{ K}$ , and  $\sigma = 1.5 \mu\text{m}$

Many authors have tried to measure the temperature rise during laser irradiation in APT [15,18–21]. The variation in temperature on the tip apex can be scanned as a function of time by measuring  $K_{evap}(t) = \exp(-Q/kT(t))$ . Due to the exponential decay of the evaporation rate  $K_{evap}(t)$ , most of the atoms are evaporated in the very first moments

of the cooling process. The evaporation time ( $\tau_{evap}$ ) is defined as the time necessary to divide by 10 the maximum value of  $K_{evap}(t)$ , the expression for  $\tau_{evap}$  can be written as [22]

$$\tau_{evap} = \ln(10) \times \frac{k_B T_{rise}}{Q_n} \times \frac{\sigma^2}{D} = 0.1 \frac{\sigma^2}{D} = 0.1 \tau_{cooling} \quad (2.10)$$

Thus the key factors controlling the cooling time ( $\tau_{cooling}$ ) are the thermal diffusivity ( $D$ ) of the material and the size of the heated zone ( $\sigma$ ). It was shown by Houard *et al.* [22] that in the case of the metallic samples the extent of the area where the absorption takes place can be chosen by adjusting the wavelength and the direction of the electric field of the laser pulse.

The evaporation rate as a function of time i.e.  $K_{evap}(t)$ , as measured for aluminum and stainless-steel specimens, is shown in Fig. 2.5 (a) and (b) respectively, for different laser wavelengths [22]. The field evaporation-rate measurement is derived from the ion ToF spectra. For aluminum specimen analyzed at  $\lambda=1600$  nm,  $\tau_{evap}$  is 2.5 ns while for all other wavelengths it is 1.5 ns (Fig. 2.5 (a)). On the other hand, for steel with shorter wavelength (320 nm) the evaporation time is shorter ( $\tau_{evap} \sim 2$  ns) and for longer wavelength ( $\lambda = 1200$  nm) it is longer (measured up to 20 ns) (Fig. 2.5 (b)). The heated zone ( $\sigma$ ) which is estimated from equation (2.10), is found to be 300 nm for wavelength of 320 nm and up to 1  $\mu\text{m}$  for  $\lambda = 1200$  nm.

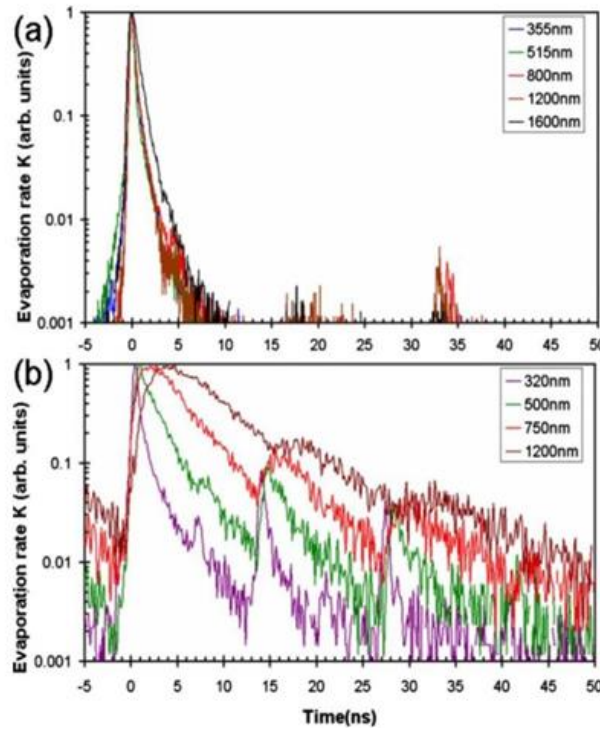


**Figure 2.5 :** Evaporation rate as a function of time obtained (a) from an aluminum tip & (b) from a stainless-steel tip, for different wavelengths in axial polarization

Houard *et al.* [22] also calculated the absorption density along the tip axis by solving the Maxwell equations using finite difference time domain (FDTD) method. Profiles are shown in Fig. 2.6 for different wavelengths. From Fig. 2.6, it can be seen that absorption is maximum at the end of the tip and the absorption density rapidly decays to zero few micrometers away from apex. For shorter wavelengths, the first absorption maxima are closer to the apex of the tip. Moreover, the heated area (calculated as the width of the first peak at  $1/e^{1/2}$ ) is smaller at shorter wavelength. Consequently shorter evaporation times and better the mass resolution in shorter wavelengths (typically in UV range) are expected.

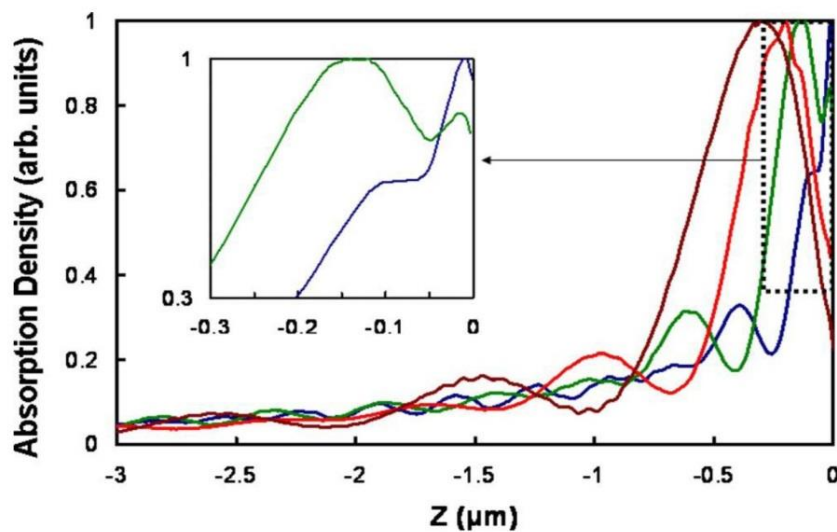


**Figure 2.6 :** Normalized absorption density profile along the tip axis computed for  $\lambda = 360$  nm blue,  $\lambda = 515$  nm green,  $\lambda = 800$  nm red, and  $\lambda = 1200$  nm brown. Inset: zoom of absorption profiles at the end of the tip for  $\lambda = 360$  nm blue and for  $\lambda = 515$  nm green.

These results shows that, in the case of metallic samples it is possible to deduce the optical absorption properties by the absorption distribution at different wavelengths and analyzing the ToF spectrum obtained from the LaAPT analysis. The numerically calculated absorption maps using FDTD can be used to understand qualitatively the magnitude of this absorption at different wavelengths. The information obtained with these calculations will serve as input parameters to calculate the thermal diffusivity of the nanometric samples using thermal pulse model (TPM). An example is shown in fig. 2.7, where the experimental data obtained from metallic glass sample at different wavelength is fitted using only changing one parameter, i.e. thermal diffusivity [23]

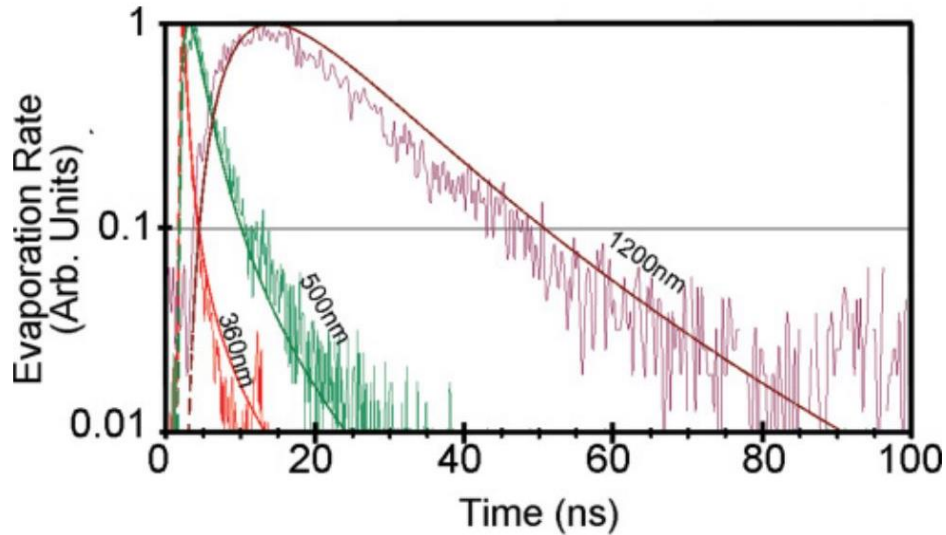


**Figure 2.7** : Experimental (thin line) and theoretical (thick line) evaporation rate of a metallic glass tip analyzed at  $\lambda = 360$  nm [red (black)],  $\lambda = 500$  nm [green (half-gray)], and  $\lambda = 1200$  nm [violet (gray)]

### 2.3.2 SEMICONDUCTORS AND INSULATORS

To understand the absorption behavior in case of semiconductors and insulators it is even more challenging. This is mainly due to the difference of electronic structures between semiconductors, oxides and metals. In a metal, there is no energy gap in the excitation spectrum of electrons; most of the electronic process involves electrons whose energy is very close to the Fermi energy. In a semiconductor however, the presence of a gap between the conduction band and the valence band leads to electronic process (such as excitation) involving electrons, from valence band to conduction band. This complicates the treatment of field ionization and field evaporation process in poor conducting materials. All these interactions of ultra-fast laser with the nanometric tip and the difficulties to understand the same are reviewed in [24,25]

The optical properties of semiconductors are related to their band structure [25,26]. In the case of direct-band-gap semiconductors, the absorption of photons with energy ( $E_{ph}$ ) lower than the band gap ( $E_{ph} < E_g^{direct}$ ) is negligible, and it becomes very strong for ( $E_{ph} \geq E_g^{direct}$ ). In this latter case, the penetration depth of the light is a few nanometers and all the photon energy is absorbed at the surface by valence electrons promoted to the conduction band which creates an electron-hole pair [26,27]. For indirect band gap semiconductors, the absorption of photons with ( $E_{ph} > E_g^{indirect}$ ) is assisted by phonons and it is very low when the photon energy is close to the band gap energy ( $E_{ph} \sim E_g^{indirect}$ ). In this case the penetration depth can be large, up to 1 mm [28]. Therefore for

APT specimens, light can pass through the specimen readily and absorption takes place in the entire illuminated volume.

Because the band structure of semiconductors strongly depends on doping and defects, the value of the photon energy threshold for absorption changes with the doping level and the defect density. When a specimen is heavily absorbing, such as semiconductors for photon energies above their band gap, there is little penetration of the laser beam inside the specimen. However, this general behavior of the optical properties of materials should be reconsidered when a semiconductor is shaped at the nanometric scale, as in the case of APT specimens. It was recently reported, both experimentally and theoretically, that in the case of semiconductor nanowires, the optical properties strongly depend on the ratio ( $\lambda/R$ ) with  $\lambda$  the laser wavelength and  $R$  the radius of the nanowire [29]. This behavior is due to the excitation of resonant modes inside the nanostructure (which can only happen if surface absorption is not strong). Furthermore, the optical properties of bulk semiconductors can also be affected by the presence of a strong static electric field [30,31]. This field modifies the band structure of the materials, changing the band gap [32] or bending the bands [33,34]. By increasing the value of the external electric field, sub-band gap absorption ( $E_{ph} < E_g$ ) becomes possible.

Bogdanowicz et. al. [30] has developed a simplified light-absorption theory for conical nanoparticles based on the assumption that the conical shaped tip is a stack of cylinders with varying radius. This theory predicts that, the light couples and is therefore absorbed in these objects at specific locations, where the local radius corresponds to a resonance of the Mie theory developed for cylindrical particles. To prove this hypothesis they have irradiated a Si-tip with high power IR laser in an atom probe set-up, and the SEM image after irradiation is shown in figure 2.8 (a). It is clear that, regions of preferential absorption are located on the shank and, more specifically, in the cross sections where the local radius allows for constructive interference between the multiple internal reflections. But when similar experiment is carried out in Green wavelength [35] the regions of preferential absorption are absent and only near apex region of the tip is affected as shown in figure 2.8 (b). It can indeed be shown that, while resonant coupling of green light into a sub-100-nm apex is possible, only very little IR light can be coupled into such a small apex [30]. In other words, during an APT experiment on a Si specimen, the contribution of the apex to green light absorption can be significant (Fig. 2.8(b)), whereas the absorption of IR light will occur far from the tip apex along the tip shank.

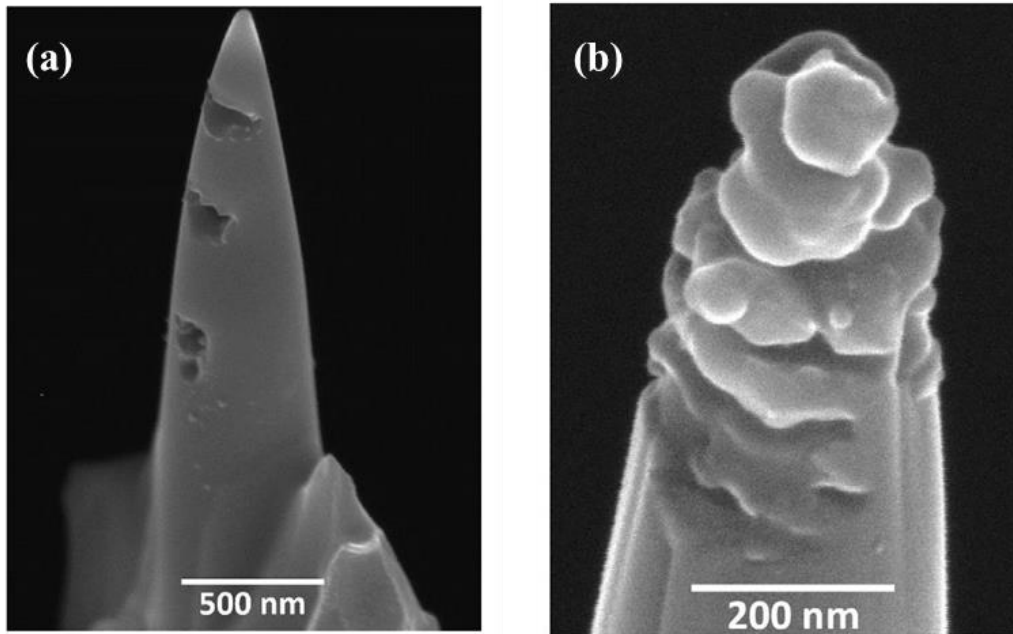


**Figure 2.8** : SEM image of a Si specimen irradiated with 20mW average-power (a) IR pulses, holes indicative of locally enhanced absorption are observed only along the shank of the specimen, i.e. far from the apex and (b) green pulses, trenches indicative of locally enhanced absorption are observed in proximity to the apex region

Mazumder et al. [36] analyzed the Silicon tips in LaAPT as function of laser intensity. The n-doped silicon tip was subjected to the infra-red (IR) laser pulse ( $\lambda = 1030$  nm) with laser intensity from  $0.53 \text{ J/m}^2$  to  $12.6 \text{ J/m}^2$ . The time-of-flight spectra of silicon at 14 Da ( $\text{Si}^{2+}$ ) is shown in Fig.2.9 (a). It can be seen that the ToF spectra obtained for lower laser energies are very different than for higher laser energies. With increasing laser energy, there is a broad peak appearing after the main peak of Si and thereby covering the locations of isotopes at 14.5 and 15 Da. Also observed, the delay of about 10 ns between the first Si peak (fast peak) and the second broad peak (hump). Such a behavior was not observed during analyses under UV ( $E_{\text{UV}}=3.6 \text{ eV}$ ) and green laser ( $E_{\text{green}}=2.4 \text{ eV}$ ) as shown fig. 2.9 (b) for green laser.

This hump (delayed evaporation) in IR has been attributed to the resonant absorption far from the apex in IR wavelength as observed in figure 2.8 (a) and predicted by Bogdanowicz [30]. The two peaks (one narrow and the other broad) can correspond to two cooling process related to two heated zones. The first zone is very small and located at the apex of the tip. The absorption is localized in this small zone due to the band bending which is stronger at the apex due to the electrostatic field applied. The second zone is larger and localized at a distance far from the apex. The cooling process related to the small heated zone is very rapid and hence the evaporation process is very short (which

corresponds to a narrow peak in the TOF spectrum). Concerning the cooling process related to the absorption far from the apex, the related ToF peak presents a long rise time due to the heat propagation from the center of the heated zone to the tip apex. The absence of this hump in case of Green wavelength analysis (fig. 2.9(b)) can be explained on the basis of the absorption localized in near apex region unlike the case of IR light as observed in fig. 2.8(b). The heated zone created at the near apex region will try to cool down along the axis of the tip and hence decaying tail is observed in the ToF spectra of Green analysis (see fig. 2.9(b)).

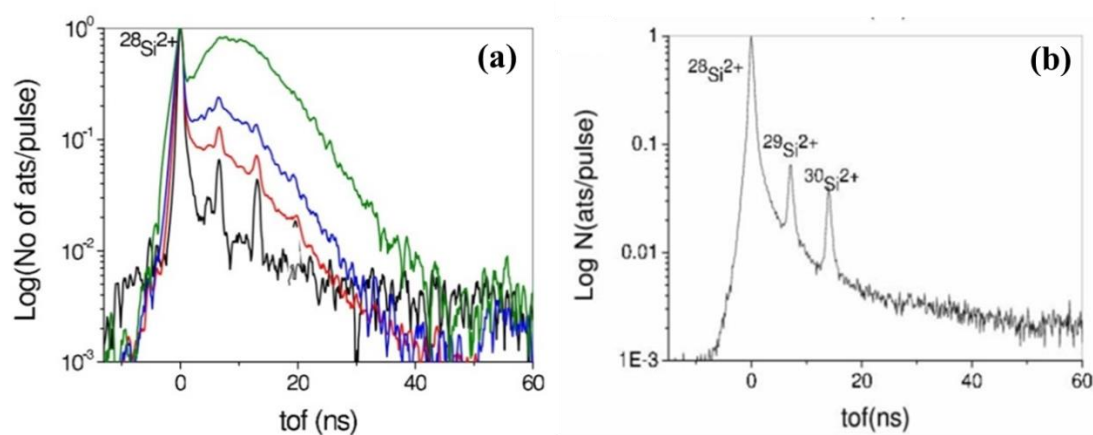


**Figure 2.9 :** Normalized evaporation rate as function of time obtained from an Si tip (a) for IR laser, using the laser intensities bottom to top  $I= 0.2 \text{ GW/cm}^2$ ,  $I= 1.2 \text{ GW/cm}^2$ ,  $I= 2.2 \text{ GW/cm}^2$ , and  $I= 5.7 \text{ GW/cm}^2$ , respectively; (b) Green laser light  $9.1 \text{ J/m}^2$

These studies clearly demonstrate the correlation between the wavelengths of laser and the absorption properties of the material. Also studying the delayed evaporation i.e the position of the hump on time scale with respect to the laser power used one can deduce the thermal properties as well.

In case of bulk insulating oxide layer sandwiched in metallic layers, the evaporation conditions change drastically from a metal layer to an oxide layer [37]. To obtain the 3D image of a tunnel barrier (Fe/ MgO/ Fe), as reported in Fig 2.10(a), the laser power and the static field applied to the tip had to be carefully modified during the analysis. Looking at the different shapes of the time of flight spectra obtained for Mg ions and Fe ions as shown in Fig 2.10(b), we can observe that the rise time of the Mg peak is 10 times faster than the Fe peak. This rapid evaporation is related to a confinement and an enhancement of the light absorption at the tip apex as shown previously in case of aluminium tips.

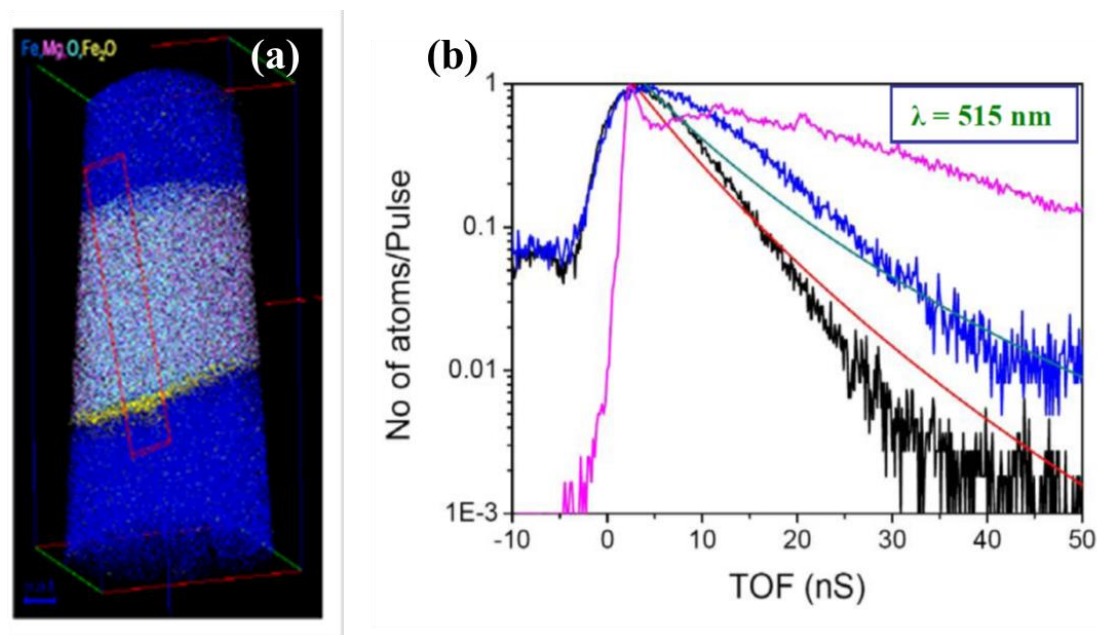


**Figure 2.10** : (a) 3D reconstructed volume of Fe/MgO/Fe tunnel barrier, (b) ToF spectra of Fe ions from the first and last layers (blue and black line, respectively) and Mg ions (pink line)

The change of optical absorption properties in the oxides layer can be ascribed to the band bending effect under the high electric field at the tip apex [33]. Consequently, the surface electronic states can change completely from bulk states. This confinement of the absorption thus leads to drastic consequences on the field evaporation.

Since the photon energy is not uniformly absorbed at the tip apex, the evaporation is spatially inhomogeneous [38]. This changes the tip shape during the evaporation and induces aberrations in the image reconstruction. For instance, such problems are visible in Fig 2.10(a), where an oxide FeO layer is observed at the second interface. In fact, this layer does not exist; it is due to surface oxygen atoms migration under the field gradient during the analysis related to the uncontrolled tip shape evolution during the evaporation.

In addition, the analysis of bulk MgO can illustrate the complexity of light absorption processes in La-APT. Indeed, the MgO is a large band gap oxide ( $E_g = 7.8$  eV) but could be analysed in La-APT using photon energy of 3.6 eV, 2.4 eV and, 1.2 eV (which are smaller than the energy gap  $E_g$ ). The absorption of the light can thus only be explained taking into account the presence of oxygen defects which create some electronic levels inside the band gap [36]. Recently, Silaeva et. al. [39] have shown that the high electrostatic field of the order of  $0.1\text{V}/\text{\AA}$  inside a dielectric nanostructure strongly enhances its laser absorption up to the value typical for metals and found to be in good agreement with their first-principle DFT calculations for atomic clusters of MgO crystal.

In summary, semiconductors and insulators or the materials with energy band gap shows two types of evaporation behaviour. We can separate these evaporation processes as fast and slow evaporation. The fast evaporation process evidenced by the sharp narrow peak in ToF spectrum can give the information on the surface absorption under high DC field. The slow evaporation process is due to the absorption of laser light far from the apex. The presence of this absorption can be verified by second peak or hump observed few 10's to 100's of nanosecond after fast peak in ToF Spectrum. By analysing the position (on time scale) and magnitude of the hump or delayed evaporation on ToF spectrum acquired from LaAPT analysis, it is possible to obtain the essential information on the absorption map far from the tip apex. On the other hand, studying the effect of change in laser parameters (and field conditions) on the delayed evaporation process; qualitative estimates of the thermal diffusivity of the analysed material at nanoscale dimensions also can be calculated with the help of numerical calculations based on thermal pulse model.

These results from the existing literature and the discussion given in this section shows that La-APT can be used not only to image materials in 3D at near atomic resolution but can also give the information on absorption and thermal properties of the materials as well. By combining these two aspects of the technique i.e. understanding structural and optical properties at the same time and correlation between these properties can be the ultimate characterization tool for nanoscale materials in near future.

## **2.4 Scanning Transmission Electron Microscopy (STEM)**

The scanning transmission electron microscope (STEM) is an invaluable tool for the characterization of nanostructures, providing a range of different imaging modes with the ability to provide information on elemental composition and electronic structure at the ultimate sensitivity, that of a single atom. The STEM works on the principle of combination of normal scanning electron microscope (SEM) and transmission electron microscope (TEM), by forming a focused beam of electrons that is scanned over the sample while some desired signal is collected to form an image [40]. The difference with SEM is that thin specimens are used so that electron beam can be transmitted through the sample.

When an electron nanoprobe interacts with a specimen inside a STEM instrument, a variety of electron, electromagnetic and other signals can be generated. Figure 2.11

shows a schematic diagram illustrating the common signals that are used in a dedicated STEM instrument. All these signals can be used to form images or diffraction patterns of the specimen or can be analyzed to provide spectroscopic information. For example, by collecting high-angle scattered electrons with an annular detector, high-angle annular dark-field (HAADF) images (also called Z-contrast images) can be formed to provide information about structural variations across the sample on an atomic level. Electron energy-loss spectroscopy (EELS), which is based on the energy analysis of the inelastically scattered electrons, can provide information on the electronic structure, oxidation states, and chemical composition on an atomic or subnanometer scale. X-ray energy dispersive spectroscopy (XEDS) can give quantitative data describing changes of elemental composition associated with inhomogeneous structures of the sample. The combination of XEDS and EELS with HAADF imaging technique can provide detailed information on the composition, chemistry, and electronic and crystal structure of nanoscale systems with atomic resolution and sensitivity [41]

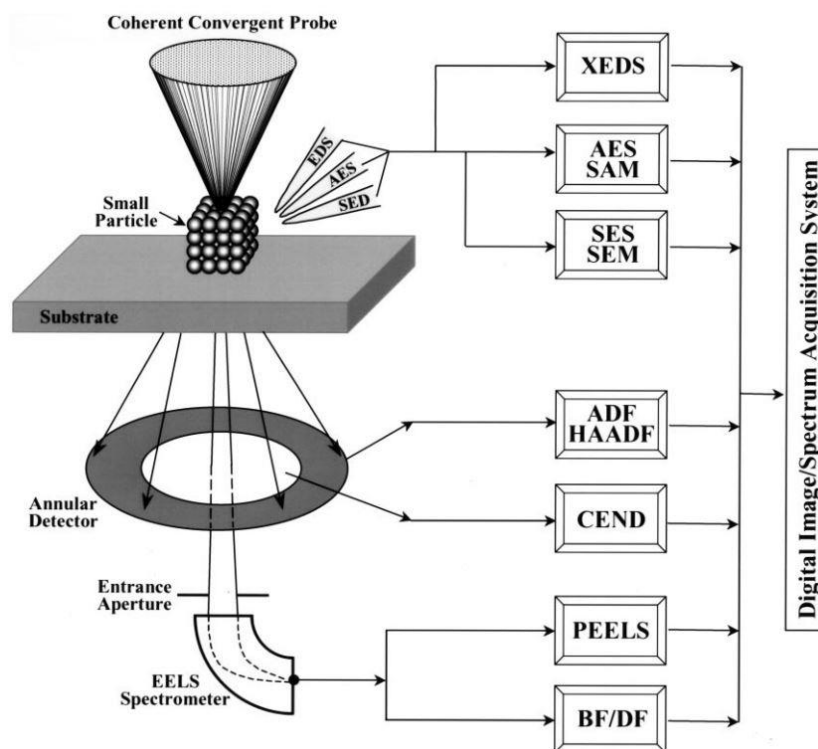


**Figure 2.11** : Schematic diagram illustrates the various signals generated inside a scanning transmission electron microscope that can be used to form high-resolution images, nanodiffraction patterns or spectra of the region-of-interest. X-ray energy dispersive spectroscopy (XEDS); Auger electron spectroscopy (AES) and scanning Auger microscopy (SAM); secondary electron spectroscopy (SES) and secondary electron microscopy (SEM); annular dark-field (ADF) and high-angle annular dark-field (HAADF); coherent electron nanodiffraction (CEND); parallel electron energy-loss spectroscopy (PEELS); bright-field (BF) and dark-field (DF), After [41].

### 2.4.1 High Angle Annular Dark Field (HAADF) imaging

The STEM also offers significant benefits in dark field operation with a unique imaging mode, High Angle Annular Dark Field (HAADF) imaging. In this mode, the inner angle of the annular dark field detector is made so large that no Bragg diffracted electrons are collected. The images therefore come from elastically scattered electrons which have passed very close to the atomic nuclei in the sample. Single atom column resolution is possible with no unwanted diffraction contrast which can mask structural information. The HAADF signal is directly proportional to the density and thickness of the specimen and proportional to  $Z^{3/2}$  where  $Z$  is the atomic number. Thus it is possible to produce images which shows contrast due to the mass-thickness (i.e. the signal is proportional to the number of atoms) or  $Z$  contrast images (where the signal is proportional to the atomic number of the sample). Due to these reasons we have employed HAADF-STEM imaging mode to image our samples. An example of protruding Au-nano-particle from the atom probe tip specimen of Au-NPs in MgO matrix is presented in fig. 2.12 where single atoms from an Au-NP can be visualized.

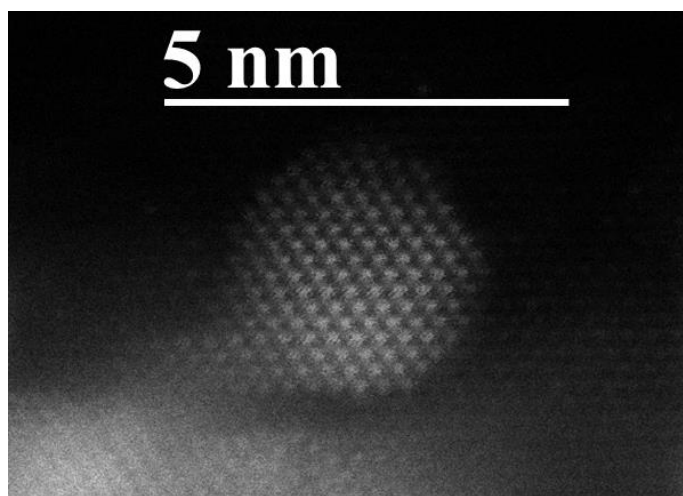


**Figure 2.12** : HAADF-STEM of the Au-nanoparticle. The Au-NP is protruding from the surface of the atom probe tip specimen of Au-NPs embedded in MgO matrix. (Image courtesy: W. Lefebvre)

### 2.5 Micro-photoluminescence ( $\mu$ -PL) Spectroscopy

The  $\mu$ PL studies were carried out at the Institut d'Electronique Fondamentale, University Paris Sud, Orsay, France. The schematic of the  $\mu$ PL experimental set-up is shown in fig. 2.13.

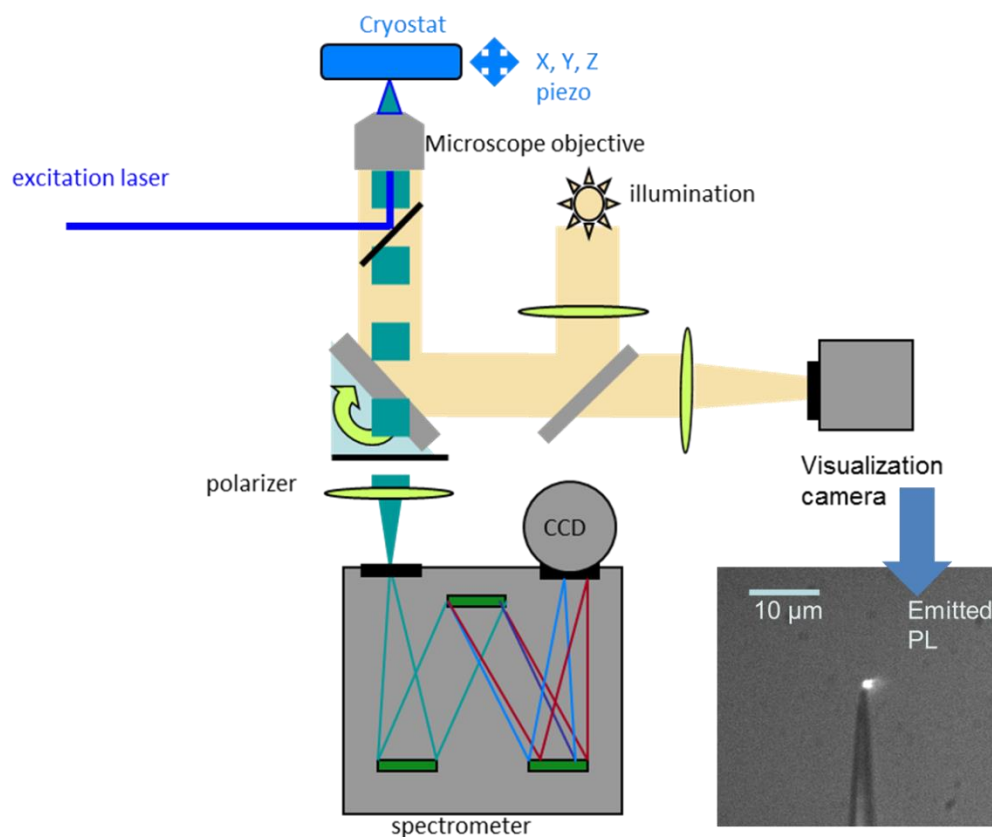


**Figure 2.13** : Experimental set-up for micro-photoluminescence Spectroscopy (PL signal observed with the camera is shown in the right bottom corner of the figure)

The sample placed at cryogenic temperature ( $4^{\circ}\text{K}$ ) is illuminated by the excitation laser ( $\lambda=244\text{nm}$ ) with beam waist size of  $2\mu\text{m}$  and focused to diffraction limit and with incident power of around  $50\mu\text{W}$ . The emitted signal can be recorded by the visualization camera or sent to the spectrometer to record the characteristic properties of emitted light. The PL signal was analyzed in a 460 mm focal length grating spectrometer, with a spectral resolution roughly equal to 1 nm. An example of the emitted PL signal recorded by the camera is also shown in fig. 2.13. The emitted light passes through the polarizer before recorded by the spectrometer, which gives the information about the polarization of emitted light from the sample. The samples analyzed were attached to the Tungsten (W) microposts and were prepared by using Focused Ion beam (FIB) sample preparation method and also by manipulating and welding the micro-wire samples under the optical microscopes. The luminescence spectrum corresponding to different regions can be obtained by illuminating the different regions of the single microwire. An example of one such measurement is given in figure 2.14, where a  $\mu\text{PL}$  signal recorded by camera from an InGaN/GaN microwire (nearly  $18\text{-}20\mu\text{m}$  in length) attached to the W-post is shown.

The spectrums were recorded from three different regions viz. base, middle and top of the microwire. This spatial selectivity of analyzing the sample is helpful to understand and distinguish the emission properties of quantum confined structures to that of bulk emitter within the same sample e.g. base of the InGaN/GaN microwire contains only GaN and hence the PL signal obtained at the base and at top region will have different emission characteristics.

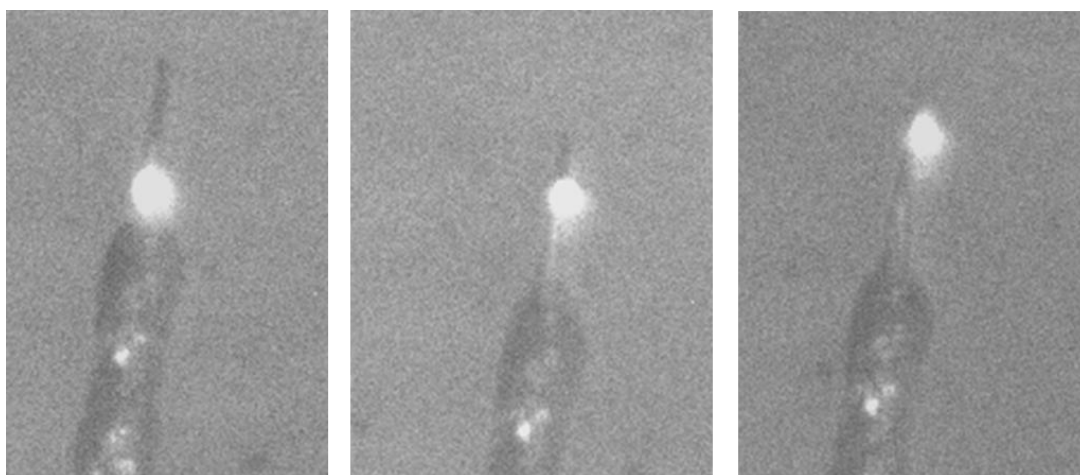


**Figure 2.14** : The  $\mu$ PL signal recorded by camera from three different regions of same InGaN/GaN microwire. (From left to right) PL signal emitted when the base, middle and, top region of the microwire is illuminated by the laser light.

## 2.6 Spatial Modulation Spectroscopy (SMS)

The study of understanding the optical absorption properties of nanotips using LaAPT is in itself novel way. In order to compare the information obtained on the optical absorption using LaAPT, we have decided to use a method known as Spatial Modulation Spectroscopy (SMS). SMS is far field optical technique based on modulating the spatial position of the nano-object under illumination and measuring the change in modulated transmitted optical signal. The modulated signal along with lock-in detection helps to measure the extinction cross-sections of the order of few  $\text{nm}^2$  [1] for single isolated nano-object. The schematic of SMS technique for measuring extinction cross-section of nanoparticle is shown in fig. 2.15.

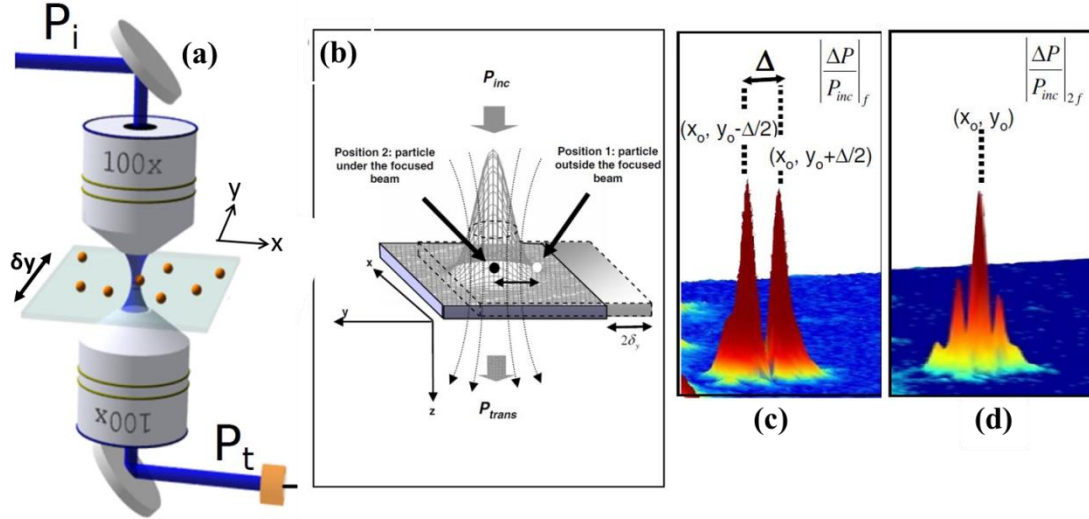


**Figure 2.15 :** (a) Schematics of SMS, laser beam is illuminated through 100X objective on the nano-object, while the spatial position is modulated along Y-direction. The light transmitted is collected using another 100X objective and the signal is recorded using lock-in amplifier, (b) Position of particle during modulation, (c) normalized change in transmission induced by single nanoparticle at modulation frequency of ' $f$ ' and (d) at modulation frequency of ' $2f$ '

As shown in fig. 2.15, the laser beam is incident on single nanoparticle, while its position is modulated along Y-axis with amplitude of  $\delta y$ . The laser beam is incident on a nanoparticle at the position  $(x_0, y_0)$ , then the transmitted power is given by,

$$P_t \cong P_i - \sigma_{ext} I(x_0, y_0) \quad (2.11)$$

Where,  $I(x_0, y_0)$  is the intensity spatial profile. Due to modulation of particle position at frequency  $f$  along  $y$  direction, it also modulates the transmitted signal,

$$P_t \cong P_i - \sigma_{ext} I[x_0, y_0 + \delta y \sin(2\pi f t)] \quad (2.12)$$

$$P_t \approx P_i - \sigma_{ext} I(x_0, y_0) - \sigma_{ext} \delta y I'(x_0, y_0) \sin(2\pi f t) - \left(\frac{\sigma_{ext}}{2}\right) (\delta y) 2I''(x_0, y_0) \sin^2(2\pi f t) \quad (2.13)$$

From eq. (2.13), it is seen that the normalized transmission change  $\frac{\Delta P}{P} = \frac{P_t - P_i}{P_i}$  contains components at  $f$  and  $2f$  proportional to the first,  $I'$ , and second,  $I''$ , derivative of  $I(x_0, y_0)$  relative to the  $y$  variable, respectively. The signal measured at  $f$  as a function of the particle position (i.e., scanning  $x$  and  $y$ ), is thus zero when the particle is at the beam center and exhibits two extrema in the  $y$  direction (Fig. 2.15(c)). In contrast, for  $2f$  detection it is maximum, when the particle is in the center of the laser beam (Fig. 2.15(d)). This change in transmission by varying the laser wavelength will result in the absolute extinction spectra of the nanoparticle under observation. Moreover, the change in transmission can also be studied as function of polarization of laser light. We have used

the SMS technique to understand the optical absorption in case of tip shaped samples used in atom probe experiments. The results are given in chapter 3.

## 2.7 Conclusion

In conclusion, this chapter introduces different experimental methods used during the course of this thesis. Basic principle of atom probe tomography is given in the beginning of the chapter and more attention is given to explain the methodology to use the data obtained from LaAPT experiment to deduce the optical absorption and thermal properties of the material at nanoscale. This approach is further used in chapter 3 and 4 to have the information on absorption and thermal properties of Au-MgO and Au-Fe<sub>2</sub>O<sub>3</sub> samples respectively. Furthermore, short introduction to the other techniques like STEM,  $\mu$ -PL-spectroscopy and spatial modulation spectroscopy (SMS) are incorporated at the end of the chapter.

## References

1. Arbouet A, Christofilos D, Del Fatti N, Vallée F, Huntzinger JR, Arnaud L, Billaud P, Broyer M. Direct Measurement of the Single-Metal-Cluster Optical Absorption. *Phys Rev Lett* (2004) **93**:127401. doi:10.1103/PhysRevLett.93.127401
2. Gault B, Vurpillot F, Vella A, Gilbert M, Menand A, Blavette D, Deconihout B. Design of a femtosecond laser assisted tomographic atom probe. *Rev Sci Instrum* (2006) **77**:043705. doi:10.1063/1.2194089
3. Oppenheimer JR. Three Notes on the Quantum Theory of Aperiodic Effects. *Phys Rev* (1928) **31**:66–81. doi:10.1103/PhysRev.31.66
4. Fowler RH, Nordheim L. Electron Emission in Intense Electric Fields. *Proc R Soc Lond Math Phys Eng Sci* (1928) **119**:173–181. doi:10.1098/rspa.1928.0091
5. Müller EW. Die Abhängigkeit der Feldelektronenemission von der Austrittsarbeit. *Z Für Phys* (1936) **102**:734–761. doi:10.1007/BF01338540
6. Müller EW. Abreißen adsorbierter Ionen durch hohe elektrische Feldstärken. *Naturwissenschaften* (1941) **29**:533–534. doi:10.1007/BF01481175
7. Müller EW, Bahadur K. Field Ionization of Gases at a Metal Surface and the Resolution of the Field Ion Microscope. *Phys Rev* (1956) **102**:624–631. doi:10.1103/PhysRev.102.624
8. Müller EW, Panitz JA, McLane SB. The Atom-Probe Field Ion Microscope. *Rev Sci Instrum* (1968) **39**:83–86. doi:10.1063/1.1683116
9. Costa GD, Vurpillot F, Bostel A, Bouet M, Deconihout B. Design of a delay-line position-sensitive detector with improved performance. *Rev Sci Instrum* (2005) **76**:013304. doi:10.1063/1.1829975
10. Bas P, Bostel A, Deconihout B, Blavette D. A general protocol for the reconstruction of 3D atom probe data. *Appl Surf Sci* (1995) **87–88**:298–304. doi:10.1016/0169-4332(94)00561-3

11. Gault B, Moody MP, Cairney JM, Ringer SP. *Atom Probe Microscopy*. New York, NY: Springer New York (2012). Available at: <http://link.springer.com/10.1007/978-1-4614-3436-8> [Accessed June 10, 2015]
12. Miller MK, Cerezo A. *Atom Probe Field Ion Microscopy*.
13. Larson DJ, Prosa TJ, Ulfing RM, Geiser BP, Kelly TF. *Local Electrode Atom Probe Tomography*. New York, NY: Springer New York (2013). Available at: <http://link.springer.com/10.1007/978-1-4614-8721-0> [Accessed May 4, 2015]
14. Bunton JH, Olson JD, Lenz DR, Kelly TF. Advances in Pulsed-Laser Atom Probe: Instrument and Specimen Design for Optimum Performance. *Microsc Microanal* (2007) **13**:418–427. doi:10.1017/S1431927607070869
15. Vurpillot F, Gault B, Vella A, Bouet M, Deconihout B. Estimation of the cooling times for a metallic tip under laser illumination. *Appl Phys Lett* (2006) **88**:094105. doi:10.1063/1.2181654
16. Gault B, Vella A, Vurpillot F, Menand A, Blavette D, Deconihout B. Optical and thermal processes involved in ultrafast laser pulse interaction with a field emitter. *Ultramicroscopy* (2007) **107**:713–719. doi:10.1016/j.ultramic.2007.02.004
17. Vurpillot F, Houard J, Vella A, Deconihout B. Thermal response of a field emitter subjected to ultrafast laser illumination. *J Phys Appl Phys* (2009) **42**:125502. doi:10.1088/0022-3727/42/12/125502
18. Cerezo A, Smith GDW, Clifton PH. Measurement of temperature rises in the femtosecond laser pulsed three-dimensional atom probe. *Appl Phys Lett* (2006) **88**:154103. doi:10.1063/1.2191412
19. Kellogg GL. Determining the field emitter temperature during laser irradiation in the pulsed laser atom probe. *J Appl Phys* (1981) **52**:5320–5328. doi:10.1063/1.329390
20. Cerezo A, Grovenor CRM, Smith GDW. Pulsed laser atom probe analysis of semiconductor materials. *J Microsc* (1986) **141**:155–170.
21. Marquis EA, Gault B. Determination of the tip temperature in laser assisted atom-probe tomography using charge state distributions. *J Appl Phys* (2008) **104**:084914. doi:10.1063/1.3006017
22. Houard J, Vella A, Vurpillot F, Deconihout B. Optical near-field absorption at a metal tip far from plasmonic resonance. *Phys Rev B* (2010) **81**:125411. doi:10.1103/PhysRevB.81.125411
23. Houard J, Vella A, Vurpillot F, Deconihout B. Three-dimensional thermal response of a metal subwavelength tip under femtosecond laser illumination. *Phys Rev B* (2011) **84**:033405. doi:10.1103/PhysRevB.84.033405
24. Kelly TF, Vella A, Bunton JH, Houard J, Silaeva EP, Bogdanowicz J, Vandervorst W. Laser pulsing of field evaporation in atom probe tomography. *Curr Opin Solid State Mater Sci* (2014) **18**:81–89. doi:10.1016/j.cossms.2013.11.001
25. Vella A. On the interaction of an ultra-fast laser with a nanometric tip by laser assisted atom probe tomography: A review. *Ultramicroscopy* (2013) **132**:5–18. doi:10.1016/j.ultramic.2013.05.016
26. Wiley: Introduction to Solid State Physics, 8th Edition - Charles Kittel. Available at: <http://eu.wiley.com/WileyCDA/WileyTitle/productCd-EHEP000803.html> [Accessed May 4, 2015]
27. Ashcroft NW, Mermin ND. *Solid State Physics*. 1 edition. New York: Cengage Learning (1976).
28. Dash WC, Newman R. Intrinsic Optical Absorption in Single-Crystal Germanium and Silicon at 77 K and 300 K. *Phys Rev* (1955) **99**:1151–1155. doi:10.1103/PhysRev.99.1151
29. Ding G-H, Chan CT, Zhang ZQ, Sheng P. Resonance-enhanced optical annealing of silicon nanowires. *Phys Rev B* (2005) **71**:205302. doi:10.1103/PhysRevB.71.205302

30. Bogdanowicz J, Gilbert M, Innocenti N, Koelling S, Vanderheyden B, Vandervorst W. Light absorption in conical silicon particles. *Opt Express* (2013) **21**:3891. doi:10.1364/OE.21.003891
31. Keldysh L. Ionization in the field of a strong electromagnetic wave. *J Exp Theor Phys* (1965) **20**:1307.
32. Karahka M, Kreuzer HJ. Field evaporation of oxides: A theoretical study. *Ultramicroscopy* (2013) **132**:54–59. doi:10.1016/j.ultramic.2012.10.007
33. Tsong TT. Pulsed-laser-stimulated field ion emission from metal and semiconductor surfaces: A time-of-flight study of the formation of atomic, molecular, and cluster ions. *Phys Rev B* (1984) **30**:4946–4961. doi:10.1103/PhysRevB.30.4946
34. Tsong TT. Field penetration and band bending near semiconductor surfaces in high electric fields. *Surf Sci* (1979) **81**:28–42. doi:10.1016/0039-6028(79)90503-X
35. Bogdanowicz J, Gilbert M, Koelling S, Vandervorst W. Impact of the apex of an elongated dielectric tip upon its light absorption properties. *Appl Surf Sci* (2014) **302**:223–225. doi:10.1016/j.apsusc.2013.10.150
36. Mazumder B, Vella A, Vurpillot F, Martel G, Deconihout B. Surface carrier recombination of a silicon tip under high electric field. *Appl Phys Lett* (2010) **97**:073104. doi:10.1063/1.3473816
37. Mazumder B, Vella A, Deconihout B, Al-Kassab T. Evaporation mechanisms of MgO in laser assisted atom probe tomography. *Ultramicroscopy* (2011) **111**:571–575. doi:10.1016/j.ultramic.2010.11.017
38. Vella A, Mazumder B, Costa GD, Deconihout B. Field evaporation mechanism of bulk oxides under ultra fast laser illumination. *J Appl Phys* (2011) **110**:044321. doi:10.1063/1.3610523
39. Silaeva EP, Arnoldi L, Karahka ML, Deconihout B, Menand A, Kreuzer HJ, Vella A. Do Dielectric Nanostructures Turn Metallic in High-Electric dc Fields? *Nano Lett* (2014) **14**:6066–6072. doi:10.1021/nl502715s
40. Muller DA. Structure and bonding at the atomic scale by scanning transmission electron microscopy. *Nat Mater* (2009) **8**:263–270. doi:10.1038/nmat2380
41. Liu J. Scanning transmission electron microscopy and its application to the study of nanoparticles and nanoparticle systems. *J Electron Microsc (Tokyo)* (2005) **54**:251–278. doi:10.1093/jmicro/dfi034

# Chapter 3

## **Au-nanoparticles in MgO matrix : Understanding optical absorption using LaAPT**

### **3.1 Introduction**

Gold nanoparticles and their unique optical properties have been of interest to scientists and artists for many centuries. History documents their earliest applications to the early 17<sup>th</sup> century, where their brilliant colors made them ideal for pigments in chinaware [1] and in stained glasses [2]. For last few decades the system of metal nanoparticles embedded in a dielectric matrix are widely studied due to their potential application in opto-electronics, plasmonics, nonlinear optics etc. owing to their strong coupling to an incident electromagnetic radiation [3–5]. The nanoparticles absorb electromagnetic radiation strongly around their surface plasma resonant wavelength. This resonant absorption depends on various parameters like size, shape, density and dielectric environment of the nanoparticles and with the advent of various synthesis techniques one can tune this resonant absorption as per requirement. A consequence of this strong absorption of radiation associated with the surface plasma resonance (SPR) is heat generation in nanoparticles and there subsequent thermalization (or cooling) to the surroundings. Many efforts has been made to study the interplay between the optical and thermal properties of metal nanoparticles in liquids [6], polymers [7] as well as in solid matrix [8,9].

Although, APT can provide 3D chemical analysis at near atomic spatial resolution for various materials, analyzing heterogeneous materials is always been challenging due to application of high DC electrostatic field in APT. The evaporation field, i.e. electric field required to remove the surface atom from APT specimen is different for different materials. The trajectories of ions field evaporated from the surface of APT specimen will depend on the evaporation field of the sample's constituents, in our case it is nanoparticle and dielectric matrix. This change in evaporation field will change the surface morphology which further results in change in ion trajectories of the evaporated species. This effect is commonly known as local magnification effect [10,11]. Because of this effect, the ion trajectories of the matrix and precipitate will overlap which will give rise to the incorrect measurement of the precipitate/nanoparticle composition. Devaraj et. al. thoroughly studied this effect in case of Au nanoparticles embedded in MgO matrix [12], the maximum Au concentration observed in the core of the nanoparticles in this study were 22 at.% and the deficit is attributed to the differences in evaporation field of Au (High field particle) and MgO (Low field matrix). Despite local magnification effects the core composition of the precipitate/particle is expected to be pure, but this is not the case when analyzing Au nanoparticles in MgO matrix. This discrepancy in the measurement of composition hinders the use of APT to analyze metallic nanoparticles embedded in dielectric matrix, which also reflects in APT literature with just handful number of reports on these technologically important types of material [12–14]. To overcome this difficulty one has to understand the underlying physical mechanism of this behavior apart from local magnification effects, which is possible to some extent by studying these structures with respect to the wavelength of laser light used to trigger the field evaporation. In addition, this analysis will also shed some light on the complex laser-tip interactions involve in the APT experiment.

In this regard, this chapter is making an attempt to understand the effect of the wavelength used to trigger the field evaporation process on the evaporation dynamics, studied using Time of flight (ToF) spectra obtained after APT analysis of Au-NPs embedded in MgO matrix. More attention is given to the optical absorption of Au-NPs and its consequences on the evaporation dynamics with temporal evolution of temperature induced by absorption of the laser light of different wavelengths. To support the experimental results, numerical calculations based on the model available in literature are also used along with the absorption computation of tip-shaped samples using finite difference time domain (FDTD) calculations.

## 3.2 Materials and Characterization

The sample with Au-nanoparticles (Au-NPs) embedded in MgO matrix was received from the Dr. Arun Devaraj from Pacific Northwest National Laboratory (PNNL), Washington, US. As explained in chapter 1, this specimen was synthesized by ion beam implantation of 2MeV Au<sup>2+</sup> ions on single crystalline MgO substrate followed by annealing at 1275°K for 10 hours. A band of cubic Au-nanoparticles with sizes ranging from 3-8nm Gaussian density distribution in depth is formed nearly 200nm from the MgO surface. The cross-sectional STEM image showing the distribution of Au-NPs along the depth of the sample is represented in fig. 3.1(a), also the size and shape of the NPs in high resolution (HR) image in (b)

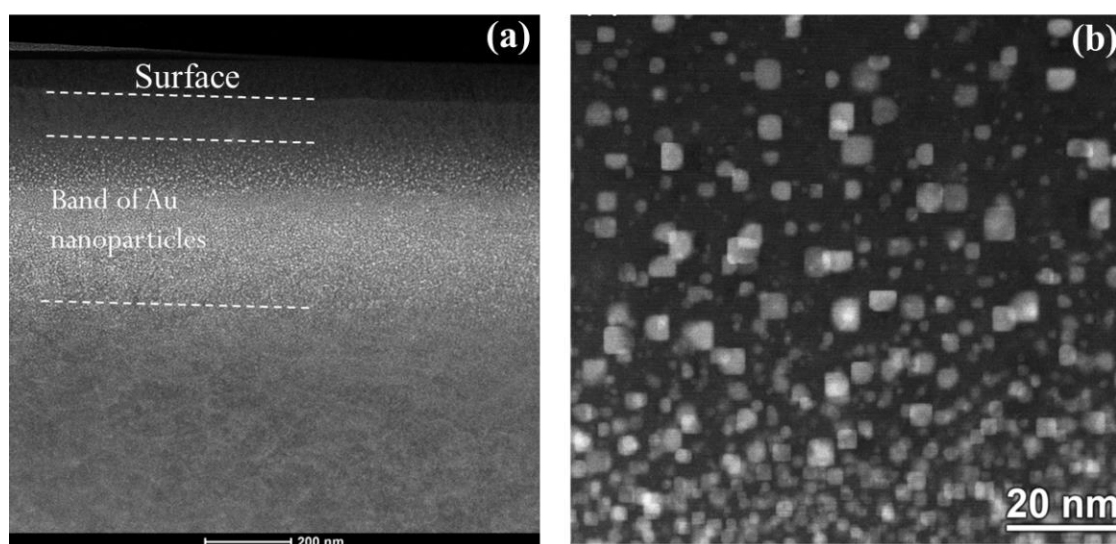


**Figure 3.1** : Cross-sectional STEM image of the Au-NPs embedded in MgO matrix, (a) Band of Au-NPs formed nearly 200nm from the surface of the MgO, (b) high resolution image from the less dense region of Au in (a) showing the variation in size distribution of Au-NPs

### 3.2.1 Bulk optical absorption

The absorption spectra for bulk sample is measured by illuminating the Au irradiated region of the specimen. By measuring the transmitted signal the absorbance is calculated and plotted in fig. 3.2. In addition, the spectrum is also measured from non-irradiated region of the sample, i.e. pure MgO for comparison.

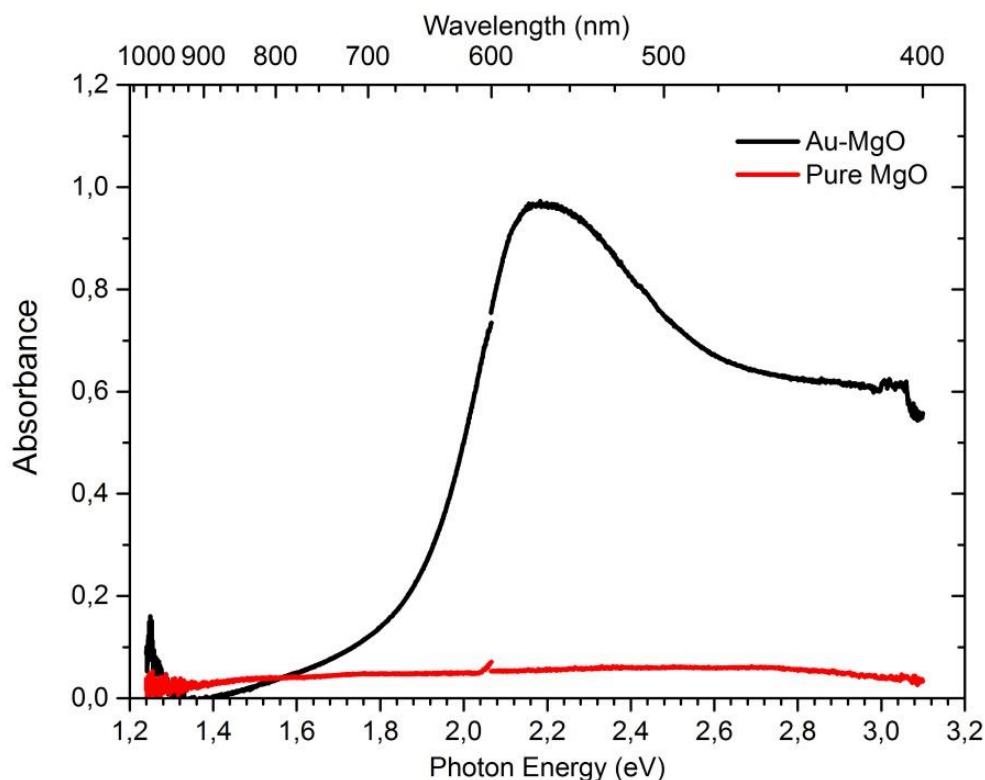


**Figure 3.2 :** Bulk Optical absorption spectra for pure MgO and Au-NP's embedded in MgO

The pure MgO is nearly transparent to the wavelengths used to measure the absorption (400nm – 1000nm) which is expected considering the electrical insulating properties of MgO. But when the Au irradiated region is illuminated, a broad absorption band with absorption maximum situated around 570nm is observed. This strong absorption in the green region is due to the resonant absorption of Au-NPs due to plasmon resonance. The broadness of the absorption peak can be related to the non-uniform size and density distribution of the Au-NPs in the sample [15].

### 3.2.2 Sample preparation for APT

To prepare the tip shaped samples for atom probe experiments standard focused ion beam (FIB) based method [16] were employed. The detailed sample preparation protocol is similar to described in Chapter 4 and 5. The tip shaped samples were prepared from the bulk sample as shown in fig. 3.3.

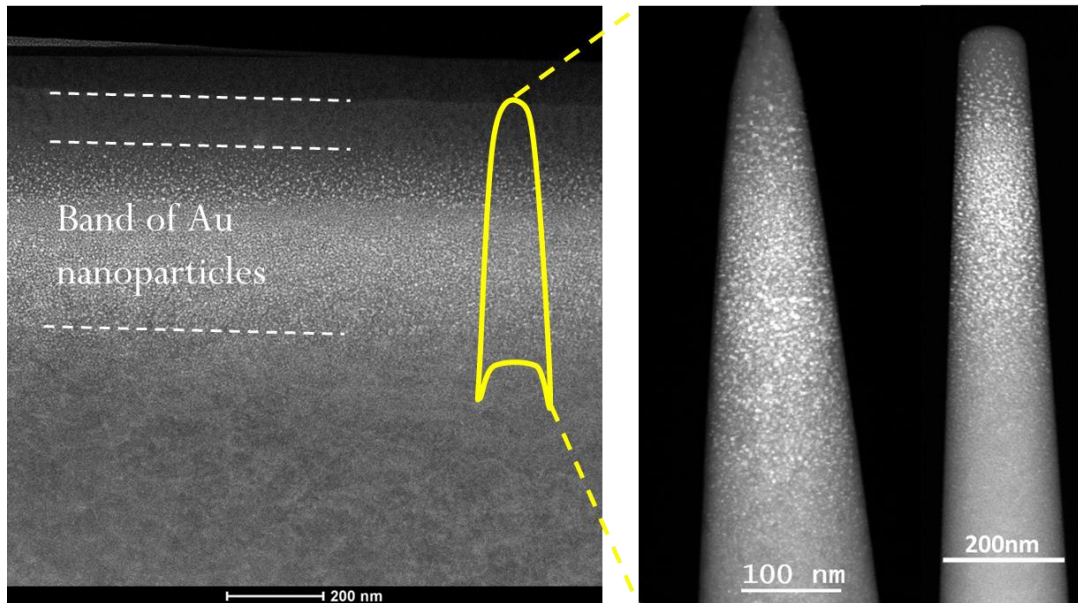


**Figure 3.3 :** Sample preparation for atom probe experiments, tip shaped samples prepared from bulk sample using FIB based protocol.

### 3.3 Influence of the Laser Wavelength

The tip with high concentration of Au-NPs near apex region was analyzed by LaAPT using Green wavelength ( $\lambda=515$  nm). The Au-NPs region further extends to nearly 200nm from the tip apex with decrease in concentration. The STEM-HAADF image of the tip is shown in fig 3.4. In this analysis we have observed the delayed evaporation behavior.

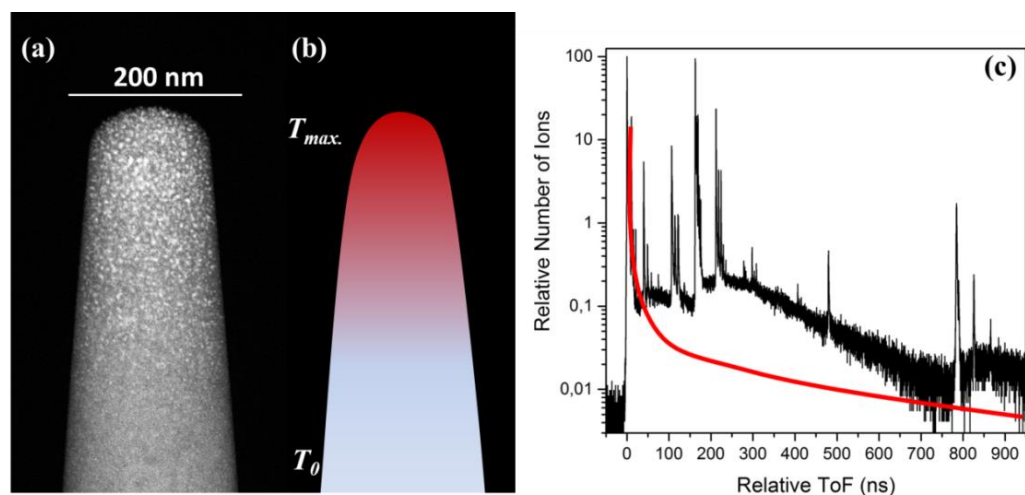


**Figure 3.4 :** (a) HAADF-STEM image of the tip, the bright contrasted spots are Au-NPs covering the apex region, (b) Expected temperature profile when the tip shown in (a) is illuminated by laser light of wavelength 515 nm,  $T_{max}$  : maximum temperature rise due to absorption of Au-NP's,  $T_0$  : Base temperature (c) ToF spectrum obtained after analyzing the tip shown in (a), displays the delayed evaporation as a hump in ToF spectrum. The red solid line corresponds to the temperature evolution at the apex of the tip corresponding to the temperature profile shown in (b).

The HAADF-STEM image of the tip in fig. 3.4(a) clearly shows the apex of the tip is fully covered with high dense Au-NP's. The tip is analyzed by LaAPT at constant flux of 0.005-0.009 at./pulse and at constant laser energy of 1.5mW (15nJ/pulse). Due to non-zero shank angle, the voltage on the tip is gradually increased to keep the evaporation flux constant. The voltage used was in the range of 9.9kV-10.2 kV. Nearly one million atoms were collected during the analysis and the ToF spectrum was plotted and is represented in fig. 3.4(c). The ToF spectrum clearly shows the evidence of delayed evaporation (or hump) several nanoseconds (100ns) after the fast evaporation peak. The presence of delayed evaporation degrades the quality of data obtained in LaAPT by decreasing the signal to noise (S/N) ratio. The existence of this slow evaporation process as explained in the chapter 2 is due to the thermal absorption inside the atom probe sample under laser illumination. This delayed evaporation is more evident if the absorption far from the tip apex is higher in magnitude compared to that of near apex region. This behavior was already reported in case of Si-emitter when illuminated with high power Infrared (IR) Laser [17]. Most of the light is expected to be absorbed by Au NPs region, creating a hot zone at the apex and cooling of this hot zone along the tip axis should give rise to decaying tail of evaporation rate with respect to time. This heating and cooling mechanism is depicted schematically in fig. 3.4(b), where the tip apex temperature increases ( $T_{max.}$ ) due to the absorption of Au-NP's and thermalizes to the base temperature ( $T_0$ ) along the tip axis. The expected consequence of this process on the nature of ToF spectrum is shown by the red curve in fig. 3.4(c). But this is not the case, which means either there is still resonant absorption far from the apex which is comparable to the strong absorption due to the Au NP's or some other mechanism which causes this delayed evaporation. To understand this, we have performed the finite difference time domain (FDTD) numerical calculations on Au-NP's embedded in MgO tip. The absorption maps obtained are represented in fig. 3.5

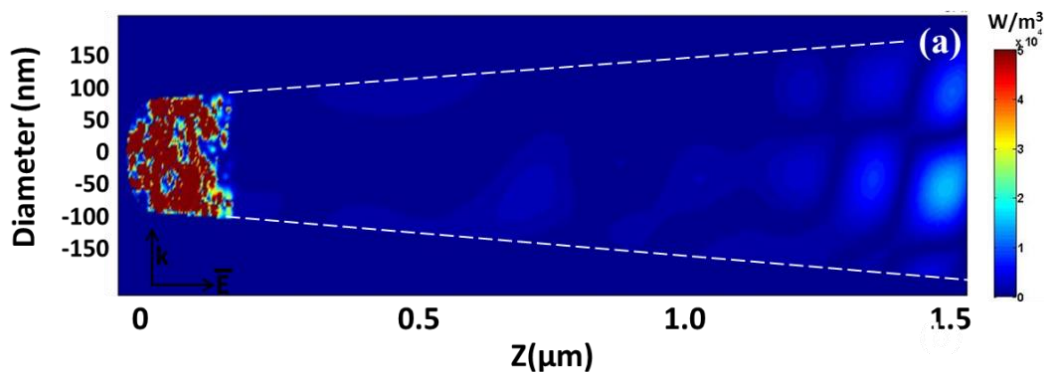


**Figure 3.5** : Absorption map in the incident plane ( $y, z$ ) at  $\lambda=515$  nm calculated by Lumerical or Au-NP's embedded in MgO matrix. The Au-NP's are present only in near apex region (The dotted white line is drawn to guide the eye).

To consider the actual tip geometry, tip is represented by a cone terminated by hemispheric cap. The radius (75 nm) and cone angle (5.5 deg.) measured from the HAADF-STEM image (fig. 3.4(a)) was used as input parameters. Spherical Au-NP's of size ranging from 3-8nm in diameter with random distribution was placed near apex of the tip. This geometry is placed in simulated space and surrounded by perfectly matched layers (PML), avoiding any field reduction. For  $\lambda=515$ nm, the optical constants for Au, MgO and W were taken from Palik [18]. The computation of divergence of Poynting vector leads to the absorption map shown in fig. 3.5. The length of the tip, i.e. the distance from apex of the tip to the interface between MgO/W-pretip is nearly  $1.5\mu\text{m}$  in this case and hence used this length to simulate the absorption. The absorption map shown in fig. 3.5 clearly reveals the strong absorption at near apex region due to the Au-NP's absorption which is expected and clearly understood considering the tendency of Au-NP's absorption at green wavelength. Also, the absorption far from the apex is negligible when compared to the absorption at near apex region, which rules out the possibility of assigning the delayed evaporation to the resonant absorption far from the apex. This absorption map can be directly correlated to the schematic of temperature profile shown in fig. 3.4(b) and its implication on the ToF spectrum shown by red curve in fig. 3.4(c). But these calculations are not able to explain the delayed evaporation observed in the experimental ToF spectrum shown in fig. 3.4(c). Moreover our numerical calculations don't take into account non-linear effects which can be induced in the high-field regions inside the MgO matrix. These non-linear effects are able to explain the delayed evaporation reported in case Si emitters using IR light [19].

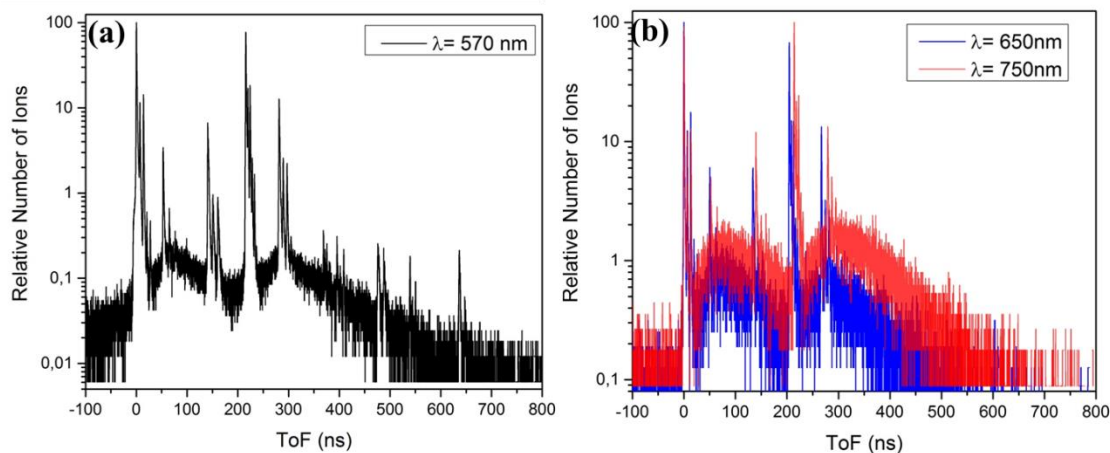


**Figure 3.6 :** ToF spectra obtained from Au-MgO tip at laser wavelength of (a) 570nm and (b) 650nm and 750nm

To understand if the non-linear absorption in MgO matrix is the physical origin of the delayed evaporation or not, we changed the laser wavelength. Considering the bulk absorption spectra obtained (see fig. 3.2), we decided to conduct the LaAPT experiment at plasmon resonance wavelength ( $\lambda_{\text{SPR}} = 570\text{nm}$ ). For a laser illumination closed to the plasmonic resonance, we expect a strong absorption of the tip apex (where NPs are located) which will completely mask the delayed evaporation. Hence changing the laser wavelength to plasmonic resonance we expect to improve the S/N ratio of our APT analysis and hence the detectability of the instrument. However, looking at the ToF spectra reported in fig. 3.6(a) obtained at  $\lambda_{\text{SPR}}$  (570nm), we can note that the delayed evaporation is still observable and its amplitude is found to be increased as the illumination wavelength is further increased as observed for the wavelength of 650nm and 750nm (fig. 3.6(b)).

These experimental results are proof that the delayed evaporation is not due to the hot field spots inside the MgO matrix and even the change of the laser wavelength to plasmon resonance of Au-NPs cannot suppress this delayed evaporation. New physical origin/s has to be determined in order to diminish this long-time emission process.

### 3.4 Influence of the length of the tip and tip support

In the previous section we did not consider the contribution of W-pretip support. Considering the laser beam waist size in our atom probe experiment ( $60\mu\text{m}$ ), the W-pretip is also illuminated by laser which will absorb the green light efficiently. In this regard we have performed another simulation with Au-MgO tip attached to the W-pretip support. The absorption map obtained is presented in fig. 3.7 and shows similar behavior of

absorption in near apex region as calculated without W-pretip support (fig. 3.5). But the interesting feature in this calculation is the significant absorption of metallic W-pretip. This strong absorption will create another hot zone nearly  $1.5\mu\text{m}$  from the apex which corresponds to the distance from apex to the tip/W-pretip interface and could be the reason for the delayed evaporation observed.

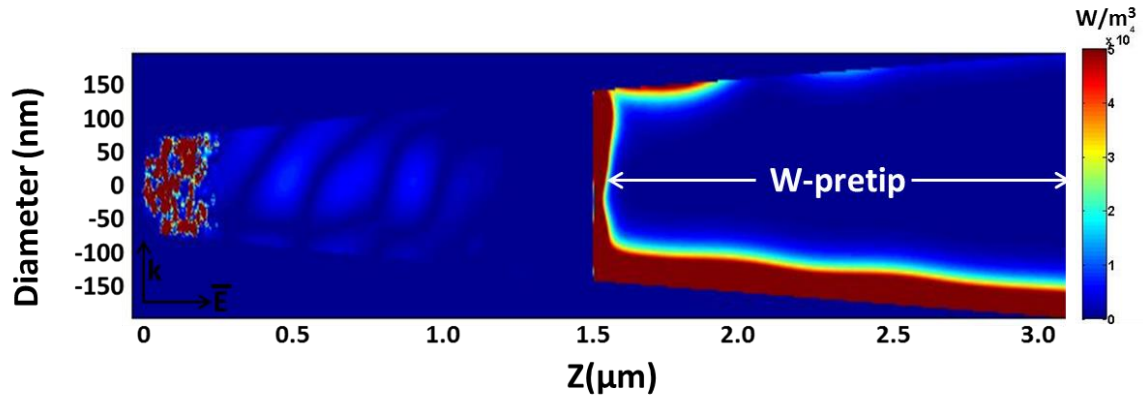


**Figure 3.7 :** Absorption map in the incident plane ( $y, z$ ) at  $\lambda=515\text{ nm}$  calculated by Lumerical for Au-NP's embedded in MgO matrix with W-pretip support. The Au-NP's are present only in near apex region.

Moreover, the absorption maxima of W are not changed when the similar calculations were carried out at 570nm, 650nm and 750nm wavelength (not shown here). This can explain why the delayed evaporation is visible experimentally at these wavelengths.

### 3.4.1 Experimental Results and discussion

The one way to prove this hypothesis experimentally is to shift the tip/W-pretip interface farther from the apex and observe the evaporation rate with respect to the ToF. In order to perform this analysis we prepared another tip of Au-MgO with length up to  $4.2\text{-}4.3\mu\text{m}$  and carried out the atom probe experiment with similar experimental conditions as that of the previous experiment carried out on the tip with length of  $1.5\mu\text{m}$ . In addition, the data was collected from nearly the same region of interest of Au concentration as that of the previous analysis. To compare the length of the both tips an SEM image is shown in Fig. 3.8(a) and (b). The interface between metallic W-pretip and the MgO is represented by slanted black line for clarity.

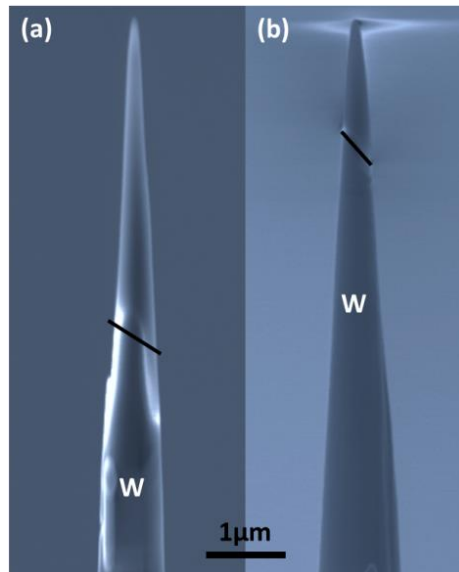


**Figure 3.8 :** Comparison of the length of the tip, SEM image of Au-MgO tip (a) 4.2 $\mu\text{m}$  long and (b) 1.5 $\mu\text{m}$  long tip. The length is defined as the distance between the tip apex and the interface of tip/W-pretip support, the slanted black line represents the tip/W-pretip interface.

After collecting one million atoms, the data obtained is optimized and the ToF spectrum is plotted and compared with ToF spectrum obtained with previous analysis with length of 1.5  $\mu\text{m}$ . The comparison is shown in fig. 3.9.

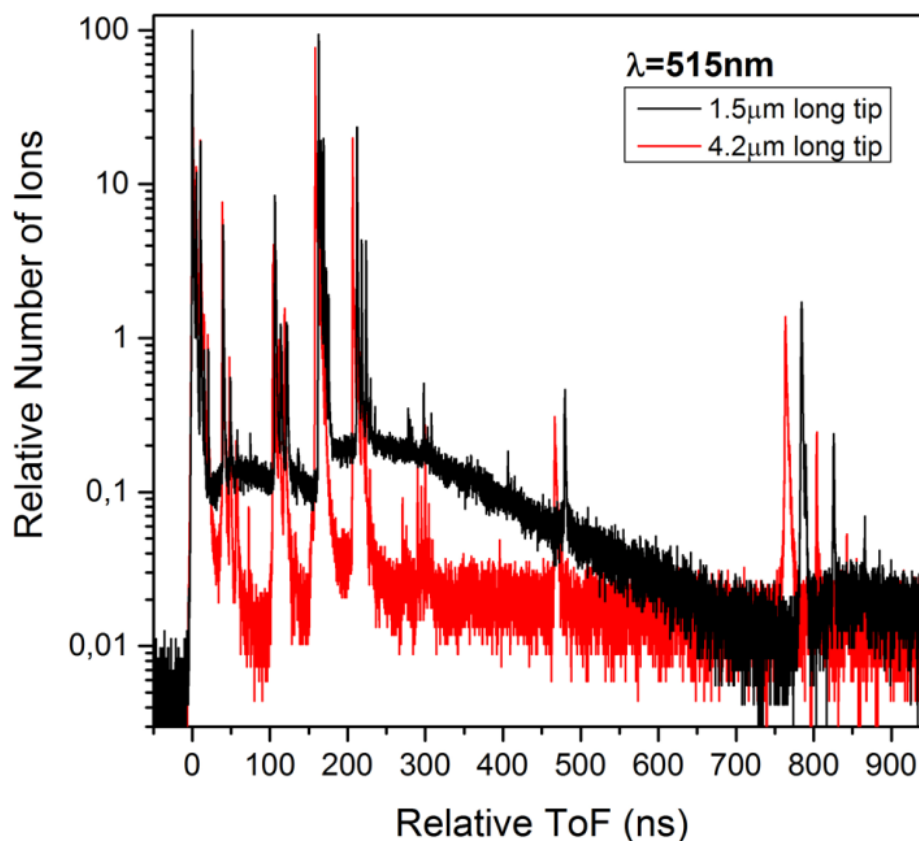


**Figure 3.9 :** Comparison of time of flight (ToF) spectra obtained for short tip (black curve) and long tip (red curve) at  $\lambda=515\text{nm}$ .

Fig. 3.9 prominently demonstrates the suppression of delayed evaporation for longer tip. The 4.2  $\mu\text{m}$  long tip doesn't show any sign of hump or delayed evaporation as observed in short tip. In addition, in case of long tip the evaporation rate decreases rapidly after the fast evaporation peak, this is because the long tip cools down faster to the base temperature which also results in improved signal to noise ratio. This clearly suggests that, there is significant contribution of absorption due to the metallic W-pretip which gives rise to the delayed evaporation in case of short tip. So the presence of delayed evaporation strongly depends on how far is the tip/W-pretip interface. When this interface is nearly 1.5-1.8 $\mu\text{m}$  far from apex, the interaction of two cooling processes, one from apex to the tip axis and another from tip/W-pretip interface towards apex will raise the temperature of the tip as a whole above base temperature (70K). This elevated temperature 1.5  $\mu\text{m}$  away from the tip apex will take its time to reach the tip surface to increase its temperature and this will result in increased evaporation rate but delayed in time.

In order to compare these experimental findings with the numerical calculations, we have used the one dimensional thermal model as discussed in chapter 2 [20]. Using this model the temperature evolution at the tip apex can be predicted and further using this temperature evolution as an input parameter it is possible to understand the evaporation rate as a function of time and can be correlated to the experimental ToF spectra. More details are explained in next section.

### 3.4.2 Numerical calculations of temperature evolution

As explained earlier in chapter 1, the field evaporation of oxides (and more generally of non-metallic samples) is a complex physical process which led to a long debate in the APT community for over a decade. As it was recently reviewed in Refs.[19,21] two kinds of evaporation behaviors are experimentally reported during the analysis of non-metallic samples: a fast evaporation and a long (and sometimes delayed) evaporation. The physical origin of the fast evaporation is under discussion and photo-ionization [22,23], optical field process and non-equilibrium thermal process are proposed [24–26]. However, the long and delayed evaporation is thermally activated evaporation after the interaction with the laser. This explanation is also widely accepted in atom probe community [19,21]. In this regard, the total number of ions evaporated with respect to time ( $N_{ions}(t)$ ) follows an Arrhenius law [27] :

$$N_{ions}(t) = \kappa \exp(-Q/k_B T(t)) \quad (3.1)$$

where,  $\kappa$  depends on the number of kink site atoms at the tip surface, surface atom vibration frequency, DC field, duration of the evaporation during each pulse and detector efficiency;  $Q$  is the field-dependent activation energy and  $T(t)$  the temporal evolution of the apex temperature. From eq. (3.1), if the temperature at the tip surface decreases slowly a long evaporation process is experimentally reported. A schematic representation of the temperature evolution and the related evaporation rate is reported in fig. 3.10(a) and (b) respectively. The blue curve represents the heating and cooling process when the absorption is localized near tip apex, while the red curve is for absorption located far from the tip apex.

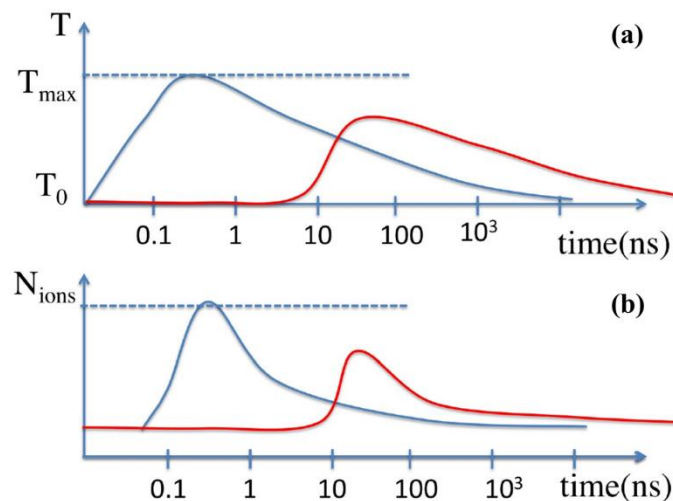


**Figure 3.10** : Temperature evolution at the tip apex (a) and associated number of evaporated ions per pulse  $N_{ions}$  (b) for an absorption located at the apex (blue line) and far from the apex (red line).

From fig. 3.4(c), we can note that the maximum of the delayed evaporation is observed about 100ns after the fast evaporation process (narrow peaks in ToF spectrum) for each peak. Owing to the heating of the sample due to Au-NP's absorption we considered that the sample is heated to around 400K, the thermal diffusivity of the MgO at this temperature is reported as  $D = 8 \times 10^{-2} \text{ cm}^2/\text{s}$  [28]. Considering the tip as nanowire [20], if the sample is heated in a region at a distance  $z_0$  from the apex, the time required to reach this heat at the tip apex and, hence, induce the evaporation of surface atoms is:

$$\tau = \frac{z_0^2}{D} \quad (3.2)$$

From eq. (3.2), considering  $\tau = 100 \text{ ns}$ , the value of  $z_0$  obtained is around  $1 \mu\text{m}$ . This value is quite close to the length of the tip shown in fig. 3.8(b), i.e.  $1.5 \mu\text{m}$ . This

again signifies that the delayed evaporation observed in case of shorter tip (fig. 3.4(c)), can be due to the contribution of second heating zone situated far from the apex due to absorption of metallic W-pretip.

To evaluate the temperature evolution at the tip apex due to these two heating regions, we use a 1D model, considering the tip as a nanowire. The two heated zone are described by two Gaussian functions with amplitude  $A_1$  and  $A_2$ , and width  $\omega_1$  and  $\omega_2$ , respectively, as schematically shown in Fig. 3.11(d). The first Gaussian function is centered on the tip apex, the second on a distance equal to  $z_0$ . These variables can be deduced from the absorption maps obtained with the FDTD calculations as shown in fig. 3.7.

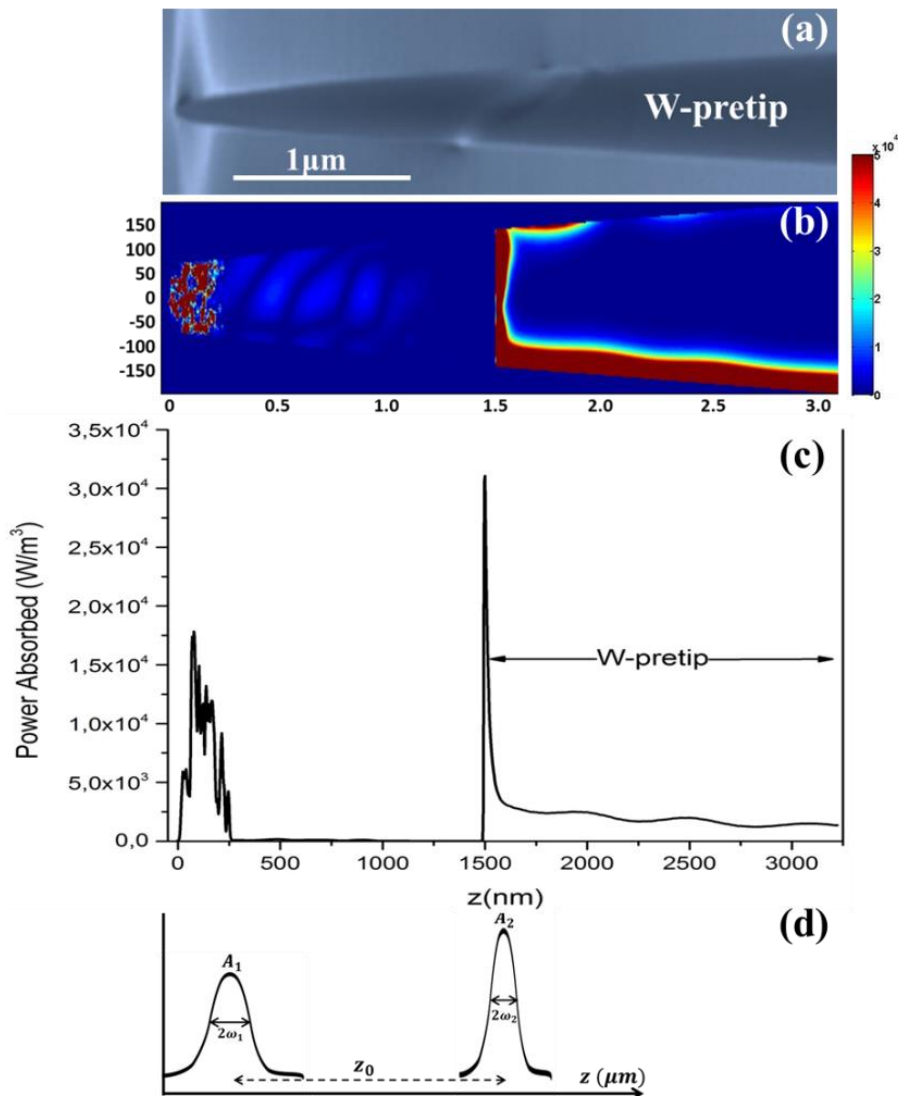


**Figure 3.11** : SEM image of the sample, (b) Absorption map in the incident plane ( $y, z$ ). The color bar corresponds to the power absorption density for an incoming intensity of  $1 \text{ W/m}^2$ . (c) Absorption density profile along the tip computed from absorption map shown in (c) and (d) Schematic representation of the two Gaussian heated zones along the tip axis ( $z$ ).

By solving analytically the heat diffusion equation the temperature evolution at the tip apex can be obtained as [20] :

$$T(t) = T_{max} \left[ \frac{A_1}{\sqrt{1+\frac{tD}{\omega_1^2}}} + \frac{A_2}{\sqrt{1+\frac{tD}{\omega_2^2}}} \exp\left(-\frac{z_0^2}{2\omega_2^2(1+\frac{tD}{\omega_2^2})}\right) \right] \quad (3.3)$$

with,  $T_{max} = T_0 + T_{rise}$ , the maximum temperature equal to the sum of the base temperature  $T_0 = 70\text{K}$  and the increase of the temperature due to the laser heating:  $T_{rise}$ . This temperature evolution is introduced in Eq. (3.1) to calculate the number of atoms evaporated for each laser pulse. The comparison between the experimental TOF spectra and the theoretical prediction of  $N_{ions}(t)$  is reported in Fig. 3.12.

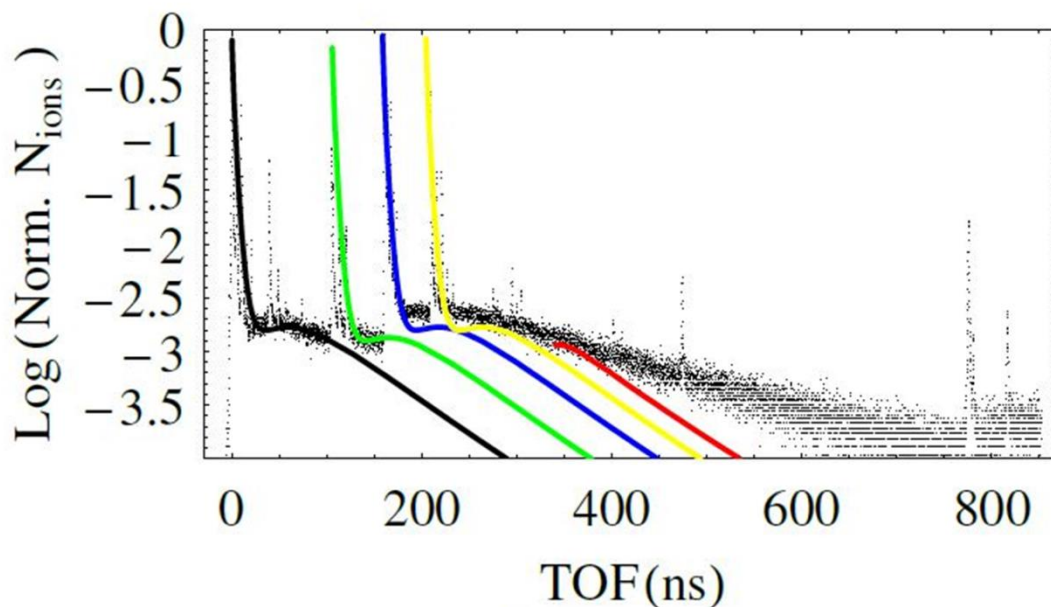


**Figure 3.12** : Log of the normalized number of detected ions  $N_{ions}$  as a function of ToF at 515nm wavelength for the 1.5 $\mu\text{m}$  length sample. The origin of ToF corresponds to the ToF of  $\text{Mg}^{2+}$  ions. Black, green, blue and yellow lines correspond to the evolution of  $\text{Log}(N_{ions})$  from Eq.(3.1) and Eq.(3.3) with:  $\omega_1 = \omega_2 = 100 \text{ nm}$ ,  $A_1=1$ ,  $A_2=1.5$ ,  $D=7 \times 10^{-2} \text{ cm}^2/\text{s}$ ,  $Q=0.1 \text{ eV}$ ,  $T = 450\text{K}$  and  $z_0 = 1 \mu\text{m}$ . Red line is obtained by the sum of blue and yellow line.

The value of the width of first heating zone  $\omega_1$  is fixed to 100 nm considering the Au concentration profile along the depth as can be seen from HAADF-STEM image and 1D concentration profile obtained by APT analysis reported in Fig 3.15. The value of width of second heating zone,  $\omega_2$  is obtained from the numerical absorption-density profile (see Fig. 3.11(c)), considering that the absorption map of Fig. 3.11(b) corresponds to the heated map for free carriers (electrons in the case of W pretip) and taking into

account the electron diffusion depth  $L_c = 70\text{nm}$  for an electronic temperature lower than 2500K [29], an increase of the size of the second heated zone up to 100 nm is estimated.

As can be seen from fig. 3.12, a good qualitative agreement between the experimental TOF spectra and the prediction of the  $N_{ions}$  evolution by the thermal model, is obtained using, as adjustable parameters, the diffusivity  $D = 7 \times 10^{-2} \text{ cm}^2/\text{s}$  and the ratio  $(\frac{Q}{k_B T_0})$ . The value of the thermal diffusivity is in good agreement with the values reported in the literature for MgO at  $T=450\text{K}$  [28]. Hence, using  $T_{max.} = 450\text{K}$ , a value of  $Q=0.1\text{eV}$ , the activation energy, is obtained which is expected for the high field condition fixed during the analysis, which can be characterize by the charge state ratio of the Mg ions ( $\text{Mg}^+/\text{Mg}^{2+} = 5\%$ )[30].

On long time scales (more than 200 ns after each TOF peak) the theoretical model predicts a faster decrease of the number of evaporated ions than what is experimentally reported. However, adding the contributions of each peak to the long evaporation process, a better agreement is also reported at long time scales, as shown in Fig 3.12 with a red curve.

On the other hand for the  $4.2\mu\text{m}$  long tip, as observed experimentally by pushing the second heating zone far from the apex we have observed the suppression in delayed evaporation and improved S/N ratio (see fig. 3.9). Similarly, the calculations of  $N_{ions}$  as a function of ToF are carried out. Since the experimental conditions were comparable in both the cases (for  $1.5\mu\text{m}$  and  $4.2\mu\text{m}$  long tip), all the parameters used previously ( $Q$ ,  $\omega_1$ ,  $\omega_2$ ,  $A_1$ ,  $A_2$ ,  $D$ , and  $T_{max.}$ ) kept similar except changing the value of  $z_0$  from  $1\mu\text{m}$  to  $4\mu\text{m}$ . Only changing  $z_0$ , a good qualitative agreement is reported between experimental ToF spectra and the prediction of 1D thermal model and is presented in fig. 3.13. The calculations does not show any sign of delayed evaporation in this case, the calculated evaporation rate decreases with respect to time as observed for the experimental ToF spectra.

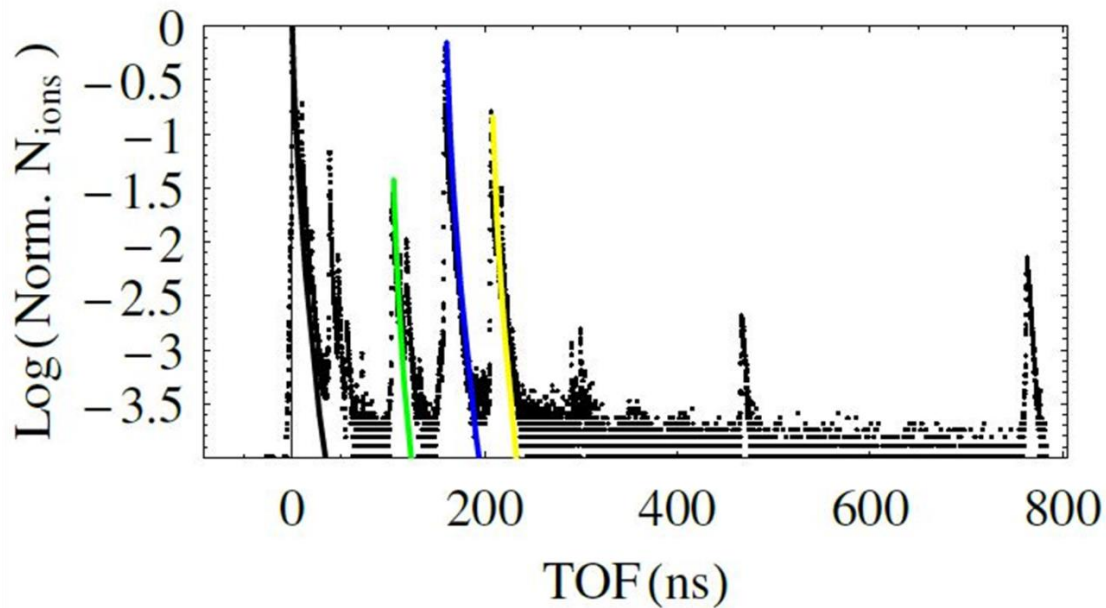


**Figure 3.13** : Log of the normalized number of detected ions  $N_{ions}$  as a function of ToF at 515nm wavelength for the 4.2 $\mu\text{m}$  length sample. The origin of ToF corresponds to the ToF of  $\text{Mg}^{2+}$  ions. Black, green, blue and yellow lines correspond to the evolution of  $\text{Log}(N_{ions})$  from Eq.(3.1) and Eq.(3.3) with:  $\omega_1 = \omega_2 = 100 \text{ nm}$ ,  $A_1=1$ ,  $A_2=1.5$ ,  $D=7 \times 10^{-2} \text{ cm}^2/\text{s}$ ,  $Q=0.1\text{eV}$ ,  $T = 450\text{K}$  and  $z_0 = 4 \mu\text{m}$ .

Both these experimental as well as numerical calculations support the idea that keeping the second heating zone farther from the apex is a good solution to improve the S/N ratio by suppressing the delayed evaporation. This analysis also suggests that, the contribution of W-pretip support cannot be neglected, particularly when the length of the tip is shorter than 2 $\mu\text{m}$ .

This analysis shows that, the optimal length for which delayed evaporation is not expected can also be qualitatively determined before performing the actual atom probe experiment using one dimensional thermal model along with FDTD calculations and taking into account the intrinsic optical and thermal properties of the material. These results are very important to improve the sensitivity of the APT for this technologically important class of metal-dielectric composite materials.

### 3.4.3 Long and delayed evaporation at 343nm and 1030nm

Considering the different wavelengths used in an atom probe experiment, it will be interesting to see the effect of wavelength on this long and delayed evaporation. In this regard, the atom probe experiments were performed at  $\lambda=343\text{nm}$  and  $\lambda=1030\text{nm}$ . The analyses conducted on short (1.5 $\mu\text{m}$ ) and long (4.0 $\mu\text{m}$ ) tips are compared. The ToF spectra obtained with UV and IR analyses are shown in fig. 3.14(a) and (b) respectively.

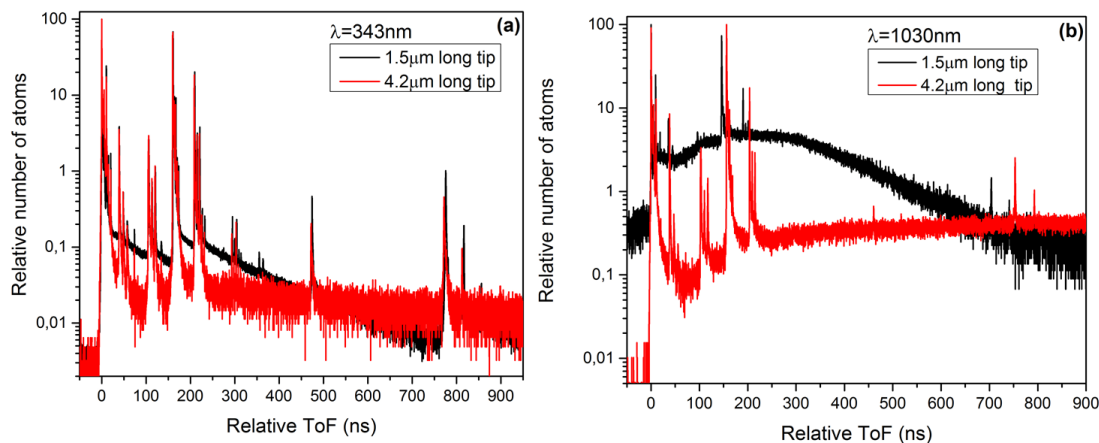


**Figure 3.14** : Comparison of ToF spectra of 1.5 $\mu\text{m}$  long tip and 4.2 $\mu\text{m}$  long tip obtained after atom probe analysis carried out at (a) UV (343nm) and (b) IR (1030nm) wavelength. All analyses were carried out in high density Au-NPs region and the experimental conditions were similar. The laser power used for UV analyses was around 1.4mW and that of for IR analyses was 30mW.

In case of IR analysis, ideally both MgO as well as Au NPs are transparent to the incident radiation but not the W-pretip support. Thus most of the laser light is absorbed by the W-pretip which creates a strong heating zone at the W/MgO interface only. When the W/MgO interface is quite close to the tip apex (1.5 $\mu\text{m}$ ) the magnitude of this delayed evaporation is found to be increased which further signifies the increased magnitude of temperature rise. While on the other hand, when this interface is far from the apex (4.2 $\mu\text{m}$ ), magnitude of this delayed evaporation is decreased by factor of 15-20, i.e. improved signal to noise ratio. Both situations are shown in fig. 3.14(b) for short (black curve) as well as long tip (red curve). The striking feature of this analysis is the position of hump or delayed evaporation on time scale is strongly dependent on the distance of W/MgO interface from the tip apex. For short tip it is closer to the fast evaporation peak (300ns) than for the long tip (approximately 900ns). This time-delay also corresponds to the ratio between length of the short and long tip, which further verifies the significance of contribution of W-pretip absorption. In view of the lower absorption of IR wavelength the laser power used to achieve the desired evaporation rate as that of used in UV and Green wavelength analysis is 30 times higher (30mW).

However, in case of UV analysis as shown in fig. 3.14(a), both short as well as long tip doesn't show any sign of delayed evaporation apart from the fact that the signal to noise ratio is improved in longer tip as in the case of Green and IR analysis. In addition, at longer time scales (afterwards 200ns); the evaporation rate decreases relatively faster in short tip than the long tip. This is due to the higher thermal diffusivity

of W-pretip support compare to the MgO. This behavior of ToF observed in case of UV analysis corresponds to the temperature profile schematically shown in fig. 3.4(b), where strong absorption in near apex region creates temperature rise in this region which further decreases along the tip apex creating the decaying tail in ToF spectra. This can be due to the magnitude of second heating zone (W-absorption) is less than that of at the apex. Though this behavior is difficult to understand only on the basis of ToF spectra, but qualitative conclusion can be drawn. The detail explanation can be given using the absorption density profiles calculated using FDTD at this wavelength and are explained in further section of this chapter (section 3.5.2.2).

### **3.5 Influence of the analysis depth**

As we know from the STEM images, the distribution and density of Au-NPs along the depth of the sample is not uniform. To study the effect of analysis depth on the field evaporation rate with respect to ToF of evaporated ions, we have carried out several experiments at different regions of Au-concentration along the depth. The results are presented in this section.

#### **3.5.1 Region before Au-NPs**

The delayed evaporation was also reported when optically strong absorptive material is only few 100's of nm away from the tip apex. In this regard, a tip of Au-NP's embedded in MgO matrix is prepared with length of around 4 $\mu$ m. But this time the high density Au-NP's region is sandwiched between the dielectric MgO matrix and the highest concentration of Au-NP's is observed around 330nm from the apex. This suggest that the distance between two heating zone,  $z_0$ , is 330nm. The value of  $z_0$  is estimated from the HAADF-STEM image as well as the 1D concentration profile plotted after the 3D reconstruction of the data obtained from atom probe analysis as shown in fig. 3.15.

In order to understand the temperature evolution at the tip apex in this case, a schematic diagram of the tip along with the HAADF-STEM image is represented in fig. 3.16. In this figure the expected temperature profile with respect to time is also presented schematically for better understanding. The absorption at near apex region due to the strong DC field [31] and the absorption due to Au-NP's far from the apex create heated zones in these two regions. Due to these two heated zones the resultant temperature at the

apex of the tip will not show a decreasing trend with respect to time rather an increase in temperature after few nanoseconds (ns) as schematically shown in fig. 3.16(c).

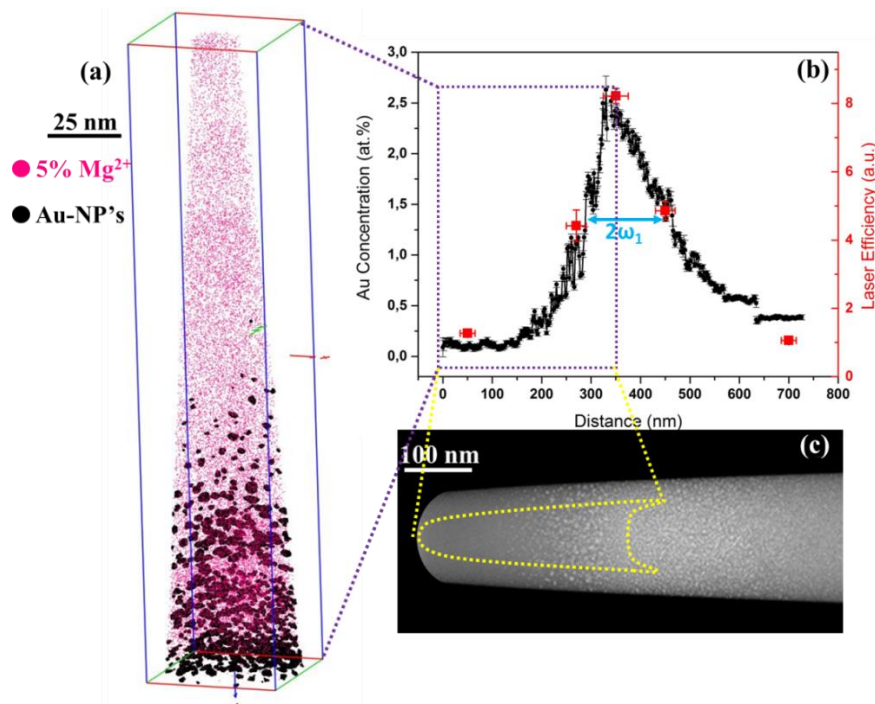


**Figure 3.15** : (a) 3D reconstructed volume obtained from the data acquired after atom probe experiment; only 5% of  $Mg^{2+}$  ions are shown for clarity, (b) corresponding 1D concentration profile; purple dotted rectangle shows the concentration profile for 3D reconstructed volume shown in (a) as well as the volume analyzed by atom probe highlighted by yellow dots in (c), (c) HAADF-STEM image of the Au-MgO tip. The laser efficiency (L.E.) of Green laser (515nm) as a function depth is shown by Red data points in (b).

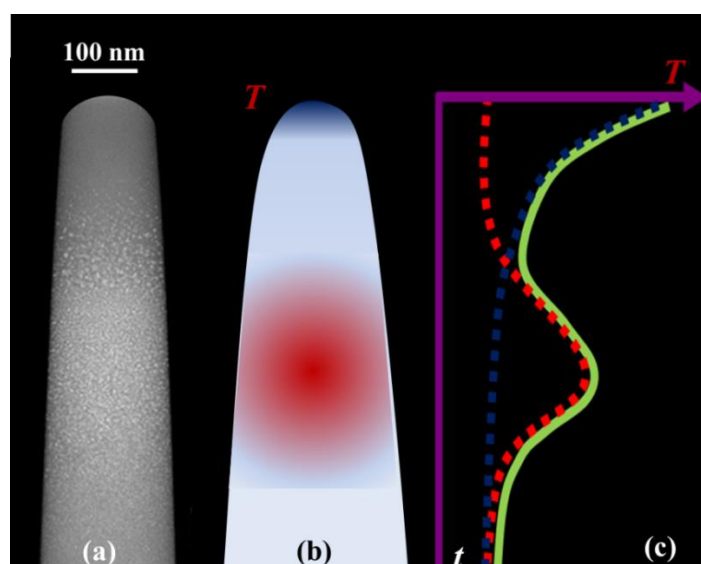


**Figure 3.16** : (a) HAADF-STEM image of the tip, (b) Schematic representation of the temperature along the tip after illuminated by Green light and (c) corresponding tip apex temperature evolution; Blue dotted curve : temperature due to near apex absorption, Red dotted curve : temperature due to Au-NP's absorption, Green solid curve : Resultant variation of temperature with respect to time,  $t$ .

The atom probe analysis was carried out on this tip with Green wavelength. The experimental conditions used were similar to previous analysis performed, i.e. constant flux of 0.005-0.009 at./pulse, base temperature of 70K. Two sets of measurements were carried out, one at laser power of 1mW and other at 0.2mW and to do so, the applied voltage was increased from 7.2kV to 9.3kV to keep the detection rate constant. The ToF spectrum is then plotted after collecting nearly 1.5 million atoms for each data set and is presented in fig. 3.17.

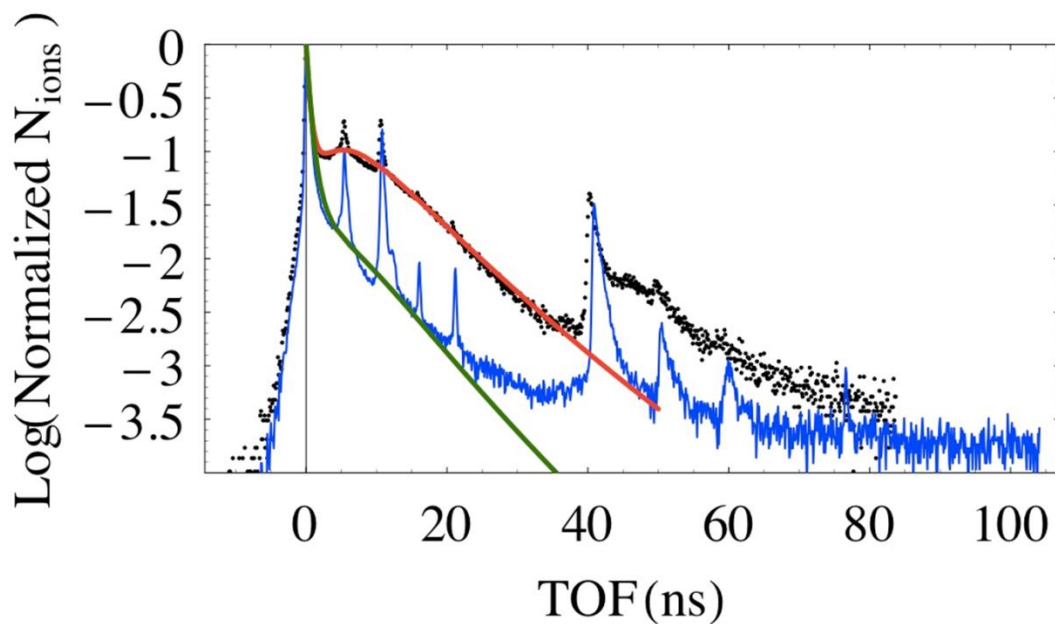


**Figure 3.17** : ToF spectra obtained after analyzing the pure MgO region before Au-NP's. Black dotted curve is for the analysis carried out at 1mW laser power and the blue solid curve is at 0.2mW laser power. The red and green lines correspond to the evolution of  $\text{Log}(N_{\text{ions}})$  from Eq. 3.1 and Eq. 3.3 with:  $\omega_1 = \omega_2 = 100\text{nm}$ ,  $A_1 = 1$ ,  $D=7 \times 10^{-2} \text{ cm}^2/\text{s}$ ,  $Q = 0.1\text{eV}$ ,  $T = 170\text{K}$ ,  $z_0=330 \text{ nm}$  and  $A_2 = 1.5$  (for red line) and  $A_2 = 1$  (for green line).

As reported in TOF spectrum obtained at 1mW laser power (black dots), the delayed evaporation happens a few ns after the fast evaporation and it is due to the strong absorption of Au NPs located 330nm far from the apex. Using the 1D thermal model, the TOF spectra can be adjusted changing the distance  $z_0=330 \text{ nm}$  and the  $T_{\text{max}}=170\text{K}$ . In fact, the laser power used (1mW) is slightly lower than the laser intensity used in previous analysis (1.5mW) reported in Fig. 3.9. Moreover, we measure experimentally the laser efficiency (L.E.) in 5 different regions along the sample, having different concentrations of Au. The laser efficiency is calculated by analyzing the variation of applied voltage with the laser power at constant detection flux [32]. As shown in Fig. 3.15(b), the L.E. follows the Au concentration profile. The L.E. in the top-most region of analysis is decreased by factor of 4 when compare to the high density Au region analysis. This

decrease of the L.E. is the reason to use the  $T_{max}$  of 170K for the analysis of the region without Au and  $T_{max}$  of 450K for the analysis of high density Au region.

On the other hand, when the ToF spectrum is obtained at 0.2mW of laser power (blue solid curve) the absence of delayed evaporation is observed. The suppression of delayed evaporation in this case is due to the increased contribution of first heated zone compared to the contribution of Au-NPs region (second heated zone). It was recently reported that the absorption of the laser energy at the apex of oxides is enhanced by the DC field [31]. The increase of the DC field (applied voltage increased to 9.3kV from 7.2kV) induces a decrease of the laser power from 1mW to 0.2mW, in order to work at constant evaporation rate. This increase of the static field allows the suppression of the delayed evaporation. A good agreement between the experimental TOF spectrum (blue line) and the prediction of the 1D thermal model (green line) is obtained by decreasing the value of the amplitude of the second heating zone  $A_2$ , from 1.5 to 1, due to the lower contribution of the second heated zone compared to the first one.

In summary, when the pure MgO located before the Au-NPs implanted region is analyzed, we have showed experimentally and numerically that the physical origin of the delayed evaporation is due to the absorption of the Au NPs illuminated by the laser beam. Even if laser beams of a few microns can be focused on the samples, this beam-size reduction is not enough to always suppress the delayed evaporation. Eventually, the absorption of all the illuminated phases (metallic, non-metallic) has to be taken into account, with a particular attention at high absorption phases such as metallic NPs or metal/oxide interfaces. We show that the increase of the DC field enhances the apex absorption reducing the thermal noise due to delayed evaporation, even when absorbing phases are located a few hundreds of nm away from the apex.

### 3.5.2 Inside the Au-NPs region

In order to perform this study, an atom probe analyses were carried out at different Au concentrations along the depth of the tip. The analyses were carried out in three different wavelengths available in the LaWATAP (UV-343 nm, Green-515 nm and IR-1030 nm) to see the effect of wavelength. The experimental conditions for all the analyses were similar with constant detection rate of 0.005-0.009 at./pulse, base temperature of 70K. The experimental procedure employed in this case is as follows. Every analysis performed in different regions begin with UV light and laser power of 1.0mW, once the desired detection rate is achieved, at least one million atoms are collected. After this

analysis, the wavelength of the analysis is changed to Green by keeping the applied voltage same as that of the end of the previous analysis in UV and adjusted the laser power in order to have the desired detection rate. Similarly, after collecting nearly one million atoms the wavelength is switched to IR and adjusted the laser power. The data collected is then plotted as function of ToF of evaporated ions and compared with the analyses carried out in different spatial regions along the depth. For UV and Green analyses it was possible to reconstruct the data in 3D as well for different regions of Au concentration.

The ToF spectra obtained for UV ( $\lambda=343\text{nm}$ ) wavelength at different spatial positions along the depth are compared and presented in fig. 3.18. The results obtained at Au concentrations of 0.3, 1.0, 2.5 and 0.5 in at.% are compared, where 2.5 at.% is the maximum Au concentration observed in the analysis (see fig. 3.15). The distribution of Au-atoms after reconstruction is also shown for the respective regions. It is possible to distinguish between the individual nanoparticles only when the density of nanoparticles is less, like the one showed for 1 at.% Au concentration in fig. 3.18. As shown in high resolution cross-sectional STEM image (see fig. 3.1(b)), in high concentration region the distance between two Au-NPs is small and due to this reason, during evaporation the trajectories of evaporated Au-ions intermix with each other owing to the local magnification effect as explained earlier. The current reconstruction protocol doesn't take into account this artefact which leads to the poor spatial resolution in case of high dense Au-region and therefore it is difficult to distinguish between individual Au-NPs in this region.

As far as ToF spectra are concern, the evaporation rate decreases successively with respect to time, from topmost analysis to the last analysis. In case of last analysis (Green curve), the amount of Au-NPs below the tip apex is very less, while for the topmost analysis (black curve) the whole layer of Au-NPs is existing below the tip apex. So that when the tip is illuminated with UV light, this whole Au-NPs layer will absorb the light more efficiently than the pure MgO which is close to the tip apex for the analysis shown by green curve. Hence, the heated zone will be larger (around 400 nm) for the analysis in the topmost region and smaller (around 100 nm) for the bottom analysis (reported with a green line in Fig. 3.18). Therefore, the apex tip temperature will cool down faster in case of last analysis compare to the topmost analysis. This eventually results in the decrease in the TOF-peak width as the Au-NPs region is progressively removed along the depth.

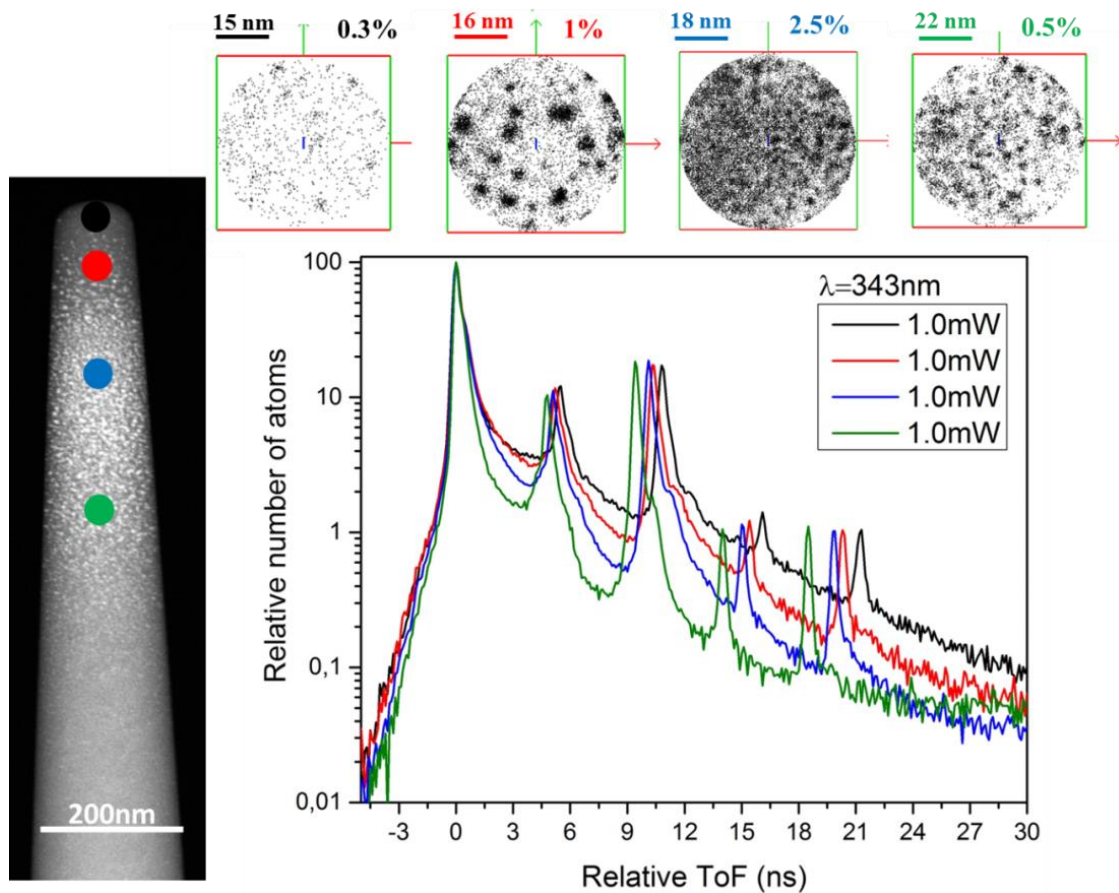


**Figure 3.18** : Comparison of ToF spectra obtained at different spatial regions for  $\lambda=343\text{nm}$  along the depth of the tip as represented by different colored circles in HAADF-STEM image of the tip. The 2D detection hit maps shown above represents the Au-atoms (black dots) distribution in these respective regions with indication of Au concentration in at.%

In similar way, the analysis is carried out in Green ( $\lambda=515\text{ nm}$ ) wavelength, the ToF spectra and the 2D detection maps of Au-atoms in different regions are presented in fig. 3.19. In this case also the Au-NPs in low dense region (1.0 at.% of Au) can be visualized after 3D reconstruction of the data obtained. Considering the ToF spectra plotted for different regions, the change in the topmost analyzed region (black curve) and the last analysis (green curve) is more significant when compare to the UV analysis.

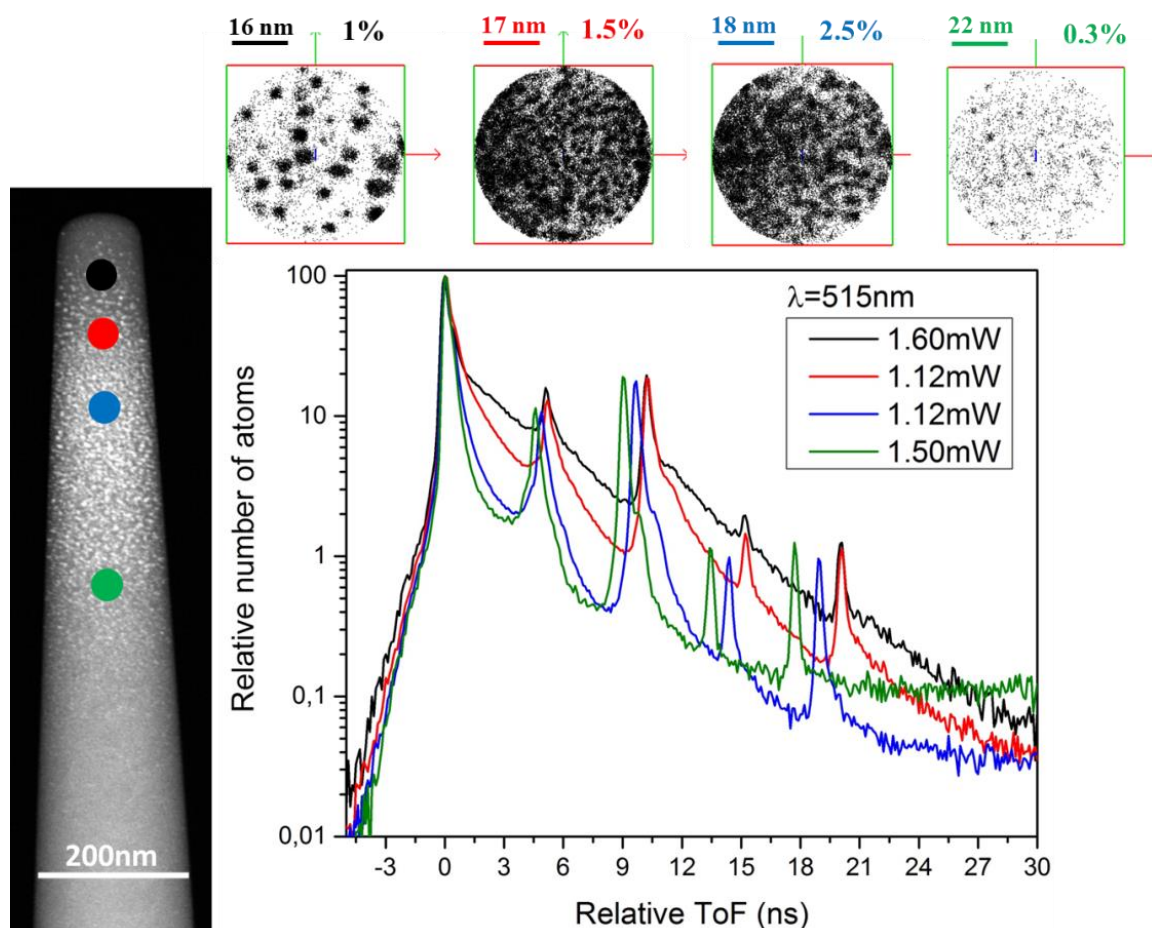


**Figure 3.19** : Comparison of ToF spectra obtained at different spatial regions for  $\lambda=515\text{nm}$  along the depth of the tip as represented by different colored circles in HAADF-STEM image of the tip. The 2D detection hit maps shown above represents the Au-atoms (black dots) distribution in these respective regions with indication of Au concentration in at.%

The explanation for this significant change can be given on the basis of analysis carried out in the previous section of this chapter, i.e. the two heating zone model. In the very first analysis (black curve), the second heating zone created by the highest Au-concentration is nearly 200 nm away from the tip apex, this distance is quite close to see a well separated second peak in ToF spectrum due to delayed evaporation as observed in fig. 3.17, when the distance between two heating zones were 330nm. Although, it is difficult to separate the contribution of second heating zone, the slow decrease in evaporation rate is consequence of the contribution of this second heating zone. Due to this reason the analysis carried out before the highest Au-concentration region (2.5 at.%) shows (black and red curve) the slow decrease in evaporation rate owing to slow cooling of the tip apex temperature. When the analysis is carried out at highest Au-concentration or below (blue and green curve respectively), due to absence of second heating zone the evaporation rate decreases faster owing to the faster cooling of the tip apex temperature.

On the other hand, when using the IR ( $\lambda=1030\text{nm}$ ) wavelength, there is no significant change in the ToF spectra whether you carry out the analysis before or at the highest Au-region as reported by red and blue curve respectively in fig. 3.20. This is mainly due to the low absorption of the sample at this wavelength as will be discussed in the next section.

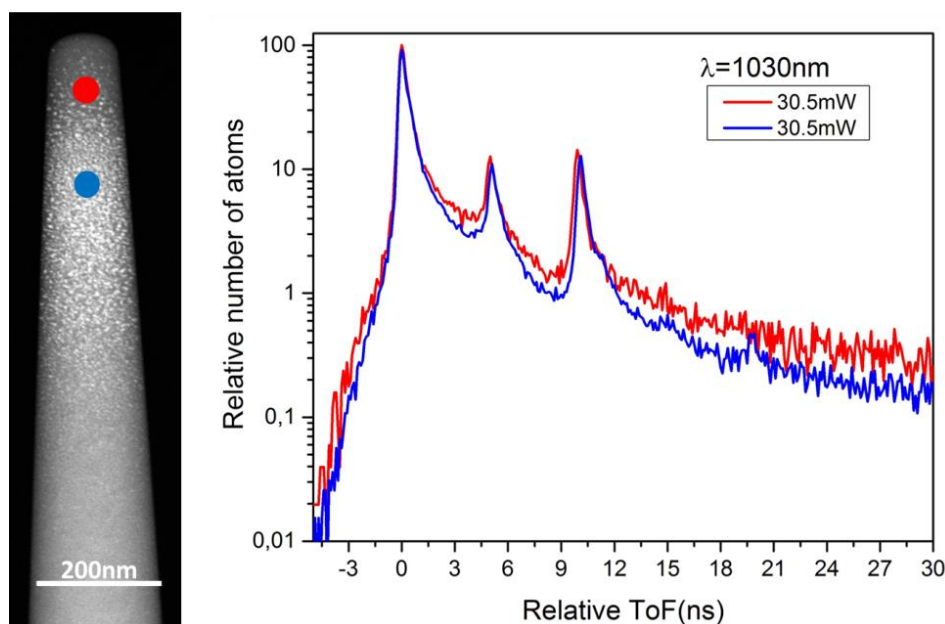


**Figure 3.20** : Comparison of ToF spectra obtained at two different spatial regions for  $\lambda=1030\text{nm}$  along the depth of the tip as represented by different colored circles in HAADF-STEM image of the tip.

As mentioned earlier in this section, each analysis begins with UV wavelength and laser power of  $1.0\text{mW}$  ( $10\text{nJ/pulse}$ ). During switching the wavelength from UV to Green and Green to IR, the applied voltage is kept constant as that of the last analysis so as to have similar field conditions. Then the laser power is adjusted in order to achieve the desired evaporation conditions. With this approach, in every region the change in laser power required to achieve the similar evaporation conditions as that of  $1.0\text{mW}$  UV analysis are reported in the respective figures. In the case of Green analysis one needs slightly higher laser power than that of UV analysis, which is contradictory to the consideration that the Green wavelength gets absorbed more efficiently than UV owing to Au-NPs plasmonic excitation near this wavelength. To understand this behavior we have performed absorption computation on Au-MgO tip using FDTD method as reported previously in this chapter. But instead of using Au-NPs geometry in the simulation, the effective refractive indices were calculated using Maxwell-Garnett effective medium

theory [33]. The calculations of volume fraction and the effective refractive indices were performed by Nicolas Guth, Julien Cardin and co-workers from CiMAP, Caen, France. The volume fraction of Au were calculated from the Au-concentration (in at.%) obtained from the atom probe analysis and is reported in fig. 3.21.

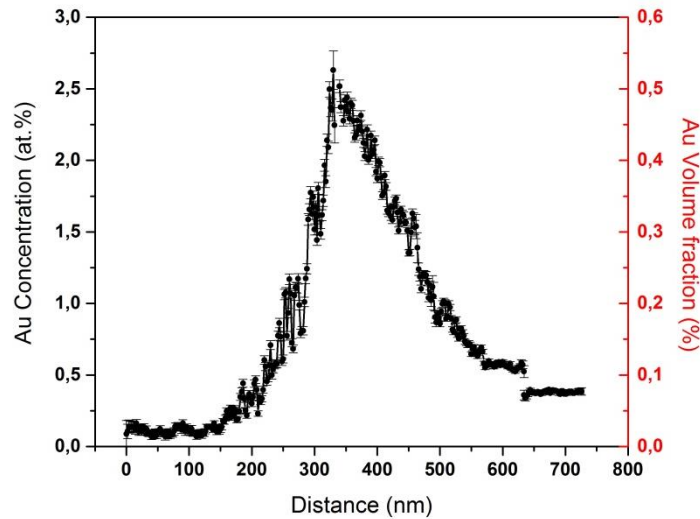


**Figure 3.21** : Au concentration obtained from atom probe analysis, in atomic % and in volume fraction

From fig. 3.21, the maximum Au concentration corresponds to the 0.5% of volume fraction. Using the calculated values of volume fraction, the effective refractive indices at 0.1%, 0.25% and 0.5% of Au volume fractions were calculated and are presented in fig. 3.22

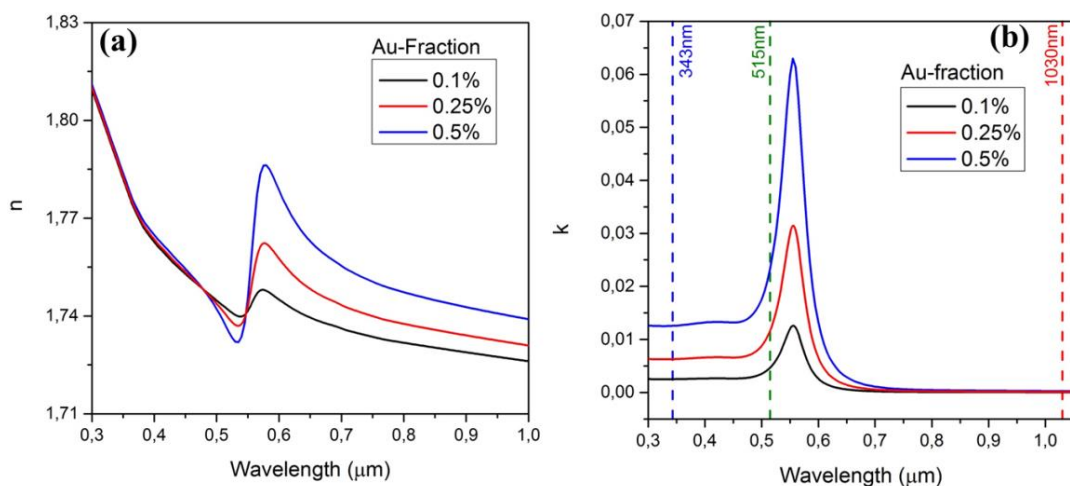


**Figure 3.22** : (a) Real,  $n$  and (b) imaginary,  $k$  part of complex refractive index calculated for Au-NPs embedded in MgO matrix with Au volume fractions of 0.1%, 0.25% and 0.5%.

Taking into account these optical constants the absorption maps and corresponding absorption density profiles of tip shaped samples were calculated using FDTD method and are shown in fig. 3.23.

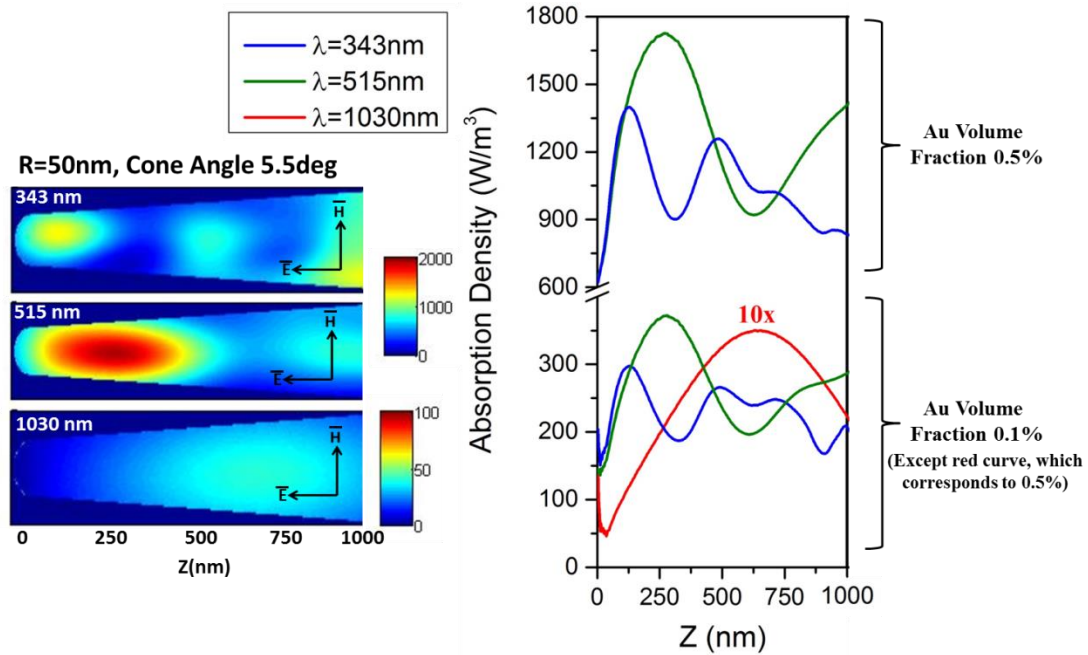


**Figure 3.23** : Absorption maps (left) calculated for tip of radius  $R=50\text{nm}$  and cone angle of  $5.5\text{deg}$  at wavelength of  $343\text{nm}$ ,  $515\text{nm}$  and  $1030\text{nm}$ . The Au volume fraction used to calculate these maps is  $0.5\%$  and the direction of laser incidence is into the paper. The absorption density profile (right) plotted from the absorption maps obtained for Au-fraction of  $0.5\%$  (top curves in the graph) and  $0.1\%$  (bottom curves in the graph, except the red curve which corresponds to  $0.5\%$  of Au fraction)

As shown in the absorption maps and profiles, although the magnitude of absorption is higher in case of Green wavelength, the absorption maximum is more close to the tip apex for UV wavelength. i.e. absorption maxima is observed around  $120\text{nm}$  far from the apex for UV while around  $250\text{nm}$  for Green wavelength. In addition, the absorption zone is narrower in case of UV illumination. The behavior is similar for Au volume fraction of  $0.5\%$  and  $0.1\%$  except magnitude of the absorption is increased for  $0.5\%$  of Au volume fraction.

Considering the case of topmost analysis where Au-NPs region ( $400\text{nm}$  of Au-region) is below the tip apex (case of  $0.5\%$  Au volume fraction), the maximum absorption far from the apex in Green ( $250\text{nm}$ ) raises the temperature far from the apex creating second heating zone. Hence, the ToF spectra obtained from this analysis show large TOF peaks, due to the convolution of the evaporation process induced by the first and second heated zone. However, in case of UV analysis, owing to the absorption near to the apex, the first and second heated are close to the apex and they will be merged.

The consequence of this spatial location of absorption for UV and Green wavelength is the reason to use less laser power in case of UV, even though Green light has higher absorption maximum due to Au-NPs absorption. Hence, also if the Green light

is close to the plasmonic resonance, the efficiency of this wavelength on the evaporation will be lower than in the case of UV light due to the spatial distribution of the absorption maxima along the tip axis. In the case of UV light, the maximum of absorption corresponds with the maximum of Au NPs concentration profile, however, for Green light, for all the analysis reported in fig. 3.19, the maximum of the absorption is away from the region of high Au NPs concentration. Therefore, Green light becomes less efficient than UV light and high laser power has to be used in experimental analysis with Green light. So that, it is a matter of where the absorption takes place instead of how strong the absorption is.

Now we know that in case of UV wavelength the absorption is located near apex region, it is possible to explain why we have not observed the delayed evaporation in case of short tip (fig. 3.14(a)). The strong absorption near the apex reduces the absorption of W-post and hence instead of observing delayed evaporation we have observed the decaying tail of evaporation rate with respect to time.

In case of IR, the absorption is low and even farther (nearly 600nm) from the apex, far away from the region containing Au NPS, for both the analyses reported in fig 3.20. This is the reason why the ToF spectra of fig. 3.20 show no change in for the two different positions in depth.

In summary, the study of ToF spectra at different depths inside the Au-NPs region show that the optical properties of the Au-NPs layer are well described using the Maxwell-Garnett effective medium theory, however to explain the APT results the nanometric geometry of the sample have to be taken into account. Only the coupling between the absorption profile along the tip axis with the change of the refractive index according to the Au content, can explain the behavior reported in ToF spectra at different wavelength and different depths inside the Au NPs layer.

### **3.6 From optical properties to thermal properties**

As explained in chapter 2, when the absorption maps of the sample are established and hence the size of the heated zones are well determined, then the TOF spectra obtained for different wavelength can give information on the thermal diffusivity of the sample, or the temperature rise due to the interaction with the laser.

As we will discuss in details in the next chapter, the change in the thermal diffusivity of oxides matrix adding metallic nanoparticle, is generally of a few % when the

nanoparticles are well separated or when the layer of interconnected NPs is thin compared to the oxide thickness (as in the case of our Au-MgO sample). Hence we can consider the thermal diffusivity of our sample unchanged compared to the case of pure MgO (we already did this assumption in section 3.4 and 3.5). In this case the comparison of ToF spectra obtained under similar experimental conditions (same tip shape, same field and laser conditions) can give information on the enhancement on the absorption and heating at nano-scale, as we will show in the next chapter for Au NPs in Fe<sub>2</sub>O<sub>3</sub> matrix. However, to do that the absorption maps of pure MgO and Au-MgO samples, under high field, have to be well known.

For Au-MgO nanotips we know now how to model the Au NPs layer and its absorption, however, in the case of pure MgO, its absorption under high field is still not well known. Are the maxima located away from the apex strong enough to increase the heated zone? In fact, we know that, at the surface, the dc field enhances the absorption on a thin layer of only a few nanometers.

In order to answer this question, we tried to measure the absorption of a 1  $\mu\text{m}$  long pure MgO tip, by SMS (spatial modulation spectroscopy) technique, introduced in chapter 2, in the framework of the collaboration with the team of Natalia Del Fatti at the “Institut lumière matière” in Lyon.

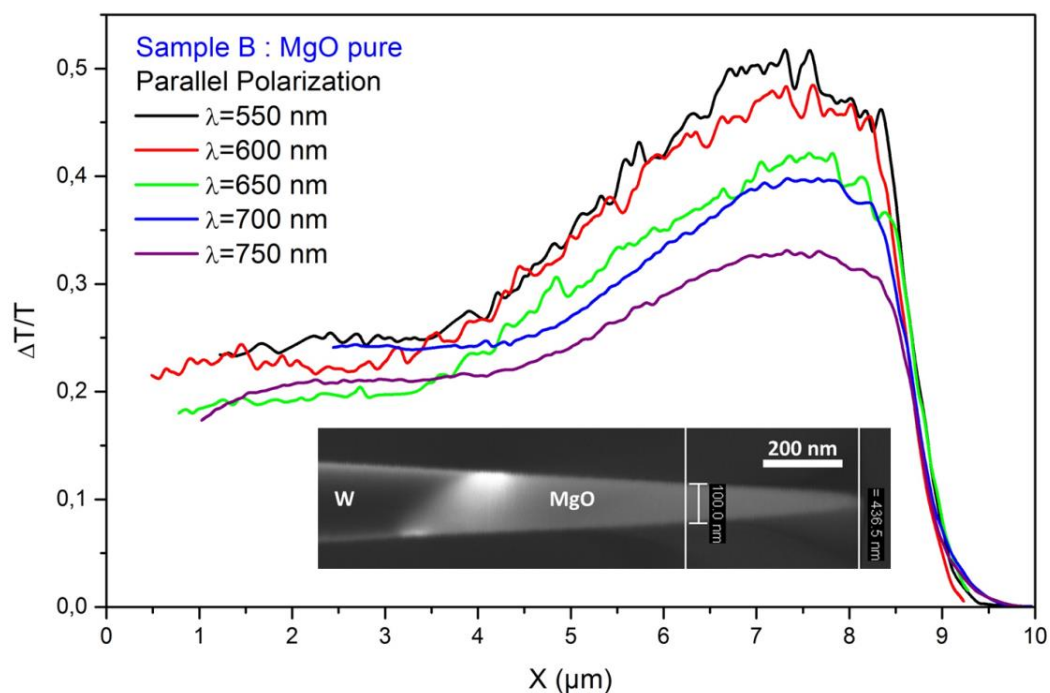


**Figure 3.24:** Relative change in the transmitted light as a function of the laser spot position along the tip axis.  $X=10 \mu\text{m}$  corresponds to the tip apex. The SEM image of the analyzed tip is also shown.

As shown in fig. 3.24, the relative variation in the transmitted signal (which is combination of the absorption and scattering), have almost the same behavior on the first micron (between  $x=9$  to  $x=10$   $\mu\text{m}$  in fig. 3.24), region where the MgO layer is located. We can note that the  $1\mu\text{m}$  MgO tip is attached to a W pre-tip, and the signal reported in fig 3.24 is dominated by the optical response of the W-pretip that is too close to the MgO tip. Further analysis is scheduled on longer MgO tips, in order to have more clear information on absorption maps of pure oxides samples.

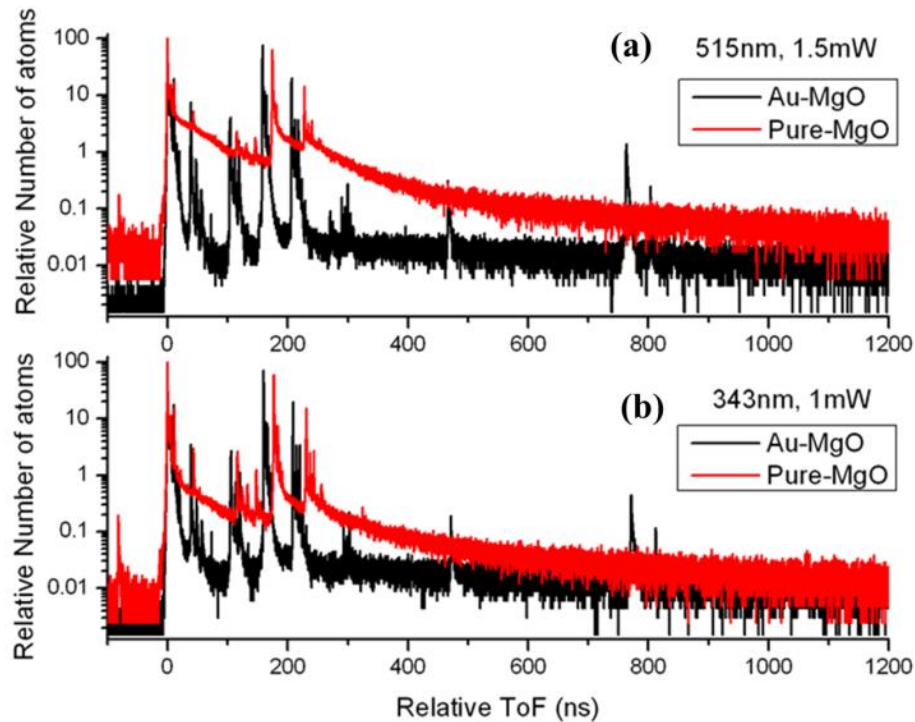


**Figure 3.25:** Comparison of ToF spectra obtained for pure MgO (red curve) and Au-MgO (black curve) at wavelength of (a) 515 nm and (b) 343 nm. The field conditions are comparable in these analyses.

Looking at the ToF spectra of pure MgO and Au-MgO (fig. 3.25) nanotips of  $4\mu\text{m}$  length, we can note that the inclusion of Au decreases the evaporation time (both for UV and for Green light), increasing the sensibility of the APT analysis. A similar trend is observed in case of Au- $\text{Fe}_2\text{O}_3$  sample and will be presented in next chapter.

However, we cannot conclude on the enhancement of the tip heating due to the inclusion of Au-NPs because, even if the field conditions were similar for all the analyses, the size of the heated zone is certainly different between pure MgO and Au-MgO samples. In fact, as shown in fig 3.26, the absorption maps are strongly non-uniform along the tip axis and the maxima of absorption are located around 500 nm from the apex for Green light and 250 nm for UV. When compared to the case of Au-MgO sample as

reported in fig. 3.23 earlier, we note the absorption zones should be larger for pure MgO, hence the ToF spectra cannot be adjusted using similar cooling time (as we did for Fe<sub>2</sub>O<sub>3</sub> samples). For this reason we are not able, at the moment, to draw conclusion on the thermal properties of the Au-MgO sample.

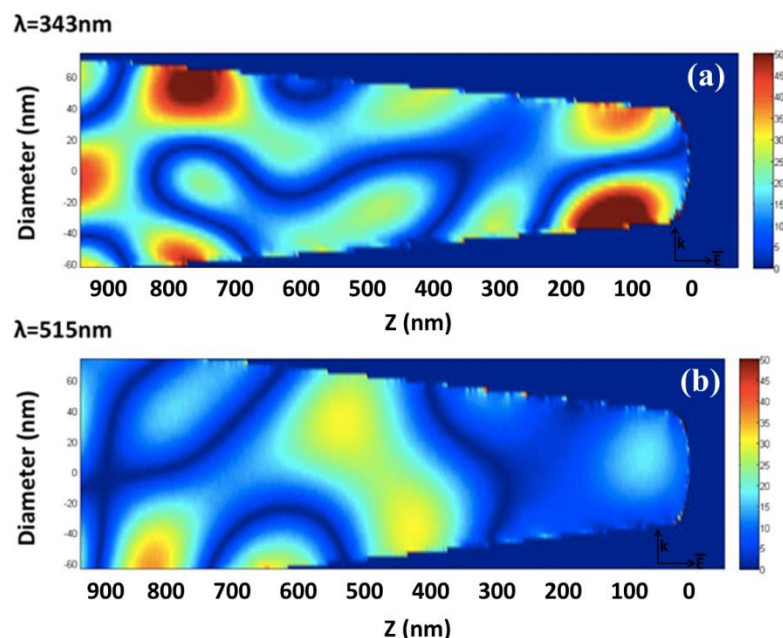


**Figure 3.26** : Absorption maps calculated for Pure MgO tip with  $R=50$  nm and cone angle of  $5.5\text{deg}$ . at wavelength of (a) 343 nm and (b) 515 nm

### 3.7 Analyzing single Au-Nanoparticle

As mentioned earlier the structural characterizations using LaAPT on this sample have been already carried out [12,13] and the composition of Au-NPs in these studies were found to be diluted or impure and attributed the local magnification effect owing to the differences in evaporation field of Au and MgO. Considering the availability of different wavelengths in our atom probe set-up, to understand the effect of the wavelength on the Au-NPs composition we have analyzed the low dense region of Au-NP's using UV and Green wavelength. The results obtained are compared and presented in this section.

The first analysis commenced at UV wavelength, with 1.0mW of laser power. Then keeping the applied voltage same, wavelength changed to Green and the laser power is increased to 1.6mW. After this analysis the laser power in Green is increased to 3.0mW and 5.0mW. Please note that this increase in laser power is compensated by decrease in applied voltage and hence the overall macroscopic field to keep the detection flux constant. The acquired data is then reconstructed in 3D and the composition of Au inside

individual Au-NP is measured using erosion composition profile measurement protocol [34] and are shown in fig. 3.27.

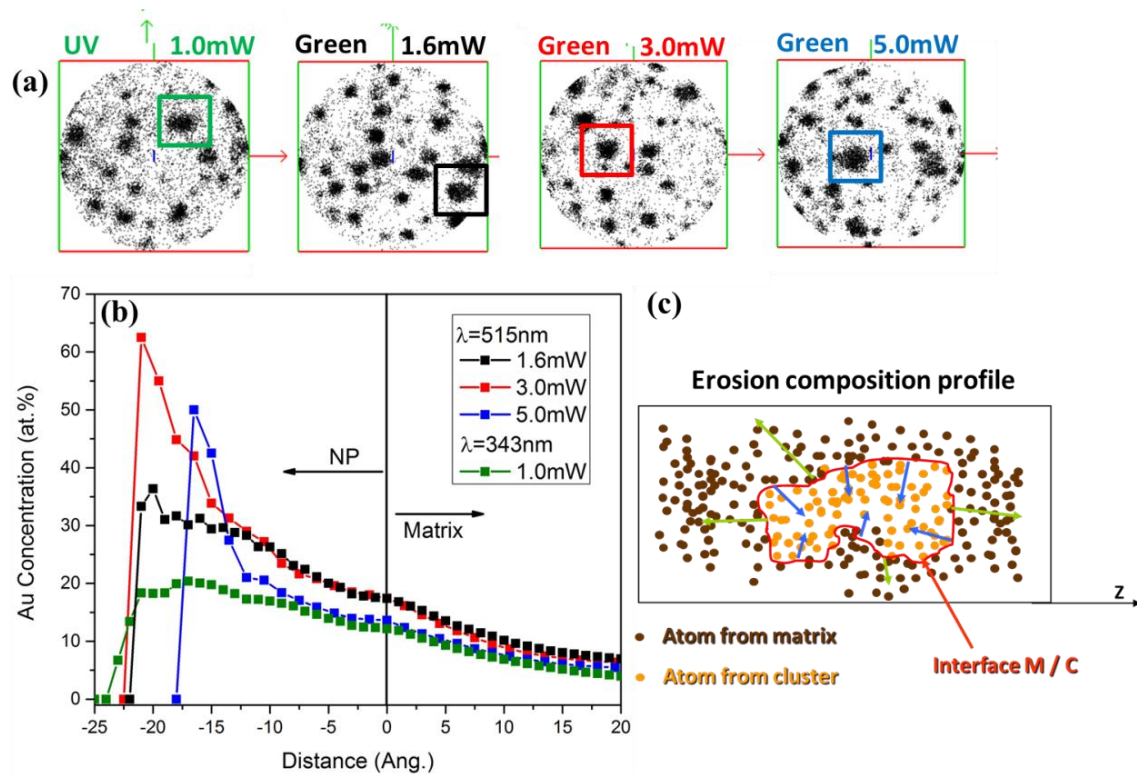


**Figure 3.27 :** (a) 2D representation of Au-atoms (black dots) distribution for UV and Green wavelength analyses with different laser powers for Green analyses, (b) Cumulated Erosion composition profile measured for the single Au-NP highlighted by square in (a), and (c) Schematic showing the composition measurement using erosion protocol.

The erosion profile shown in fig. 3.27(b) represents the concentration of Au inside particular Au-NP. The concentration is measured from the interface between NP and matrix in all 3D and is plotted as function of distance from the interface. The schematic of composition measurement using erosion is also shown in fig. 3.27(c). For UV (1.0mW) analysis, the maximum concentration of Au observed at the core of NP is around 20 at.% which is consistent with the analysis carried out by Devaraj et. al. [12] in UV wavelength (355nm). When the laser wavelength is changed to Green, at 1.6mW of laser power the 3D reconstruction displays that the Au-NPs are more well define than that observed in UV analysis. Moreover, measurement of composition in this case yielded a higher value of Au-concentration (37 at.%). Further increasing the laser power in Green (3.0mW) increases the Au-concentration to the value of 63 at.%. After increasing the laser power to 5.0mW decrease in Au-concentration is evident but higher than that of as observed in 1.6mW analysis. Please note that the size of the Au-NPs analyzed in case of 5.0mW analysis is smaller when compared to the other analyses, this is due to the absence bigger

Au-NPs comparable to the previous analyses in the analyzed volume. The decrease in Au-concentration in case of 5.0mW analysis can be due to this lower size of Au-NPs as previously observed by [13] using UV wavelength. In addition, it is also possible that due to the use high laser power Au-NPs are deformed during evaporation and induces formation of small clusters in 3D reconstruction of atom probe data and can be observed by the increased number of smaller clusters compared to the analyses carried out at 1.6mW and 3.0mW (see fig. 3.27(a)). From this analysis, it is obvious that by increasing the laser power, the Au-concentration inside the NP increases. The explanation for this behavior can be given as follows: As explained in the chapter 2, the field evaporation process depends mainly on two parameters applied electric field and temperature. The dilute composition of Au-NPs is attributed to the local magnification effect which depends on the magnitude of the differences between evaporation field for Au and MgO. When the laser power is increased, it is possible that the local temperature of the individual Au-NP will also increase. At the same time, owing to the lower thermal diffusivity of MgO matrix, the matrix temperature is not raised as high as local Au-NP temperature. To compensate for the high local temperature around Au-NP, the electric field around the NP surface during evaporation will be getting reduced. This will lower the difference between evaporation field of Au and MgO, and eventually the less effect of local magnification.

To support this hypothesis, data obtained from Green wavelength (5.0mW) is used and shown in fig. 3.28. The figure shows the spatial position of Au-NPs is highly correlated with the distribution of  $Mg^+$  ions. The  $Mg^+$  charge state is the low field charge state than  $Mg^{2+}$ , which means at relatively low fields the probability of evaporation of  $Mg^+$  increases. When looking from another orientation,  $Mg^+$  ions are found to be in high concentration just above the NP (middle image in fig. 3.28(b)). In addition, during this analysis, two mass peaks, one at 52amu and another at 80amu were observed. The presence of these peaks is seen only when using the high laser power. The peaks were attributed to the  $Mg_3O_2^{2+}$  and  $Mg_2O_2^+$  respectively. The spatial distribution of these ionic species are also shown in fig. 3.28(bottom).

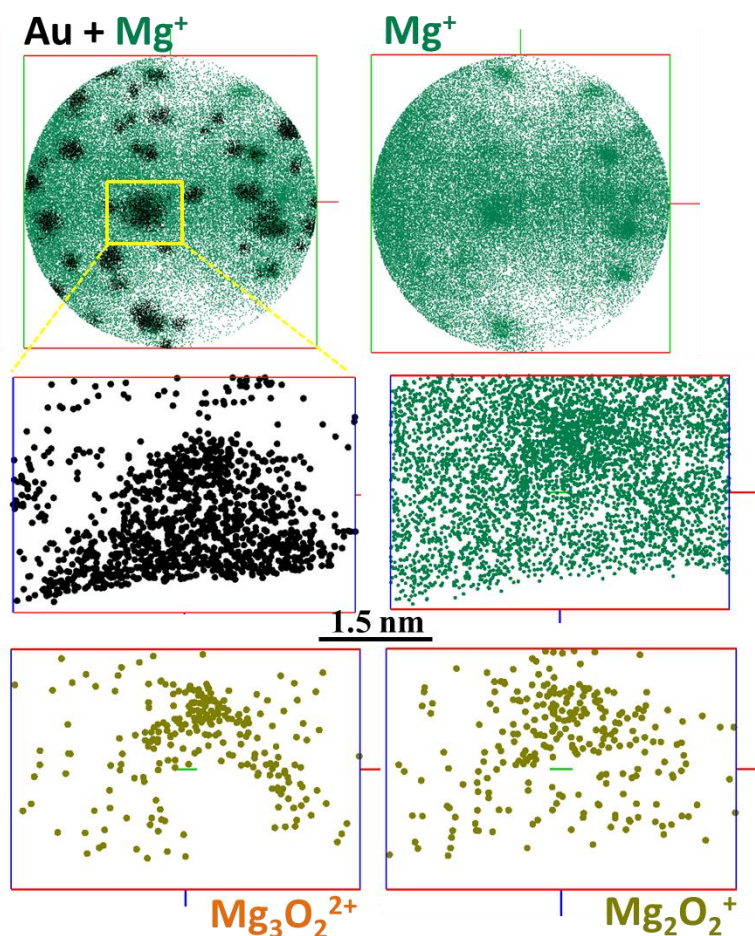


**Figure 3.28** : 3D reconstructed data obtained after analysis carried out Green wavelength and 5.0mW of laser power. (Top) Distribution of Au and  $Mg^+$  ions in (X,Y) plane and in (Y,Z) plane shown in middle. Distribution of  $Mg_3O_2^{2+}$  and  $Mg_2O_2^+$  ions in (Y,Z) plane (bottom)

The  $Mg_3O_2^{2+}$  and  $Mg_2O_2^+$  are found only at the top of the NP, the evaporation of these ionic species from matrix has not been observed. The formation of cluster ions at higher laser intensities (lower field) is observed in case of GaSb [35]. It is possible that, the enhanced surface migration of Mg and O atoms at higher temperatures leads to the formation of cluster ions. So that in our case, if the temperature rise is higher the probability of forming a cluster ion is more, which makes sense with the absent of these molecular species at low laser powers.

In order to understand this behavior in UV wavelength, data from another tip from the low dense region of Au-NPs with increasing laser power is studied and is shown in fig. 3.29. A similar trend is observed in this case as well. At high laser powers, the spatial distribution of Au-NPs and high density of  $Mg^+$  ions is correlated like in the case of Green wavelength. The spatial 2D maps recorded at 5mW and 10mW of laser power are presented in fig. 3.29(a).

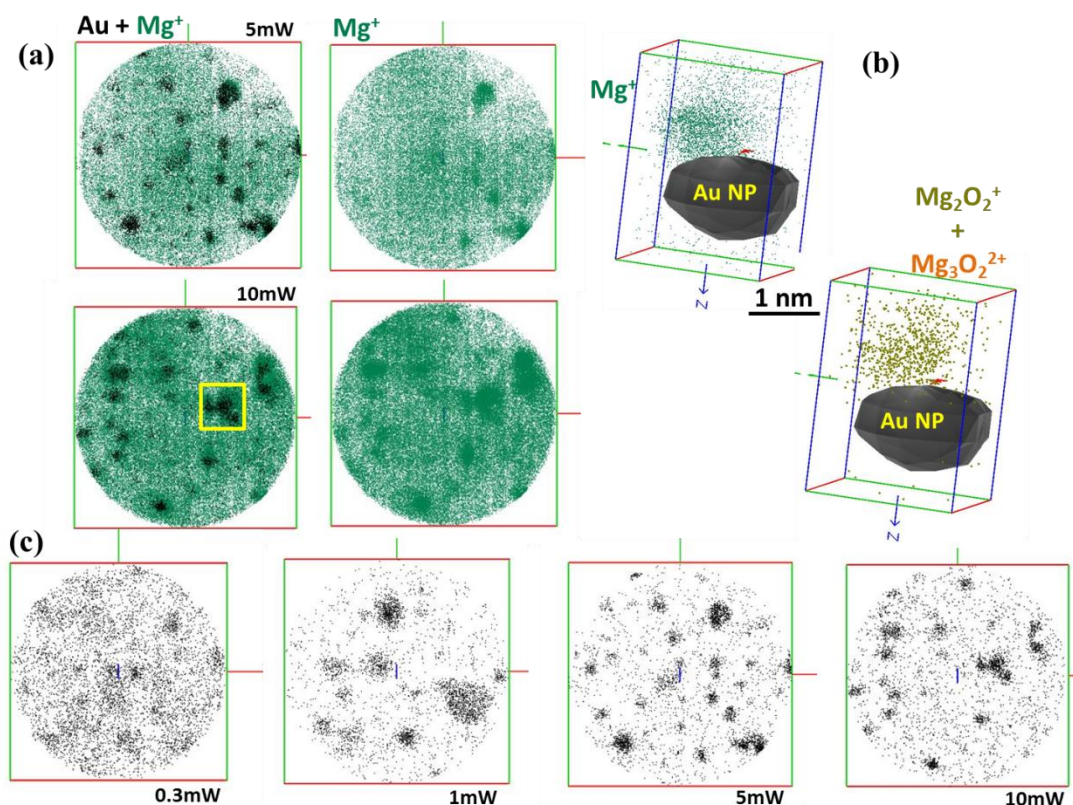


**Figure 3.29 :** (a) 2D Spatial distribution of Au and Mg<sup>+</sup> ions obtained from UV wavelength analysis at 5mW and 10mW of laser power, (b) 3D atomic distribution of Mg<sup>+</sup>, Mg<sub>3</sub>O<sub>2</sub><sup>2+</sup> and Mg<sub>2</sub>O<sub>2</sub><sup>+</sup> ions in the vicinity of Au-NP highlighted by yellow square in (a). The Au-NP here is represented by the 5 at.% iso-surface. (c) 2D atomic distribution maps of Au obtained at different laser powers.

The 3D distribution of Mg<sup>+</sup>, Mg<sub>3</sub>O<sub>2</sub><sup>2+</sup> and Mg<sub>2</sub>O<sub>2</sub><sup>+</sup> ions in the vicinity of the Au-NP from the 10mW data set (fig. 3.29(b)), also displays the similar behavior as observed in green analysis, i.e. the number density of these ionic species is found to be increased above the NP surface. In addition, when the analysis is performed with the low laser power (0.3mW), it is difficult to see the clustering of Au-atoms (fig. 3.29(c)) at all. In this case the field evaporation process is field dominant and hence the effect of local magnification as explained earlier is high in magnitude. While progressively increasing the laser power (and hence decreasing the applied field) leads to the occurrence of Au-atom clustering.

With these analyses down to single nanoparticles, it is clear that the absorption of laser can strongly influence the appearance and composition of the Au-NP. The behavior observed at high laser powers is quite interesting and at the same time useful to understand the evaporation behavior of metal-dielectric composites owing to the localized absorption of metal nanoparticles. However, observation of similar trend in case of UV

and Green wavelength illumination is the key findings of this analysis, although a quantitative description of laser efficiency is not possible at the moment owing to the differences in size of the nanoparticles analyzed in both the analysis.

### 3.8 Conclusion

In conclusion, in this chapter the effect of optical absorption properties of Au-NPs embedded in MgO matrix are studied using data obtained from LaAPT analysis. After introducing the bulk structural and optical absorption properties, the nanotips with high dense Au-NPs region at the apex of the tip are studied using different wavelengths. It is observed that, when analyzing the high dense Au-NPs region even at the  $\lambda_{\text{SPR}}$  (570nm), obtained from bulk absorption spectra, the presence of delayed evaporation is evident. In the subsequent section it is proved that, this delayed evaporation is due to the geometry of the tip and absorption from the W-pretip support is the reason behind this observation. Shifting the W-pretip support farther from the tip apex by increasing the length of the tip suppresses this delayed evaporation. A good qualitative agreement between the experimental and calculated evaporation behavior using 1D thermal model is presented to support the hypothesis that, the metallic W-pretip absorption leads to the delayed evaporation.

During analyzing the Au-regions of different concentrations in depth, laser power required to achieve the similar evaporation conditions in Green is slightly more in every analysis, even though the absorption efficiency of Au-NPs is more in Green wavelength compared to the UV. To explain this behavior, FDTD numerical simulations of absorption measurements were performed using the effective refractive indices obtained from Maxwell-Garnett effective medium theory. The results of this simulation provided fruitful information on the absorption properties and with the help of these results it is possible to comment that, owing to the diffraction effects the absorption maxima in case of Green wavelength illumination is far from the tip apex when compare to that of in UV. This absorption far from the apex is attributed to the use of higher laser power in Green wavelength with underlining that the spatial position of absorption will matter more instead of the magnitude (or efficiency) of the absorption.

To have an idea on the thermal properties, the ToF spectra obtained at UV and Green wavelength, with and without Au inclusions are compared. But due to difficulty in

understanding the heated zone in case of Pure MgO, it is not feasible to comment on the change in thermal properties due to Au-NPs presence.

In the last section of the chapter structural analysis of single Au-nanoparticles using 3D reconstruction of the data obtained from LaAPT analysis is presented. With the increase in laser power, the Au-concentration inside Au-NP is found to be increased. By analyzing the 3D distribution of molecular ions and  $Mg^+$  ions around the Au-NP surface, the behavior is ascribed to the local temperature rise around the Au-NP due to laser absorption and subsequent reduction in local field causing the change in trajectories of Au ions evaporated from the Au-NP. This behavior is observed in both case i.e. in UV as well as in Green wavelength analysis.

## References

1. Colombari P. The Use of Metal Nanoparticles to Produce Yellow, Red and Iridescent Colour, from Bronze Age to Present Times in Lustre Pottery and Glass: Solid State Chemistry, Spectroscopy and Nanostructure. *J Nano Res* (2009) **8**:109–132. doi:10.4028/www.scientific.net/JNanoR.8.109
2. Vilarigues M, Silva RC da. Ion beam and infrared analysis of medieval stained glass. *Appl Phys A* (2004) **79**:373–378. doi:10.1007/s00339-004-2538-9
3. Noguez C. Surface Plasmons on Metal Nanoparticles: The Influence of Shape and Physical Environment. *J Phys Chem C* (2007) **111**:3806–3819. doi:10.1021/jp066539m
4. Moores A, Goettmann F. The plasmon band in noble metal nanoparticles: an introduction to theory and applications. *New J Chem* (2006) **30**:1121–1132. doi:10.1039/B604038C
5. Compton D, Cornish L, Lingen E van der. The third order nonlinear optical properties of gold nanoparticles in glasses, part I. *Gold Bull* (2003) **36**:10–16. doi:10.1007/BF03214860
6. Ali FM, Yunus WMM. Study of the Effect of Volume Fraction Concentration and Particle Materials on Thermal Conductivity and Thermal Diffusivity of Nanofluids. *Jpn J Appl Phys* (2011) **50**:085201. doi:10.1143/JJAP.50.085201
7. Mohamed MB, Ahmadi TS, Link S, Braun M, El-Sayed MA. Hot electron and phonon dynamics of gold nanoparticles embedded in a gel matrix. *Chem Phys Lett* (2001) **343**:55–63. doi:10.1016/S0009-2614(01)00653-4
8. Juvé V, Scardamaglia M, Maioli P, Crut A, Merabia S, Joly L, Del Fatti N, Vallée F. Cooling dynamics and thermal interface resistance of glass-embedded metal nanoparticles. *Phys Rev B* (2009) **80**:195406. doi:10.1103/PhysRevB.80.195406
9. Link S, Furube A, Mohamed MB, Asahi T, Masuhara H, El-Sayed MA. Hot Electron Relaxation Dynamics of Gold Nanoparticles Embedded in MgSO<sub>4</sub> Powder Compared To Solution: The Effect of the Surrounding Medium. *J Phys Chem B* (2002) **106**:945–955. doi:10.1021/jp013311k
10. Vurpillot F, Bostel A, Blavette D. Trajectory overlaps and local magnification in three-dimensional atom probe. *Appl Phys Lett* (2000) **76**:3127–3129. doi:10.1063/1.126545
11. Blavette D, Vurpillot F, Pareige P, Menand A. A model accounting for spatial overlaps in 3D atom-probe microscopy. *Ultramicroscopy* (2001) **89**:145–153. doi:10.1016/S0304-3991(01)00120-6

12. Devaraj A, Colby R, Vurpillot F, Thevuthasan S. Understanding Atom Probe Tomography of Oxide-Supported Metal Nanoparticles by Correlation with Atomic-Resolution Electron Microscopy and Field Evaporation Simulation. *J Phys Chem Lett* (2014) **5**:1361–1367. doi:10.1021/jz500259c
13. Kuchibhatla SVNT, Shutthanandan V, Prosa TJ, Adusumilli P, Arey B, Buxbaum A, Wang YC, Tessner T, Ulfig R, Wang CM, et al. Three-dimensional chemical imaging of embedded nanoparticles using atom probe tomography. *Nanotechnology* (2012) **23**:215704. doi:10.1088/0957-4484/23/21/215704
14. Larson DJ, Giddings AD, Wu Y, Verheijen MA, Prosa TJ, Roozeboom F, Rice KP, Kessels WMM, Geiser BP, Kelly TF. Encapsulation method for atom probe tomography analysis of nanoparticles. *Ultramicroscopy* doi:10.1016/j.ultramic.2015.02.014
15. Kreibig U, Vollmer M. *Optical Properties of Metal Clusters*. Berlin, Heidelberg: Springer Berlin Heidelberg (1995). Available at: <http://link.springer.com/10.1007/978-3-662-09109-8>
16. Miller MK, Russell KF, Thompson K, Alvis R, Larson DJ. Review of Atom Probe FIB-Based Specimen Preparation Methods. *Microsc Microanal* (2007) **13**:428–436. doi:10.1017/S1431927607070845
17. Bogdanowicz J, Gilbert M, Innocenti N, Koelling S, Vanderheyden B, Vandervorst W. Light absorption in conical silicon particles. *Opt Express* (2013) **21**:3891. doi:10.1364/OE.21.003891
18. Palik ED. *Handbook of Optical Constants of Solids*. Academic Press (1998).
19. Kelly TF, Vella A, Bunton JH, Houard J, Silaeva EP, Bogdanowicz J, Vandervorst W. Laser pulsing of field evaporation in atom probe tomography. *Curr Opin Solid State Mater Sci* (2014) **18**:81–89. doi:10.1016/j.cossms.2013.11.001
20. Vurpillot F, Houard J, Vella A, Deconihout B. Thermal response of a field emitter subjected to ultra-fast laser illumination. *J Phys Appl Phys* (2009) **42**:125502. doi:10.1088/0022-3727/42/12/125502
21. Vella A. On the interaction of an ultra-fast laser with a nanometric tip by laser assisted atom probe tomography: A review. *Ultramicroscopy* (2013) **132**:5–18. doi:10.1016/j.ultramic.2013.05.016
22. Mazumder B, Vella A, Gilbert M, Deconihout B, Schmitz G. Reneutralization time of surface silicon ions on a field emitter. *New J Phys* (2010) **12**:113029. doi:10.1088/1367-2630/12/11/113029
23. Tamura H, Tsukada M, McKenna KP, Shluger AL, Ohkubo T, Hono K. Laser-assisted field evaporation from insulators triggered by photoinduced hole accumulation. *Phys Rev B* (2012) **86**:195430. doi:10.1103/PhysRevB.86.195430
24. Silaeva EP, Vella A, Sevelin-Radiguet N, Martel G, Deconihout B, Itina TE. Ultrafast laser-triggered field ion emission from semiconductor tips. *New J Phys* (2012) **14**:113026. doi:10.1088/1367-2630/14/11/113026
25. Silaeva EP, Shcheblanov NS, Itina TE, Vella A, Houard J, Sévelin-Radiguet N, Vurpillot F, Deconihout B. Numerical study of femtosecond laser-assisted atom probe tomography. *Appl Phys A* (2012) **110**:703–707. doi:10.1007/s00339-012-7189-7
26. Vella A, Silaeva EP, Houard J, Itina TE, Deconihout B. Probing the thermal response of a silicon field emitter by ultra-fast Laser Assisted Atom Probe Tomography. *Ann Phys* (2013) **525**:L1–L5. doi:10.1002/andp.201200182
27. Miller MK, Cerezo A, Hetherington MG, FRS GDWS. *Atom Probe Field Ion Microscopy*. Clarendon Press | Monographs on the Physics and Chemistry of Materials 52 (1996).
28. Slack GA. Thermal Conductivity of MgO, Al<sub>2</sub>O<sub>3</sub>, MgAl<sub>2</sub>O<sub>4</sub>, and Fe<sub>3</sub>O<sub>4</sub> Crystals from 3° to 300°K. *Phys Rev* (1962) **126**:427–441. doi:10.1103/PhysRev.126.427

29. Colombier JP, Garrelie F, Faure N, Reynaud S, Bounhalli M, Audouard E, Stoian R, Pigeon F. Effects of electron-phonon coupling and electron diffusion on ripples growth on ultrafast-laser-irradiated metals. *J Appl Phys* (2012) **111**:024902. doi:10.1063/1.3676221
30. Vella A, Mazumder B, Costa GD, Deconihout B. Field evaporation mechanism of bulk oxides under ultra fast laser illumination. *J Appl Phys* (2011) **110**:044321. doi:10.1063/1.3610523
31. Silaeva EP, Arnoldi L, Karahka ML, Deconihout B, Menand A, Kreuzer HJ, Vella A. Do Dielectric Nanostructures Turn Metallic in High-Electric dc Fields? *Nano Lett* (2014) **14**:6066–6072. doi:10.1021/nl502715s
32. Houard J, Vella A, Vurpillot F, Deconihout B. Conditions to cancel the laser polarization dependence of a subwavelength tip. *Appl Phys Lett* (2009) **94**:121905. doi:10.1063/1.3095829
33. Garnett JCM. Colours in Metal Glasses and in Metallic Films. [Abstract]. *Proc R Soc Lond* (1904) **73**:443–445.
34. Gault B, Moody MP, Cairney JM, Ringer SP. *Atom Probe Microscopy*. New York, NY: Springer New York (2012). Available at: <http://link.springer.com/10.1007/978-1-4614-3436-8> [Accessed June 10, 2015]
35. Müller M, Saxey DW, Smith GDW, Gault B. Some aspects of the field evaporation behaviour of GaSb. *Ultramicroscopy* (2011) **111**:487–492. doi:10.1016/j.ultramic.2010.11.019



# Chapter 4

## Au-nanoclusters in Fe<sub>2</sub>O<sub>3</sub> matrix: Optical and thermal Investigations using LaAPT

### 4.1 Introduction

Iron oxides have widespread relevance to many areas of science and technology. Recently, there has been a renewed interest in iron oxides for their potential as light harvesting materials. Their low cost, abundance, processability, optical absorption, and minimal environmental foot-print makes oxides of iron a promising candidate [1]. There are many different types of iron oxides with different phases and crystal properties. Their structural properties and applications in various different fields are summarized in great details in [2]. Out of all the iron oxides, hematite ( $\alpha$ -Fe<sub>2</sub>O<sub>3</sub>) constitutes one of the most promising semiconductor materials for the conversion of sunlight into chemical fuels by water splitting. Its inherent drawbacks related to the long penetration depth of light and poor charge carrier conductivity are being progressively overcome by employing nanostructuring strategies and improved catalysts [3,4]. Photoelectrochemical (PEC) water splitting using semiconductor photoelectrodes provides a promising technology for storing solar energy as hydrogen, which is regarded as a green energy carrier of the future. But relatively low absorption coefficient for visible light is one of the key drawbacks using  $\alpha$ -Fe<sub>2</sub>O<sub>3</sub> as a photoanode. To improve the light absorption efficiency, various researchers have integrated the plasmonic metal nanostructures with the  $\alpha$ -Fe<sub>2</sub>O<sub>3</sub> nanostructures. Thimsen et.al. [5] studied the effect of bare spherical Au particles on the photoactivity performance of Fe<sub>2</sub>O<sub>3</sub> electrodes with the Au nanoparticles (NPs) embedded

in the hematite layer and on its surface. The embedded Au NPs were found to have no effect on hematite performance whereas the configuration of the surface coating on hematite nano-plates provided a spectroscopic effect on the photocurrent response. So the effect is improved upon nanostructuring the  $\text{Fe}_2\text{O}_3$ . Similar kind of analyses was carried out on hematite nanoflakes decorated by Au-nanoparticles [6] and layer of hematite deposited on Au-nanopillars [7]. In both the cases, significant improvement in the photocurrent is evidenced owing to the inclusion of Au-nanostructures. Interestingly, all these progresses are studied in relatively recent times and this gives us motivation to analyze the Au- $\text{Fe}_2\text{O}_3$  system using Laser assisted atom probe tomography (LaAPT). With LaAPT, it is an advantage to analyze the material at nanoscale itself and hence the structural, chemical, optical, and thermal properties deduced from LaAPT analysis will be beneficial to understand and improve the properties of Au- $\text{Fe}_2\text{O}_3$  system as a whole.

In this context, this chapter will be devoted to the analysis of Au- $\text{Fe}_2\text{O}_3$  system using LaAPT. In addition the analysis with pure  $\text{Fe}_2\text{O}_3$  is carried out to compare the results obtained with Au- $\text{Fe}_2\text{O}_3$ . The main motivation is to understand whether the inclusion of Au-nanoparticles will change the optical and thermal behavior of the  $\text{Fe}_2\text{O}_3$  system or not at nanometric scale. As explained in the previous chapter (Chapter 2), the methodologies used to investigate the optical and thermal behavior using LaAPT will be applied to the data obtained with Au- $\text{Fe}_2\text{O}_3$  sample and are correlated to their 3D structural and chemical properties obtained after tomographic reconstruction and Scanning transmission electron microscopic (STEM) analysis.

The chapter will first introduce the method used to synthesize the Au- $\text{Fe}_2\text{O}_3$  composite and then to confirm the formation of Au-nanoclusters in  $\text{Fe}_2\text{O}_3$  matrix characterization techniques based on X-ray diffraction and electron microscopy were employed. In the next section the sample preparation for LaAPT analysis is introduced along with the 3D tomographic reconstruction of data analyzed. The 3D reconstruction results are compared and correlated with the STEM analysis.

## **4.2 Materials and characterization**

### **4.2.1 Synthesis of Au- $\text{Fe}_2\text{O}_3$ films**

As introduced in the Chapter 1, the Au- $\text{Fe}_2\text{O}_3$  composites were synthesized by using Pulsed Laser deposition (PLD) technique. The target was prepared by mixing the commercially available Au- and  $\text{Fe}_2\text{O}_3$ -powder with different concentration of Au in at.%

(e.g. 5 at.% and 10 at% Au). The films were deposited on Si substrate as well as on transparent substrate like quartz for optical and structural characterization.

#### 4.2.2 Structural Characterization of Bulk samples

To confirm the presence of Au-nanocluster formation, all thin films were analyzed using X-ray diffraction (XRD) and scanning electron microscopy (SEM). The film deposited with 10 at.% Au concentration and at 500°C deposition temperature showed commendable results. The formation of Au-nanoclusters (NCs) is evident from both the analysis and shown in figure 4.1.

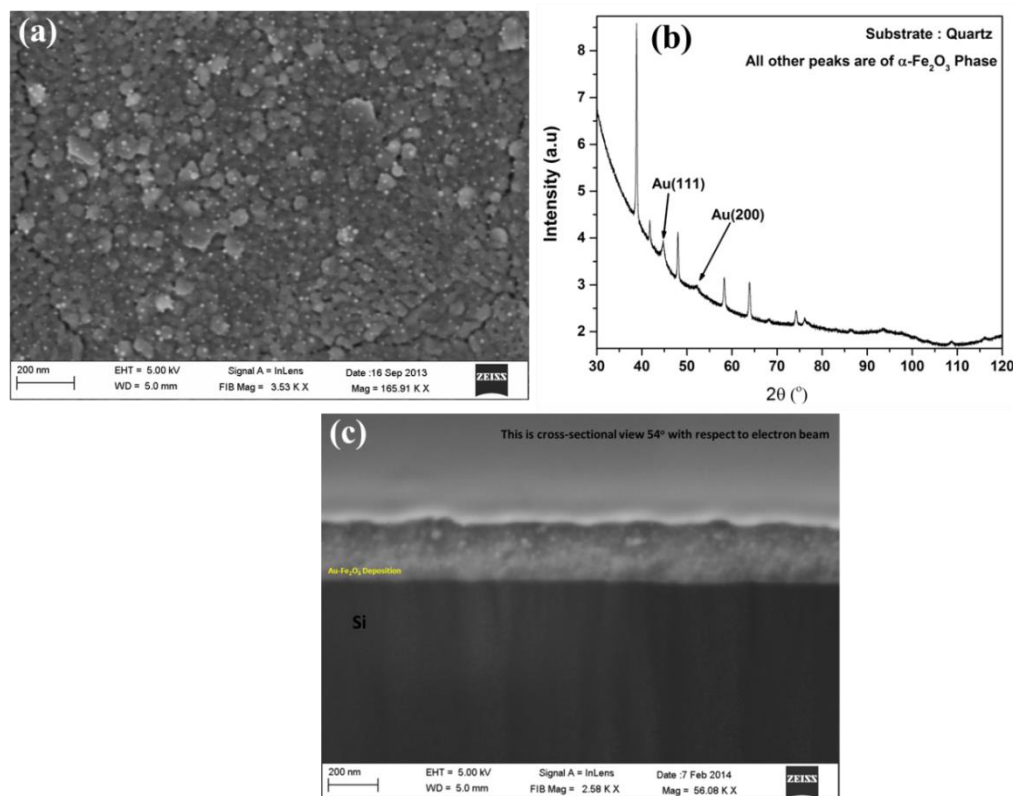


**Figure 4.1** : Characterization of Au-Fe<sub>2</sub>O<sub>3</sub> film (a) Top-down SEM image showing the surface of the film deposited on Si-substrate, the bright tiny spots corresponds to the Au-NCs, (b) XRD pattern recorded for the same film deposited on Quartz substrate, Au-peaks are indexed and all other unindexed peaks corresponds to the α-Fe<sub>2</sub>O<sub>3</sub> phase, (c) Cross-sectional SEM image showing the presence of Au-NCs inside the Fe<sub>2</sub>O<sub>3</sub> matrix.

The top-down view of the Au-Fe<sub>2</sub>O<sub>3</sub> film deposited on Si-substrate is shown in fig. 4.1(a), the SEM image shows several bright contrast tiny spots spread all over the surface of the film. These bright contrast (termed as Z-contrast) spots are due to the high Z (atomic number) of Au compare to the matrix, which signifies that the Au-NCs are spread all over the surface. To make sure the formation of NCs inside the film, a small portion of the film was milled using the focused ion beam (FIB) of Ga ions and then

imaged  $54^\circ$  with respect to the electron beam and is shown in fig.4.1 (c). The cross-sectional SEM image shows dark contrast Si-Substrate and nearly 250nm thick Au-Fe<sub>2</sub>O<sub>3</sub> film deposited on it. The smooth surface in this image is due to the Pt-deposition, to prevent the Ga ion beam damage to the film. As shown in fig. 4(c), even inside the film the presence of bright spots, as observed on the surface of the film is clearly visible which confirms the formation of Au NCs inside the film as well. To understand the crystallographic nature of the film and to confirm that the bright spots observed in SEM images are nothing but the Au-NCs, we have performed XRD analysis on the films deposited on quartz substrate. As shown in fig. 4.1(b), the XRD pattern shows several sharp peaks, all unindexed peaks in this pattern corresponds to the  $\alpha$ -Fe<sub>2</sub>O<sub>3</sub> phase of iron oxide. The several peaks observed confirm the polycrystalline nature of the film. The formation of Au-NCs is also confirmed by the XRD, peaks indexed by Au(111) and Au(200) in this pattern corresponds to the Au-NCs.

### 4.2.3 Optical Characterization of bulk sample

The optical absorption measurements were carried out on the films deposited on transparent quartz substrate. Measurements were carried out in JASCO UV-VIS-NIR Spectrophotometer with double beam and Deuterium lamp as a light source. To eliminate the contribution of quartz substrate (even though it is transparent in visible region), signal obtained from pure quartz substrate was subtracted from the thin film spectra. The absorption spectra obtained in the UV-visible-NIR range is shown in fig. 4.2.

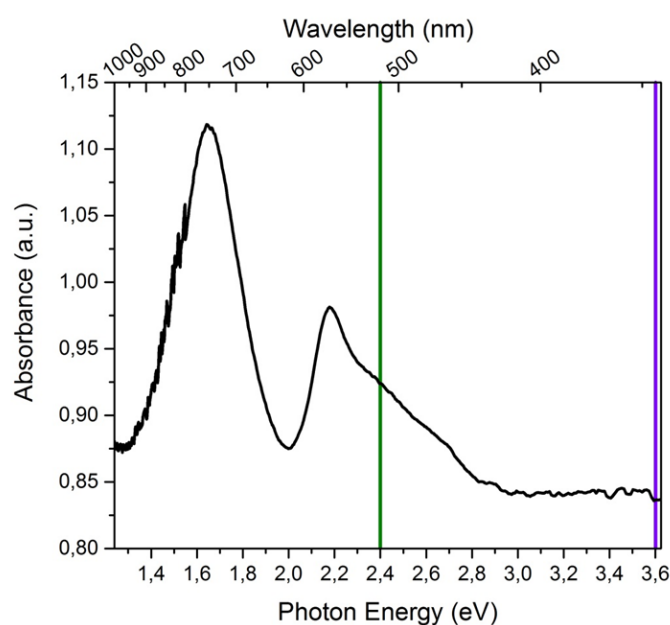


**Figure 4.2** : Absorption spectra obtained from thin film of Au-Fe<sub>2</sub>O<sub>3</sub> deposited on Quartz

As shown in fig. 4.2, the absorption spectrum is recorded in the photon energy range of 1.24eV to 3.64eV. Two absorption maxima's are seen in this spectrum, one at nearly 750nm (1.65eV) and another one at 570nm (2.17eV). These absorption maxima can be due to the plasmonic absorption of Au-NCs. It is very well known that for odd shaped plasmonic nanostructures the absorption signatures in near IR region of the spectrum can be expected along with the absorption in visible range and their relative magnitude depends on the angle of polarization of incident light. The wavelengths used for the atom probe experiments in this study also shown by vertical Green (515nm) and Violet (343nm) lines.

### 4.3 Sample Preparation for LaAPT

As the requirement of the LaAPT experiment, the specimen should be in the form of sharp needle shape or usually termed as a tip with apex diameter less than 100nm. As the sample in our study is in the form of thin film deposited on flat substrate the conventional method to prepare the atom probe sample is focused ion beam (FIB) based lift-out method followed by annular milling. The general protocol for atom probe sample preparation is described in [8]. In general, to prepare the atom probe specimen from bulk specimen we have used the standard focused Ion Beam based lift-out method followed by annular milling using NVISION-40 ZEISS dual beam microscope. To prevent the Ga ion beam damage, 100nm thick Pt layer was deposited using GIS. The lamella was prepared and mounted on the W-pretip with flat end. Then the annular milling with 30kV accelerating voltage in the beginning and with 2kV for final stages was employed to prepare the tip shaped specimen for atom probe analysis

The general approach is summarized in figure 4.3. As shown in fig. 4.3(a), the tip is prepared across the thin film, the highlighted tip shaped area in this image shows the demonstrative area from which the tip has been prepared. The final atom probe tip prepared after annular milling is shown fig. 4.3(b), where, Si and W denotes the Si-substrate and W-pretip respectively. The magnified view of the near apex region of the tip is shown in fig. 4.3(c). The diameter of the tip is nearly 40nm. Few bright contrast spots observed in the tip corresponds to the Au-NCs and the interface between the film and the substrate is denoted by white arrow. In similar manner several tips were prepared and analyzed in the LaAPT. Although the sample preparation was effective, analyzing these tips in LaAPT was unfortunately quite tricky and most of the tips were fractured or

flashed in the very beginning of the analysis. The success rate was very less, one out of five tips were successfully analyzed.

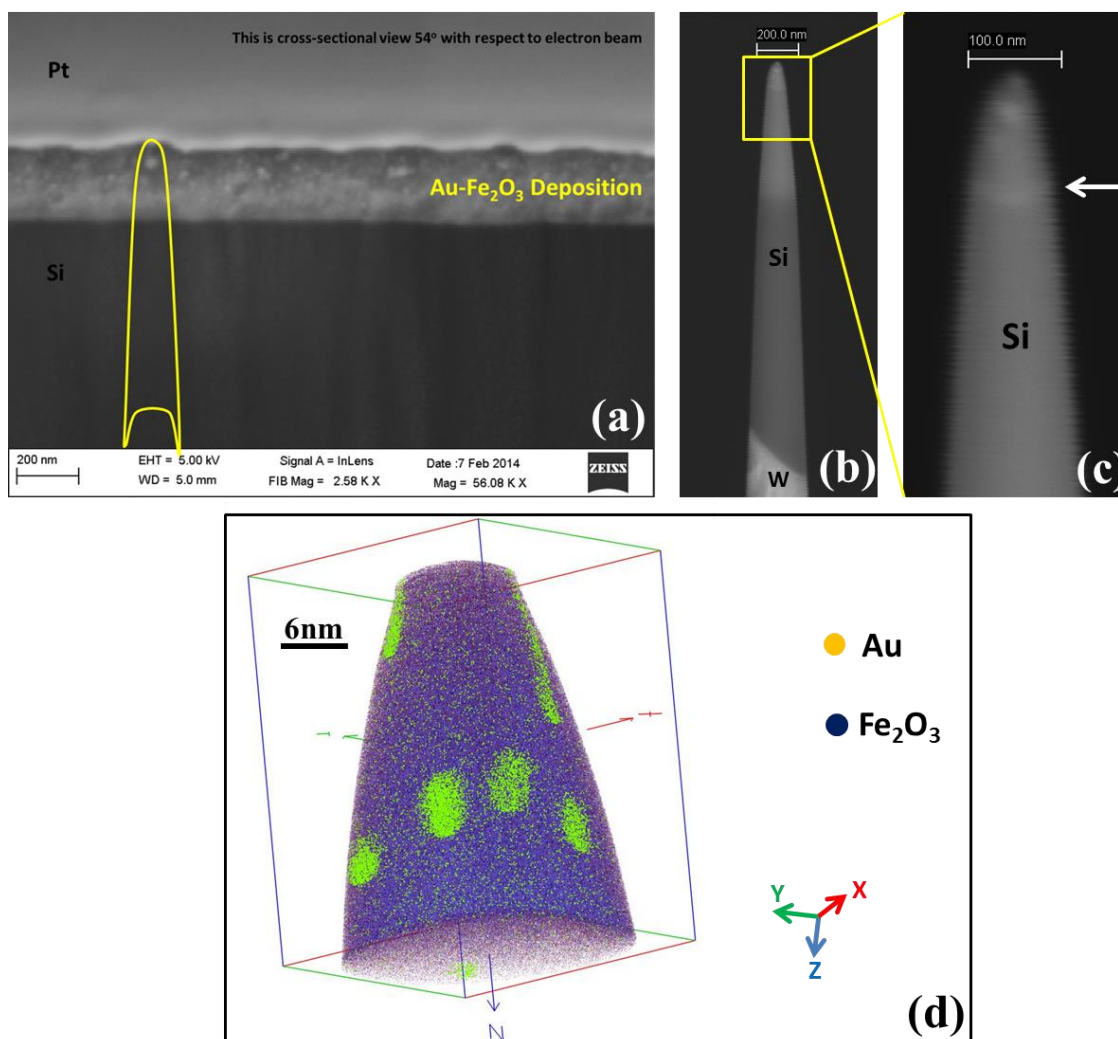


**Figure 4.3 :** (a) Cross-sectional SEM image of Au-Fe<sub>2</sub>O<sub>3</sub> showing film and Si-substrate, yellow highlighted tip shaped area shows the region from which tip is prepared, (b) Final atom probe tip prepared from (a), high magnification image is shown in (c), the interface between and film and substrate is denoted by white arrow, also the bright contrast Au-NCs are clearly visible, and (d) 3D tomographic reconstruction obtained by analyzing the tip shown in (b)-(c).

The 3D tomographic reconstruction obtained from one of the successful analysis is shown in fig. 4.3(d). The Au atoms are represented by Green dots and Fe<sub>2</sub>O<sub>3</sub> matrix by blue dots. This analysis was also followed by the tip fracture; a closer look at the bottom of the 3D reconstruction shown in fig 4.3(d) shows an abrupt change or a discontinuity from the matrix, similar abrupt changes were also observed in the voltage curve of this analysis. From this observation we concluded that, it is quite possible that the adhesion between the film and the substrate is not good enough to sustain the stress generated by the strong electrostatic field applied in LaAPT experiment and could be the reason for low success rate in atom probe analysis. To overcome this difficulty we

decided to prepare the atom probe sample along the thin film instead of across the thin film as shown in fig. 4.3. The idea here is not to have the interface between film and Si-substrate anywhere in the tip. For this a thick layer (nearly  $1\mu\text{m}$ ) Si was deposited on the thin film, i.e. the film is now sandwiched between Si layer and Si-substrate. This geometry is then lifted out and glued to the W-pretip horizontally instead of conventional way of gluing the lamella perpendicular to the W-pretip. The general method is shown in fig. 4.4.

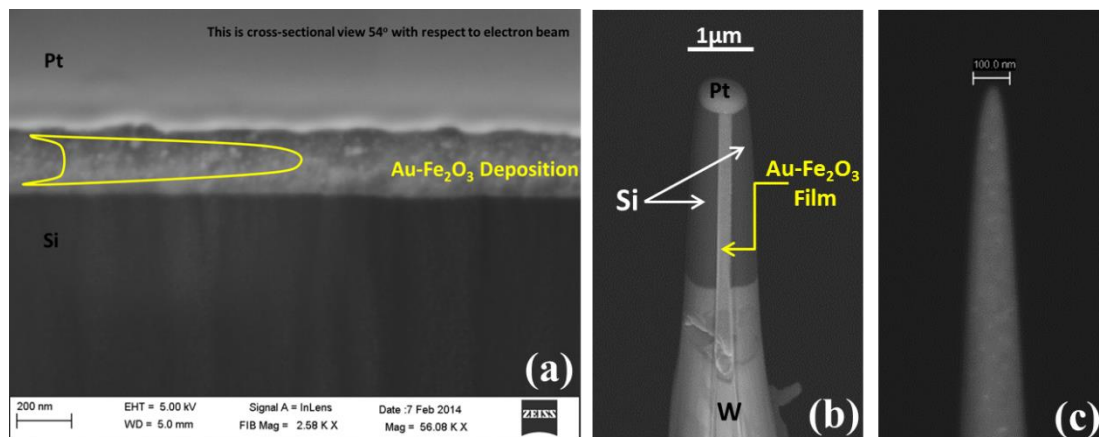


**Figure 4.4 :** (a) Cross-sectional SEM image of the Au-Fe<sub>2</sub>O<sub>3</sub> film, yellow highlighted tip shaped area shows the region from which tip is prepared, (b) SEM image during the initial stage of annular milling (c) final atom probe tip

The region of interest for tip preparation along the thin film is shown yellow highlighted region in fig. 4.4(a). Fig. 4.4(b) shows the initial stage of annular milling, where bright contrast Au-Fe<sub>2</sub>O<sub>3</sub> film sandwiched between Si can be clearly seen, the film is now parallel to the axis of the W-pretip unlike the previous case. A 100nm thick Pt is deposited to prevent Ga ion beam damage during the annular milling process. The annular milling is followed in such a way that both the Si-layer should be milled out thoroughly and only Au-Fe<sub>2</sub>O<sub>3</sub> film should exist during the final stages of the milling. Following this procedure, the final atom probe tip prepared by this method is shown in fig. 4.4(c). To have better understanding of the size and density distribution of the Au-NCs, high angle annular dark field - scanning transmission electron microscopy (HAADF-STEM) was employed to the tips prepared by this method. HAADF-STEM images of the tip are shown in fig. 4.5.

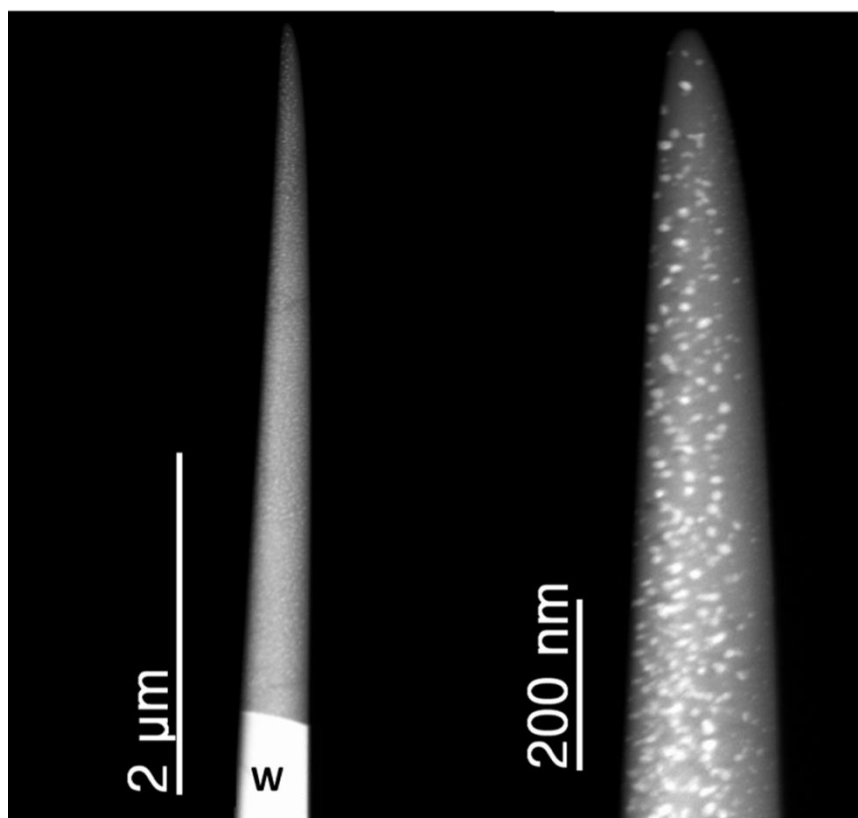


**Figure 4.5 :** HAADF-STEM image of Au-Fe<sub>2</sub>O<sub>3</sub> tip prepared along the thin film : Low magnification image showing Au-NCs are distributed all over the tip, the length of the tip is nearly 4 μm (left) and magnified view from the near apex region (right).

As shown in fig 4.5, the whole tip is decorated with the Au-NCs, considering the lower sputtering yield of Au compare to Fe<sub>2</sub>O<sub>3</sub> for Ga ion milling; it is quite possible that some of the Au-NCs are on the surface of the tip. The Au-NCs are uniformly distributed and are oddly shaped. The high magnified image on the right shows that the size distribution of Au-NCs, the average size is in the range 10-13nm and is in good agreement with the particle size calculated using the XRD pattern.

Tips prepared with this geometry are then analyzed in the LaAPT and the success rate of analysis in this case is quite excellent unlike the previous case, almost every single tip analyzed in this geometry has produced successful atom probe results. The mass spectrum obtained from one of the successful analysis is shown in fig. 4.6 (top). In this spectra several peaks related to ionic species of Fe and O are observed along with Au mass peak at 197amu, most of the peaks are indexed. As far as 3D tomographic reconstruction is concern, excellent correlation with the HAADF-STEM image is obtained and also shown in fig. 4.6 (bottom). Au atoms are represented in Green while the Fe<sub>2</sub>O<sub>3</sub> matrix in Blue.

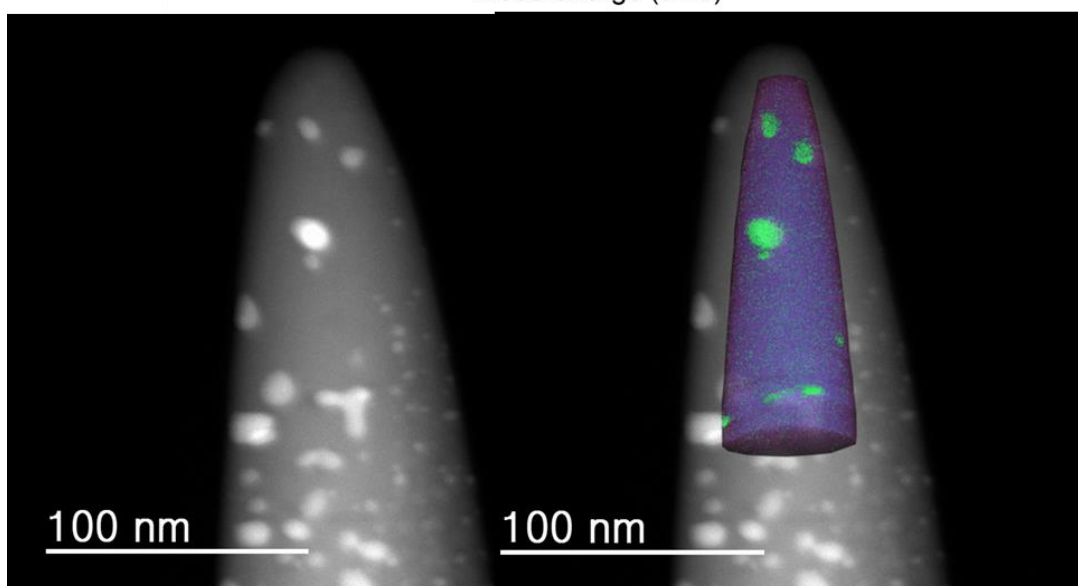
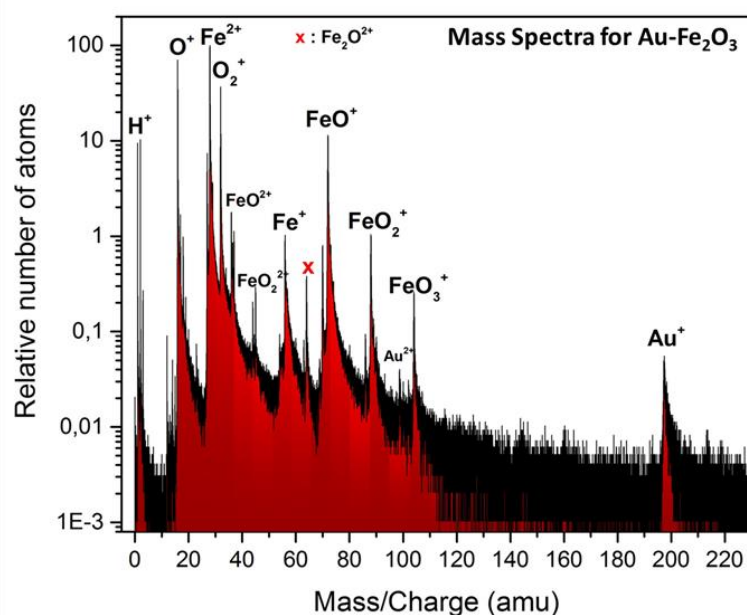


**Figure 4.6 :** Typical mass spectra obtained from the Au-Fe<sub>2</sub>O<sub>3</sub> tip prepared along the thin film (top) and direct correlation of the 3D tomographic reconstruction of atom probe data to HAADF-STEM image (bottom)

#### 4.4 Structural Characterization of Single Nanoparticles

The optical properties of Au-nanoparticles are strongly dependent on the size, shape, composition and their dielectric environment [9]. Analyzing these properties using atom probe has advantage over other techniques owing to its unmatched qualities to probe the material structurally and chemically in 3 dimensions at near atomic scale. In this study the nanoparticle size distribution estimated from XRD analysis and HAADF-STEM analysis is quite consistent with the atom probe analysis as well. To have an idea on the size and shape of the nanoparticles we have used concentration isosurfaces [10]. By

constructing a 10% Au concentration isosurfaces, the size and shape of the Au-NCs is clearly revealed and are shown in fig 4.7. The threshold of 10 at.% is chosen to avoid the statistical variations in lesser concentrations and the higher threshold will underestimate the size of the Au-NCs. Two Au-NCs from the analyzed volume were characterized by isosurfaces. The 10% Au isosurfaces of Au-NCs highlighted by red and black rectangle in 3D tomographic reconstruction are shown in fig. 4.7. The NC highlighted in red rectangle is completely embedded in the matrix and hence the complete structure of NC can be revealed while on the other hand NC highlighted in black rectangle shows partial structure, this is because other half part of the NC was not in the field of view of atom probe detector. The shape of both Au-NCs are not spherical, they are bit oval in shape.

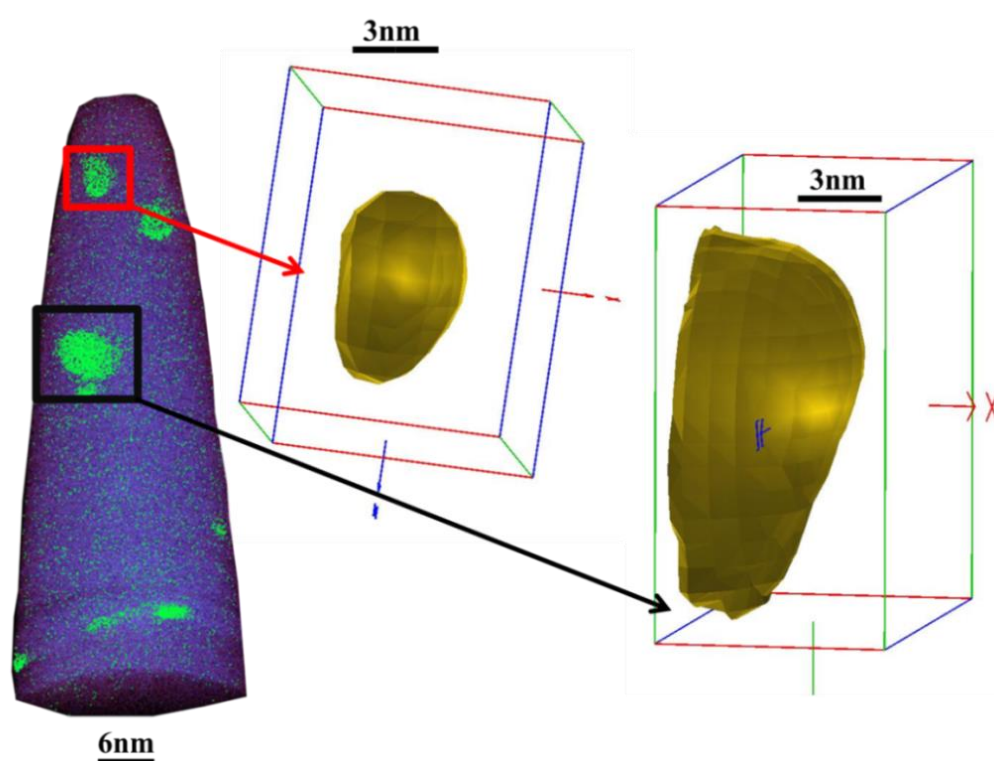


**Figure 4.7 :** 3D tomographic reconstruction and 10% Au concentration isosurfaces.

The composition of Au-NCs inside the cluster is measured using the erosion profile [10]. A typical erosion profile measured from the atom probe data of Au-NCs shown in fig. 4.7 are shown in figure 4.8. As shown in this figure, the composition is measured around and inside the Au-NCs. The interface between the Au-NC and  $\text{Fe}_2\text{O}_3$  matrix is represented on the X-axis of the figure 4.8. The interface is defined by the threshold concentration of 10at.% Au, like the isosurfaces analysis. It is clearly evident that the Au-NCs are generally composed of Au atoms only, particularly the core of NCs shows highly pure Au fraction.

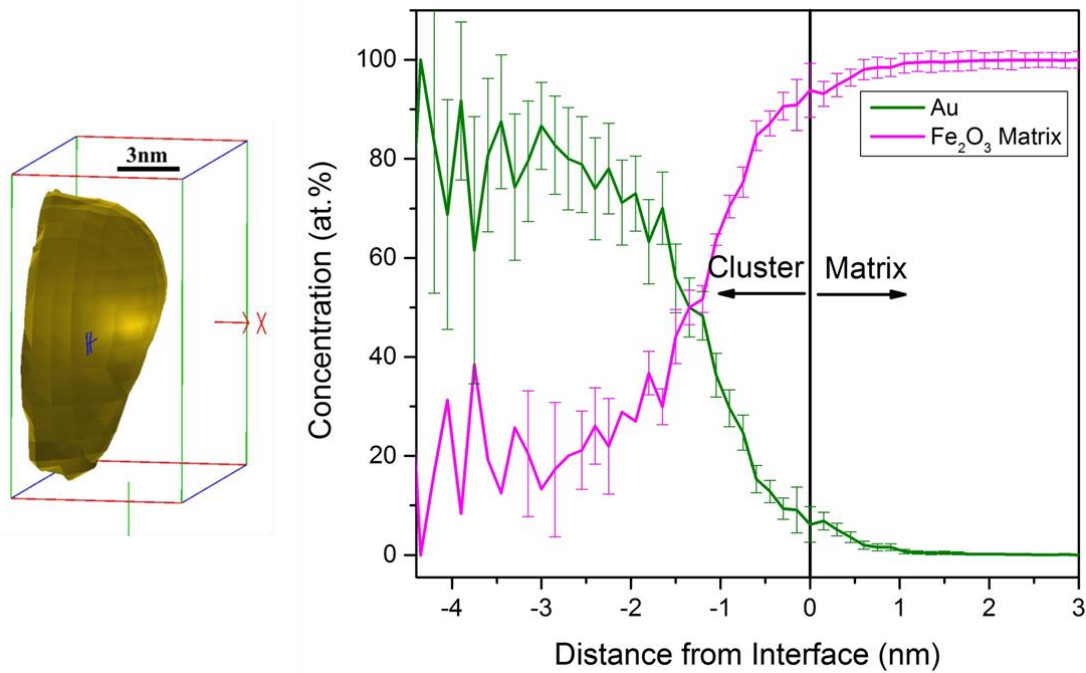


**Figure 4.8** : Structural and chemical characterization of single Au-NC in 3D : 10% Au isosurface (right) and corresponding erosion profile (left)

The dilute concentration or the depletion of Au content near the interface is related to the artefact of 3D reconstruction protocol used in atom probe analysis. This artefact usually termed as local magnification effect [11] and arises due to the differences in evaporation field of atomic species, in this case Au has high evaporation field (54V/nm) compared to that of  $\text{Fe}_2\text{O}_3$  matrix. Owing to this effect, during evaporation; changes in local radius causes Au ion to change their trajectories in radially outward direction and hence depletion in the overall Au concentration near the interface region. The local magnification effect or the trajectory aberration has already been observed in the atom probe analysis of various multi-phase binary materials [12] and the effect is found to be enhanced when the differences in evaporation fields is larger. The evaporation field for  $\text{Fe}_2\text{O}_3$  is not known, but considering the observed trend in voltage curve during the evaporation one can figure out that the field of evaporation of Au NCs is high compared to the  $\text{Fe}_2\text{O}_3$  matrix. When the Au-NC is on the surface, more voltage is required to keep the detection flux constant than the matrix. This behavior is consistently observed throughout the experiments and is shown in fig. 4.9.

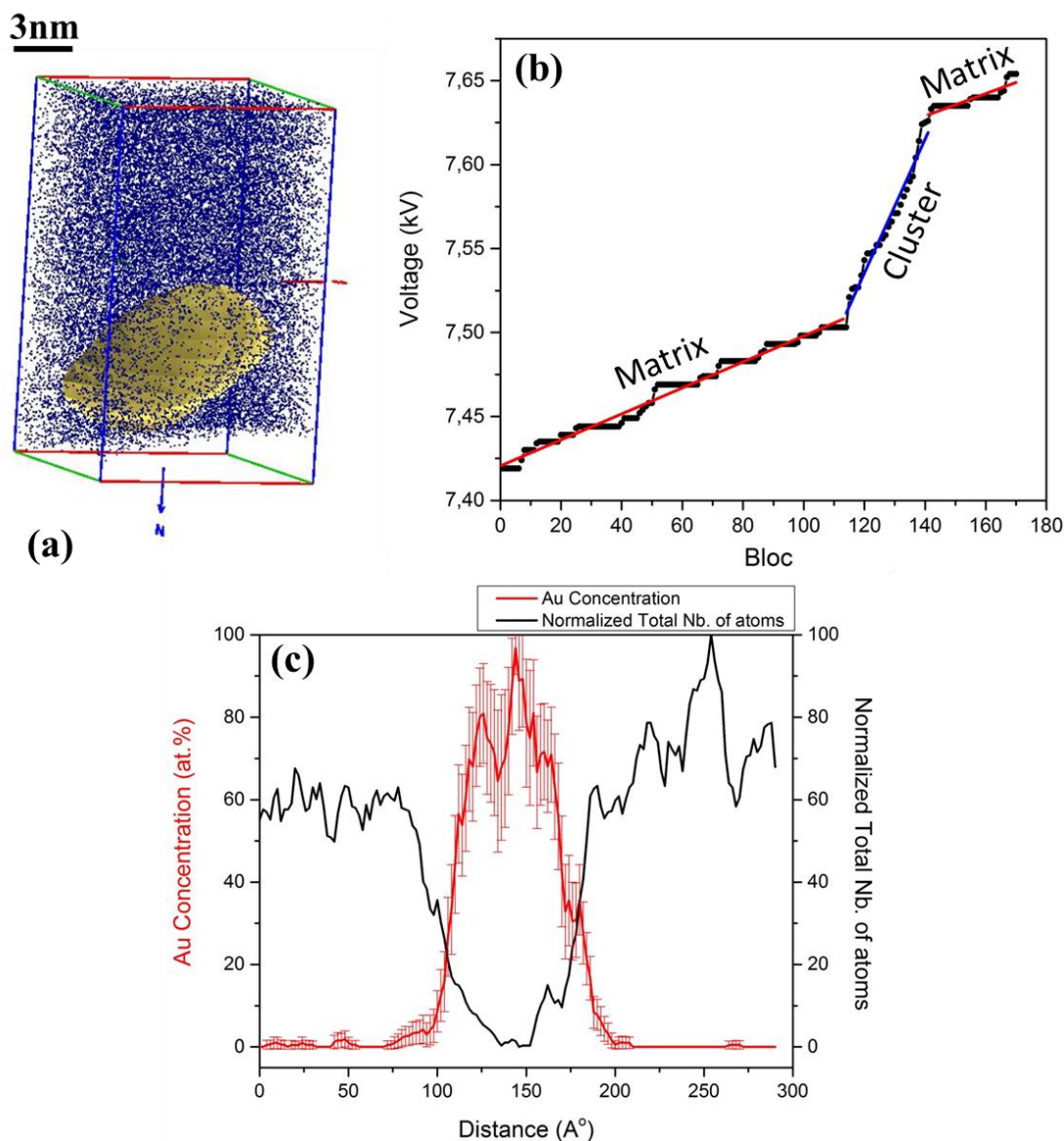
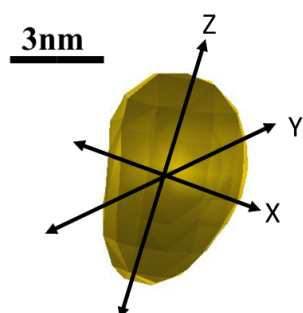


**Figure 4.9 :** Voltage curve (b) measured for the 3D reconstruction shown in (a) and corresponding number density of atoms inside and outside Au-NC (c)

As shown in fig. 4.9(a) a sub-volume from the 3D reconstructed data is taken which contains uniform matrix and an Au-NC at the bottom. The volume is then divided in blocs along the Z-direction with each bloc containing 100 atoms. The voltage curve shown in fig. 4.9(b) is obtained from the evaporation sequence of 3D sub-volume shown in fig. 4.9(a). The voltage curve shows steady increase when the matrix is evaporating owing to the tip size evolution. But when the Au-NC arrives on the surface of the tip to evaporate, sudden increase in the slope of voltage curve is observed. This abrupt increase is due to the high field of evaporation of Au, and to keep the detection flux constant voltage is raised. When the Au-NC evaporates completely, the evaporation of matrix shows similar trend of voltage evolution as before. The slope of the curve before and after

evaporation of Au-NC is found similar, while it is increased by factor of 5 when Au-NC begins to evaporate. This behavior suggests that the field required to evaporate Au is 5 times higher than the field of evaporation of Fe<sub>2</sub>O<sub>3</sub> matrix. But the change in local radius around the nanoparticle due to the dissimilar evaporation field will also contribute to this effect. The consequence of this dissimilar field of evaporation is the change in the density of atoms inside the cluster. It is reported by Vurpillot et. al. [11] that for high field cluster the density of atoms inside the cluster should be decrease owing to the trajectory overlaps and local magnification effect. In this context the measured density of atoms inside the Au-NC shown in fig. 4.9(a) is plotted in fig. 4.9(c) along with the Au-concentration. It is clearly evident that the total number of atoms is reduced to almost zero inside the Au-NC. Similar behavior was also observed by Devaraj et. al. [13] for Au NCs in MgO matrix. Their simulated data matches quite well with our experimental results and comparing the analysis reported in [11,13] to our data the evaporation field for Fe<sub>2</sub>O<sub>3</sub> matrix can be qualitatively estimated with respect to evaporation field of Au. The ratio of evaporation field of Fe<sub>2</sub>O<sub>3</sub> to Au is estimated around 1:2. Hence the change in the slope of fig. 4.9(b) during the evaporation of Au-NCs is combine effect of increase of factor 2 of change in evaporation field as well as decrease of local radius of around factor of 3.

The composition of each ionic species is measured from the interface to the core of NCs in all the three dimensions using erosion profile [10]. Consequently it is possible to measure the size of the Au-NCs with near atomic resolution. The size of Au-NCs measured from 3D reconstructed atom probe data is in the range of 3nm to 6nm in radius as also observed in the HAADF-STEM image of the tip as shown in fig. 4.6. The shape of the Au-NCs in this study is mixed; some of the Au-NCs particularly the one which are smaller in size are near spherical in shape and the bigger NCs are either oval or odd shaped. This might be related to processes involved in the formation of bigger NCs from smaller ones, like coalesces for example. Due to the local magnification effect it is possible to observe the spherical NCs oval in shape, but size and shape of the Au-NCs observed in the HAADF-STEM is quite consistent with the atom probe reconstruction, which explains the odd shape is not due to reconstruction artefact. To have an idea about real size and shape of the Au-NCs, we have measured the radii of different Au-NCs obtained from atom probe 3D reconstruction in three directions viz. X, Y and Z. The measured radii along with the aspect ratio for different Au-NCs are summarized in Table 4.1. The measured values along X and Y axes as represented below found to be nearly similar and hence representing it as  $R_x=R_y$ ,



Au Nanocluster	$R_x=R_y$ (nm)	$R_z$ (nm)	Aspect Ratio ( $R_z/R_x$ )
1	3.2	4.6	1.43
2	1.9	3.1	1.63
3	3.0	5.2	1.73
4	4.7	5.3	1.12
5	2.7	3.3	1.22
6	1.9	3.0	1.57
7	2.5	3.8	1.52
8	1.6	2.3	1.43
<b>Average</b>	<b>2.7</b>	<b>3.8</b>	<b>1.5</b>

**Table 4.1** : Measured radii for different Au-NCs and their aspect ratio. (Image on the left is shown to represent the axes of measurements)

The average aspect ratio obtained from these measurements is nearly 1.5. This shows that the Au-NCs are not spherical in shape. For these measurements only Au-NCs completely embedded in matrix are considered, however the Au-NCs bigger than the average size are also present in the matrix. An example is the Au-NC shown in fig. 4.8 whose  $R_z$  is nearly 7nm, which was analyzed partially due to the limited field of view of atom probe detector. The STEM observation also supports this observation. In addition, closer look at the STEM image shown in fig. 4.6 (see the right edge of the tip) shows number of smaller Au-NCs which were not analyzed by atom probe due to the limited field of view of the instrument. But the information obtained on size and shape of the Au-NCs using both the techniques (STEM and LaAPT) balances each other's drawbacks and completes the picture. The measurement of size and shape of Au-NCs realized from HAADF-STEM and atom probe analyses are comparable and this information will play an important role to understand the optical and thermal properties of Au-Fe<sub>2</sub>O<sub>3</sub> nanotips by using LaAPT.

## 4.5 Optical characterization of nano-objects

In this section the optical absorption of Au-NCs in Fe<sub>2</sub>O<sub>3</sub> matrix is calculated using the size and shape of Au-NCs obtained from the atom probe analysis as well as STEM observations. In addition, the absorption maps for the tip shaped samples are also calculated using FDTD method.

### 4.5.1 Optical absorption of Au-NCs

With the information obtained in the previous section on the size and shape of the Au-NCs, we have calculated the optical absorption response of ellipsoidal Au-NC in Fe<sub>2</sub>O<sub>3</sub> matrix. The values of dielectric constants were taken from [14] for Au and from [15] for Fe<sub>2</sub>O<sub>3</sub>. The absorption of single isolated ellipsoidal Au-NC embedded in Fe<sub>2</sub>O<sub>3</sub> matrix is calculated using the analytical treatment in the electrostatic approximation of an ellipsoid with semi-axes  $a_1 \leq a_2 \leq a_3$ , specified by,

$$\frac{x^2}{a_1^2} + \frac{y^2}{a_2^2} + \frac{z^2}{a_3^2} = 1 \quad (4.1)$$

as given by Maier [16]. A treatment of scattering problem in ellipsoidal coordinate leads to the following expression of polarizabilities along the principal axes ( $i = 1, 2, 3$ )

$$\alpha_i = 4\pi a_1 a_2 a_3 \frac{\epsilon(\omega) - \epsilon_m}{3\epsilon_m + 3L_i(\epsilon(\omega) - \epsilon_m)} \quad (4.2)$$

where,  $\epsilon(\omega)$  is frequency dependent dielectric constant for Au-NPs,  $\epsilon_m$  is the dielectric constant of the matrix (Fe<sub>2</sub>O<sub>3</sub>) and  $L_i$  is the geometrical factor which satisfies  $\sum L_i = 1$ , and for sphere  $L_1 = L_2 = L_3 = 1/3$ . The absorption cross-sections were then calculated by substituting the value of  $\alpha_i$  in following expression,

$$C_i^{abs.} = \frac{2\pi}{\lambda} \alpha_i \quad (4.3)$$

The calculations are performed with  $a_1 = a_2 < a_3$  as observed from the atom probe results. The values of  $a_1$ ,  $a_2$ , and  $a_3$  are chosen from the average values obtained from Table 4.1 as well as from the STEM observations. The parameters ( $a_1$ ,  $a_2$ ,  $a_3$ ) in nm's used for NP#1, #2, #3 and #4 are (2.7, 2.7, 3.8), (3.0, 3.0, 7.0), (2.0, 2.0, 4.0) and (3.0, 3.0, 6.0) respectively. The NP#1 represents the average size obtained from Table 4.1; NP#2 represents the Au-NC partially analyzed by LaAPT as shown in fig. 4.6 and NP#3 and #4 representing the STEM observed Au-NCs. The experimental bulk absorption spectra and the calculated one are compared in fig. 4.10.

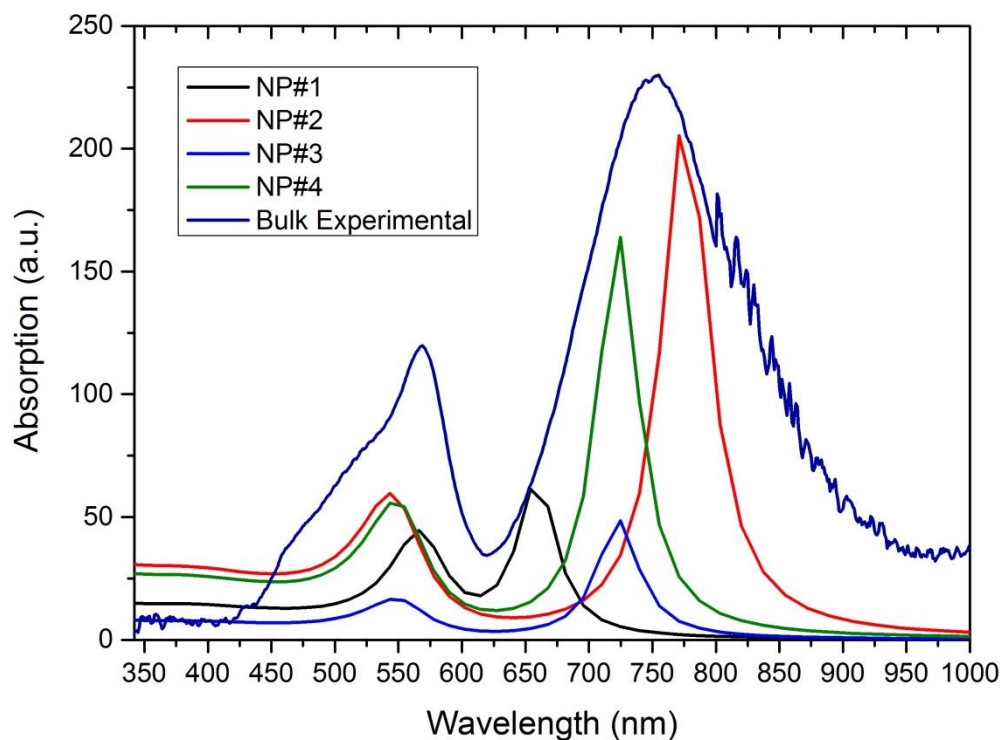


**Figure 4.10** : Calculated optical absorption spectra for Au-NCs of different aspect ratios (see text) embedded in  $Fe_2O_3$  matrix compared with the experimentally measured absorption spectra obtained from bulk thin-film sample.

As shown in the fig. 4.10 the calculated absorption cross-section strongly depends on the size parameters used, but for all the NP's two SPR peaks are observed. For larger NPs (NP#2) SPR peak in IR region is around 775nm and that of in Green region is around 530nm. By decreasing the aspect ratio, the SPR peak in IR region is found to be blue shifted and that of in Green region is red shifted. The measured bulk absorption spectrum envelops all the calculated spectra quite well which clearly suggest the ensemble effect on the bulk absorption spectra. Moreover, spectra calculated for NP#2 and #4 suggest that most of the Au-NPs belong to the size range between these NPs, i.e.  $a_1 = a_2 \sim 3\text{nm}$  and  $a_3$  smaller than 7nm but bigger than 4 nm. The STEM image of the tip reported in fig. 4.5 also supports this observation. It is clear now that both the absorption maxima (570nm and 750nm) are related to the plasmonic absorption due to the Au-NCs. The reason to observe the two absorption maxima is due to the elongated shape of the nanoparticles which gives rise to plasmonic excitations along the major and minor axes of the nanoparticles.

### 4.5.2 Optical absorption of nanotips using FDTD method

Before analyzing the tips in atom probe, their absorption behavior upon illumination of laser light is simulated using finite difference time domain (FDTD) method. For these calculations commercial software of Lumerical is used [17]. To consider the actual tip geometry, tip is represented by a cone terminated by hemispheric cap with radius 20nm and shank angle of  $5.5^\circ$ . For Au- $\text{Fe}_2\text{O}_3$  tip, spherical Au NP's of size ranging from 3-6nm in radius with random distribution was placed all over the tip. The density of the nanoparticles in the simulation geometry was considered from the observed density in the HAADF-STEM images. This geometry is placed in simulated space and surrounded by perfectly matched layers, avoiding any field reflection. The optical constants for Au and  $\text{Fe}_2\text{O}_3$  were taken from [14,15] respectively. The computation of divergence of Poynting vector leads to the 3D absorption maps shown in fig. 4.11(a). Absorption profiles are obtained from the absorption maps by averaging the power absorbed over volume along the tip axis and are plotted in fig. 4.11(b).

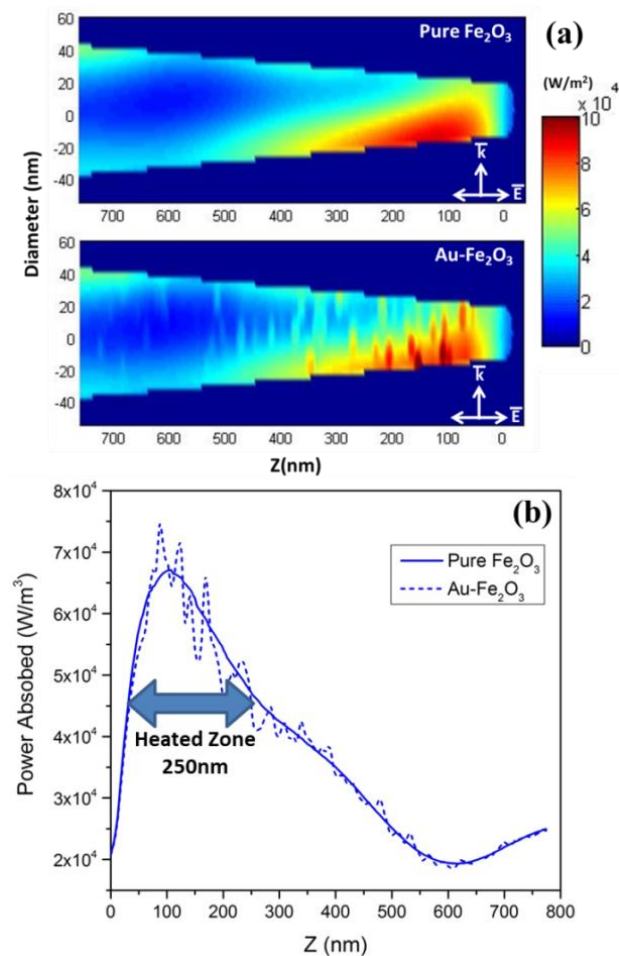


**Figure 4.11** : (a) Absorption maps calculated for  $\lambda=343\text{nm}$  illumination using FDTD method for Pure  $\text{Fe}_2\text{O}_3$  and Au- $\text{Fe}_2\text{O}_3$  nanotips and (b) corresponding absorption profiles obtained from (a)

As shown in fig. 4.11(a), the absorption map for Pure  $\text{Fe}_2\text{O}_3$  and Au-  $\text{Fe}_2\text{O}_3$  shows similar absorption distribution inside the tip upon UV ( $\lambda=343\text{nm}$ ) light illumination except the enhancement of the absorption by the Au-NCs which are in the penetration depth of UV light in the sample. The absorption profiles shown in fig. 4.11(b) clearly indicate that the absorption behavior for both the tips is nearly similar. In both the cases the absorption maxima observed is nearly 100nm from the tip apex. According to our calculation of  $\lambda_{\text{SPR}}$ , the wavelength used for this analysis (i.e.  $\lambda=343\text{nm}$ ) does not belong to  $\lambda_{\text{SPR}}$  and due to this reason the difference reported in the absorption maps for Pure  $\text{Fe}_2\text{O}_3$  and Au-  $\text{Fe}_2\text{O}_3$  nanotips is not more than 15%. However we believe that, this increase in the absorption is underestimated due to the mesh size used to perform the calculations (3nm). Using the smaller mesh size requires powerful computational resources as well as more time. From these absorption profiles we can estimate the size of the zone where the laser energy is absorbed. The absorption maximum is nearly at 100nm from the apex. The heating zone can be estimated from this absorption profile by measuring the width of the peak at 2/3 of the maximum absorption as reported by Houard et. al. [18]. The heated zone obtained in this case is around 250nm.

Similarly, the absorption maps upon illumination of Green light are simulated using FDTD method and are shown in fig. 4.12.

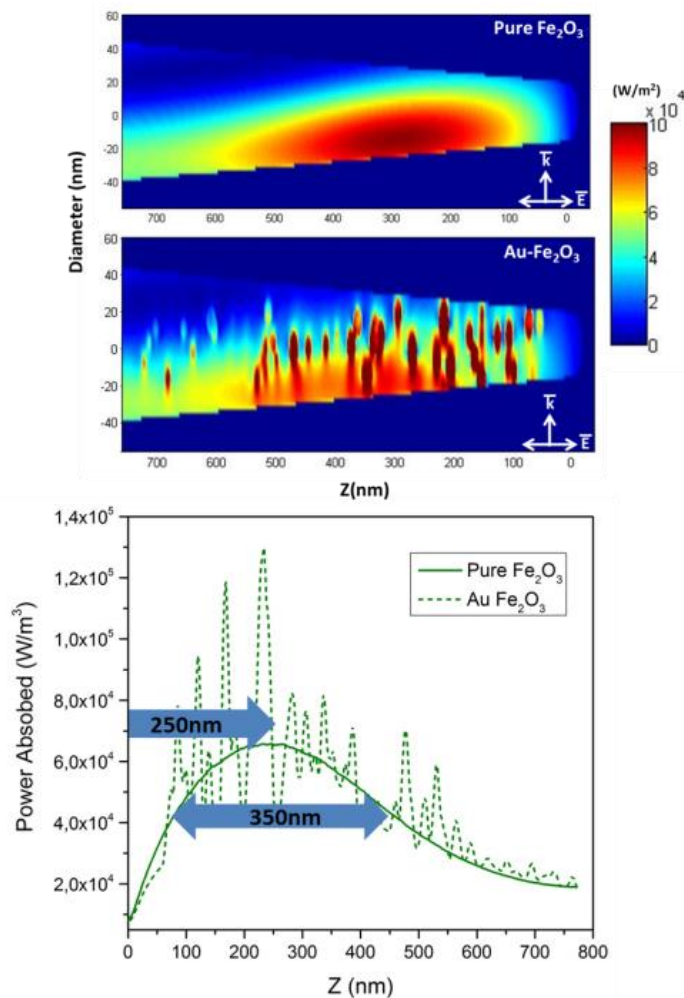


**Figure 4.12 :** a) Absorption maps calculated for  $\lambda=515\text{nm}$  illumination using FDTD method for Pure  $\text{Fe}_2\text{O}_3$  and  $\text{Au-Fe}_2\text{O}_3$  nanotips and (b) corresponding absorption profiles obtained from (a)

The absorption maps for Pure  $\text{Fe}_2\text{O}_3$  and  $\text{Au-Fe}_2\text{O}_3$  nanotips are shown in fig. 4.12(a) which displays similar nature of absorption as in the case of UV illumination. But, the position of absorption maxima relative to the tip apex is farther (250nm) and in addition the width of the absorption zone or heated zone as explained earlier is increased to 350nm in this case. The Green wavelength used (515nm) is near to one of the plasmonic absorption peaks observed (570nm). Owing to this fact the absorption of  $\text{Au-Fe}_2\text{O}_3$  tip shows enhanced absorption due to the Au-NCs unlike the case in UV illumination. This increased absorption can be seen in the absorption maps as well as in the absorption profiles shown in fig. 4.12(b). Again, we are not confident of the absolute value of the absorption in the case of  $\text{Au-Fe}_2\text{O}_3$  sample; due to the large spatial meshes (3 nm) used for the calculations. However, the trend of the absorption profiles along the tip axis, showed in Fig 4.12(b), will probably be unaffected by this mesh size choice. The increased absorption by factor of 2 is reported in presence of Au-NCs due to the

plasmonic resonance. The absorption far from the apex will have its consequences on the ToF spectra measurements.

## 4.6 Analyzing Time of Flight (ToF) Spectra

As explained in the previous chapter, the ToF spectra obtained from the LaAPT experiment is able to provide the good amount of information that can be utilized to understand the optical and thermal properties of the nanotips. The ToF spectra gives understanding on the evaporation dynamics, it is nothing but the total number of atoms evaporated (rate of evaporation) plotted against the time of flight of evaporated ions. The rate of evaporation is governed by the electrostatic field applied and the temperature, which further depends on the efficiency of the laser absorption. The cooling of temperature raised due to laser absorption along the axis of nanotip will have an effect on the nature of ToF spectra and this behavior is used to deduce the thermal diffusivity of the nanotips. To study the optical and thermal properties of nanotips using LaAPT, a rigorous set of experimental protocol is designed and employed. More details of this experimental protocol are explained in next section.

### 4.6.1 Experimental Methods used in LaAPT

The geometry of the nanotip affects a lot in LaAPT experiment, the effect of tip radius and/or shank angle on the quality of data is already reported [19]. Along with this, the laser parameters (e.g. wavelength, laser intensity) and field conditions used to conduct the experiment has strong consequences on the data collected [20,21]. In this context, the experiments are designed in such a way that the tip shape effects will have minimal influence, if not completely avoidable.

The first task was sample preparation, as explained in the section 4.3 of this chapter the Au-Fe<sub>2</sub>O<sub>3</sub> nanotips were prepared by using FIB based sample preparation method along the Au-Fe<sub>2</sub>O<sub>3</sub> thin film. Moreover nanotips without Au-NCs (Pure Fe<sub>2</sub>O<sub>3</sub>) are prepared using the same protocol. The pure Fe<sub>2</sub>O<sub>3</sub> thin films were also prepared by using PLD technique on Si-substrate. Special care was taken during sample preparation, in order to have identical size and shape of the nanotips with and without Au. Hence the effect of geometry on the data obtained by APT on the two samples will be minimized. The SEM images of the two nanotips are shown in fig. 4.13 for comparison.

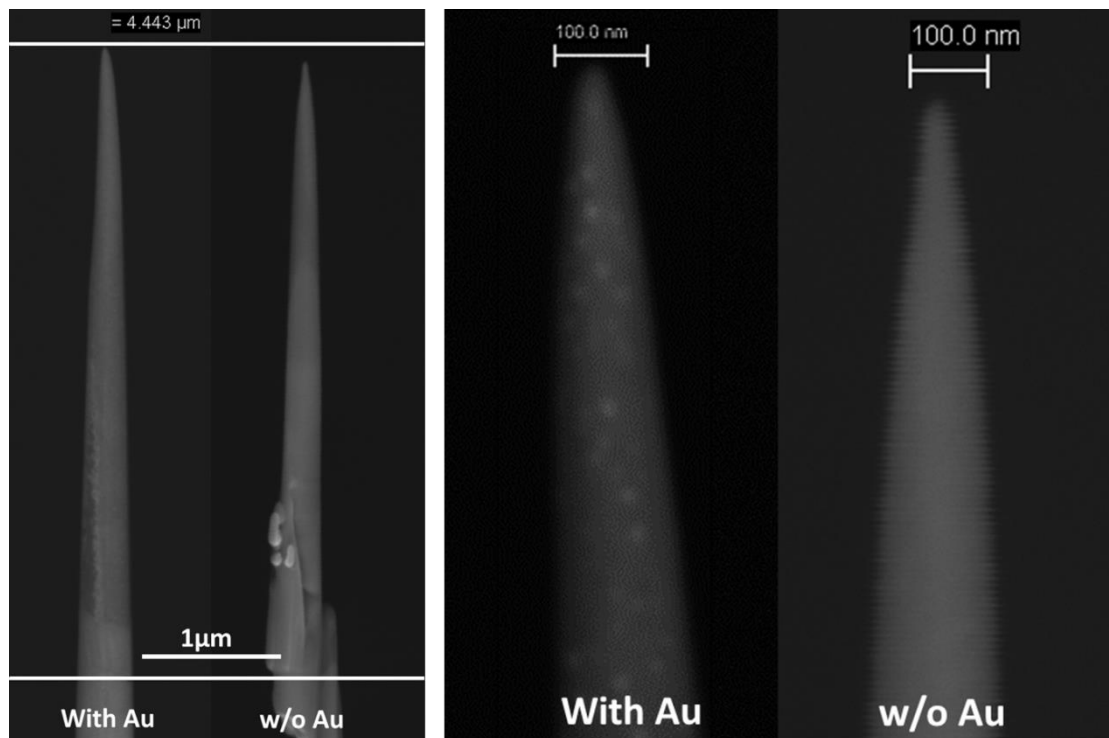


**Figure 4.13** : Comparaison of Au-Fe<sub>2</sub>O<sub>3</sub> and Pure Fe<sub>2</sub>O<sub>3</sub> nanotips : Low magnification SEM image (Left) and high magnified view of the near apex region (right)

As can be seen from fig. 4.13 the length of both the nanotips is around 4 $\mu$ m and the high magnified view shows that the shape and size is nearly similar if not completely identical. The radius and cone angle (half shank angle) are 20nm and 5.5 $^{\circ}$  for Au-Fe<sub>2</sub>O<sub>3</sub> tip, and 15nm and 5.2 $^{\circ}$  for Pure Fe<sub>2</sub>O<sub>3</sub> respectively. The cone angles are measured taking into account the whole length of the tip instead of measuring near apex region.

The next task is to set the parameters for atom probe experiment. The atom probe used in this study is Laser assisted Wide Angle Tomographic Atom Probe (LaWaTAP), a linear atom probe which has a 10cm flight length and equipped with an amplified laser operating at 100kHz, generating pulses of 500fs with tunable energy and wavelength. The experiments in both the cases were carried out at 70K base temperature. The evaporation rate of the ions (ion flux) used was 0.004-0.009 ions/pulse.

For experiments carried out in UV (343nm) wavelength, the laser power used in both the case was 2mW (20nJ/pulse). As far as field conditions are concerned, the voltage is applied to generate nearly same magnitude of macroscopic field ( $E=V/kR$ ). Where, k is the field factor which depends on the shape of the tip. Considering the measured radius and cone angle from SEM and/or STEM images, the initial voltage applied in case of Au-Fe<sub>2</sub>O<sub>3</sub> nanotip was around 4kV and for pure Fe<sub>2</sub>O<sub>3</sub> it was around 3kV; which creates a macroscopic field of nearly 21V/nm in both the cases. This equivalence of electrostatic

field conditions is further confirmed qualitatively by comparing the charge state ratio of  $\text{Fe}^{2+}/\text{Fe}^+$  for both analyses as explained by Kingham [22] using post-ionization theory.

To plot the ToF spectra 500,000 atoms were collected for each data set and similar methods of mass spectra optimization were employed to both the data sets so as to avoid the statistical errors.

#### **4.6.2 Time of flight (ToF) Spectra at $\lambda=343\text{nm}$**

The ToF spectra obtained from Pure  $\text{Fe}_2\text{O}_3$  and Au-  $\text{Fe}_2\text{O}_3$  nanotips are shown in fig. 4.14. As explained in the previous section the experimental protocol employed for both the nanotips is similar which gives us opportunity to compare the ToF spectra of Pure  $\text{Fe}_2\text{O}_3$  and Au-  $\text{Fe}_2\text{O}_3$  nanotips and draw the conclusions therein.

The ToF is plotted relative to the ToF of  $\text{Fe}^{2+}$  peak and to compare the evaporation dynamics at long as well short time scale the ToF is plotted in long time scale (upto 850ns) in fig. 4.14(a) and in short time scale (upto 80ns) in fig. 4.14(b). Different information can be acquired from both these plots at different time scale.

As shown in fig. 4.14(b), the width of the  $\text{Fe}^{2+}$  peak at half and tenth maximum is nearly similar for both the analyses. The sharp peaks are related to the fast evaporation process, where the atoms are evaporated in first few nanoseconds (ns) after laser pulse irradiate the tip. Most of the atoms on the surface of the tip are evaporated during the fast evaporation process and contribute to the sharp peaks observed in the ToF spectra. The existence of this peak is related to the field assisted evaporation, while the width of the peak at 1/10th of the maximum is dependent on the absorption zone (or heated zone), bigger the heated zone; bigger is the width of the peak. As can be understood from the absorption maps and profiles shown in fig. 4.11(a) and (b) the heated zone is nearly similar for both the analyses which reflects in the ToF spectra showing similar width of the peak for Pure  $\text{Fe}_2\text{O}_3$  and Au-  $\text{Fe}_2\text{O}_3$  nanotips.

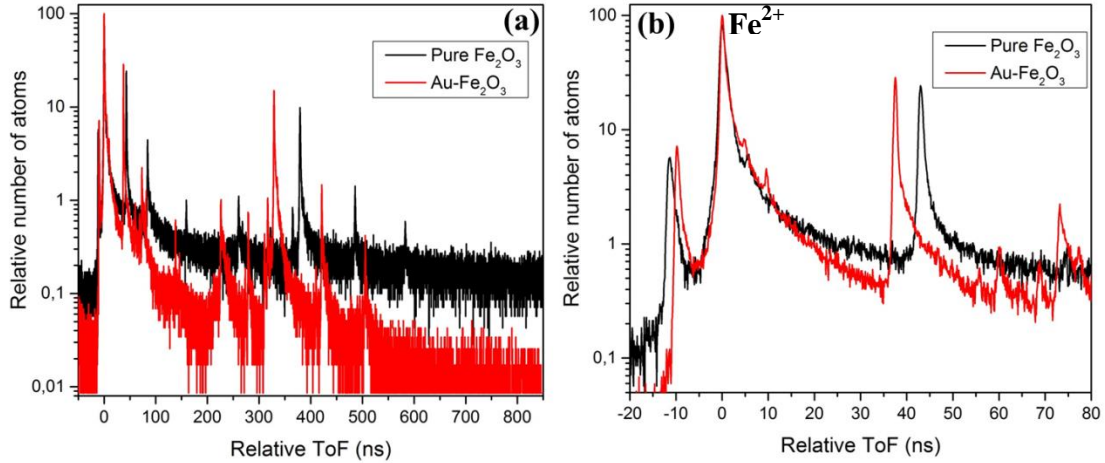


**Figure 4.14** : Time of flight (ToF) spectra comparison of Pure  $Fe_2O_3$  and Au-  $Fe_2O_3$  nanotips obtained at  $\lambda=343nm$  and laser power of  $2mW$  in log time scale (a) and magnified view of the  $Fe^{2+}$  peak (b)

On the other hand, the ToF spectra at long time scale show different signal to noise (S/N) ratio (fig. 4.14(a)). This S/N ratio is related to the cooling dynamics of the tip [19]. The absorption of laser light raises the temperature of the tip apex, this temperature tries to cool down along the axis of the tip and give rise to the thermal tail in ToF spectra. In case of Pure  $Fe_2O_3$ , evaporation rate decreases very slowly as compare to Au- $Fe_2O_3$ . Which means the cooling rate is quite fast in case of Au-  $Fe_2O_3$  nanotip. As far as the experimental conditions are concern, we have nearly similar geometry, the field conditions are comparable, and the nature of absorption of light is also identical in both the analyses. So the fast cooling process in case of Au- $Fe_2O_3$  can be related to the intrinsic property of the material. Inclusion of the Au-NCs can change the thermal diffusivity of the nanotips which give rise to the fast cooling process.

To understand this behavior, the experimental ToF spectra at long time scale are fitted with the calculated one by using the Arrhenius equation of field evaporation [23]

$$K_{norm}(t) \propto \exp\left(\frac{-Q(F)}{k_B T(t)}\right) \quad (4.4)$$

where,

$K_{norm}(t)$  is the normalized evaporation rate given by  $K_{evap}(t) / K_{evap}(t_0)$

$Q(F)$  : Height of the barrier as a function of the applied electric field

$k_B$  : Boltzmann's Constant, and

$T(t) = T(0,t)$  : apex temperature as a function of time and is given by,

$$T(t) = T(0, t) = T_0 + \frac{T_{rise}}{\sqrt{1 + \frac{2Dt}{\sigma^2}}} \quad (4.5)$$

where,

$T_0$  : Base temperature of the tip : 70K

$T_{rise}$  : temperature rise

$D$  : thermal diffusivity

$t$  : time, and

$\sigma$  : Heated Zone : 250nm (from absorption profiles)

The thermal diffusivity of  $Fe_2O_3$  was fixed to  $D= 2.5 \times 10^{-2} cm^2/s$  as reported in ref. [24]. Then, two free parameters  $Q(F)$  and  $T_{rise}$  were used to fit the experimental data. The base temperature used in the analysis and heated zone obtained from absorption profiles are same for both the analyses. As explained earlier, the field conditions are comparable in both the cases, the value of activation barrier  $Q(F)$  can be fixed to nearly 0.09eV. The change in thermal diffusivity ( $D$ ) and temperature rise ( $T_{rise}$ ) will decide the nature of the thermal tail. First the ToF spectra for Pure  $Fe_2O_3$  nanotip was fitted and then keeping all other parameters similar (owing to similar experimental conditions) except thermal diffusivity or temperature rise, the ToF spectra for Au- $Fe_2O_3$  is fitted. The experimental and fitted data is presented in figure 4.15.

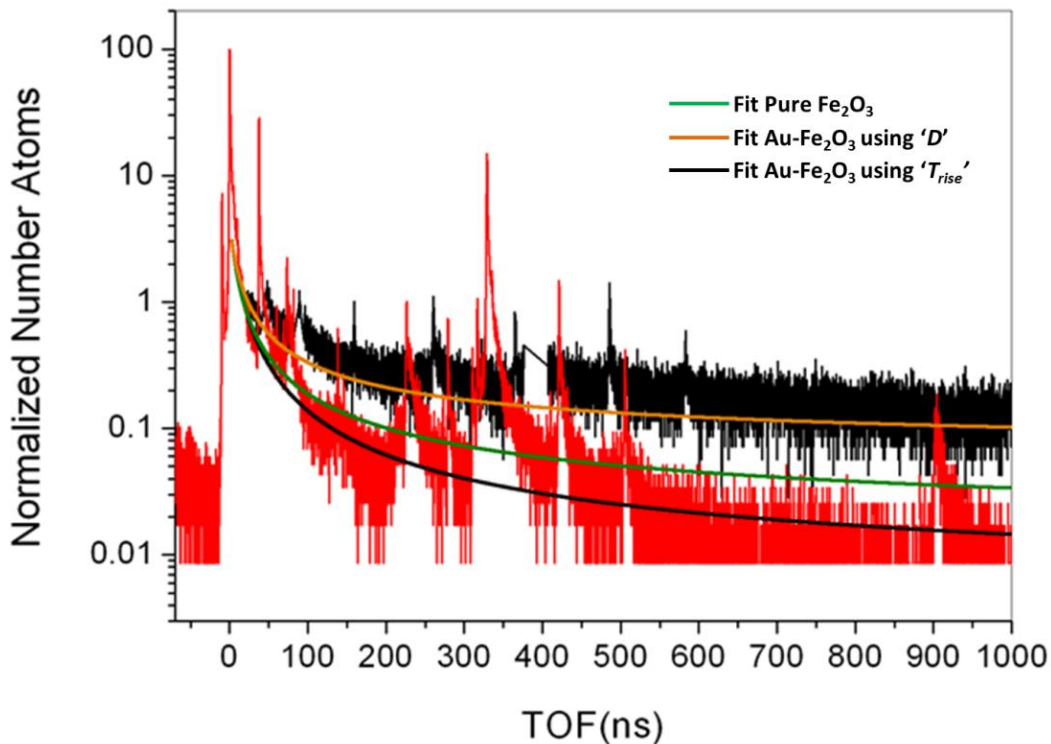


**Figure 4.15** : Experimental and simulated evaporation rate as a function of time for a Pure  $Fe_2O_3$  and Au- $Fe_2O_3$  specimen in APT. Fit parameters:  $D=2.5 \times 10^{-2} cm^2/s$  and  $T_{rise}= 50K$  (orange line),  $D=6 \times 10^{-2} cm^2/s$  and  $T_{rise}= 50K$  (green line) and  $D=2.5 \times 10^{-2} cm^2/s$  and  $T_{rise}= 100K$  (black solid line).

The parameters used to fit the ToF spectrum of pure Fe<sub>2</sub>O<sub>3</sub> are  $Q(F) = 0.09$  eV and  $T_{\text{rise}} : 50^\circ\text{K}$ . Keeping the same values for the barrier and the temperature rise, the ToF spectrum of Au-Fe<sub>2</sub>O<sub>3</sub> is fitted adjusting the value of the thermal to  $6 \times 10^{-2} \text{cm}^2/\text{s}$ , showing more than factor of two increase in thermal diffusivity (the fit is showed by a green line in Fig. 4.15).

An increase of the thermal diffusivity of the sample due to the inclusion of Au NPs is expected for cermet composites [25]. However, when the NPs are well separated (such as in our case) the increase of the thermal conductivity is expected to a few percent, as we can calculate using the formula given in [26]

$$k_c = \frac{k_{mc}[1+2V_{rd}(1-Q)(2Q+1)^{-1}]}{1-V_{rd}(1-Q)(Q+1)^{-1}} \quad (4.6)$$

where,  $Q$  is the ratio of  $k_{mc}$  and  $k_{rd}$ ,  $k_c$  the thermal conductivity,  $V$  the volume fraction and the subscripts ‘mc’ and ‘rd’ refer to the matrix and dispersed particles, respectively.

Hence the large increase of the thermal diffusivity reported experimentally can be related to Au atoms distributed in all the volume. To have information on the Au atoms distribution inside the oxide matrix, we collected the data from different parts of the 3D reconstructed volume. In one volume the presence of Au-NCs is clearly visible, while the other volume doesn’t contain any Au-NC. Then the mass-spectra for both the volumes are plotted and are shown in fig. 4.16. As shown in fig. 4.16, the mass spectra obtained from the volume containing Au-NCs in it clearly shows the presence of Au<sup>+</sup> peak (197amu), which is expected. But, the mass-spectra obtained from the volume without containing any Au-NC also shows the Au<sup>+</sup> mass peak; this clearly signifies the presence of Au in non-clustered form in the matrix.

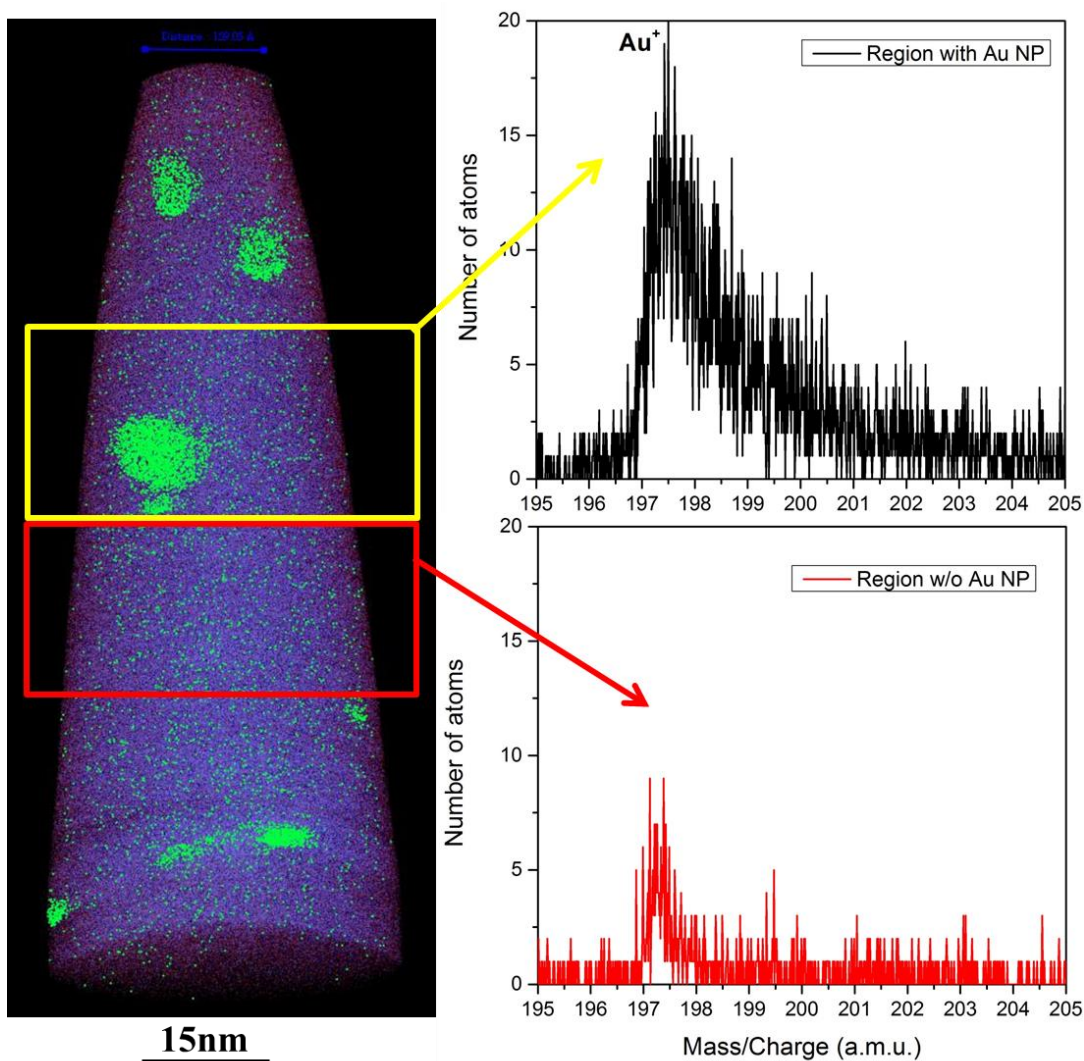


**Figure 4.16** : Comparison of Mass-spectra from two different volumes one with Au-NC in it and one without Au-NCs

This matrix “doping” with metallic Au atoms, can change the diffusivity of the materials increasing the number of phonon frequency modes. Moreover the Au doping can induce network topological effects such as rigidity percolation, chemical ordering, etc. In many glassy systems such as  $\text{As}_x\text{Te}_{100-x}$ ,  $\text{Ge}_x\text{Te}_{100-x}$ , etc., it has been observed that thermal diffusivity increases with the addition of higher coordinated atoms which increase the network connectivity and rigidity [27]. In the case of Mg doped p-type  $\text{BiCuSeO}$  oxiselenides an increase of 30% in the diffusivity is reported for a Mg doping fraction of 5% [28]. However, this increase of the thermal diffusivity is always lower than the increase reported in our case. Connected Au NPs can also strongly increase the diffusivity due to the Au contribution [29]. However, from TEM and APT images, no connections are visible between large or small Au NPs.

All these considerations are supporting the idea that the TOF spectrum obtained on Au-Fe<sub>2</sub>O<sub>3</sub> sample cannot be adjusted changing the thermal diffusivity. Instead the value of the temperature rise can be adjusted.

Hence, we kept the value of the diffusivity as  $2.5 \times 10^{-2} \text{cm}^2/\text{s}$ , as used for pure Fe<sub>2</sub>O<sub>3</sub> sample and we fit the data with the variable parameter: the temperature rise. As shown in Fig.4.15 with the back line, the fit follows well the experimental behavior also at long time scale, better than the previous fit (green line), for a value of  $T_{\text{rise}} = 100\text{K}$ .

Hence, the analysis of the TOF spectra allows the direct measure of the temperature rise at the apex of the sample after the interaction with the laser pulse. Moreover, the comparison between pure Fe<sub>2</sub>O<sub>3</sub> samples and samples containing Au NPs, is a good way to directly determine the enhancement of the heating of the material due to the Au NPs inclusion. In our case an enhancement of a factor two is reported.

Looking at the absorption map, calculated numerically and reported in Fig. 4.11, an enhancement of a factor 1.2 is expected. However, we want to stress that these calculations were done with a mesh size in space too large compared to the NPs dimensions. Due to this we are not confident about the absolute value of the absorption calculated for Au-Fe<sub>2</sub>O<sub>3</sub> sample. This value can be strongly underestimated due to the large mesh size used. More accurate calculations are scheduled.

### 4.6.3 Time of flight (ToF) Spectra at $\lambda=515\text{nm}$

The atom probe experiments with Green wavelength (515nm) were also performed. The experimental protocol, specimen tips and general methods of analysis used were similar to the UV analysis and are explained in the previous sections of this chapter.

The ToF spectra obtained for Pure Fe<sub>2</sub>O<sub>3</sub> and Au-Fe<sub>2</sub>O<sub>3</sub> nanotips are shown in fig. 4.17. Note that the experimental conditions viz electrostatic field, base temperature, evaporation rate were similar in both the analyses like the previous analysis in UV, except the laser power used in this case was around 3mW (30nJ/pulse).

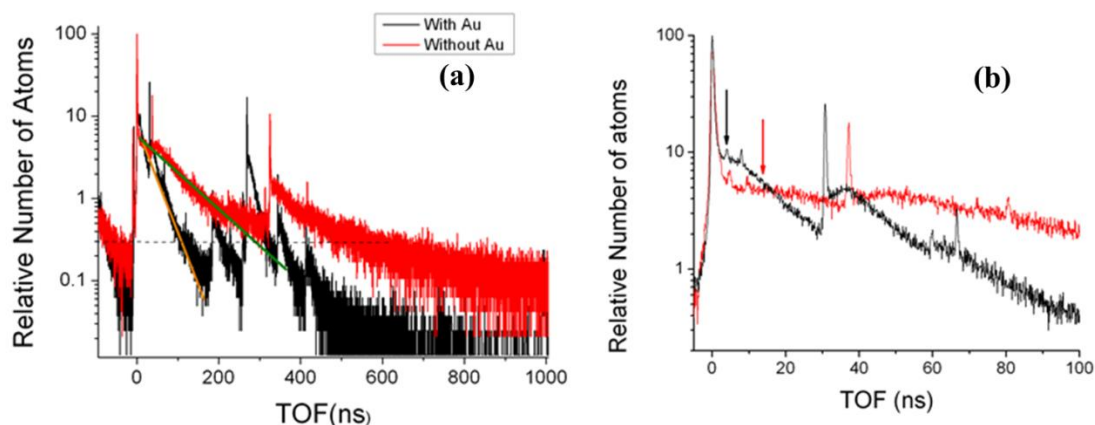


**Figure 4.17 :** Time of flight (ToF) spectra comparison of Pure  $\text{Fe}_2\text{O}_3$  and Au-  $\text{Fe}_2\text{O}_3$  nanotips obtained at  $\lambda=515\text{nm}$  and laser power of  $3\text{mW}$  at long time scale in (a) and at short time scale in (b)

As explained in the previous section the width of the sharp peaks at half and tenth maximum depends on the size of heated zone, the absorption maps and profiles shown in fig. 4.12 confirms that the size of heated zone is nearly same for pure  $\text{Fe}_2\text{O}_3$  and Au- $\text{Fe}_2\text{O}_3$  nanotips. Hence the width of the fast peak is identical for Pure  $\text{Fe}_2\text{O}_3$  and Au- $\text{Fe}_2\text{O}_3$  nanotips as shown in fig. 4.17(b). The ToF spectra at long time scale in fig. 4.17(a) shows that the relative number of atoms decreases three times faster for Au- $\text{Fe}_2\text{O}_3$  nanotips than pure  $\text{Fe}_2\text{O}_3$ , as highlighted in Fig 4.17(a) by the orange and green lines. Following these lines, we can observe that the number of detected ions is divided of a factor ten after 100 ns, for the sample with Au NPs, and after 300 ns, for the sample without Au NPs. This behavior is related to the different rise temperature, which should be three times higher for the Au- $\text{Fe}_2\text{O}_3$  nanotip compared to pure  $\text{Fe}_2\text{O}_3$  tip. These results confirm the behavior observed experimentally during the analysis using UV wavelength. The decreased S/N ratio in case of pure- $\text{Fe}_2\text{O}_3$  nanotip is due to the slow cooling rate of the temperature raised due to the lower laser absorption, and, hence, the lower gradient of the temperature between the apex and the base of the sample.

The striking feature in the analysis of ToF spectra obtained with Green wavelength analysis is the presence of delayed evaporation in pure as well as Au- $\text{Fe}_2\text{O}_3$  nanotip. The delayed evaporation can be identified as a hump next to the fast evaporation peak in ToF spectra shown in fig. 4.17(b). The black and red arrows in this figure show the presence of delayed evaporation for respective curves. The discussion on delayed evaporation is thoroughly explained in chapter 3 and how it can be controlled using geometry of the tip as well as electric field conditions. In this case, as understood from the absorption maps and profiles, the absorption maxima are around 250nm from the tip

apex in both the cases (fig. 4.12). This absorption far from the apex will create the second heating zone around 250nm from the apex and will give rise to the evaporation events delayed in time after the fast evaporation process. Although, we have observed the delayed evaporation in both the nanotips, the position on the time scale is different. For Au-Fe<sub>2</sub>O<sub>3</sub> the hump is closer to the fast evaporation peak than the pure-Fe<sub>2</sub>O<sub>3</sub> (about 13 ns after). Quantitatively, the peak position of the hump in Au-Fe<sub>2</sub>O<sub>3</sub> is around 4 ns and in case of pure-Fe<sub>2</sub>O<sub>3</sub> is around 13 ns from the fast peak. This difference is due to the difference in the temperature rise. Again, if the temperature rise for sample with Au-NPs is three times higher than for pure Fe<sub>2</sub>O<sub>3</sub> sample, the temperature gradient between the heated region at 250 nm from the apex and the apex region will be three times stronger. This will give rise to a three-time faster heat diffusion process and a three time shorter delay for the delayed evaporation (second peak, highlighted by an arrow in Fig. 4.17b).

This explains the data obtained with the analysis in Green wavelength is supporting our findings acquired with the UV wavelength analysis. In both the analyses i.e. UV and Green analysis it is evidenced that the higher absorption of Au NPs in Au-Fe<sub>2</sub>O<sub>3</sub> nanotip is found to increase by factor 2 (for UV) or 3 (for green) the local temperature rise when compare to pure-Fe<sub>2</sub>O<sub>3</sub> nanotips.

## 4.7 Conclusion

In conclusion LaAPT is used to deduce optical properties of the material at nanoscale and the following temperature rise, using Au-nanoclusters embedded in Fe<sub>2</sub>O<sub>3</sub> matrix as a material under study. The results were compared with the pure Fe<sub>2</sub>O<sub>3</sub>. It is found that at the wavelength of  $\lambda=343\text{nm}$  or  $\lambda=515\text{nm}$ , the absorption profile along the tip axis are nearly similar for both the materials, but the enhancement of absorption in case of Au-Fe<sub>2</sub>O<sub>3</sub> nanotip (due to the presence of NPs) is the key findings of this work. The two (three) fold increase in the value of temperature rise can be attributed to the inclusion of Au-NCs as predicted by the calculation of absorption spectra for elongated Au NPs. These results support the use of La-APT as a new and original set-up to measure the temperature increase at nanometric scale after the interaction with a laser pulse.

## References

1. Sorenson S, Driscoll E, Haghghat S, Dawlaty JM. Ultrafast Carrier Dynamics in Hematite Films: The Role of Photoexcited Electrons in the Transient Optical Response. *J Phys Chem C* (2014) **118**:23621–23626. doi:10.1021/jp508273f
2. Cornell RM. *The Iron Oxides: Structure, Properties, Reactions, Occurrences and Uses*. Germany: Wiley-VCH Verlag GmbH & Co. (2003).
3. Sivula K, Le Formal F, Grätzel M. Solar Water Splitting: Progress Using Hematite ( $\alpha$ -Fe<sub>2</sub>O<sub>3</sub>) Photoelectrodes. *ChemSusChem* (2011) **4**:432–449. doi:10.1002/cssc.201000416
4. Wheeler DA, Wang G, Ling Y, Li Y, Zhang JZ. Nanostructured hematite: synthesis, characterization, charge carrier dynamics, and photoelectrochemical properties. *Energy Environ Sci* (2012) **5**:6682–6702. doi:10.1039/C2EE00001F
5. Thimsen E, Le Formal F, Grätzel M, Warren SC. Influence of Plasmonic Au Nanoparticles on the Photoactivity of Fe<sub>2</sub>O<sub>3</sub> Electrodes for Water Splitting. *Nano Lett* (2011) **11**:35–43. doi:10.1021/nl1022354
6. Wang L, Zhou X, Nguyen NT, Schmuki P. Plasmon-Enhanced Photoelectrochemical Water Splitting Using Au Nanoparticles Decorated on Hematite Nanoflake Arrays. *ChemSusChem* (2015) **8**:618–622. doi:10.1002/cssc.201403013
7. Gao H, Liu C, Jeong HE, Yang P. Plasmon-Enhanced Photocatalytic Activity of Iron Oxide on Gold Nanopillars. *ACS Nano* (2012) **6**:234–240. doi:10.1021/nn203457a
8. Miller MK, Russell KF, Thompson K, Alvis R, Larson DJ. Review of Atom Probe FIB-Based Specimen Preparation Methods. *Microsc Microanal* (2007) **13**:428–436. doi:10.1017/S1431927607070845
9. Kreibig U, Vollmer M. *Optical Properties of Metal Clusters*. Berlin, Heidelberg: Springer Berlin Heidelberg (1995). Available at: <http://link.springer.com/10.1007/978-3-662-09109-8>
10. Gault B, Moody MP, Cairney JM, Ringer SP. *Atom Probe Microscopy*. New York, NY: Springer New York (2012). Available at: <http://link.springer.com/10.1007/978-1-4614-3436-8> [Accessed June 10, 2015]
11. Vurpillot F, Bostel A, Blavette D. Trajectory overlaps and local magnification in three-dimensional atom probe. *Appl Phys Lett* (2000) **76**:3127–3129. doi:10.1063/1.126545
12. Larson DJ, Giddings AD, Wu Y, Verheijen MA, Prosa TJ, Roozeboom F, Rice KP, Kessels WMM, Geiser BP, Kelly TF. Encapsulation method for atom probe tomography analysis of nanoparticles. *Ultramicroscopy* doi:10.1016/j.ultramic.2015.02.014
13. Devaraj A, Colby R, Vurpillot F, Thevuthasan S. Understanding Atom Probe Tomography of Oxide-Supported Metal Nanoparticles by Correlation with Atomic-Resolution Electron Microscopy and Field Evaporation Simulation. *J Phys Chem Lett* (2014) **5**:1361–1367. doi:10.1021/jz500259c
14. Johnson PB, Christy RW. Optical Constants of the Noble Metals. *Phys Rev B* (1972) **6**:4370–4379. doi:10.1103/PhysRevB.6.4370
15. Madelung O, Rössler U, Schulz M eds. “Hematite ( $\alpha$ -Fe<sub>2</sub>O<sub>3</sub>): optical properties, dielectric constants,” in *Non-Tetrahedrally Bonded Binary Compounds II* (Berlin/Heidelberg: Springer-Verlag), 1–5. Available at: [http://materials.springer.com/lb/docs/sm\\_lbs\\_978-3-540-31361-8\\_552](http://materials.springer.com/lb/docs/sm_lbs_978-3-540-31361-8_552)
16. *Plasmonics: Fundamentals and Applications*. Boston, MA: Springer US (2007). Available at: <http://link.springer.com/10.1007/0-387-37825-1> [Accessed July 10, 2015]
17. Lumerical Solutions, Inc. (<http://www.lumerical.com/tcad-products/fdtd/>) Available at: <http://www.lumerical.com/tcad-products/fdtd/>

18. Houard J, Vella A, Vurpillot F, Deconihout B. Three-dimensional thermal response of a metal subwavelength tip under femtosecond laser illumination. *Phys Rev B* (2011) **84**:033405. doi:10.1103/PhysRevB.84.033405
19. Arnoldi L, Vella A, Houard J, Deconihout B. Antenna effect in laser assisted atom probe tomography: How the field emitter aspect ratio can enhance atomic scale imaging. *Appl Phys Lett* (2012) **101**:153101. doi:10.1063/1.4757884
20. Gault B, Chen YM, Moody MP, Ohkubo T, Hono K, Ringer SP. Influence of the wavelength on the spatial resolution of pulsed-laser atom probe. *J Appl Phys* (2011) **110**:094901. doi:10.1063/1.3657846
21. Mancini L, Amirifar N, Shinde D, Blum I, Gilbert M, Vella A, Vurpillot F, Lefebvre W, Lardé R, Talbot E, et al. Composition of Wide Bandgap Semiconductor Materials and Nanostructures Measured by Atom Probe Tomography and Its Dependence on the Surface Electric Field. *J Phys Chem C* (2014) **118**:24136–24151. doi:10.1021/jp5071264
22. Kingham DR. The post-ionization of field evaporated ions: A theoretical explanation of multiple charge states. *Surf Sci* (1982) **116**:273–301. doi:10.1016/0039-6028(82)90434-4
23. Vurpillot F, Houard J, Vella A, Deconihout B. Thermal response of a field emitter subjected to ultra-fast laser illumination. *J Phys Appl Phys* (2009) **42**:125502. doi:10.1088/0022-3727/42/12/125502
24. Clauser C, Huenges E. “Thermal Conductivity of Rocks and Minerals,” in *Rock Physics & Phase Relations*, ed. T. J. Ahrens (American Geophysical Union), 105–126. Available at: <http://onlinelibrary.wiley.com/doi/10.1029/RF003p0105/summary> [Accessed December 5, 2015]
25. Kingery WD. Introduction to ceramics. (1960) Available at: <http://www.bcin.ca/Interface/openbcin.cgi?submit=submit&Chinkey=81664> [Accessed December 5, 2015]
26. Wildan M, Edrees HJ, Hendry A. Ceramic matrix composites of zirconia reinforced with metal particles. *Mater Chem Phys* (2002) **75**:276–283. doi:10.1016/S0254-0584(02)00076-7
27. Velinov T, Gateshki M, Arsova D, Vateva E. Thermal diffusivity of Ge-As-Se(S) glasses. *Phys Rev B* (1997) **55**:11014–11017. doi:10.1103/PhysRevB.55.11014
28. Li J, Sui J, Barreateau C, Berardan D, Dragoe N, Cai W, Pei Y, Zhao L-D. Thermoelectric properties of Mg doped p-type BiCuSeO oxyselenides. *J Alloys Compd* (2013) **551**:649–653. doi:10.1016/j.jallcom.2012.10.160
29. Hu W, Guan H, Sun X, Li S, Fukumoto M, Okane I. Electrical and Thermal Conductivities of Nickel-Zirconia Cermets. *J Am Ceram Soc* (1998) **81**:2209–2212. doi:10.1111/j.1151-2916.1998.tb02611.x



# Chapter 5

## **InGaN/GaN quantum wells : Correlation between structural and optical emission properties**

### **5.1 Introduction**

As mentioned in Chapter 1, the optical properties of solids are strongly dependent on their structural properties like size, shape, and chemical composition. The optical properties of solids at nanoscale changes drastically in comparison to their bulk counterparts owing to their changes in the electronic structure upon nanostructuring. Various attempts have already been made in last few years in order to understand the optical properties of nanostructures and further correlate them with their structural properties [1–3]. However most of the efforts were based on the complementary use of Transmission Electron Microscopy (TEM) correlated with different optical spectroscopy techniques. In this approach, the optical properties and the structural properties are studied on different portions of a materials sample. So the one-to-one correlation between structural and optical properties of nanoscaled material is not accomplished thoroughly, although a good amount of information is made available from these studies. In the quest of one-to-one correlation of structural and optical properties Lim et. al. [4] and Zagonel et.al. [5] have studied single nanowire heterostructures using an in-situ approach instead of ex-situ like the reports mentioned above. They have reported the cathodoluminescence (CL) studies along with the structural characterization studied by TEM on the same object. These reports and others clearly show that, with the increasing importance of nanostructured and nanoscale functional materials in the domain of photonics and

optoelectronics, more and more attention is dedicated to the problem of determining the relationship between structural and optical properties of these systems.

As the local variations in elemental chemical composition can strongly influence the optical properties of materials, having knowledge of it will have a strong impact on the study of correlation between structural and optical properties. Atom probe Tomography (APT), with its ability to extract the elemental chemical composition of material in 3-dimensions (3D) at nearly atomic resolution along with the structural information will play a crucial role in this correlative approach.

In this regard, this chapter is dedicated to the study of correlation between structural and optical properties of single nanoscale object containing a set of InGaN/GaN multiple-quantum wells (QWs). The InGaN/GaN QWs have been analyzed by micro-photoluminescence spectroscopy ( $\mu$ PL), high-resolution scanning transmission electron microscopy (HR-STEM) and atom probe tomography (APT). The correlated measurements constitute a rich and coherent set of information which will be presented in subsequent sections in this chapter. The prime objective of this work is to perform the structural and optical characterization on same nanoscale object so as to obtain the direct one-to-one correlation between structural and optical properties. The work presented in this chapter is published in *ACS Nano Letters* [6].

Several tasks were involved in this work, from sample preparation to analyzing the samples by each technique (i.e.  $\mu$ PL, STEM and APT) individually in the beginning and later on the same nano-object. Although I was involved in every aspect of this work, considering my thorough contribution to the APT analysis, more attention will be given to the APT analysis in this chapter. Numbers of attempts were made to analyze the sample using APT until good experimental parameters which results in an accurate composition measurement are encountered. The results obtained with these trial APT experiments are quite interesting and are useful to understand the impact of experimental parameters on the quality of data obtained. Working with incorrect conditions leads to inaccuracy to compositional measurement as well as on the 3D reconstruction of the data. The detailed analysis and the explanations are incorporated in this chapter.

## 5.2 Materials and methods

### 5.2.1 Synthesis of microwires

The InGaN/GaN multi-QW system were synthesized at CEA/CNRS/Universite Joseph Fourier, Grenoble, France and are extracted by FIB milling from self-assembled GaN microwires grown by MOVPE on c-sapphire substrates [7]. Previous studies assessed that these wires present a diameter in the range of 0.7 – 3  $\mu\text{m}$  and are oriented along the c-axis and have m-plane lateral facets [8,9]. The base of the wires is grown at 1040°C using trimethylgallium (TMG) and ammonia precursors as well as silane addition to get n++-doping and to promote the wire geometry. The silane addition is switched off after about 15  $\mu\text{m}$  length to grow an unintentionally-doped GaN part (about 10  $\mu\text{m}$  long) at the top of the wires. The GaN wires are coated at their top with twenty unintentionally doped radial InGaN/GaN quantum wells grown at 750°C (GaN barriers are grown at 870°C). The scanning electron microscopy (SEM) image in fig. 5.1(a) shows a typical as-grown wire. The heterostructure scheme in a longitudinal and transversal cross section is illustrated in fig. 5.1(b) on the SEM image itself and the pictorial representation of the whole nanowire from lateral and top view is shown fig. 5.1(c).

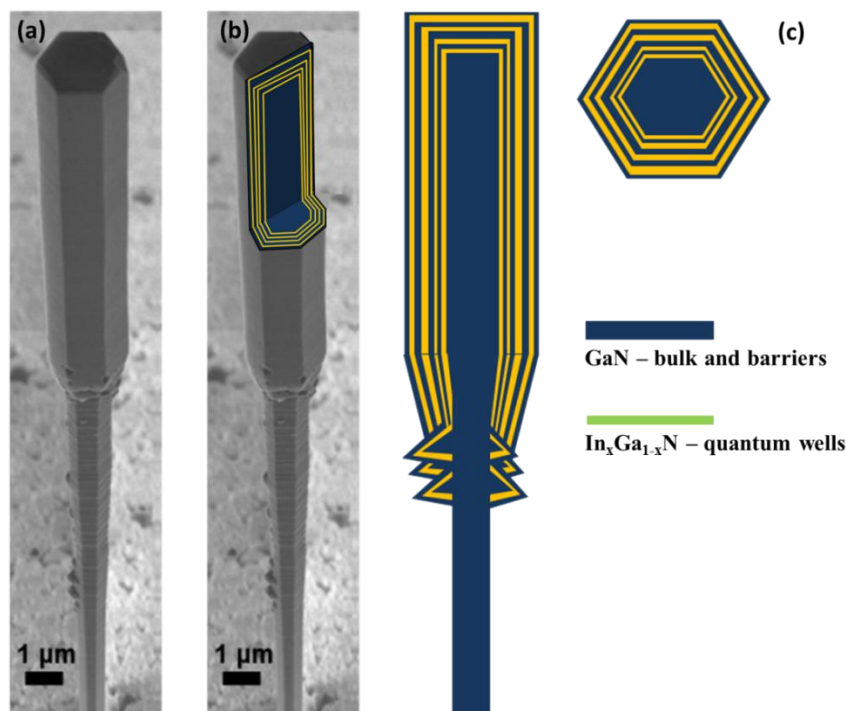


**Figure 5.1 :** (a) Scanning electron micrograph of a GaN wire containing an InGaN/GaN multi-QW system. (b) Schematic illustration of the heterostructure geometry, with the quantum well system depicted in Green and GaN barriers and core in Blue. (c) Pictorial representation of the nanowire from lateral and top view

### 5.2.2 Microphotoluminescence ( $\mu$ PL) and Scanning Transmission Electron Microscopy (STEM)

Micro-photoluminescence spectroscopy was performed at liquid helium temperatures ( $T=4\text{K}$ ). The excitation of the sample was provided by a Ultra-Violet (UV) laser of wavelength 244 nm, with diffraction limited focused beam-waist of the order of 1  $\mu\text{m}$ . The incident power used was around 50  $\mu\text{W}$ . The photoluminescence was analyzed in a 460 mm focal length grating spectrometer, with a spectral resolution roughly equal to 1 nm. The detail experimental set-up is explained in the chapter 2.

High angle annular dark field (HAADF) STEM observations were performed on a JEOL ARM 200F microscope equipped with a Schottky field emitter operating at 200 kV. This instrument is equipped with a spherical aberration Cs-probe corrector correcting the third order spherical aberration. High resolution-STEM (HR-STEM) measurements were also performed to identify the crystallographic orientation and interface geometry of the quantum wells.<sup>3</sup>

### 5.2.3 Sample Preparation for $\mu$ PL and Atom Probe tomography

A non-negligible aspect in the correlative analysis is the sample preparation, because the sample used for  $\mu$ PL measurements and electron microscopy analysis is going to be used for atom probe analysis as well and hence various precautions must be taken. For  $\mu$ PL measurements, the as-prepared microwire as shown in fig. 5.1 can be directly used. But for one-to-one correlation of luminescence signal to the STEM and atom probe results, the geometrical parameters of samples analysed like size and shape should be comparable, if not identical in all the analyses. The whole microwire is too large to draw a representative correlation with an atom probe tip and also it is not suitable to perform the APT and STEM analyses. The differences in  $\mu$ PL signal obtained on as-prepared microwire sample and sample prepared for correlative analysis is thoroughly explained in the section 5.3.1 of this chapter. The sample preparation protocol is designed and developed for the correlative analysis of InGaN/GaN QW's which can be further used to analyse the optically active materials with this approach.

As we have used the focused ion beam (FIB) based sample preparation method, the first and foremost concern was the degradation of luminescence signal due to the energetic  $\text{Ga}^+$  ion beam used in FIB. It is already reported in case of ZnO micro-wires that the luminescence signal is significantly degraded due to the intentionally implanted

regions with different  $\text{Ga}^+$  ion beam doses [10]. To avoid this  $\text{Ga}^+$  beam damage, the extracted microwires were coated with a 400-500nm thick layer of Si using a physical evaporation based deposition method. This Si layer will act as a protective layer and will prevent  $\text{Ga}^+$  ions to penetrate into the samples. The process is schematically shown in fig. 5.2

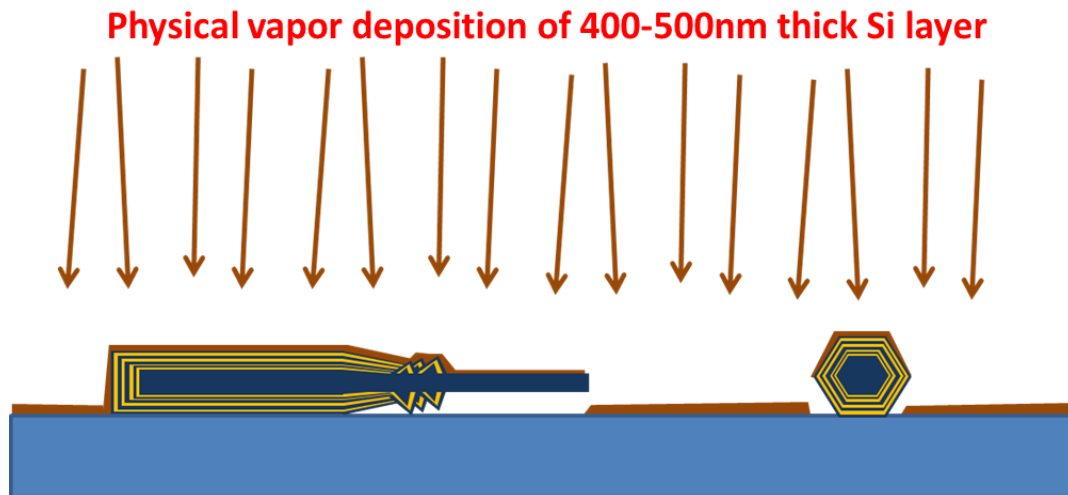


**Figure 5.2** : Schematic depicting the Si-layer deposition on InGaN/GaN micro-wires extracted on substrate (Si-deposition is represented by red color)

The next step is the Lift-off process, which literally means lifting the microwires from the substrate using the  $\mu$ -manipulator available in SEM-FIB dual beam system. The  $\mu$ -manipulator is moved towards the microwire until it touches the microwire, then it is glued using the FIB assisted Pt-C deposition using gas injection system (GIS). Once the deposition is complete and confirmed using SEM imaging, the microwire is lifted-off for further processing. The schematic as well as the SEM image of this process is illustrated in fig. 5.3 (a) and (b)

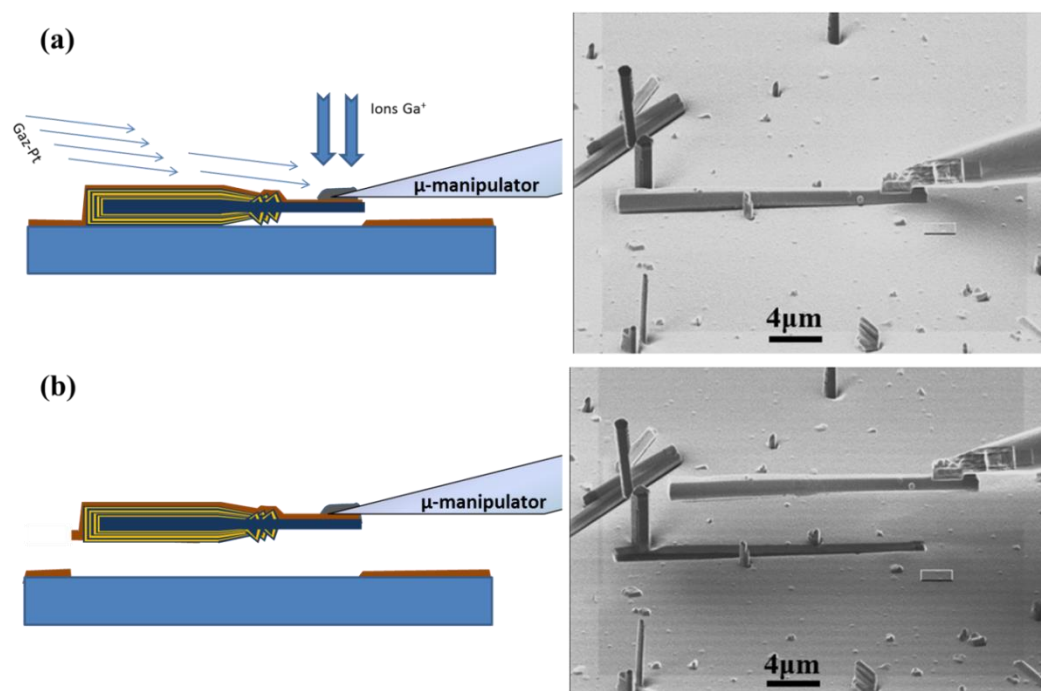


**Figure 5.3 :** Schematic and corresponding SEM image of  $\mu$ -manipulation of microwires, (a) Welding  $\mu$ -manipulator to the microwire using Pt-C deposition, (b) Lift-off process

Once the microwire is lifted-off from the substrate, the next step is to weld it on flat top Tungsten (W) microposts. For that a series of pre-sharpened W-posts were introduced inside the SEM-FIB chamber which later were flattened by using Ga-beam milling in FIB so as to create a firm base for the lifted-off microwire. The process is described using a series of schematics as shown in figure 5.4. At least three good tip specimens can be prepared from a single microwire. Along with the schematics, SEM images of the few steps shown in fig. 5.4 are presented in figure 5.5. The electron beam in these images is parallel to the axis of W-post and hence giving a top view.

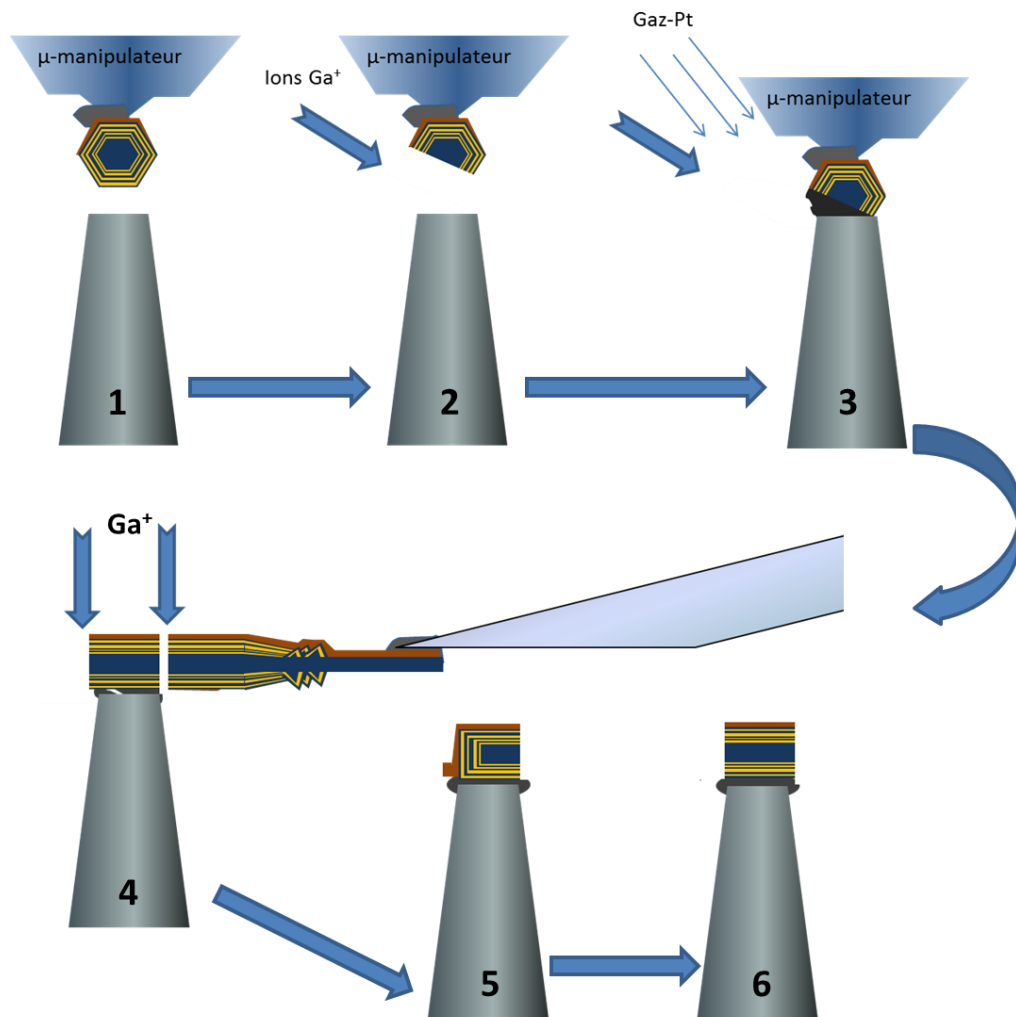


**Figure 5.4 :** Welding the microwire on W-post; (1) Aligning the microwire on top of the W-post, (2) Making groove for Pt-deposition by cutting the base of microwire using Ga ions, (3) FIB assisted Pt-deposition to weld the microwire on W-post, (4) Making a cut through microwire using Ga ions, (5) & (6) Repeating the steps (3 & 4) to prepare another couple of samples from the same microwire.

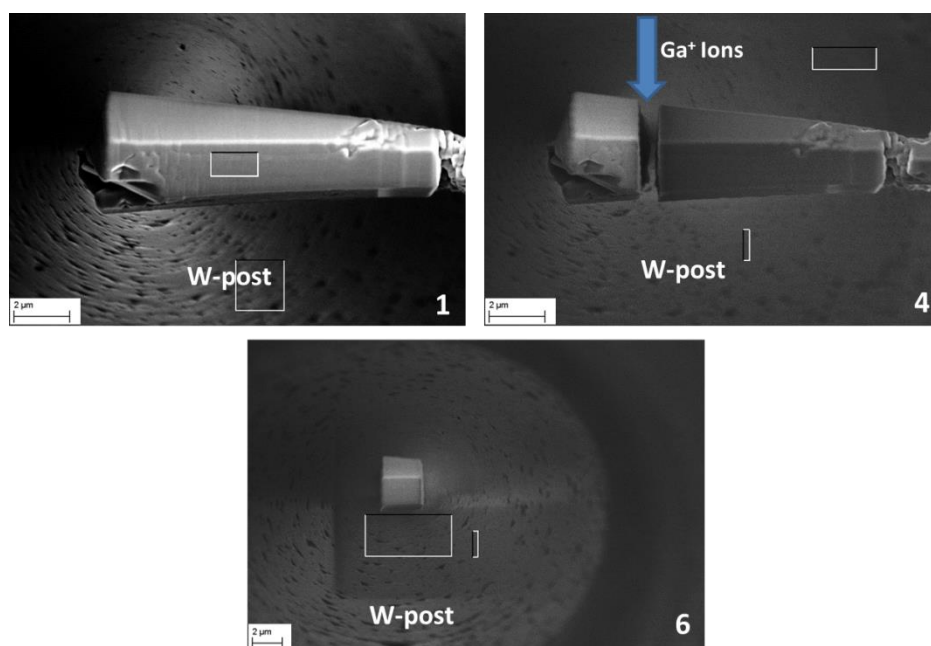


**Figure 5.5 :** SEM images (top view) of the steps (1), (4) and (6) shown in fig. 5.4. (The  $\mu$ -manipulator attached to the microwire is not shown here)

The last step in the sample preparation is annular milling. The sub-portions of microwire previously welded to the W-post are now kept under the ion beam. This time the W-post axis is aligned with the ion beam. The FIB annular milling is performed in two steps. In a first step, performed at ion beam currents in the range 1 nA – 200 pA and beam energy of 30 keV, the volume of the wire section is reduced to a small cylinder whose diameter is of the order of 500-400 nm. This step also eliminates the multi-QWs present on the lateral sides of the wire section from the active volume, leaving intact only the multi-QW system at the top, immediately under the Si coating, as visualized in fig. 5.6(b). The volume, on the other hand, is large enough to preserve the optical properties of the multi-QW system. The nano-object obtained, to which we refer to as “cut-out cylinder” is then ready for the  $\mu$ PL experiment. After performing  $\mu$ PL spectroscopy, a second annular milling step is carried out. In fact, the object volume must be further reduced in order to obtain a sufficiently thin tip to be transparent to electron illumination in the HR-STEM (axial diameter lower than 100-150 nm) and for analysis in the atom probe (apex radius lower than 50-75 nm). This milling step is performed at ion beam current of 50 pA and beam energy of 30 kV. The milling is then concluded with a cleaning step at ion beam current of 50 pA and 2 kV energy in order to obtain a sharp tip and to eliminate the external layer amorphised at 30 keV. The obtained field-emission tip

is visualized in fig. 5.6(c). The schematics and corresponding SEM images of annular milling process is shown in fig. 5.6.

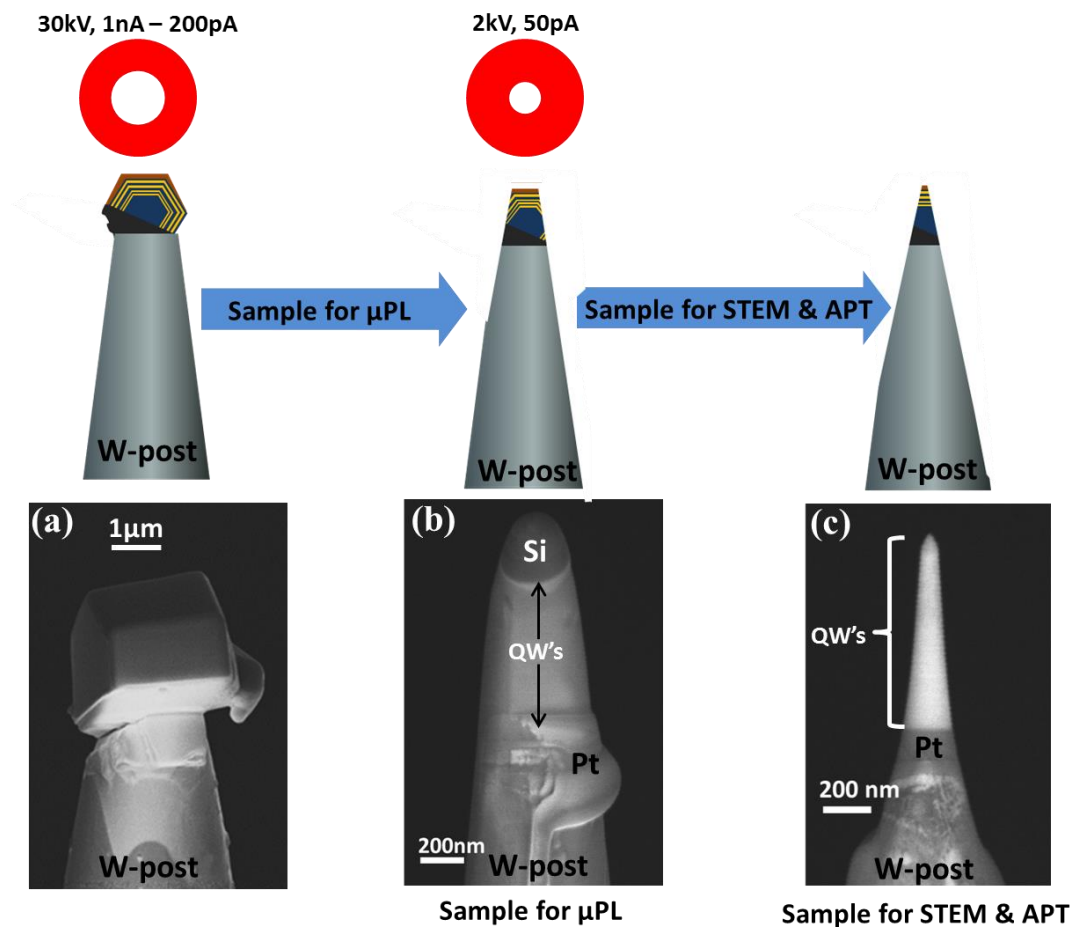


**Figure 5.6 :** Process of annular milling, (a) First step of high current milling, (b) cut-out cylinder ready for  $\mu$ PL measurements, (c) tip sample ready for STEM and APT analysis (Si : Silicon protective layer, QW's : region of set of InGaN/GaN QW's, Pt : Platinum deposition used for welding)

#### 5.2.4 Atom probe tomography of InGaN/GaN QW's

Analyzing InGaN/GaN QW's by Laser assisted atom probe tomography (LaAPT) is one of the crucial tasks involved in this work. Even though it is now possible to analyze the semiconducting as well as dielectric materials using LaAPT, finding the experimental parameters which results in an accurate measurement of the elemental composition is a real task. And hence before performing the correlative analysis on same nano-object several attempts were made to analyze the InGaN/GaN QW's tips in LaAPT so as to obtain the good experimental conditions for an accurate measurement. The measurement of composition is accurate only if all atomic species present in the analyzed specimen are field evaporated and detected with the same rate: unfortunately, this hypothesis does not

generally hold in the case of nonmetallic compounds. Due to different physical mechanisms, compound semiconductors and dielectrics exhibit a complex field evaporation behavior, translating into phenomena such as the detection of molecular ions and ion clusters in the mass spectra [11,12] or the dissociation of molecular ions after evaporation [13]. These complex mechanisms, which are not fully understood yet, can also lead to an erroneous measurement of the elemental composition of the sample. In addition to this, the inhomogeneous geometric or crystallographic properties of the tip surface will also contribute to the inaccurate measurement in composition [14].

The quantum well thickness and elemental composition of InN alloy fraction are the decisive parameters for correlation between  $\mu$ PL signal and the structural properties. An inaccurate measurement of composition would result in misleading conclusions at the end and hence it is important to know how the system of InGaN/GaN QW's behaves in the context of LaAPT experimental condition. In this regard, in the beginning we have analyzed samples without quantum wells (GaN tips) to understand the compositional biases in Laser assisted Wide angle Tomographic Atom Probe (LaWaTAP).

All the experiments were performed using UV wavelength (343nm). The base temperature, atom flux (atoms/pulse), applied voltage ( $V_{dc}$ ) and Laser energy has been optimized to get the stoichiometric elemental composition of Ga and N as (1:1). The effect of laser energy on the total fraction of Ga and N is studied and the results are shown in fig. 5.7

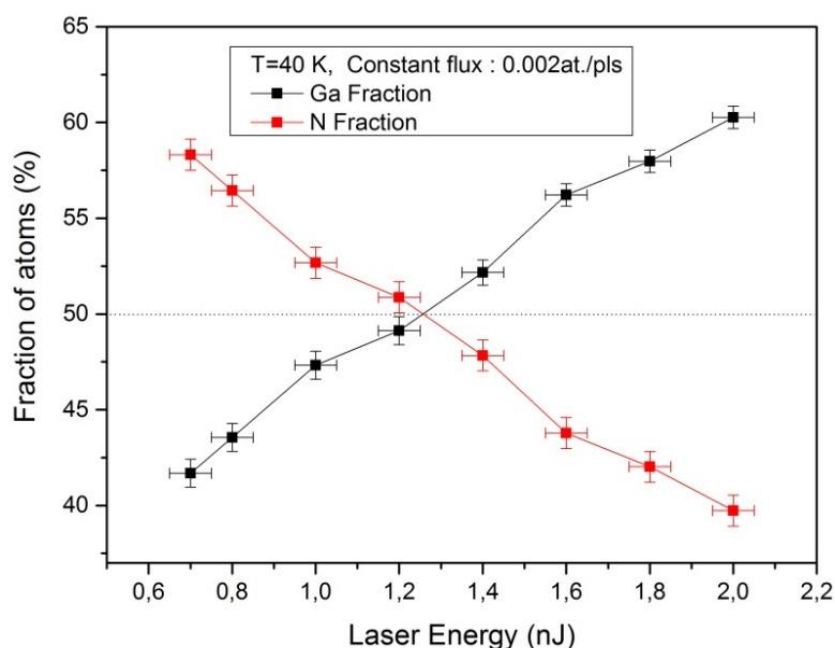


**Figure 5.7 :** Total fraction of Ga and N as a function of Laser energy at constant flux.

The fig. 5.7 is obtained by keeping the evaporation rate constant (0.0022at./pulse) and the laser energy is varied to observe the trend of Ga and N fraction. Please note that when changing the laser energy, voltage applied to the tip is also changed and hence the effective electric field on the tip surface to keep the evaporation rate constant. From fig. 5.7, it is clear that it is possible to achieve reliable 1:1 Ga-N fraction at relatively low laser energies, but it is due to the effect of low laser energy or the higher field created at the surface of the tip due to increase in tip voltage to keep the flux constant or the combination of both. Due to this reason we believe that, analyzing the fraction of Ga and N as a function of laser energy is not a good way to figure out the optimal experimental conditions resulting in accurate measurement of composition. Although qualitative information can be deduced from the plot shown in fig. 5.7, i.e. at low field conditions (at high laser energy) the composition is Ga rich and to obtain good stoichiometry relatively low laser energies (or high field) can be used.

To understand the effective contribution of electric field and/or laser energy on the total fraction of Ga and N, we have performed two different experiments by varying laser energy (applied voltage) and keeping the applied voltage (Laser energy) constant. The trend observed is plotted and presented in figure 5.8

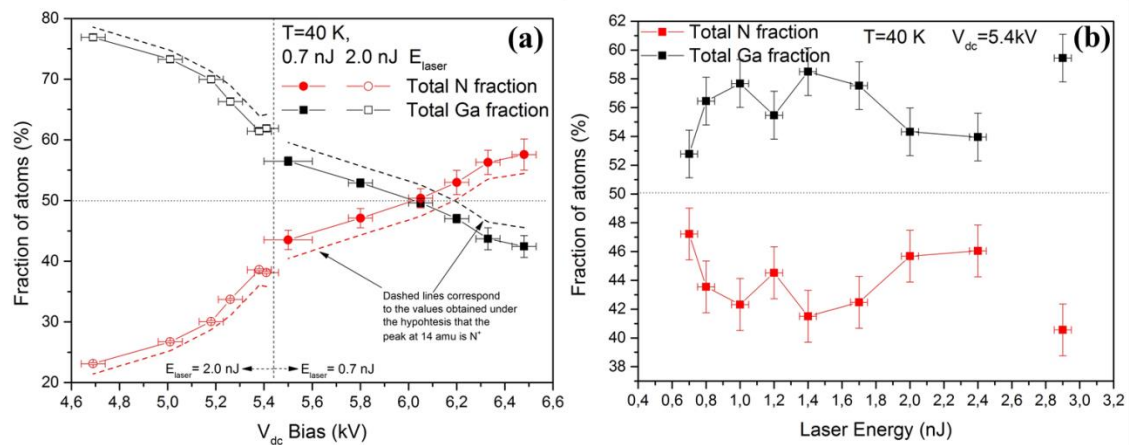


**Figure 5.8 :** Total Ga and N fractions as a function of (a) applied voltage ( $V_{dc}$ ) at constant laser energy (0.7nJ and 2.0nJ) and (b) laser energy at constant applied voltage ( $V_{dc}=5.4$ kV). From [15].

For constant laser energy measurements two sets of measurements were carried out. Considering the analysis at constant flux (fig. 5.7), the laser energy from two extremities viz. low (0.7nJ) and high laser (2.0nJ) energy were chosen to observe the tendency. The applied voltage was then increased in steps and collected nearly 20,000 to 30,000 atoms per data set. The mass spectrum then optimized with similar parameters of

optimization for all data sets and the mass ranges used were also similar. To measure the total Ga and N fractions, special care was taken to consider the total number of atoms as sum of all individual atomic species that were evaporated as ionic species and molecular ions (e.g.  $\text{GaN}^{2+}$ ,  $\text{GaN}_3^+$ ,  $\text{N}_2^+$ ). In addition, the fractions are plotted by considering the peak at 14amu both as  $\text{N}^+$  and  $\text{N}_2^{2+}$  ions in order to observe the difference. As shown in fig. 5.8(a) at constant laser energy of 2.0nJ, the increased in voltage results in the trend towards stoichiometric composition. At low applied voltage (4.7kV) the composition is Ga rich and excess of Ga fraction decreases with the increased in  $V_{\text{dc}}$ . Although stoichiometric composition was not observed in this case, but the overall trend suggests that further increase in  $V_{\text{dc}}$  will result in accurate measurements. Similarly, at constant laser energy of 0.7nJ, the composition is Ga rich at high  $V_{\text{dc}}$  and decrease in total Ga fraction with increased  $V_{\text{dc}}$  is evident. But, in this case at certain  $V_{\text{dc}}$  (6.1kV), the stoichiometry of 1:1 Ga-N fractions is observed. Further increase in the  $V_{\text{dc}}$  results in Ga depleted (N rich) composition and overall stoichiometry is disturbed. The solid line in the plot of fig. 5.8(a) is with the consideration that the peak at 14amu in the mass spectrum is due to the evaporation of  $\text{N}_2^{2+}$  ions. The composition calculated by assigning this peak to  $\text{N}^+$  ions is shown by the dashed line. With this consideration slight change in the overall measured composition is observed but doesn't change the overall tendency of decrease in Ga fraction with the increase in  $V_{\text{dc}}$ . Both these analyses at constant laser energy suggest a strong dependence of the measurement of total Ga and N fractions on  $V_{\text{dc}}$ .

On the other hand, measurements carried out at constant  $V_{\text{dc}}$  are shown in fig. 5.8(b). In this case the applied voltage kept was constant (5.4kV) and the laser energy is increased in steps. The measured total Ga and N fractions as a function of laser energy is plotted and as can be seen from this plot there is no specific trend observed as the laser energy is increased. The amount of Ga and N is barely dependent on the laser energy unlike the case when laser energy is kept constant and applied voltage is varied (fig. 5.8(a)). This analysis clearly shows that the measured composition is highly dependent on the voltage applied or in other words it is more function of applied electric field than the laser energy.

Although it is difficult to calculate the microscopic electric field experienced by the individual atomic species evaporated, an estimate of effective electric field can be made using the charge state ratio of the metallic constituent atoms as described by Kingham [16]. The charge state ratio is an easily measurable quantity in an atom probe experiment and can be directly related to the effective electric field applied. In addition, it

could be a universal parameter to compare the results obtained with different experimental environments (e.g. atom probes, base temp. etc.). In this regard, we have plotted the fraction of atoms as a function of Ga charge state ratio ( $Ga^{2+}/Ga^+$ ) for the data sets acquired at constant flux (fig. 5.7) and at constant laser energies (fig. 5.8) and are reported in fig. 5.9.

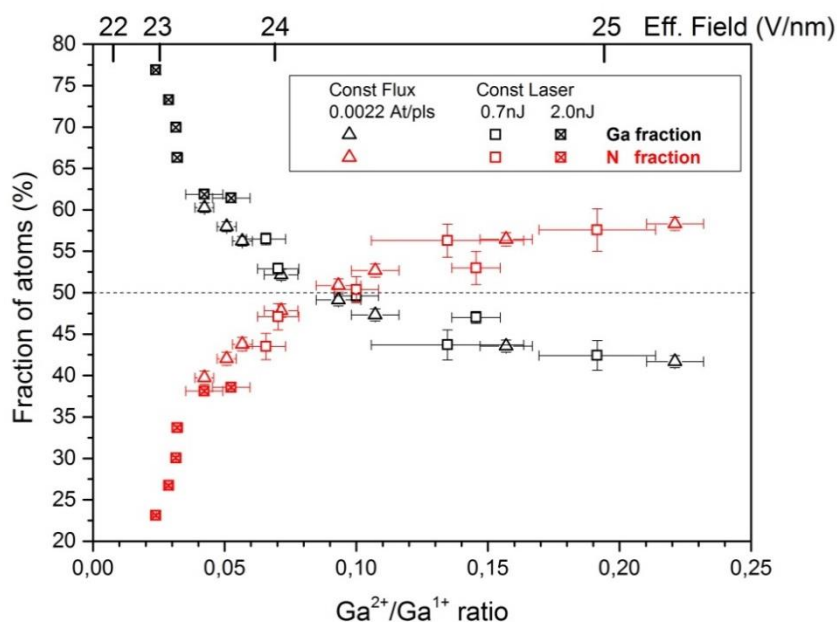


**Figure 5.9** : Total Fraction of atoms as a function of Ga charge state ratio ( $Ga^{2+}/Ga^+$ ). The data acquired at constant flux (fig. 5.7) and constant laser energies (fig. 5.8) were used. The effective field is calculated after Kingham [16]

As shown in fig. 5.9, when the data obtained at constant flux and laser energy is plotted as a function of Ga charge state ratio, it is possible to quantify the experimental condition in terms of charge state ratio (and hence as effective electric field) where the desired stoichiometry is achieved. From fig. 5.9, it is evident that the 1:1 Ga-N ratio is achieved when the  $Ga^{2+}/Ga^+$  charge state ratio is around 0.1, which corresponds to the effective field of nearly 24.3 V/nm calculated after Kingham [16]. The trend is quite similar for both data sets, which again confirms the dependence of applied electric field on the total measured fractions of the Ga and N. As this charge state ratio is further increased (decreased) from 0.1, which signifies the further increase (decrease) in field conditions, the overall composition becomes N rich (Ga rich). This dependency of charge state ratio (or field conditions) on the total Ga and N fractions will be used to characterize the optimal condition which will result in accurate measurement of composition.

In nutshell, from these measurements it is clear that the composition of binary compounds like GaN is strongly dependent on the field conditions used during the atom

probe experiment. The field conditions can be qualitatively represented as a function of charge state ratio of Ga. We found that, when  $\text{Ga}^{2+}/\text{Ga}^+$  ratio is around 0.1, the desired stoichiometric composition can be obtained in case of GaN. To further verify this hypothesis we have studied another binary (AlN, MgO, ZnO) and ternary (InGaN, InAlN) compounds with this approach. The results are published in [15] and suggests that, the surface electric field is the dominant parameter to attain the accurate measurement of composition in these compounds.

Although the composition measurement is predominantly field dependent, one cannot ignore the contribution of asymmetric laser absorption on the variations in composition measurement from laser illuminated side of the tip to the dark side. To observe this effect, data sets at constant flux and laser energies of 0.7nJ and 2.0nJ were selected and concentration maps of  $\text{Ga}^+$  and  $\text{Ga}^{2+}$  on the detector are recorded and represented in fig. 5.10.

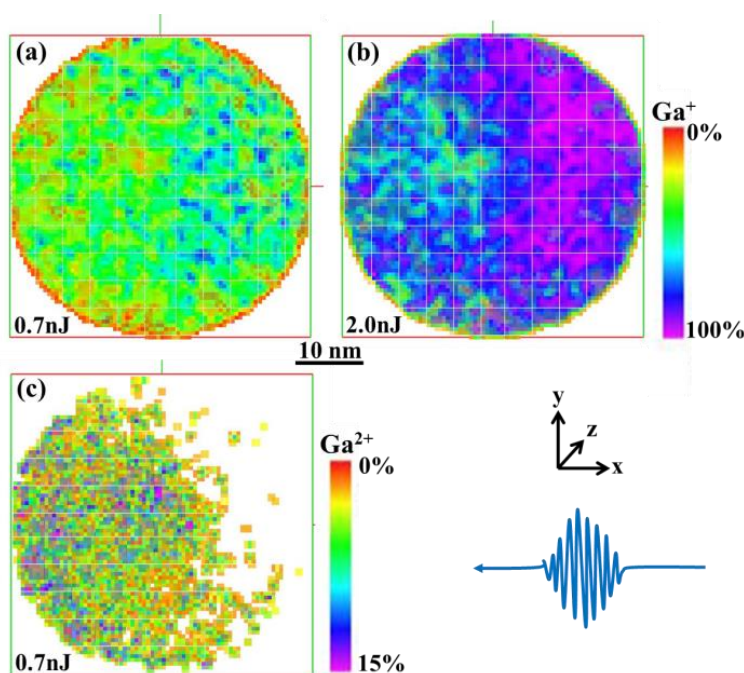


**Figure 5.10** : Concentration maps recorded from the detector at constant flux and laser energy of 0.7nJ for (a)  $\text{Ga}^+$ , (c)  $\text{Ga}^{2+}$  and for laser energy of 2.0nJ for (b)  $\text{Ga}^+$  (The direction of laser incidence is shown at the bottom right of the figure)

As shown in fig. 5.10, at low laser energy (0.7nJ), the distribution of  $\text{Ga}^+$  is fairly uniform with slight increase from the laser illuminated side, also evaporation of  $\text{Ga}^{2+}$  ions is more evident from the dark side (fig. 5.10(c)). While on the other hand at higher laser energy (2.0nJ) most of the Ga evaporates as  $\text{Ga}^+$  ions and that too from the laser illuminated side (fig. 5.10(b)). The concentration of  $\text{Ga}^{2+}$  in this case is below the threshold limit used (1%) to calculate the concentration maps and hence not reported.

Considering the zero barrier evaporation field [17] for  $\text{Ga}^+$  (15 V/nm) and  $\text{Ga}^{2+}$  (39 V/nm), this behavior can be explained as follows. During the analysis, the electric field can be more intense on the dark side of the tip than on the illuminated side; this is due the tip side that is illuminated by the laser is heated more than the dark side which results in more rapid evaporation on the illuminated side. Because of this the evaporation of  $\text{Ga}^{2+}$  ions is more evident from the dark side even at lower laser energy. A Similar behavior was also observed in the case of Si tips when illuminated with UV laser [18]. The behavior is attributed to the deformations of the tip shape due to an inhomogeneous temperature distribution induced by the laser which results in evaporation of large fraction of singly charged ions from the illuminated side. An equilibrium situation and uniform evaporation is established when the tip radius of the illuminated side becomes sufficiently larger than the dark side. Thus, the electric field on the surface of the tip of the illuminated side is lower than the dark side. However, the effect could not be completely rectified but can be minimized by using minimal laser energies in case of materials which has strong absorption coefficient at the wavelengths used during atom probe experiment. This effect also depends on the intrinsic thermal properties of the material like thermal diffusivity (conductivity).

With these analyses we have learnt that the optimal conditions which results in accurate measurement of composition during LaAPT experiment can be attained by governing the surface field conditions using charge state ratio of metallic ions. But it will be quite interesting to see the effect of bad experimental conditions on the data obtained with LaAPT analysis. An example of using very high electric field is given in figure 5.11. The data were collected at constant flux and constant laser energy of 1.6nJ, but the applied voltage was in the range of 11-12.5kV, which creates a very high electric field at the surface of the tip. The  $\text{Ga}^{2+}/\text{Ga}^+$  ratio was on the order of 0.4-0.25 throughout the analysis (fig. 5.11(c)), which corresponds to the field of nearly 26 V/nm. This value of electric field is larger compared to the field (24.3 V/nm) at which accurate measurement of composition is expected. Due to this very high field a strange behavior was observed during the evaporation and is reported in fig. 5.11(a, b) using 3D reconstructed volume of the data obtained.

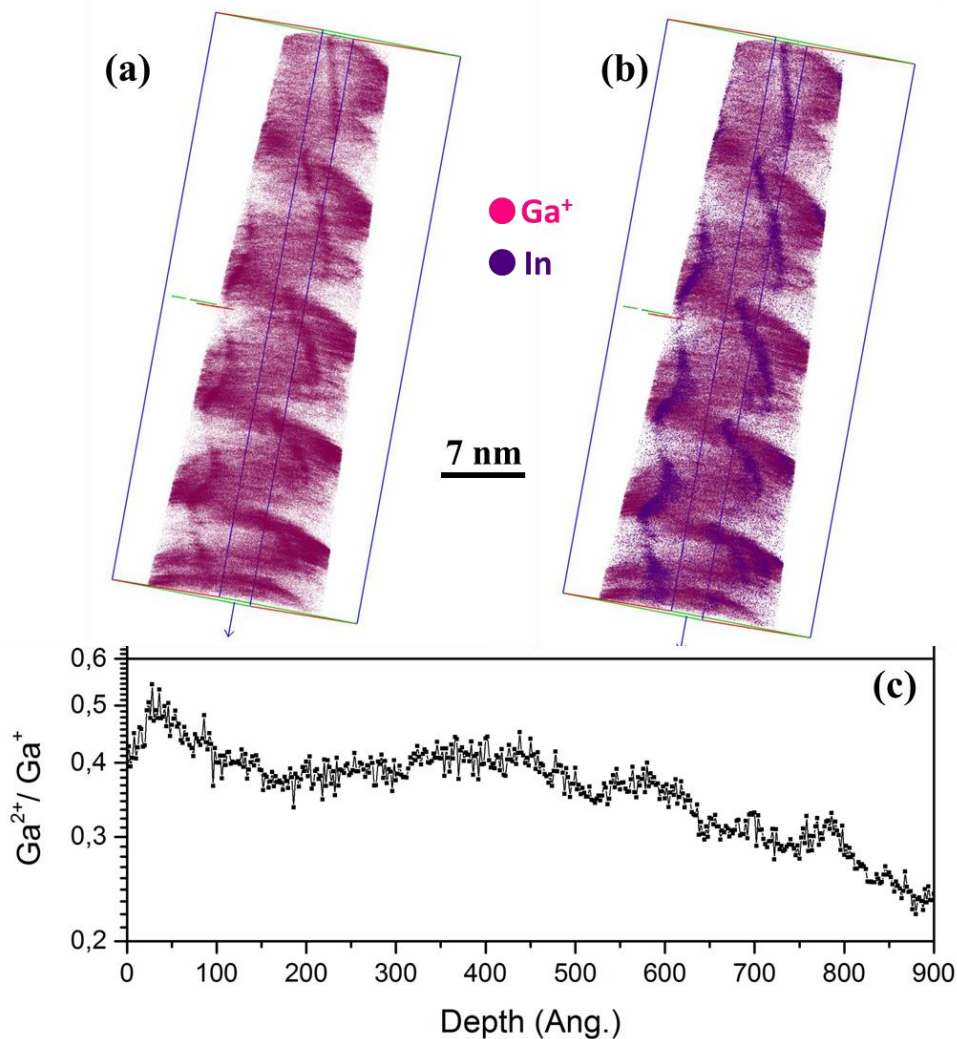


**Figure 5.11** : Effect of high field conditions on the data acquired, 3D reconstructed volume showing only Ga atom distribution in (a), Ga and In atom distribution in (b) and (c) corresponding Ga charge state ratio measured along the depth of the 3D volume shown in (a,b)

The 3D reconstruction showed in fig. 5.11(a) displays a helical structure throughout the analysis, though the reason behind this behavior was not clear. The distribution of all atomic species follows the similar behavior as shown for Ga in this figure. The In QW was nearly parallel to the axis of the tip in this analysis as can be seen from fig. 5.11(b). Looking at the 3D distribution of Ga atoms in fig. 5.11(a) and comparing to that of In atomic distribution in 5.11(b), it is evident that the Ga concentration is found to be increased inside the In QW, which is absolutely erroneous conclusion. A Similar trend was observed in another experiment when working with high electric field. In this case the 3D reconstruction of the data analyzed is significantly better than the analysis shown in 5.11. The Ga charge state ratio was in the range of 0.4-0.2 (corresponds to high field conditions). The 3D reconstructed volume and the analysis therein are presented in fig. 5.12.

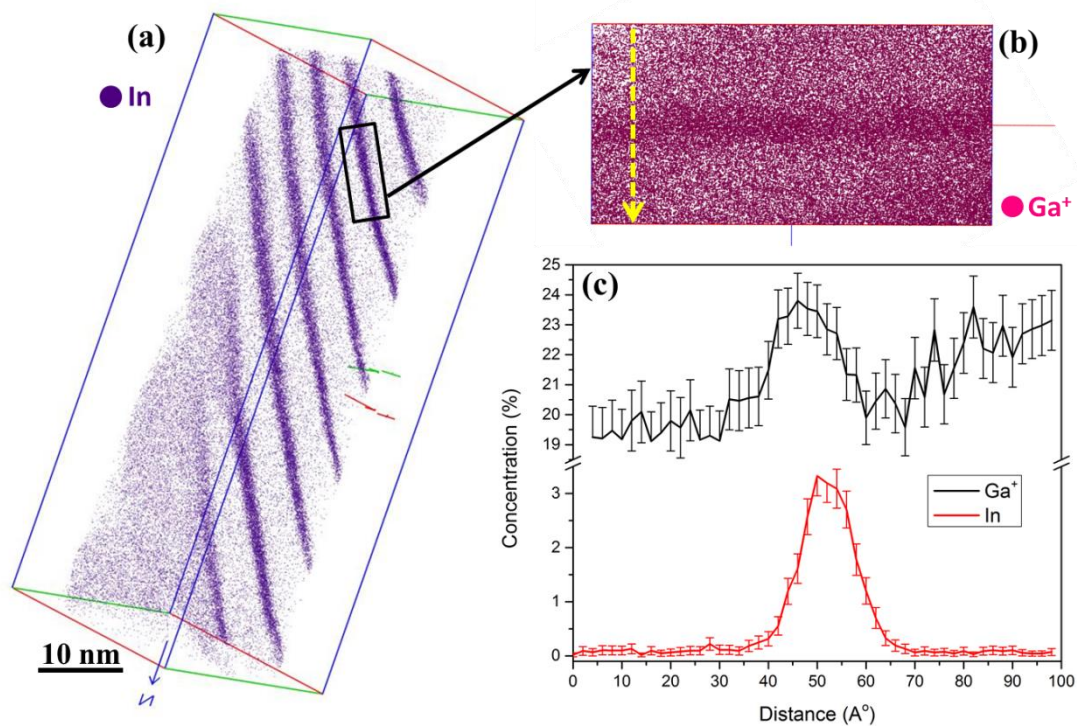


**Figure 5.12 :** Effect of high field conditions on the data acquired, (a) 3D reconstructed volume showing only In atom distribution, (b) Sub-volume extracted from (a) showing only Ga<sup>+</sup> ions and (c) linear concentration profile of sub-volume shown in (b) in the direction shown by Yellow arrow.

The 3D reconstruction displayed in fig. 5.12(a) shows the distribution of In atoms. Total 7 QW's were observed in this analysis of which first five QW's are found to be very well defined and the orientation of QW's is tilted with respect to the axis of the tip. To study the local composition of the QW, a sub-volume from one of the QW's is selected and is shown in fig. 5.12(b). The linear concentration profile is measured from this volume and is reported in fig. 5.12(c). As can be seen in fig. 5.12(b) and measured in fig. 5.12(c) the concentration of Ga<sup>+</sup> ions is increased inside the QW, which is completely misleading. This behavior is surprising and difficult to explain its existence, but probably occurring due to the artefact of the APT technique known as trajectory aberration [19]. Considering the relatively lower field of evaporation for In (12 V/nm), during evaporation the interface between GaN (barrier) and InGaN (QW) is not smooth, which changes the trajectories of Ga ions and intermix with the In ions evaporated from QW. Taking into account the high field conditions in both the analyses presented above, this effect can be further magnified. Though this explanation is quite vague, but can be studied thoroughly to understand the field evaporation behavior of multiphase materials.

With all these trail LaAPT experiments on GaN and InGaN/GaN samples, we are now capable to produce the reliable data set which gives accurate measurement of the composition. So we performed another APT experiment on InGaN/GaN sample with long run collecting nearly 30M atoms with constant laser energy of 0.4nJ, constant flux of 0.05-0.09 at./pulse and at constant base temperature of 20K. Special care was taken to maintain the Ga charge state ratio near to 0.1. In this analysis we were able to analyze the 10 QW's out of 20. The mass spectrum acquired is shown in fig. 5.13. Most of the peaks are indexed. The mass spectrum shows the peaks corresponding to the expected components:  $\text{Ga}^+$ ,  $\text{Ga}^{2+}$ ,  $\text{Ga}^{3+}$ ,  $\text{In}^+$ ,  $\text{In}^{2+}$ ,  $\text{N}^+$  ( $\text{N}_2^{2+}$ ),  $\text{N}^{2+}$ . The presence of molecular species is also noted, more of  $\text{N}_2^+$  at 32amu, but other species such as  $\text{GaN}^{2+}$ ,  $\text{GaN}_3^{2+}$  and  $\text{N}_3^+$  are also present. There is no any parasitic or unknown peak observed. The presence of  $\text{H}^+$  is due to the hydrogen present in the analysis chamber.

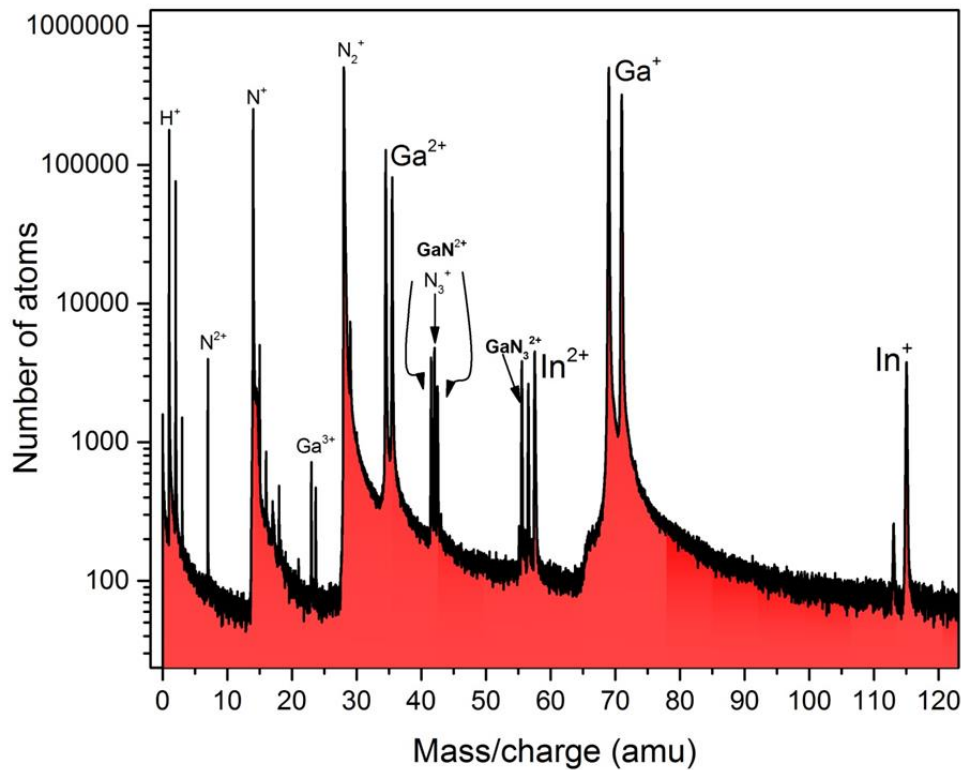


**Figure 5.13** : Mass Spectrum acquired from InGaN/GaN QW's sample

The 3D reconstruction of the data acquired is reported in fig. 5.14 and clearly shows 10 out of 20 QW's. QW's observed are slightly tilted with respect to the analysis direction. This may be due to the inclination of the wire during the analysis, or to the intrinsic tilt of QW's with respect to the axis of W-post. Most of the QWs are well defined except two QW's in the middle. It is possible that these QW's have structural

defect/s which results in thicker QW's. The composition profile, plotted from the 3D reconstructed volume is also shown in fig. 5.14. A sub-volume perpendicular to the QW planes is taken for these calculations.

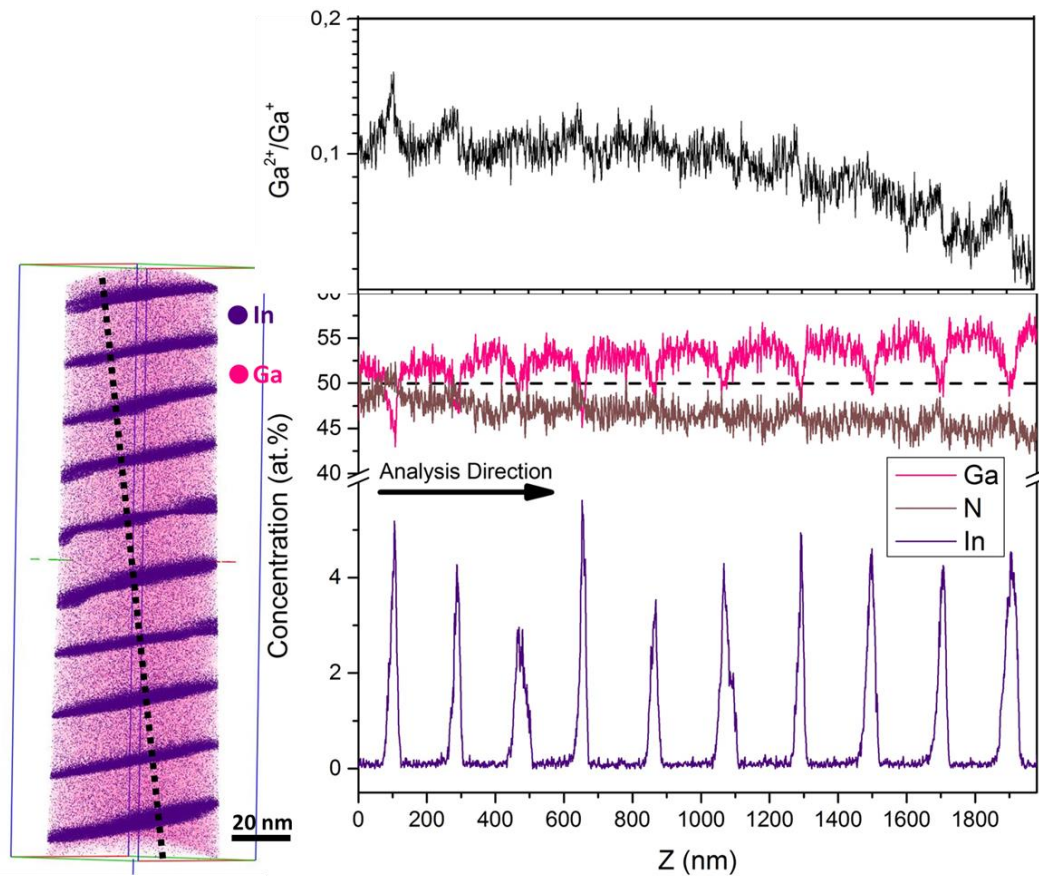


**Figure 5.14** : 3D reconstructed volume and the corresponding composition profile obtained. A sub-volume along the dotted black line drawn on 3D reconstruction used to calculate the composition. The Ga charge state ratio along the analysis depth is also shown (top)

The increased in total Ga concentration along the depth of analyzed volume as shown in fig. 5.14 is a consequence of the tip evolution during analysis. The atom flux throughout the experiment was constant (0.005-0.009 at./pulse). The total flux is proportional to the tip apex surface area which is function of apex tip radius. During the analysis due to the non-zero cone angle of the tip the tip apex radius increases with the analyzed depth and a lower field is needed in order to keep the total flux constant when the tip radius increases. This decrease in field conditions results in increase of overall Ga concentration, which has also been observed during analysis of Ga/N ratio as function of laser energy (fig. 5.7), where increase in laser energy (i.e. decrease in field conditions) gives rise to increase in Ga concentration. In addition, the increase in Ga concentration along the depth can be due to the orientation of sub-volume selected for the measurement (shown by dotted black line on 3D reconstruction). As described previously the

composition is Ga rich on the laser illuminated side than the dark side and to keep the sub-volume perpendicular to the QW's we moved from dark side to the laser illuminated side. The Ga charge state ratio ( $\text{Ga}^{2+}/\text{Ga}^+$ ) is also plotted along the depth of the analysis to display the field conditions. As can be seen from this plot, the Ga charge state ratio is around 0.1 at the beginning of the analysis and decreases slowly representing the decrease in field conditions due to tip evolution as explained earlier. This plot again validates our observation that, when charge state ratio is around 0.1, the stoichiometric conditions can be achieved.

As far as the In fraction in the QW's is concerned, from fig. 5.14 it is seen that it is independent of the stoichiometry of Ga-N or in other words has not affected due to the lowering of field conditions owing to the evolution of tip radius. The overall In concentration for all analyzed QW's is nearly comparable except for the QW number 3 and 5 (thicker QW's). This non-correlating behavior of In with respect to change in field distribution was also reported by our results published in [15]. In addition, Riley et. al. [20] has performed APT analysis on  $\text{In}_x\text{Ga}_{1-x}\text{N}$  QW's with different crystal orientations to examine the influence of surface structure and polarity on the In mole fraction extracted from 3-D APT reconstructions. While the apparent N stoichiometry and the detection probability of group-III ions varied with the polarity of the evaporation surface and the In content, the In mole fraction within QW's was constant throughout the reconstruction. This demonstrates that the compositional inhomogeneity within the In QW's is independent of the crystal structure and polarity of the nanowires as well. For our correlative approach this behavior is very significant as the  $\mu\text{PL}$  signal is strongly dependent on the structural and compositional inhomogeneity in the In-QW's.

The analysis conditions used in LaAPT experiment and its consequences on the structural as well as stoichiometry are summarized in Table 5.1 for a quick review of the discussion presented in this section.

Field Conditions	$\text{Ga}^{2+}/\text{Ga}^+$	Analyses	Stoichiometry
<b>High</b>	0.4 – 0.2	Helical evaporation, increase of Ga inside QW's	Ga depleted
<b>Moderate</b>	0.07 – 0.12	Ideal conditions to work, good reconstruction, Ga depletion inside QW's	Near to stoichiometry
<b>Low</b>	0.02 – 0.04	Change in local radius of the tip from illuminated side	Ga rich

**Table 5.1** : Summary of the analysis conditions and its consequences on the data obtained

With all these aspects and the analyses carried out on different InGaN/GaN QW's tips, we have identified the good experimental conditions which can give a reliable atom probe data. The information acquired during these analyses gave us confidence to successfully perform the correlative analysis of  $\mu\text{PL}$ , STEM and APT on the same nano-object. The results and analysis are presented in the next section of this chapter.

### 5.3 Correlation of $\mu\text{PL}$ Spectroscopy, STEM and APT on single nano-object

To perform the correlative analysis the sample was prepared as explained in the section 5.2.3 of this chapter. The analysis initiated by analyzing the sample by  $\mu\text{PL}$  spectroscopy.

#### 5.3.1 Micro-Photoluminescence ( $\mu\text{PL}$ )

The  $\mu\text{PL}$  study performed on whole as synthesized microwires as well as on the sample prepared by FIB processing as explained in section 5.2.3 (fig. 5.6(b)). The FIB processed sample is like a cylinder of reduced dimensions ( $\sim 500\text{nm}$  in diameter) and hence we called it cut-out cylinder. The results of this study are described in fig. 5.15.

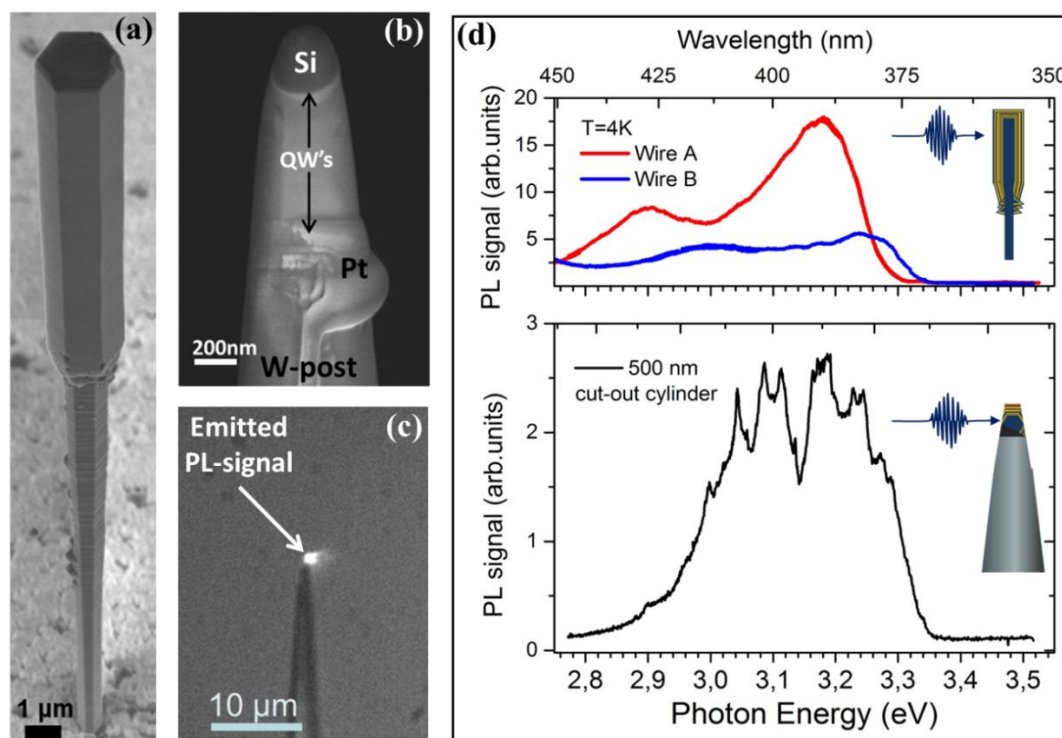


**Figure 5.15 :** (a) SEM image of one of the analyzed microwires; (b) SEM image of analyzed cut-out cylinder; (c) Optical microscopic image of the PL (highlighted by the arrow) emitted by cut-out cylinder mounted on a tungsten tip under excitation with a 244 nm cw laser at 4K. (d)  $\mu$ PL spectra of two whole microwires A and B mounted on a tungsten tip (Red and blue curve, upper part of the graph) and of cut-out cylinder which have been subsequently analyzed by STEM and APT.

The as synthesized whole microwire and the cut-out cylinder prepared from the microwire are shown in fig. 5.15 (a) and (b) respectively. Fig. 5.15(d) reports the  $\mu$ PL spectra recorded under 244 nm cw laser excitation at 4K. The spectra displayed in the upper part of the fig. 5.15(d) were collected from whole microwires like the one shown in fig. 5.15(a), while the spectra in the lower part were issued by the cut-out cylinder as shown in SEM image of fig. 5.15(b). The PL spot emitted by cut-out cylinder is also visualized in the microscopic image of fig. 5.15(c).

The spectra obtained with whole microwires consist of widespread band with two main components or maxima's. On the other hand when analyzing cut-out cylinder, the spectra obtained shows a number of narrow lines dispersed in the interval of photon energy of 2.9 - 3.3 eV unlike the whole microwires where no fine structure was observed. This behavior suggests that the cut-out cylinder is composed of the emitters with well-defined energy which gives rise to the narrow emission lines as observed in PL spectrum. Although the laser beam is tightly focused to spot of  $\sim 1\mu\text{m}$  size, in case of whole microwires the laser still illuminates much larger volume compared to the cut-out cylinder. In addition, the  $\mu$ PL may effectively probe a much larger volume in the case of

a whole wire, due to carrier diffusion and light scattering inside the wire. The PL spectra obtained with cut-out cylinder also follows the broad emission band observed in the PL spectra of whole wire, but with multiple narrow emission lines within this narrow band. This is probably due to the localization phenomena, i.e. the excited charge carriers (electrons in conduction band and holes in valence) form electron-hole pairs which further recombines in the local potential minima which results in the well-defined energy for the emitted photons. Moreover, the energy dispersion, as explained in chapter 1, can originate from the non-uniformity in thickness and compositional fluctuations within the QW and/or from one well to another.

After analyzing the cut-out cylinder by  $\mu$ PL spectroscopy, the second annular milling process by FIB is carried out so as to prepare a tip shaped sample with diameter less than 100nm for further analysis in STEM followed by APT. The process is explained in section 5.2.3 (fig. 5.6(c)). The next step in this correlative study is STEM analysis.

### 5.3.3 Scanning Transmission Electron Microscopy (STEM)

After the second milling step, high angle annular dark field (HAADF) STEM observations were performed on a JEOL ARM 200F microscope equipped with a Schottky field emitter operating at 200 kV. This instrument is equipped with a spherical aberration Cs-probe corrector correcting the third order spherical aberration.

Electron beam can strongly induced the clustering of In atoms, which could significantly influence the interpretation of the correlated  $\mu$ PL and APT measurements [21,22]. Due to this reason only one portion of one quantum well was observed in high resolution to visualize the crystallographic orientation and to study of quantum well interface definition. In addition, to see the effect of electron beam exposure on the distribution of In atoms in atom probe, six innermost QW's were intentionally not imaged with the STEM and hence are not exposed to electron beam at all.

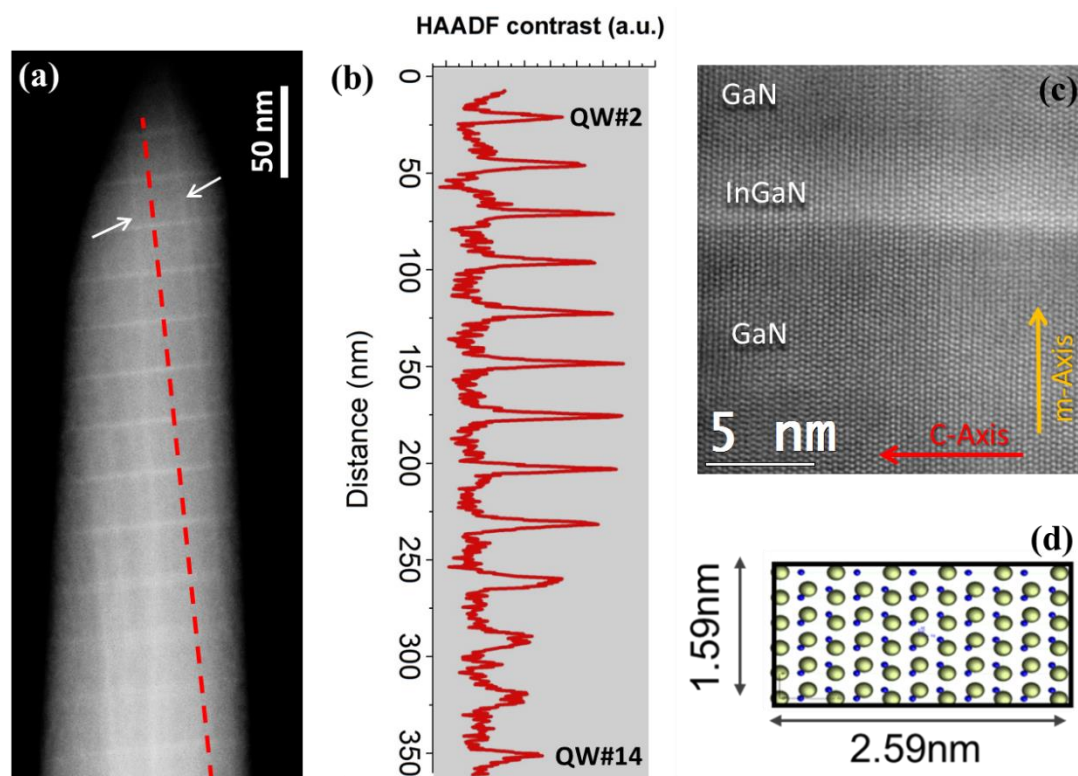


**Figure 5.16 :** (a) STEM-HAADF micrograph of a portion of the atom probe tip prepared from cut-out cylinder. (b) HAADF contrast profile extracted from the red dashed line in (a). (c) High-resolution image from QW#3, showing the details of the quantum well interface and the atomic columns observed along the  $[1\bar{1}20]$  zone axis of the GaN wurtzite crystal. (d) Schematic representation of the crystal structure as observed in (c).

Figure 5.16(a) shows a HAADF-STEM image of the atom probe tip, only first 14 QW's are imaged and the last six QW's (innermost) were not exposed to the electron beam at all. In this image, the InGaN QW's can be clearly seen as bright contrast stripes nearly perpendicular to the axis of the tip. The slight tilt of the QW's is due to the misalignment of the tip axis with respect to FIB gun during the annular milling process. The HAADF-intensity profile reported in fig. 5.16(b) is extracted from the 20nm wide line along the red dashed (perpendicular to the quantum well planes) line shown in fig. 5.16(a). The QW thickness is measured as the FWHM of the HAADF-profile and is plotted in fig. 5.19(b). The QW's are numbered from top to bottom as observed in atom probe tip (i.e. in the reverse order of the growth of the QW's). As can be seen, except QW#11 - #13 all the QW's are thin and are somehow well-defined. Please note that the QW#1 was too close to the tip apex and hence not analyzed.

A closer look at Figure 5.16(a) also reveals the presence of another brighter contrast stripes perpendicular to the QW planes and are highlighted by arrows. The

existence of these stripes was already reported when the micro-wires are grown by this method [8] and are attributed to the stacking faults formed at heterostructure interfaces. As these features are perpendicular to the QW planes and not to the tip axis; the possibility of their appearance due to the FIB processing is ruled-out.

The high-resolution HAADF image of QW #3 is presented in fig. 5.16(c). The brighter contrast region corresponds to the InGaN QW. As seen from this image that the upper and lower interface of the QW are not equivalent. The interface on the core side is more abrupt than one on the surface side. This behavior is related to the growth mechanism and is due to the different temperatures used during deposition to deposit the QW's and GaN barrier [8]. In this image, the atomic columns are also identified which further implies the hexagonal GaN crystal observed along the  $[11\bar{2}0]$  zone axis. The schematics of the atomic column arrangement as seen in high resolution STEM image is shown in fig. 5.16(d). The polar c-axis of the crystal is aligned with the quantum well planes, and the non-polar m-axis is perpendicular to the QW's plane.

### 5.3.3 Atom Probe tomography (APT)

After STEM analysis the tip is transferred to the atom probe chamber for further analysis using atom probe. The experiment was performed in the LaWATAP whose details are given in chapter 2. The analysis was carried out at constant detection flux of 0.005-0.01 at./pulse and at constant energy in the range of 1.0-1.8 nJ/pulse, while the tip is kept at cryogenic temperature of 20K. The DC voltage applied to the tip was varied from 6.2 kV to 10.2 kV to keep the detection flux constant. These parameters, especially the relatively low laser energy used which corresponds to the high surface field, are used to have the correct measurement of the composition as explained earlier in this chapter. The mass spectrum obtained doesn't show any sign of unknown peak and was similar to shown in fig. 5.8 and hence not shown here again.

The data obtained is then optimized and the 3D volume is reconstructed using cone angle-tip radius protocol [23]. The distribution of individual In atoms is presented in fig. 5.17.

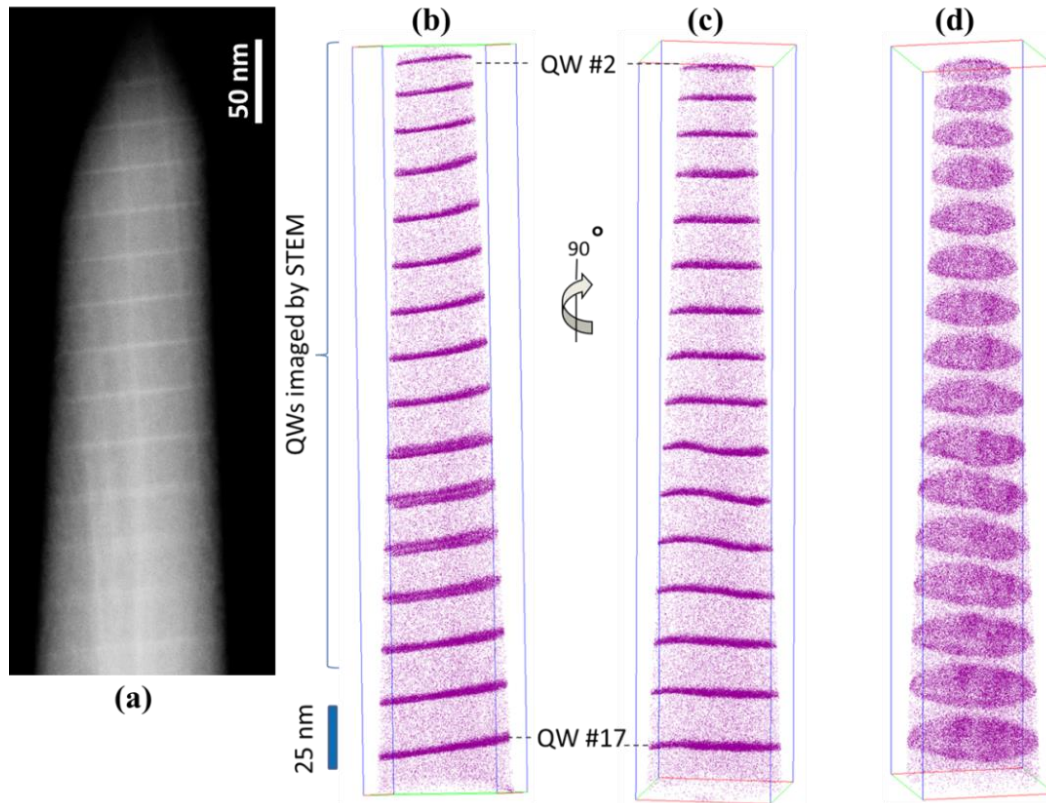


**Figure 5.17** : 3D reconstruction of the data obtained, (b) reconstructed volume oriented as observed in STEM image shown in (a), (c) and (d) reconstructed volume shown from different orientations. (showing only distribution of In atoms for clarity)

The reconstructed volume shown in fig. 5.17(b) is oriented as observed during STEM imaging of the tip, i.e. along the  $[11\bar{2}0]$  direction, and is shown in fig. 5.17(a) again for comparison. In fig. 5.17(c) and (d) the volume is oriented in another perspective, in order to show the planar nature of QW's and non-uniform In distribution within the different QW planes respectively.

Total 16 QW's were analyzed during the atom probe experiment and after 3D reconstruction the InGaN QW's are observed as the flat discs which contains high density of In and depletion of Ga when compare to the barrier regions. Taking into account the higher cone angle of the tip topmost region (see fig. 5.17(a)), the QW's analyzed in this region i.e. QW#2 - #4 appear slightly distorted and also the distance between two QW's is lower when compare to QW's analyzed from the lower part of the tip. The concentration of In atoms ( $< 0.1\%$ ) observed in the barrier region could be due to the residual In present in the barriers but also due to the background noise. The direct correspondence between 3D reconstruction and STEM image as shown in fig. 5.17(a) and (b) is clearly visible. The 3D reconstruction also shows that, except for QW#11 - #13 all other QW's are well defined and narrower. Visualizing these QW's in another orientation

in 3D reconstructed volume reveals that the QW's are little bit curved or they present a sort of smooth step. This information obtained is the advantage of this approach where the information obtained in one method is complementing to the other. The presence of three QW's showing step like feature is not clear, but can be due to the anomaly occurred during the deposition or growth process.

To understand the interface geometry and the individual QW properties, 1D profiles of the InN fraction along the QW system were plotted. The 1D profile were plotted by averaging the concentration in thin slices of material parallel to the QW's plane having cross section of  $10 \text{ nm}^2$  as shown in fig. 5.18(a). The 1D profile showing the InN fraction along the whole QW system is shown in fig. 5.18(b). This profile supports the STEM observation that the QW's have abrupt interface on core side than the surface side, this behavior is more clearly observed when the profiles of QW#4, #12 and #17 are magnified and reported in fig. 5.18(c,d,e) respectively. The QW#12 is one of the thicker QW's observe and hence showing relatively thicker and smoother profile, probably due to the misalignment of the box with the local QW interface. In addition, 3D reconstructed data showing the QW interface of QW#3 along with its HR-STEM image (see fig. 5.18(f)) are in good agreement with each other.

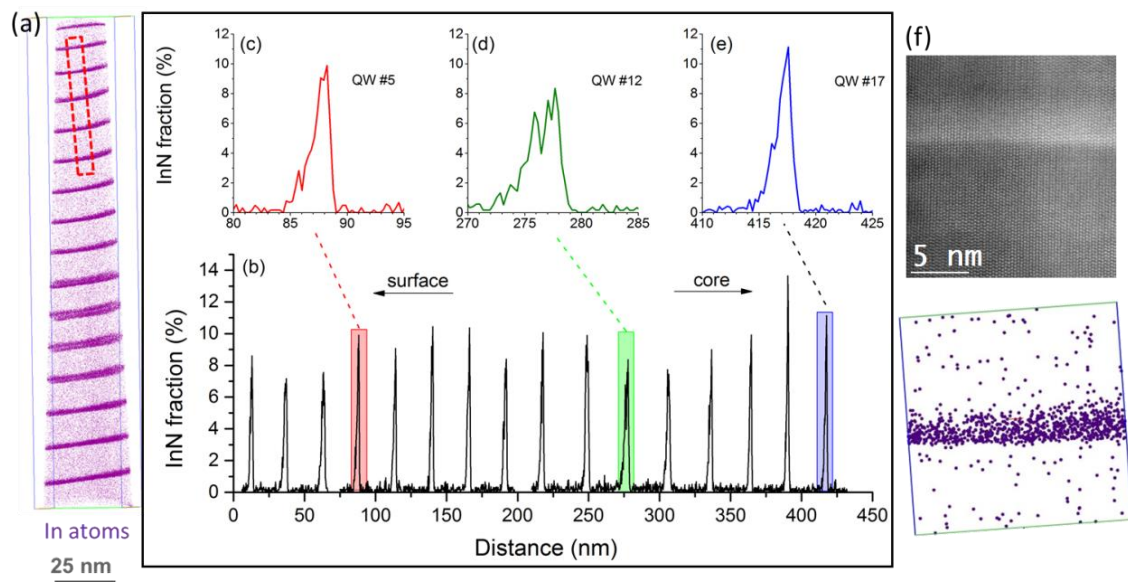


**Figure 5.18 :** (a) One-dimensional profiles of the InN fraction obtained through the analysis of boxes with their  $z$ -axis perpendicular to the QW interfaces. (b) Profile through the whole QW system; (c-d-e) Selected profiles across QWs #4, #12 and #17, respectively. (f) HR-STEM image of QW#3 and corresponding APT reconstructed image showing the interface geometry of QW.

### 5.3.4 Correlating the data obtained

The quantum well thicknesses obtained from STEM-HAADF and APT and peak InN fractions obtained from the 1D composition profile are reported in the fig. 5.19(a) and (b), respectively. The thickness measured as the FWHM of InN rich regions from APT data are in good agreement but slightly lower than those calculated from HAADF-STEM profile. This is because the thickness measurement using HAADF contrast is based on the projection over the whole tip thickness, which may overestimate the measured value of thickness. Due to this reason, the thickness values measured for QW#11 - #13 from APT measurements are more reliable than the HAADF-STEM.

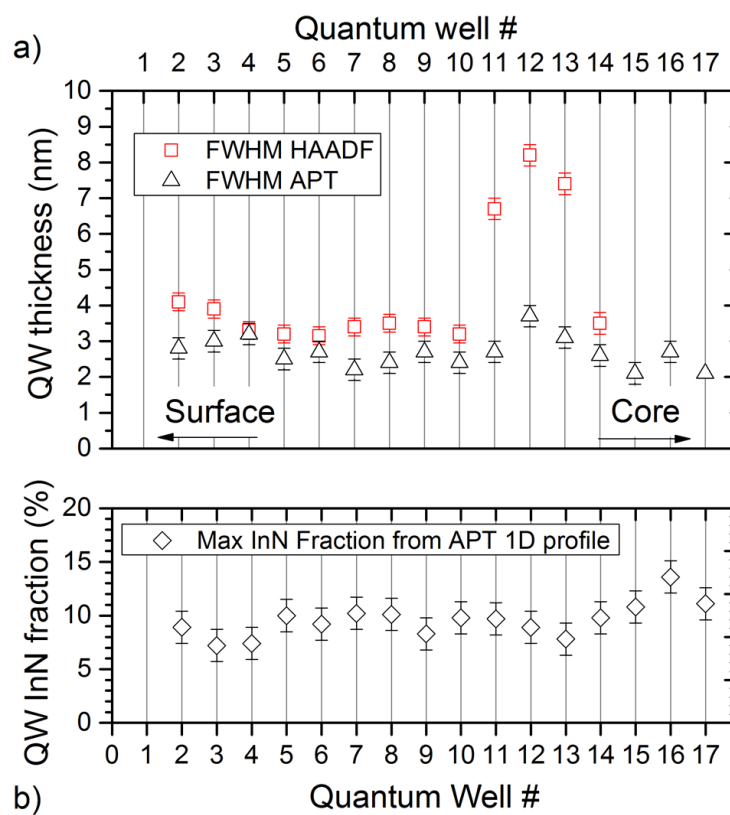


**Figure 5.19 :** (a) Measurement of quantum well thickness taking into account the FWHM of the STEM HAADF contrast profile (red empty squares) and from the APT 1D InN fraction profiles, and as the FWHM of the InN-rich region (black empty triangles). (b) Maximum InN fraction obtained from the 1D APT composition profiles.

In order to find the relation between radiative transitions observed in the PL spectra and the structural properties of QW, it is necessary to understand the local variations in composition within the individual QWs. In this regard, 3D distribution of InN within the QWs is analyzed and the concentration maps obtained for QW#4, #12 and #17 are shown fig. 5.20(a). These concentration maps clearly show that, the In

distribution within the QW's is not uniform particularly for QW#12 and #17. Moreover the 3D reconstructed volume and these concentration maps show that there are several stripe-like In-rich regions and are propagating from one QW to other as highlighted by the red and blue arrows in the image. Considering the slight tilt of the QW system with respect to the axis of the tip, this stripe-like feature progressively shifts outside the analyzed volume by APT and hence not observed in case of QW#4. This also points out that, this feature and hence the In-rich regions are intrinsically present there and are not due to the experimental conditions used to carry out the APT experiment, e.g. laser induced In segregation. Although, the origin of these In-rich regions is out of the scope of this study, but their presence could be related to the specific MOVPE growth conditions, where two different temperatures are used to deposit the QW's and barrier. This observation is also in agreement with the bright contrast stripes observed perpendicular to the QW planes in STEM observation (see fig. 5.16(a)). These stacking faults when crossing the QW planes may induce different strain states within the QW and In atoms may have gathered in higher density in the regions with more favorable strain states. In this way, it is possible that the In-rich patterns propagate throughout the multi-QW system, with a strain-driven correlation mechanism similar to that which drives the growth of self-assembled Stranski-Krastanov quantum dot superlattices in classical III-V [24] and III-nitride systems [25].

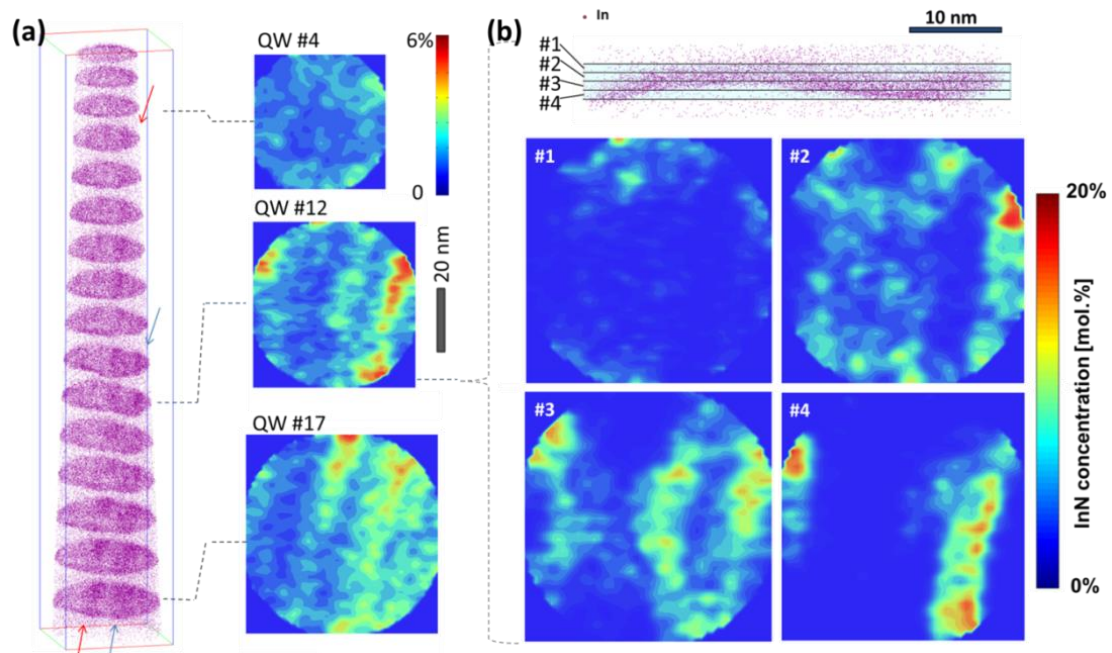


**Figure 5.20 :** (a) 3D In distribution within the QW#4, #12 and #17 (The red and blue arrow shows the propagation of stripe-like feature from well-to-well) (b) InN fraction maps calculated within the 1 nm thick slices of QW #12 shown in the upper part of the figure.

In fig. 5.20(b) the 2D concentration maps are obtained by analyzing 1 nm thick slices across the volume occupied by QW #12. This calculation within regions thinner than the QW thickness allows quantitatively to define the InN fraction. As can be seen from this maps the InN fraction reaches to maximum of 20% in some regions which is almost twice high as observed and as reported in the composition profile of fig. 5.19(b). The shape and the size of these In-rich regions shows a clustering behavior rather than random alloy fluctuations – which can themselves induce carrier localization [26]. The observed In-rich regions strongly support the hypothesis that the radiative recombination take place through the energy minima localized in In-rich regions.

In addition, the InN distribution measured from the QW's which are not exposed to the electron beam at all (QW#16 and #17) shows qualitatively similar behavior as that of the exposed ones, so it is clear that the InN distribution observed is not biased by the previous STEM observations.

All information described above allows thus for a consistent interpretation of the relationship between structural and optical properties of the nanoscale object analyzed. The main conclusions could be drawn by considering the plot in fig. 5.21, which reports on the ordinates the PL emission energy (with the  $\mu$ PL spectrum of cut-out cylinder superimposed) and on the abscissa the InN composition. The different curves represent the calculation of the PL energy of interband transitions taking place in relaxed m-plane non-polar rectangular QWs of different thickness as a function of the InN fraction. The bandgap of bulk InGaN is also reported as a reference. In the plot are also highlighted the InN fractions found by 1D profiling (up to 13%) of APT data and by 3D measurement (up to 20%).

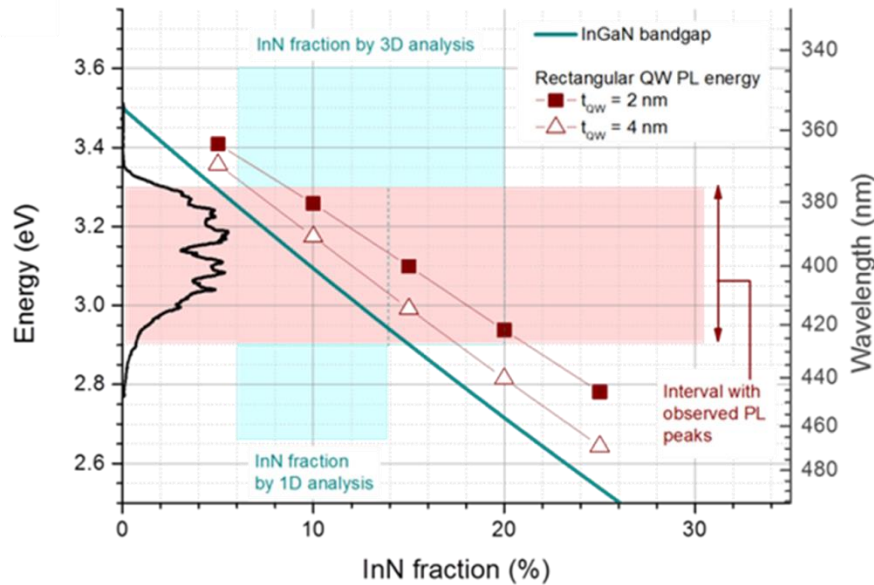


**Figure 5.21** : Dependence on InN fraction of the InGaN bandgap (blue line) and of the InGaN/GaN PL transition energies calculated for rectangular quantum wells of different thickness  $t_{QW}=2\text{nm}$  (filled squares), and  $t_{QW}=4\text{nm}$  (open triangles). The red shaded region corresponds to the interval in which the PL narrow lines have been observed in the analyzed cut-out cylinder; the  $\mu\text{PL}$  spectrum is also reported on the left-hand side axis (black line).

The conclusions that could be drawn on the basis of these calculations are summarized here. The multiple peaks correspond to regions where InN segregation creates local potential wells in which both electrons and holes localize, in a quantum dot-like confining system. The dispersion in the peak energies correspond to the different In content in these regions. The 3D measurement of InN fraction can account for all recorded PL energies, while the lowest energies could not be explained by a simpler 1D profiling.

## 5.4 Conclusion and Perspectives

Since this correlative approach is quite novel, the measures required to carry-out such kind of measurements were introduced in the first half of the chapter. Before conducting the experiments on single nano-object, various samples were analyzed by each technique individually so as to know the good experimental conditions and their implications on the results obtained thereafter. These trial experiments were essential for this correlative approach because the analysis carried out in one technique can significantly alter the conclusions obtained with another technique. In this regard, special care was taken during the sample preparations using FIB based method and its implications on the luminescence signal are mentioned. Along with this a number of

attempts have been made with APT measurements to understand the compositional biases during APT analysis. The elemental composition is found to be strongly dependent on the applied field. Using bad experimental conditions can lead to the erroneous measurement of the composition as shown by few examples in this chapter. In addition to that, the evolution of geometry of the tip shaped sample during the analysis can also influence the final results. Considering all these effects and others, optimal experimental condition for APT measurements which can give a reliable data are obtained and are explained in this chapter.

Once the optimal parameters for each technique and the effects of analysis of one technique on the other are known, the correlative analysis has been performed on the single nano-object containing a set of InGaN/GaN multi QW's. The results and analysis are incorporated in the second half of the chapter.

In summary, in this chapter it is shown that a correlative set of measurements of optical spectroscopy ( $\mu$ PL) and structural characterization (HR-STEM and APT) on the same nano-object, a set of InGaN-GaN multiple quantum wells, gives a very rich set of information. This study, based on the development of a novel nano-analysis technique and its application to the model system of InGaN/GaN quantum wells is motivating and shows a strong aptitude towards correlating the optical and structural properties of the same nano-object. Various other optically active materials like self-assembled quantum dots, quantum dots in nanowires, quantum discs can also be studied using this approach to understand the exceptional correlation between optical and structural properties.

## References

1. Spirkoska D, Arbiol J, Gustafsson A, Conesa-Boj S, Glas F, Zardo I, Heigoldt M, Gass MH, Bleloch AL, Estrade S, et al. Structural and optical properties of high quality zinc-blende/wurtzite GaAs nanowire heterostructures. *Phys Rev B* (2009) **80**:245325. doi:10.1103/PhysRevB.80.245325
2. Rigutti L, Jacopin G, Largeau L, Galopin E, De Luna Bugallo A, Julien FH, Harmand J-C, Glas F, Tchernycheva M. Correlation of optical and structural properties of GaN/AlN core-shell nanowires. *Phys Rev B* (2011) **83**:155320. doi:10.1103/PhysRevB.83.155320
3. Billaud P, Marhaba S, Cottancin E, Arnaud L, Bachelier G, Bonnet C, Del Fatti N, Lermé J, Vallée F, Vialle J-L, et al. Correlation between the Extinction Spectrum of a Single Metal Nanoparticle and Its Electron Microscopy Image. *J Phys Chem C* (2008) **112**:978–982. doi:10.1021/jp076955m
4. Lim SK, Brewster M, Qian F, Li Y, Lieber CM, Gradečak S. Direct Correlation between Structural and Optical Properties of III–V Nitride Nanowire Heterostructures with Nanoscale Resolution. *Nano Lett* (2009) **9**:3940–3944. doi:10.1021/nl9025743
5. Zagonel LF, Mazzucco S, Tencé M, March K, Bernard R, Laslier B, Jacopin G, Tchernycheva M, Rigutti L, Julien FH, et al. Nanometer Scale Spectral Imaging of Quantum Emitters in Nanowires and

- Its Correlation to Their Atomically Resolved Structure. *Nano Lett* (2011) **11**:568–573. doi:10.1021/nl103549t
6. Rigutti L, Blum I, Shinde D, Hernández-Maldonado D, Lefebvre W, Houard J, Vurpillot F, Vella A, Tchernycheva M, Durand C, et al. Correlation of Microphotoluminescence Spectroscopy, Scanning Transmission Electron Microscopy, and Atom Probe Tomography on a Single Nano-object Containing an InGaN/GaN Multiquantum Well System. *Nano Lett* (2014) **14**:107–114. doi:10.1021/nl4034768
  7. Koester R, Hwang JS, Durand C, Dang DLS, Eymery J. Self-assembled growth of catalyst-free GaN wires by metal–organic vapour phase epitaxy. *Nanotechnology* (2010) **21**:015602. doi:10.1088/0957-4484/21/1/015602
  8. Koester R, Hwang J-S, Salomon D, Chen X, Bougerol C, Barnes J-P, Dang DLS, Rigutti L, de Luna Bugallo A, Jacopin G, et al. M-Plane Core–Shell InGaN/GaN Multiple-Quantum-Wells on GaN Wires for Electroluminescent Devices. *Nano Lett* (2011) **11**:4839–4845. doi:10.1021/nl202686n
  9. Chen XJ, Perillat-Merceroz G, Sam-Giao D, Durand C, Eymery J. Homoepitaxial growth of catalyst-free GaN wires on N-polar substrates. *Appl Phys Lett* (2010) **97**:151909. doi:10.1063/1.3497078
  10. Rigutti L, Vella A, Vurpillot F, Gaillard A, Sevelin-Radiguet N, Houard J, Hideur A, Martel G, Jacopin G, Luna Bugallo AD, et al. Coupling atom probe tomography and photoluminescence spectroscopy: Exploratory results and perspectives. *Ultramicroscopy* (2013) **132**:75–80. doi:10.1016/j.ultramic.2013.02.002
  11. Mazumder B, Vella A, Deconihout B, Al-Kassab T. Evaporation mechanisms of MgO in laser assisted atom probe tomography. *Ultramicroscopy* (2011) **111**:571–575. doi:10.1016/j.ultramic.2010.11.017
  12. Tsukada M, Tamura H, McKenna KP, Shluger AL, Chen YM, Ohkubo T, Hono K. Mechanism of laser assisted field evaporation from insulating oxides. *Ultramicroscopy* (2011) **111**:567–570. doi:10.1016/j.ultramic.2010.11.011
  13. Saxey DW. Correlated ion analysis and the interpretation of atom probe mass spectra. *Ultramicroscopy* (2011) **111**:473–479. doi:10.1016/j.ultramic.2010.11.021
  14. Agrawal R, Bernal RA, Isheim D, Espinosa HD. Characterizing Atomic Composition and Dopant Distribution in Wide Band Gap Semiconductor Nanowires Using Laser-Assisted Atom Probe Tomography. *J Phys Chem C* (2011) **115**:17688–17694. doi:10.1021/jp2047823
  15. Mancini L, Amirifar N, Shinde D, Blum I, Gilbert M, Vella A, Vurpillot F, Lefebvre W, Lardé R, Talbot E, et al. Composition of Wide Bandgap Semiconductor Materials and Nanostructures Measured by Atom Probe Tomography and Its Dependence on the Surface Electric Field. *J Phys Chem C* (2014) **118**:24136–24151. doi:10.1021/jp5071264
  16. Kingham DR. The post-ionization of field evaporated ions: A theoretical explanation of multiple charge states. *Surf Sci* (1982) **116**:273–301. doi:10.1016/0039-6028(82)90434-4
  17. Miller MK, Cerezo A, Hetherington MG, FRS GDWS. *Atom Probe Field Ion Microscopy*. Clarendon Press | Monographs on the Physics and Chemistry of Materials 52 (1996).
  18. Koelling S, Innocenti N, Schulze A, Gilbert M, Kambham AK, Vandervorst W. In-situ observation of non-hemispherical tip shape formation during laser-assisted atom probe tomography. *J Appl Phys* (2011) **109**:104909. doi:10.1063/1.3592339
  19. Vurpillot F, Bostel A, Blavette D. Trajectory overlaps and local magnification in three-dimensional atom probe. *Appl Phys Lett* (2000) **76**:3127–3129. doi:10.1063/1.126545
  20. Riley JR, Detchprohm T, Wetzel C, Lauhon LJ. On the reliable analysis of indium mole fraction within In<sub>x</sub>Ga<sub>1-x</sub>N quantum wells using atom probe tomography. *Appl Phys Lett* (2014) **104**:152102. doi:10.1063/1.4871510

21. Bennett SE, Saxey DW, Kappers MJ, Barnard JS, Humphreys CJ, Smith GD, Oliver RA. Atom probe tomography assessment of the impact of electron beam exposure on  $\text{In}_x\text{Ga}_{1-x}\text{N}/\text{GaN}$  quantum wells. *Appl Phys Lett* (2011) **99**:021906. doi:10.1063/1.3610468
22. Smeeton TM, Kappers MJ, Barnard JS, Vickers ME, Humphreys CJ. Electron-beam-induced strain within InGaN quantum wells: False indium “cluster” detection in the transmission electron microscope. *Appl Phys Lett* (2003) **83**:5419–5421. doi:10.1063/1.1636534
23. Gault B, Moody MP, Cairney JM, Ringer SP. *Atom Probe Microscopy*. New York, NY: Springer New York (2012). Available at: <http://link.springer.com/10.1007/978-1-4614-3436-8> [Accessed June 10, 2015]
24. Holý V, Springholz G, Pinczolit M, Bauer G. Strain Induced Vertical and Lateral Correlations in Quantum Dot Superlattices. *Phys Rev Lett* (1999) **83**:356–359. doi:10.1103/PhysRevLett.83.356
25. Yang X, Arita M, Kako S, Arakawa Y. Formation of m-plane InGaN/GaN quantum dots using strain engineering of AlGaN/AlN interlayers. *Appl Phys Lett* (2011) **99**:061914. doi:10.1063/1.3626589
26. Watson-Parris D, Godfrey MJ, Dawson P, Oliver RA, Galtrey MJ, Kappers MJ, Humphreys CJ. Carrier localization mechanisms in  $\text{In}_x\text{Ga}_{1-x}\text{N}/\text{GaN}$  quantum wells. *Phys Rev B* (2011) **83**:115321. doi:10.1103/PhysRevB.83.115321

# Conclusion and Perspectives

This thesis is making a serious attempt to understand the possibility of using Laser assisted Atom Probe Tomography (LaAPT) as a spectroscopic tool to unveil the optical absorption properties of the material at nanoscale. The metal-dielectric composites have a potential to be used as a materials for renewable energy, owing to their improved efficiency towards light absorption. In this regard, the samples with Au-nanoparticles embedded in MgO and Fe<sub>2</sub>O<sub>3</sub> matrix are studied to understand the effect of nanostructuring on their optical absorption characteristics using LaAPT.

The results obtained with Au-MgO samples are quite commendable and displays the new findings on the absorption properties of nanotip shaped samples. Taking into account the resonant absorption for bulk samples in Green wavelength, it was expected that the results obtained with near resonance wavelength (515 nm) and at the resonance wavelength (570 nm) will be far superior to that of UV (343 nm) wavelength. But, due to nanoscale geometry of the sample, owing to the diffraction effects, it is found that the UV wavelength is more efficient. Although our numerical results shows higher magnitude of absorption for Green wavelength, when it comes to the LaAPT analysis more importance is given to the spatial position of absorption instead of its magnitude. In fact, in case of UV wavelength, the maximum absorption is located in the region of high Au NPs concentration (near the apex), however, in the case of Green, the maximum of absorption is far from the maximum of Au NPs concentration, reducing the absorption efficiency of Green light. In addition, when analysing the structure and elemental composition of Au-NPs by varying the laser power, a similar trend is observed at both wavelengths.

In case of Au-Fe<sub>2</sub>O<sub>3</sub> samples, it is even possible to comment on the temperature rise due to inclusion of Au-NPs when illuminated with UV and Green

wavelength. These results will be helpful to probe the temperature of the nanoscale objects, especially one dimensional, upon illumination of light.

We sincerely believe that, these results have shown that, LaAPT technique can be used as a potential tool to better understand the optical absorption properties of nanoscale material. But, the results and analysis presented in this thesis are more qualitative than quantitative. Using la-APT we can measure the increase of the absorption and of the temperature of the sample containing Au NPs only by comparison with the sample without Au NPs. However, the absolute value of the absorption cross-section or the absolute value of the maximum temperature cannot be measured. To realize this goal, there is need to couple the La-APT with the optical absorption set-up like SMS.

As briefly presented in this thesis, first encouraging results of SMS spectroscopy on nanometric tip have been obtained in the framework of the collaboration with the team of Natalia Del Fatti in Lyon. These results show the possibility to access to the absorption cross section along the tip apex. Now, by the combination of the La-APT and the SMS measurement, in-situ, it will be not only possible to have direct correlation between structural and optical absorption properties but will also provide quantitative information on the absorption and heating. Moreover, the high DC field applied in the atom probe experiment can substantially change the optical absorption properties of the material. Hence, measuring the absorption properties of tip shaped samples in the condition of APT analysis (with the application of the strong electric field) will open to a new research topic, concerning the optical properties of materials under high external DC field. The walk towards this goal is in progress and this thesis will serve as a first few steps towards it.

The correlative approach to understand the relation between optical emission to the structural and compositional changes, as shown in the case of InGaN/GaN quantum wells, is another example showing that the coupling of La-APT with optical emission spectroscopy will strongly improve our knowledge on the nano-materials for light emission. Also in this case, the possibility to make optical and structural analysis on the same sample, in the same chamber (in-situ) and under high electric dc field, will gives access to new information on the optical emission properties as a function of surface dc field, and, during the APT analysis, as a function of the local structural composition.

To summarize, in the quest of understanding the ultimate relation between structural and optical properties of the nanoscale material using Laser assisted Atom Probe Tomography this thesis will act like a guideline.

## Abstract

Laser assisted atom probe tomography (LaAPT) is a powerful technique for the structural and chemical analysis of materials at near atomic resolution and in 3-dimensions. Considering the nanoscale specimen and the use of ultra-fast laser pulses in the technique, this instrument can also be used to study light-matter interaction at the nanoscale. Hence the technique will not only give structural and chemical characterization at atomic scale of materials but also new insight on the optical and electrical properties at nano-scale.

In this regard, the prime objective of this thesis is to study the feasibility of LaAPT as a versatile tool to investigate structural and optical properties of the nanoscale material with particular emphasis on materials for solar-energy plant, like METallic CERamics (CERMET), and for light emission, like InGaN/GaN quantum wells. The optical absorption properties of nanotips of Au-nanoparticles embedded in MgO and Fe<sub>2</sub>O<sub>3</sub> matrix, have been studied coupling LaAPT analysis with optical and electron microscopy. Moreover, the heating process induced by the laser-energy absorption was also discussed. In the case of InGaN/GaN quantum wells, a novel correlative approach was introduced to study the direct correlation between structural and optical emission properties using LaAPT, Scanning Transmission Electron Microscopy (STEM) and micro-photoluminescence ( $\mu$ -PL) spectroscopy.

## Résumé

La sonde atomique tomographique assistée par laser (LaAPT) est une technique très performante pour la caractérisation structurale et chimique des matériaux à l'échelle atomique en trois dimensions. Considérées les dimensions nanométriques des échantillons analysés en La-APT, la La-APT est aussi un instrument de choix pour l'étude de l'interaction lumière-matière à l'échelle nanométrique.

Le premier objectif de ce travail de thèse a été de montrer la possibilité d'utiliser la La-APT comme une techniques très versatile pour l'étude des propriétés structurales et optiques des matériaux, avec un regard particulier vers les matériaux pour les centrales à énergie solaire, comme les céramiques métalliques (CERMETS), et les matériaux pour l'émission de lumière, comme les puits quantiques InGaN/GaN. Les propriétés optiques d'absorption des nano-pointes de MgO et Fe<sub>2</sub>O<sub>3</sub> avec des inclusions (nano-particules) d'or ont été étudiées en couplant les analyses de sonde atomique assistée par laser aux mesures de microscopie optique et électronique. De plus, le processus d'échauffement induit par l'absorption de l'énergie laser a été discuté. Dans le cas des puis quantiques de InGaN/GaN un nouvel approche a été introduit pour étudier la corrélation directe entre les propriétés structurales et d'émission de lumière en utilisant la LaAPT, la microscopie électronique à transmission (STEM) et la spectroscopie de micro-photoluminescence ( $\mu$ -PL).